Antarctic Circumpolar Current dynamics, and terrigenous sediment provenance variations in the Drake Passage during the last 140,000 years

Kumulative Dissertation zur Erlangung des akademischen Grades eines

Doktors der Naturwissenschaften: Doctor rerum naturalium

– Dr. rer. nat. –

am der Fachbereich für Geowissenschaften

der Universität Bremen

vorgelegt von

Shuzhuang Wu

Bremerhaven, 2020

Gutachter: Prof. Dr. Ralf Tiedemann
Alfred-Wegener-Institut Helmholtz-Zentrum für Polar- und Meeresforschung, Bremerhaven
Universität Bremen FB 5 Geowissenschaften, Bremen

Prof. Dr. Ralph Schneider
Institut für Geowissenschaften, Univeristät Kiel

Erklärung

Hiermit erkläre ich an Eides statt, dass ich die vorliegende Arbeit ohne unzulässige Hilfe Dritter und unter Verwendung keiner als der von mir angegebenen Quellen und Hilfsmittel angefertigt habe. Die aus fremden Quellen wörtlich oder inhaltlich übernommenen Informationen sind als solche kenntlich gemacht.

Bremerhaven, 2. June 2020

Shuzhuang Wu

Datum des Promotionskolloquiums: 28. August 2020

Versicherung an Eides Statt / *Affirmation in lieu of an oath*

gem. § 5 Abs. 5 der Promotionsordnung vom 18.06.2018 /*according to § 5 (5) of the Doctoral Degree Rules and Regulations of 18 June, 2018*

Ich / I, Shuzhuang Wu, Am Alten Hafen 26, 27568 Bremerhaven. 3108355

(Vorname / First *Name*, Name / *Name*, Anschrift / *Address*, ggf. Matr.-Nr. / *student ID no., if applicable)*

versichere an Eides Statt durch meine Unterschrift, dass ich die vorliegende Dissertation selbständig und ohne fremde Hilfe angefertigt und alle Stellen, die ich wörtlich dem Sinne nach aus Veröffentlichungen entnommen habe, als solche kenntlich gemacht habe, mich auch keiner anderen als der angegebenen Literatur oder sonstiger Hilfsmittel bedient habe und die zu Prüfungszwecken beigelegte elektronische Version (PDF) der Dissertation mit der abgegebenen gedruckten Version identisch ist. / *With my signature I affirm in lieu of an oath that I prepared the submitted dissertation independently and without illicit assistance from third parties, that I appropriately referenced any text or content from other sources, that I used only literature and resources listed in the dissertation, and that the electronic (PDF) and printed versions of the dissertation are identical.*

Ich versichere an Eides Statt, dass ich die vorgenannten Angaben nach bestem Wissen und Gewissen gemacht habe und dass die Angaben der Wahrheit entsprechen und ich nichts verschwiegen habe. */ I affirm in lieu of an oath that the information provided herein to the best of my knowledge is true and complete.*

Die Strafbarkeit einer falschen eidesstattlichen Versicherung ist mir bekannt, namentlich die Strafandrohung gemäß § 156 StGB bis zu drei Jahren Freiheitsstrafe oder Geldstrafe bei vorsätzlicher Begehung der Tat bzw. gemäß § 161 Abs. 1 StGB bis zu einem Jahr Freiheitsstrafe oder Geldstrafe bei fahrlässiger Begehung. / *I am aware that a false affidavit is a criminal offence which is punishable by law in accordance with § 156 of the German Criminal Code (StGB) with up to three years imprisonment or a fine in case of intention, or in accordance with § 161 (1) of the German Criminal Code with up to one year imprisonment or a fine in case of negligence.*

Bremerhaven, 02.06.2020

Ort / *Place*, Datum / *Date*

Unterschrift / *Signature*

Acknowledgements

This PhD project was funded by the Alfred Wegener Institute, Helmholtz Centre for Polar and Marine Research (AWI) and the China Scholarship Council (CSC No. 201604910671). The work presented here is the result of my four-year stay at AWI. First of all, I want to thank my supervisor Prof. Ralf Tiedemann, without his helpful guidance and support that would not have been possible. I am really grateful for the opportunity of working at AWI.

Particularly, I'd like to thank Dr. Gerhard Kuhn, Dr. Frank Lamy, Prof. Dr. Bernhard Diekmann, Dr. Lester Lembke-Jene and Dr. Xufeng Zheng, for the many stimulating scientific discussions and their support in solving technical problems. I want to thank Prof. Helge W. Arz and Dr. Norbert Nowaczyk for their great effort in improving the age models. Also, I acknowledge Prof. Dr. Ralph Schneider and Dr. Thomas Ronge for reviewing this thesis and thank the entire senior scientists from our department for their help and expertise.

I am grateful for having technical and scientific support from Dr. Christian Hass, Dr. Huang Huang, Dr. Marcus Gutjahr, Dr. Jürgen Titschack, Rita Fröhlking, Susanne Wiebe, Valea Schumacher, Michael Seebeck and Aysel Sorensen. Without their great help, I would not have been able to create such interesting datasets. I thank the master crew and science party of Research Vessel Polarstern Expedition PS97 for their professional help in retrieving the excellent samples. Furthermore, I want to thank all the legendary MarGeo PhD-students (current and former) for the great time we had.

Last but not least, I want to express my particular gratitude to my parents and all my family members, who supported me in every detail of my life. Specially, I would like to thank my fiancée Lizhen whose has put all of the time and efforts into helping me become the best version of me.

Abstract

The Antarctic Circumpolar Current (ACC) is the largest ocean current system on Earth. Through promoting deep water upwelling and new water masses formation, the ACC plays a crucial role on global ocean circulation and climate changes. The Drake Passage is the narrowest constriction for the ACC and exerts a strong control on the physical, chemical, and biological exchange between the Pacific and Atlantic Ocean. Resolving changes in the ACC through this specific channel is, therefore, important for elevating our knowledge of the Southern Ocean's role in global ocean circulation and climate variability. However, previous studies showed a significant disagreement of the ACC flow speed changes and its potential impacts on ocean circulation and climate variability remain elusive.

In Wu et al., (2019), we identified southern Patagonia and the Antarctic Peninsula as the main sources for terrigenous sediments in the modern Drake Passage region, based on a comprehensive set of surface sediment samples. We found the variability of the ACC shows a clear bottom current speed pattern in the Drake Passage responding to the dynamics of ocean fronts, in agreement with modern observation. Understanding present-day sediment provenance and transport processes is crucial for studies about the dynamics of ocean circulation, as well as for paleoclimate reconstructions in the Drake Passage.

Further, we reconstruct changes in the ACC strength in the central Drake Passage over the past 140,000 years. We found substantial reductions in ACC bottom flow speeds during the glacial periods and increased bottom currents during interglacials. The amplitude was larger during Termination II compared to Termination I. Superimposed on these long-term changes, we found strong millennial-scale fluctuations in ACC intensity, increasing in amplitude toward the Last Glacial Maximum (LGM). We hypothesize that the central ACC reacts highly sensitive to the Southern Hemisphere millennial-scale climate oscillations, likely related to westerly's wind stress, oceanic fronts and Antarctic sea ice extent during the LGM. This strong variation of ACC regulates Pacific-Atlantic water mass exchange via the "cold water

route" and could significantly affect the Atlantic Meridional Overturning Circulation (AMOC).

In a third study, the mineralogical, magnetic and geochemical properties of terrigenous sediments reveal that the fine-grained materials mainly derived from western Patagonia and the Antarctic Peninsula over the last 140 ka. The ACC might have severed as a major driver for the sediment transport in the Drake Passage region. Expansion of ice sheets in Patagonia and on the Antarctic Peninsula together with relative sea-level lowstands enhanced the efficiency of terrigenous input during glacial maxima. Our high-resolution records reflect the waxing and waning of glaciers in southern Patagonia and on the Antarctic Peninsula.

In the last study, authigenic Nd and Pb isotopic records from the central Drake Passage deciphered past water mass mixing in the Southern Ocean during the last 140,000 years. We found enhanced Pacific-derived deep waters into the deep Southern Ocean at the expense of the North Atlantic-derived waters during glacial times. A pronounced gradient between mid-depth and deep waters suggests a stratified deep ocean during glacial periods. Enhanced stratification together with a stronger biological pump would support an enhanced storage of CO_2 in the deep Southern Ocean during glacial maxima.

Finally, this thesis improves our understanding of terrigenous sediment sources, changes in the ACC dynamics and ocean circulation in the Pacific sector of the Southern Ocean over orbital to millennial time-scales. The studies provide new insights into the evolution of the ACC dynamic changes in the central Drake Passage and its potential influences on global thermohaline circulation over the past 140,000 years. Future sedimentological and palaeoceanographic work should reconstruct Quaternary changes of the ACC across a meridional transect in the Drake Passage to better quantify the ACC and throughflow transport and velocities.

Zusammenfassug

Der antarktische Zirkumpolarstrom (ACC) ist die mächtigste Meeresströmung der Erde. Durch Tiefwasseraufstieg und der Bildung neuer Wassermassen spielt der ACC eine entscheidende Rolle für die globale Ozeanzirkulation und den Klimawandel. Die Drake Passage ist die engste Stelle für den ACC und übt daher eine starke Kontrolle über den physikalischen, chemischen und biologischen Austausch der Wassermassen zwischen Pazifik und Atlantik aus. Klärung der Veränderungen des ACCs durch dieses Gateway ist daher von entscheidender Bedeutung, um unser Verständnis der Rolle des Südlichen Ozeans zur globalen Variabilität der Ozeane und des Klimas zu verbessern. Frühere Studien zeigten jedoch signifikante Uneinigkeiten über die Änderungen der ACC-Strömungsgeschwindigkeiten, und ihre möglichen Auswirkungen sowohl auf die Ozeanzirkulation als auch auf die Klimavariabilität sind weiterhin schwer fassbar.

In Wu et al. (2019) identifizierten wir Südpatagonien und die Antarktische Halbinsel als Hauptquellen für terrigene Sedimente in der rezenten Drake-Passagen Region basierend auf einem umfassenden Satz von Oberflächensedimentproben. Wir fanden heraus, dass die Variabilität des ACCs in Übereinstimmung mit der rezenten Beobachtung ein klares Geschwindigkeitsmuster der Bodenströmungen in der Drake-Passage zeigt, das auf die Dynamik der Ozeanfronten reagiert. Das Verständnis der Herkunft und der Transportprozesse von Sedimenten ist entscheidend für Studien zur Dynamik der Ozeanzirkulation sowie für Paläoklima-Rekonstruktionen in der Drake-Passage.

Darüber hinaus rekonstruieren wir Änderungen der ACC-Stärke in der zentralen Drake-Passage in den letzten 140.000 Jahren. Wir fanden erhebliche Verringerungen der ACC-Bodenströmungsgeschwindigkeiten während der Eiszeiten und erhöhte Bodenströme während der Zwischeneiszeiten. Die Amplitude war während der Termination II größer als während der Termination I. Diese langfristigen Veränderungen wurden durch starke Schwankungen der ACC-Intensität in tausendjährigen Intervallen überlagert, deren Amplitude in Richtung des letzten

Gletschermaximums (LGM) zunahm. Wir nehmen an, dass der zentrale ACC sehr empfindlich auf die tausendjährigen Klimaschwankungen der südlichen Hemisphäre reagiert, die wahrscheinlich mit dem Windstress der Westwinde, den Ozeanfronten und der Ausdehnung des Meereises in der Antarktis während der Kaltzeiten zusammenhängen. Diese starke Variation des ACCs reguliert den pazifisch-atlantischen Wassermassenaustausch über die „Kaltwasserroute“ und könnte die atlantische meridionale Umwälzzirkulation (AMOC) erheblich beeinflussen.

In einer dritten Studie zeigen die mineralogischen, magnetischen und geochemischen Eigenschaften terrigener Sedimente, dass die feinkörnigen Sediment-Komponenten in den letzten 140.000 Jahren hauptsächlich aus Westpatagonien und der Antarktischen Halbinsel stammen. Der ACC war maßgebend für den Sedimenttransport in der Drake-Passagen Region verantwortlich. Die Ausdehnung der Eisschilde in Patagonien und auf der Antarktischen Halbinsel zusammen mit dem relativen Tiefstand des Meeresspiegels verstärkten den terrigenen Eintrag während der Hauptvereisungsphasen. Unsere hochauflösenden Aufzeichnungen spiegeln das Wachsen und Abnehmen von Gletschern in Südpatagonien und auf der Antarktischen Halbinsel wider.

In der letzten Studie wurden durch Analysen der authigenen Nd- und Pb-Isotopenverhältnisse aus der zentralen Drake-Passage die Vermischung von Wassermassen im Südpolarmeer während der letzten beiden glazial-interglazialen Perioden entschlüsselt. Wir fanden während der Kaltzeiten einen verstärkten Zustrom von tiefem Pazifikwasser bei reduziertem Eintrag von Nordatlantischem Tiefenwasser im tiefen Südpolarmeer. Ein ausgeprägter Gradient zwischen mittleren und tiefen Wassermassen deutet auf einen geschichteten tiefen Ozean während der Eiszeiten hin. Eine intensivierte Schichtung zusammen mit einer stärkeren biologischen Pumpe würde eine erhöhte Speicherung von CO_2 im tiefen Südpolarmeer während der Hauptvereisungsphasen unterstützen.

Schließlich verbessert diese Arbeit unser Verständnis der terrigenen Sedimentquellen, der Veränderungen der ACC-Dynamik und der Ozeanzirkulation im pazifischen Sektor des Südlichen Ozeans für Orbital- bis Millennia-Zeitskalen. Die

Studien liefern neue Einblicke in die Entwicklung der ACC-Dynamik in der zentralen Drake-Passage und ihre möglichen Einflüsse auf die globale thermohaline Zirkulation während der letzten 140.000 Jahre. Zukünftige sedimentologische und paläozeanographische Arbeiten sollten quartäre Änderungen des ACCs über einen meridionalen Schnitt in der Drake-Passage rekonstruieren, um dort den Durchfluss des ACCs und die Geschwindigkeiten besser zu quantifizieren.

Contents

1 Introduction

1.1 Background and motivation

The Antarctic Circumpolar Current (ACC) is the world's largest current system, which plays a crucial role in distributing heat, freshwater and carbon around the globe (Marshall and Speer, 2012). Through linking the deep and shallow layers and enhancing pronounced upwelling in the interior ocean, the ACC exerts a fundamental influence on the global overturning circulation and climate change (Marshall and Speer, 2012; Rintoul, 2018; Toggweiler *et al.*, 2006). Moreover, the ACC thermally isolates Antarctica by limiting poleward meridional heat transport and thus regulates the stability of Antarctic ice sheets (Lamy *et al.*, 2015; Zachos *et al.*, 2001).

The ACC strength is mainly driven by the southern westerly winds (SWW) across the circumpolar belt, buoyancy forcing comprising heat and freshwater inputs (McCave *et al.*, 2014; Toggweiler *et al.*, 2006). The lack of continents in the latitudinal band of Drake Passage (56° S–58° S) allows the zonal transport to be focused into multiple jets (Rintoul, 2018). The Drake Passage is the most important oceanic gateway along the pathway of the ACC (Lamy *et al.*, 2015; Rintoul, 2018). Resolving changes in the ACC through this gateway is, therefore, crucial for advancing our understanding of the Southern Ocean's role in global ocean and climate variability. However, the ACC dynamics are still poorly constrained over millennial to glacial-interglacial scales.

Within this thesis, I applied multiple approaches to reconstruct past changes in the ACC and terrigenous sediment sources in the Drake Passage region over millennial to glacial-interglacial scales. The reconstructions of the ACC flow speeds showed an apparent disagreement in different sectors of the Southern Ocean (Lamy *et al.*, 2015; Lynch‐Stieglitz *et al.*, 2016; Mazaud *et al.*, 2010; McCave *et al.*, 2014; Roberts *et al.*, 2017). High-resolution sediment records from the central Drake Passage provided new insights on this issue and the potential role of ACC on the global overturning circulation and climate change. Moreover, climatic perturbations induced variations of terrigenous sediment supply and their transport mechanisms

remain elusive in the Southern Ocean (Diekmann *et al.*, 2000; Petit *et al.*, 1990; Weber *et al.*, 2012; Yamazaki and Ikehara, 2012). Resolving terrigenous sediment provenance in the past would advance our understanding of the history of weathering intensity, transport mechanism and ice sheet dynamics. Deep water stratification has been proposed as a mechanism to regulate the carbon storage in the Southern Ocean on glacial-interglacial timescales (Basak *et al.*, 2018; Charles *et al.*, 2010; Jess F. Adkins, 2002; Ninnemann and Charles, 2002; Sigman *et al.*, 2010), however, the structure and source of the Southern Ocean water masses remain equivocal. In the last study, I used geochemical tracers to reconstruct past water masses sources and mixing processes in the Southern Ocean over the last 140 ka and provided evidence to support the deep stratification closely linked to atmospheric CO_2 level in the geological past.

1.2 The Antarctic Circumpolar Current

The total ACC mean transport through the Drake Passage is ~150 ± 20 Sv (1 Sv = 10^6 m^3/s, Fig. 1.1) according to previous oceanographic studies (Cunningham *et al.*, 2003; Donohue *et al.*, 2016; Drouin and Lozier, 2019; Koenig *et al.*, 2014; Meredith *et al.*, 2011b; Renault *et al.*, 2011). Three major ACC oceanographic fronts have been identified: the Subantarctic Front (SAF), the Polar Front (PF), and the Southern ACC Front (SACCF) (Orsi *et al.*, 1995). The ACC transport through the Drake Passage is dominant in the north of PF, while the transport in the south of PF is generally less than 20% (Fig. 1.1B) (Cunningham *et al.*, 2003; Donohue *et al.*, 2016).

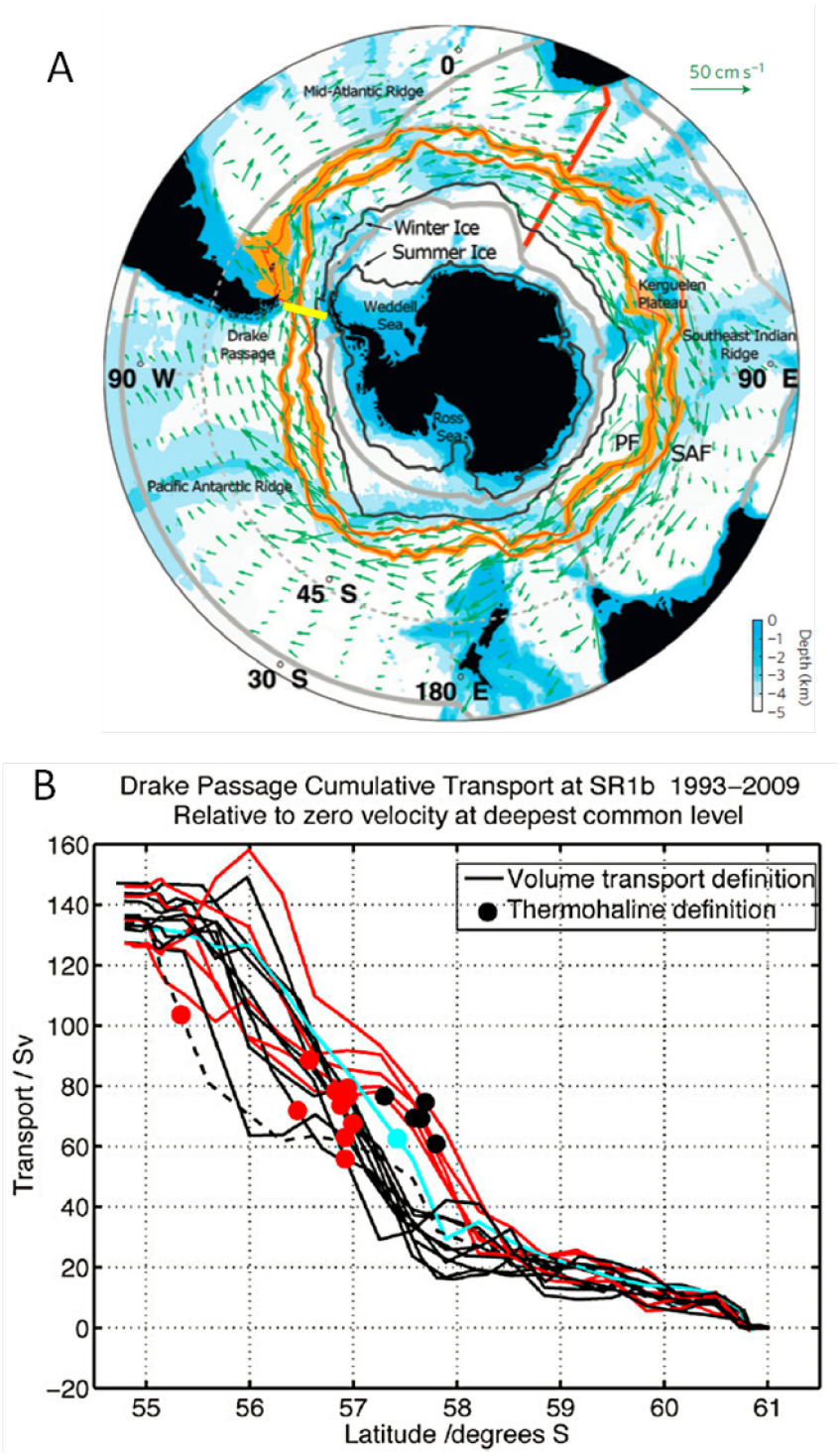

Fig. 1.1. A, The ACC flow speeds with oceanic fronts and seasonal sea ice from (Marshall and Speer, 2012). The oceanic fronts, the Subantarctic Front (SAF) and Polar Front (PF), are marked in orange lines and whose thickness the variability in the latitudinal position. The green arrows represent the observed speed and direction of surface ocean currents, which were measured by drifters floating at a depth of 15 m. The summer (minimum) and winter (maximum) extent of sea ice are marked by the black lines and the main topographic features are labeled. The yellow line indicates the section of observation transport across the Drake Passage. B, Cumulative transport across Drake Passage, accumulated south to north (Meredith *et al.*, 2011b).

The strong eastward flow of ACC carries a mixed water mass, namely Circumpolar Deep Water (CDW), which is a mixture of North Atlantic Deep Water (NADW), Antarctic Bottom Water (AABW), Pacific Deep Water (PDW) and Indian Deep Water (IDW) (Talley, 2013). Surface buoyancy fluxes and vigorous westerly winds drive the southward flowing deep waters to upwell in the Southern Ocean. The upwelled denser NADW and portions of the lighter PDW/IDW transfer to the Lower Circumpolar Deep Water (LCDW) and produce AABW. The remaining PDW/IDW forms the core of Upper Circumpolar Deep Water (UCDW), which upwells and forms the principle source of Antarctic Intermediate Water (AAIW) and Subantarctic Mode Water (SAMW) near the SAF and the Subtropical Front (STF), respectively (Talley, 2013). In contrast, the upwelled denser LCDW flows southward where sea ice is formed and its buoyancy decreases, oceanographic processes that could fuel primarily into the densest AABW (Fig. 1.2) (Talley, 2013).

The ACC connects the Pacific, Atlantic and Indian Ocean basins and transports water masses to the north, thus enabling the global ocean circulation (Fig. 1.2) (Marshall and Speer, 2012; Rintoul, 2018). Through regulating the heat, salinity and nutrients exchange between these ocean basins, the ACC therefore exerts an important influence on Earth's climate system (Marshall and Speer, 2012; Talley, 2013).

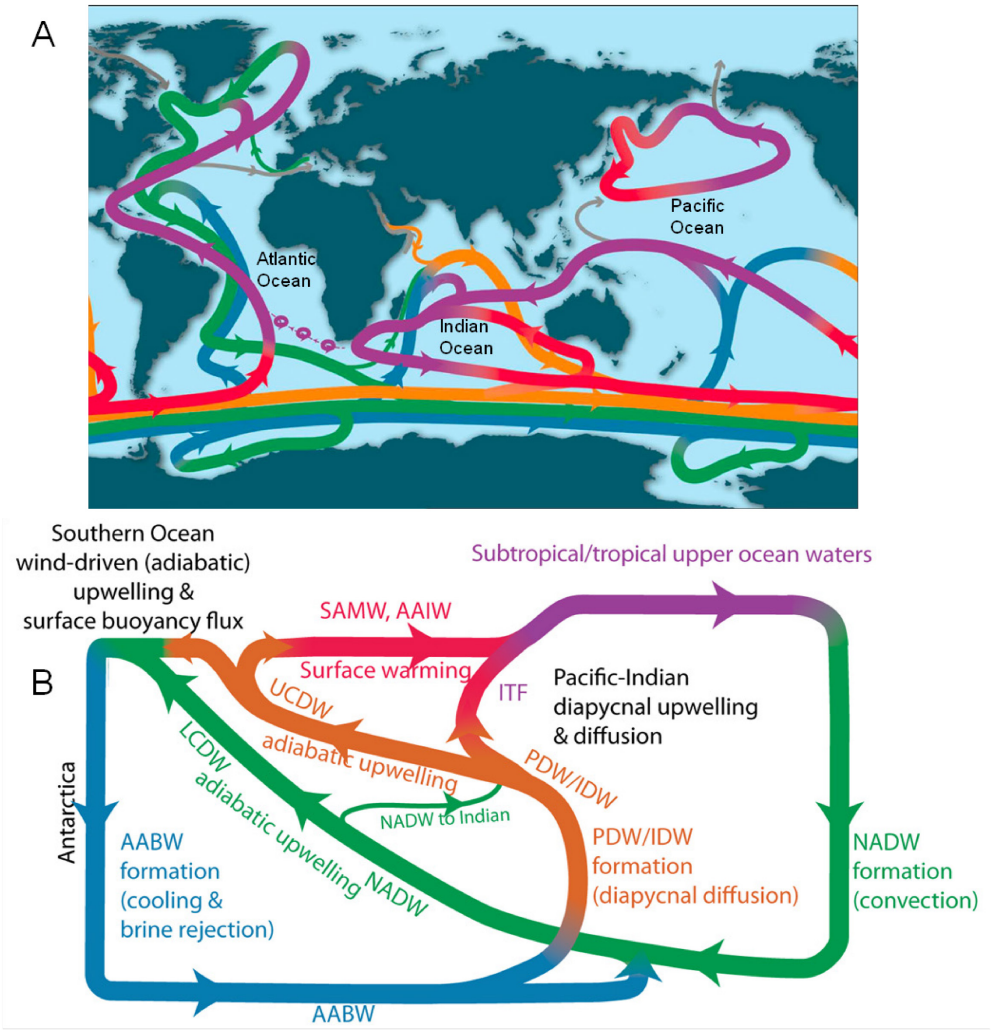

Fig. 1.2. A, Schematic of the global overturning circulation from (Talley, 2013). Purple = upper ocean and thermocline. Red = denser thermocline and intermediate water. Green = North Atlantic Deep Water (NADW). Blue = Antarctic Bottom Water (AABW). Orange = Pacific Deep Water and Indian Deep Water (PDW/IDW). Gray = Bering Strait components and Mediterranean and Red Sea inflows. B, Schematic of the overturning circulation in a two-dimensional view, with important physical processes (Talley, 2013).

1.3 The ACC gateway – Drake Passage

1.3.1 Geological setting

The Drake Passage received its name from the famous English privateer Sir Francis Drake in 1616 by a Flemish expedition (Martinic, 2019). The Drake Passage is located between South America and the Antarctic Peninsula (56°S–58°S), with a width of roughly 800 km and an average depth of ~3400 m.

The southernmost parts of South America comprises of southern Patagonia and Tierra del Fuego, which roughly correspond to physiographic units aligned parallel to

the active Pacific margin (Barker *et al.*, 1991; Diekmann *et al.*, 2000; Marinoni *et al.*, 2008). On the Pacific side, bedrock outcrops are characterized by calcalkaline tonalites and granodiorites of the Late Jurassic–Cretaceous Patagonian batholith, which intruded into metamorphosed basement rocks. A belt of deformed silicic volcanic rocks and ophiolitic assemblages, forming the western flank and the spine of the modern South Andean cordillera (Dalziel *et al.*, 1974). On the Atlantic side of the Andes, the rhyolites are overlain by Cretaceous and Cenozoic deposits of an earlier continental fore-land basin, which build up the foothills of the Precordillera and extend eastward into the Patagonian low land (Winslow, 1982). The plains on the Atlantic side are covered by large Quaternary periglacial deposits (Clapperton, 1993).

Along the Pacific-Chilean continental margin, terrigenous sediments mixed with biogenic carbonates are characterized by low quartz and low percentages of smectite, and higher amounts in chlorite and mica, which originate from low-grade metamorphic and magmatic rocks (Diekmann *et al.*, 2000; Marinoni *et al.*, 2000; Wu *et al.*, 2019). In contrast, higher quartz and smectite contents derived from more acid composition in the Atlantic sector (Diekmann *et al.*, 2000; Marinoni *et al.*, 2008).

The geology in the West Antarctic was influenced by the subduction of the (proto-) Pacific oceanic lithosphere beneath the continental margin of Gondwana and breakup-related movements of crustal blocks along the Bellingshausen Sea (Burton-Johnson and Riley, 2015; Hillenbrand *et al.*, 2009). The Antarctic Peninsula is part of a Late Mesozoic to Cenozoic magmatic arc and consists of slightly metamorphosed accretionary sedimentary rocks, which were intruded by intermediate to acidic plutonic rocks and are overlain by basic to intermediate volcanic (Barker *et al.*, 1991; Diekmann *et al.*, 2000). Recent alkaline volcanism on Deception Island (South Shetland Islands) is related to the spreading of the modern back-arc basin of the Bransfield Strait (Barker, 1982). The Antarctic Peninsula represents a deeply eroded magmatic arc of the Jurassic to late Tertiary Andean Orogeny (Elliot, 1997; Leat *et al.*, 1995; Rowley *et al.*, 1991). The Andean Orogeny led to the development of fore- and back-arc basins along the flanks of the Antarctic Peninsula batholiths (Elliot, 1997; Rowley *et al.*, 1991). Chlorite and well-crystallized smectite mainly

contribute to the clay mineral spectrum in this area (Diekmann *et al.*, 2000; Park *et al.*, 2019; Petschick *et al.*, 1996; Wu *et al.*, 2019). Another diagnostic feature is the low quartz content of this young and less evolved continental crust (Diekmann *et al.*, 2000; Petschick *et al.*, 1996; Wu *et al.*, 2019).

East Antarctica is an old shield with rocks >0.9 billion years, and is characterized by Precambrian crystalline rocks and Paleozoic to Mesozoic sedimentary rocks (Tingey, 1991). Terrigenous detritus from this acidic and weathered continental crust is characterized by high quartz contents (Diekmann *et al.*, 2000). The clay mineral assemblage in this area is dominated by Fe-Mg illite and chlorite (Diekmann and Kuhn, 1999; Petschick *et al.*, 1996). Smectite was found only locally and likely derived from Berkner Island (Diekmann and Kuhn, 1999).

1.3.2 Oceanographic setting

Since absence of continental barriers at the latitudes of Drake Passage, the compensating poleward geostrophic transport can extend to great depth. Consequently, submerged topography can influence the current transport and support a zonal pressure gradient (Meredith *et al.*, 2011b; Rintoul, 2018).

The Drake Passage is characterized by a pronounced temperature (and salinity) gradient (Fig. 1.3), that is separated by the PF and the steepness of isopycnals toward the Antarctic shelf (Grobe, 2007). The steep isopycnals provide a connection between the large deep-ocean reservoir of dissolved inorganic carbon and the surface ocean (Marshall and Speer, 2012), that contributes to the exchange between the ocean interior and the atmosphere. The outcropping isopycnals can modulate both the flux of carbon into the deep ocean as well as its release by deep convection and wind-driven upwelling (Marshall and Speer, 2012; Talley, 2013).

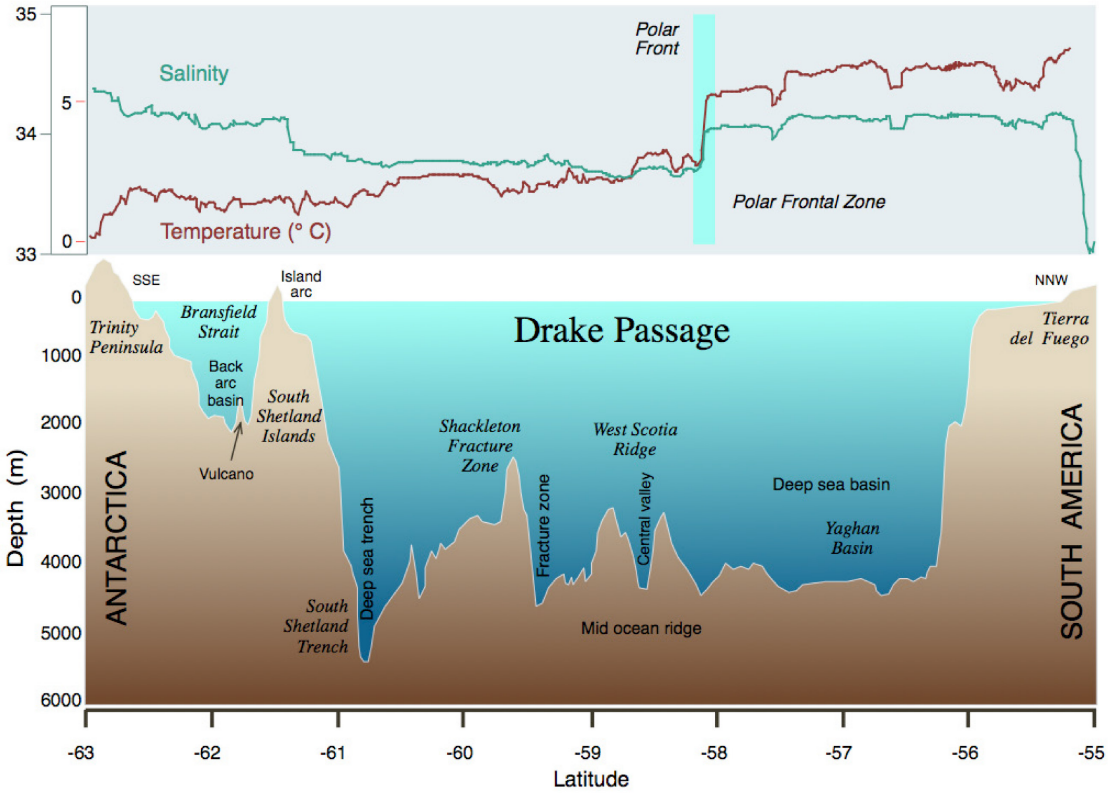

Fig. 1.3. Temperature and salinity across the Drake Passage (Grobe, 2007).

The ACC transports fresh and cold water from Pacific through the Drake Passage to the Atlantic, which is referred to the "cold water route" (Rintoul, 1991). This cold water route is one of important return water source to the South Atlantic (Lamy *et al.*, 2015; Rintoul, 1991), which potentially affects the strength of the Atlantic Meridional Overturning Circulation (AMOC) (Knorr and Lohmann, 2003), in concert with the "warm water route", on which warm and salty water masses are transported through the Agulhas leakage from Indian Ocean (Beal *et al.*, 2011; Gordon, 1986).

The position and intensity of the SWW belt plays an important role for the ACC flowing through the Drake Passage (Allison *et al.*, 2010; Marshall and Speer, 2012; Toggweiler *et al.*, 2006). Changes in both wind strength and position can affect the level of coupling with the ocean jets and hence impact on the flow (McCave *et al.*, 2014). Most climate reconstructions suggest a northward displacement of the SWW belt and the associated oceanic fronts during the Last Glacial Maximum (LGM) (Gersonde *et al.*, 2005; Kohfeld *et al.*, 2013; Toggweiler *et al.*, 2006), although other

scenarios (no changes or southward displacement) cannot be fully excluded (Kohfeld *et al.*, 2013). In contrast, under anthropogenic climate warming, both observational data and model simulations argue for an increase in the SWW strength and a poleward movement (Beal *et al.*, 2011; Swart and Fyfe, 2012). Since wind forcing is the primary mechanical energy source for the overturning circulation (Wunsch and Ferrari, 2004), any changes in the intensity of the overturning in the Southern Ocean has a significant impact on the global overturning circulation and the efficiency of carbon storage (Anderson *et al.*, 2009; Jaccard *et al.*, 2016; Toggweiler *et al.*, 2006).

1.3.3 Palaeoceanographic overview

Although the Drake Passage is a bottleneck for the ACC, its opening time remains a long-standing debate. Based on geophysical analysis, Livermore et al., (2005) postulated that the shallow interbasin connection occurred during the Early Eocene (~50 Ma), whereas the deep ocean exchange developed around the Eocene-Oligocene boundary (34–30 Ma). The paleobathymetric study from Eagel and Jokat, 2014 suggested an intermediate-depth oceanographic gateway at 50–30 Ma (Fig. 1.4). These results are consistent with the chemical tracers reconstruction, reflecting massive reorganization and homogenization of Southern Ocean water masses around ~30 Ma (Scher *et al.*, 2015). However, the exact timing especially about the deep circulation linkage remains elusive (Barker *et al.*, 2007). Nevertheless, the opening of Drake Passage initiated the ACC formation around ~34–30 Ma and thereby thermally isolated Antarctica, which is considered to have contributed to the cooling and the onset of Antarctic glaciation at 33–34 Ma (Fig. 1.5) (Zachos *et al.*, 2001).

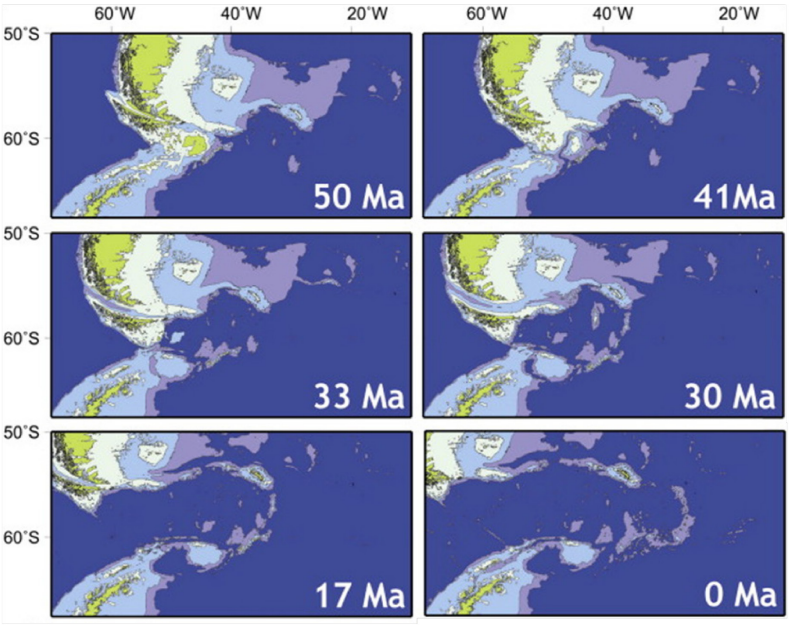

Fig. 1.4. Simple paleobathymetric reconstructions of Drake Passage based on present-day bathymetry and the tectonic reconstructions. Adapted from Eagles and Jokat (2014).

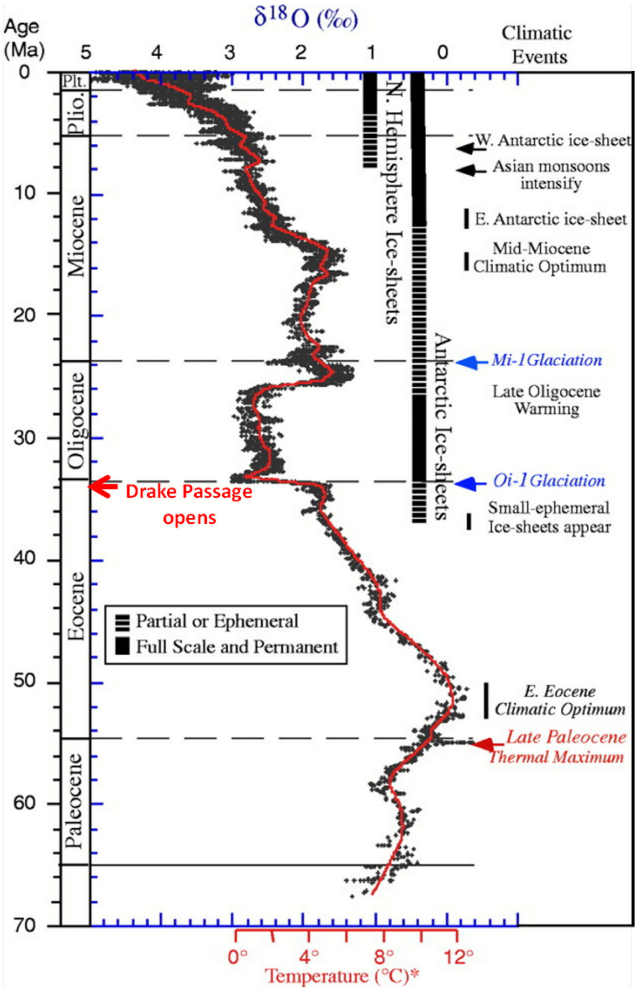

Fig. 1.5. Oxygen isotope record derived from benthic foraminifera for the Cenozoic (Zachos *et al.*, 2001). Arrows show climatic events and the open timing of Drake Passage.

1.4 Flow speed reconstructions

Palaeoceanographic studies usually apply diverse sedimentological, magnetic and geochemical properties to reconstruct paleoflow speeds (Bahr *et al.*, 2014; Lamy *et al.*, 2015; Mazaud *et al.*, 2010; McCave and Hall, 2006; McCave *et al.*, 1995; McCave *et al.*, 2017; Roberts *et al.*, 2017; Thornalley *et al.*, 2018). The terrigenous grain-size parameters have been successfully used for reconstructing near-bottom flow speeds (Lamy *et al.*, 2015; McCave *et al.*, 2014; McCave and Hall, 2006; Thornalley *et al.*, 2018). The idea bases on grain size variation across the Nova Scotia Rise between 3800 and 5000 m water depth that are related, independently of sediment supply, to changes in bottom current speeds (McCave *et al.*, 1995). Grain size sorting occurs during deposition and resuspension in the deep sea. Below 10-15 cm s^{-1}, selective deposition controls the mean grain-size in the non-cohesive 'sortable silt' range ($\overline{SS}$, mean of 10~63 μm, Fig. 1.6), whereas above that speeds winnowing may play a role on removing the fine fractions and extending the sorting range (McCave and Andrews, 2019; McCave and Hall, 2006).

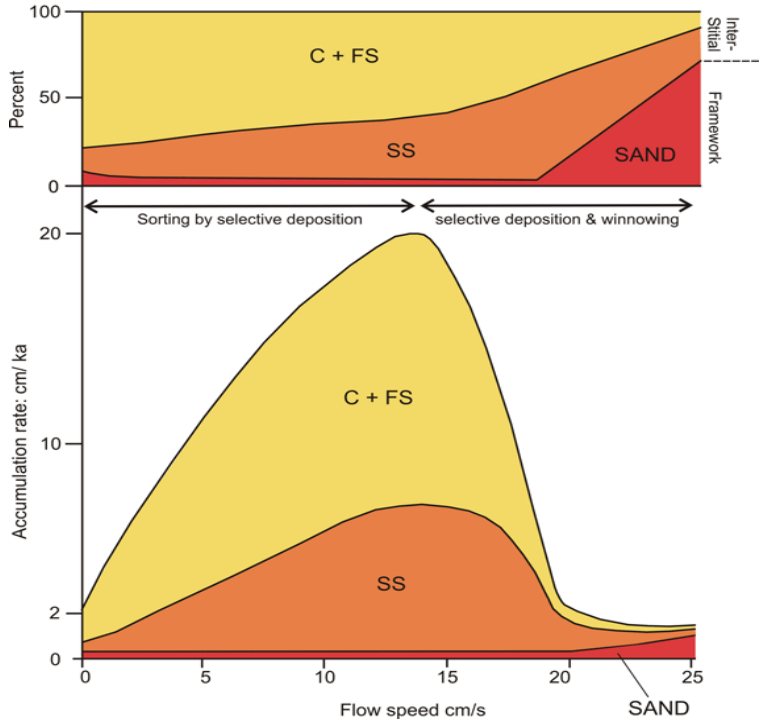

Fig. 1.6 Hypothetical variation of accumulation rate with increasing current speed. C+FS, clay and fine silt (<10 μm); SS, sortable silt (10–63 μm). Figure from McCave and Hall (2006).

The magnetic grains have also been used to reconstruct bottom speeds (Kissel *et al.*, 2009; Kissel *et al.*, 2013; Mazaud *et al.*, 2010). However, the magnetic grains are dominated by fine fraction, which mainly determine the concentration-dependent parameters (Hatfield *et al.*, 2013). Therefore, the magnetic signatures may record source signal instead of current intensity at a particular location.

Another promising proxy to reconstruct near-bottom paleocurrent speeds is Zirconium/Rubidium (Zr/Rb) ratio. Zirconium is typically accumulating in the heavy mineral fraction associated with the coarser grain sizes, while rubidium is preferentially retained in the clay mineral faction (Fralick and Kronberg, 1997). Previous studies found a positive correlation between grain size and Zr/Rb ratio (Chen *et al.*, 2006; Dypvik and Harris, 2001) and indicated that the Zr/Rb ratio can reflect changes in sediment fractions by current transport (Lamy *et al.*, 2015; Toyos *et al.*, 2020).

Available proxy data and model simulations provide limited information on the potential role of the ACC in driving changes in the global ocean circulation at glacial–interglacial and millennial timescales (Knorr and Lohmann, 2003; Lamy *et al.*, 2015; McCave *et al.*, 2014). In the Drake Passage sector, significant reductions of ACC during the last glacial were found at the Chilean continental margin (Lamy *et al.*, 2015), the entrance of Drake Passage (Toyos *et al.*, 2020) as well as south of the Falkland Islands (Roberts *et al.*, 2017). However, minimal change in the ACC flow speed was reconstructed in the Scotia Sea transect between the LGM and Holocene (McCave *et al.*, 2014). A relative decrease of abyssal current strength during glaciations was reconstructed in the north western Weddell Sea and Cape Basin (Diekmann *et al.*, 2003). In contrast, a strong ACC has been reconstructed for the last glacial in the Indian sector (Mazaud *et al.*, 2010; Molyneux *et al.*, 2007), south of Australia (Lynch-Stieglitz *et al.*, 2016) and along the eastern continental margin of New Zealand (Hall *et al.*, 2001). The reconstructed ACC strength show substantially different patterns between the Atlantic, Indian and Pacific sectors of the Southern Ocean. Therefore, the ACC intensity and its potential impacts on the global overturning circulation may have differed not only on temporal but also on spatial

scales in different sectors of the Southern Ocean.

1.5 Terrigenous sediment provenance reconstructions

Terrigenous sediments are the weathering products of rocks exposed at the Earth's surface, which are transported to the ocean by rivers, winds, and ice (Biscaye, 1965; Diekmann *et al.*, 2000; Petschick *et al.*, 1996; Wu *et al.*, 2019).

Clay mineralogy by X-ray diffraction has become a powerful tool to identify the provenance of fine-grained terrigenous sediments and weathering history in the world oceans (Biscaye, 1965; Diekmann *et al.*, 2000; Kuhn and Diekmann, 2002; Petschick *et al.*, 1996; Wu *et al.*, 2019). The clay mineral (< 2 μm fraction) comprises chlorite, illite, smectite and kaolinite, with lesser amounts of quartz and feldspars. The clay mineral assemblages in seafloor sediments show a pronounced latitudinal control (Biscaye, 1965; Griffin *et al.*, 1968; Petschick *et al.*, 1996). Chlorite and illite are concentrated at moderate and high latitudes, mainly within the glacial environment associated with weak chemical weathering; this is called the bipolar-type distribution (Biscaye, 1965; Diekmann and Kuhn, 1999; Diekmann *et al.*, 2000; Hillaire-Marcel and De Vernal, 2007; Petschick *et al.*, 1996). Whereas smectite and kaolinite are concentrated in the tropical-humid zone with intense chemical weathering; this is called the equatorial-type distribution (Biscaye, 1965; Griffin *et al.*, 1968; Hillaire-Marcel and De Vernal, 2007). These characteristics of clay mineral assemblages in deep-sea sediments have been widely applied to determine the weathering history, terrigenous sediment sources and transport mechanism in the world oceans. For example, Petschick et al. (1996) provided a detailed clay mineral distribution in the South Atlantic Ocean to constrain weathering intensity as well as sources and transportation pathways (Fig. 1.7). The kaolinite/chlorite ratios provide an important information of the sources and responsible transport processes for distributing sediments in the Atlantic Ocean (Petschick *et al.*, 1996).

Geochemical properties by X-ray fluorescence scanners allow rapid semi-quantitative estimation of major elements intensities in marine sediments. The intensities of terrestrial elements have been used to trace the supply of terrestrial

material to the ocean (Govin *et al.*, 2012; Haug *et al.*, 2001; Lamy *et al.*, 2019; Stuut *et al.*, 2007). A fundamental example is the reconstruction of rainfall in the Cariaco Basin based on Ti concentrations to infer changes in the hydrological cycle over northern South America (Haug *et al.*, 2001). A recent study used the Fe/Ca ratio of sediments to reconstruct precipitation-driven sediment input changes to the Southeast Pacific off Chile and deduce the atmosphere-ocean interaction over the past one million years (Lamy *et al.*, 2019).

Magnetic susceptibility can serve as a proxy to trace terrigenous sources as well. Precious studies found increased values of magnetic susceptibility occurred during glacial periods, since a greater supply of terrigenous ferromagnetic materials at cold stages (Diekmann *et al.*, 2000; Weber *et al.*, 2014). However, the interpretations for magnetic susceptibility in the Southern Ocean are open to debate (Diekmann *et al.*, 2000; Petit *et al.*, 1990; Weber *et al.*, 2012; Xiao *et al.*, 2016; Yamazaki and Ikehara, 2012).

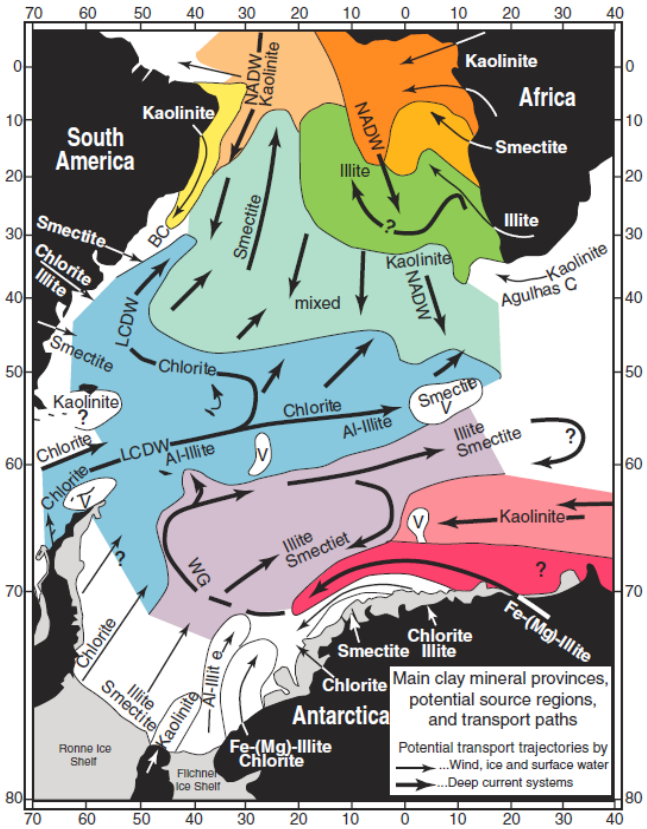

Fig. 1.7. Maps of clay mineral distribution in the South Atlantic, along with regional deep currents and local, near-continent surface currents from (Petschick *et al.*, 1996).

1.6 Water masses reconstructions

Neodymium (Nd) and lead (Pb) radiogenic isotope compositions are powerful tracers for the reconstruction of water masses mixing on different time scales (Abouchami *et al.*, 1997; Abouchami and Goldstein, 1995; Basak *et al.*, 2018; Frank, 2002; Hemming, 2003; Huang *et al.*, 2020; Molina-Kescher *et al.*, 2016).

Different continental regions and geological formations are characterized by distinctive $^{143}Nd/^{144}Nd$ ratios (Fig. 1.8). Within the samarium–neodymium (Sm-Nd) decay system, the radiogenic ^{143}Nd isotope is produced from α-decay of ^{147}Sm (half time of $^{147}Sm = 10^6$ Gyr). Sm is preferentially enriched in the mantle, whereas the Nd is enriched in the continental crust. Accordingly, the radiogenic ^{143}Nd is enriched in the mantle, whereas the non-radiogenic isotope ^{144}Nd is enriched in the crust (Frank, 2002; Jeandel *et al.*, 2007). Consequently, $^{143}Nd/^{144}Nd$ ratios are lower in crustal than in mantle material.

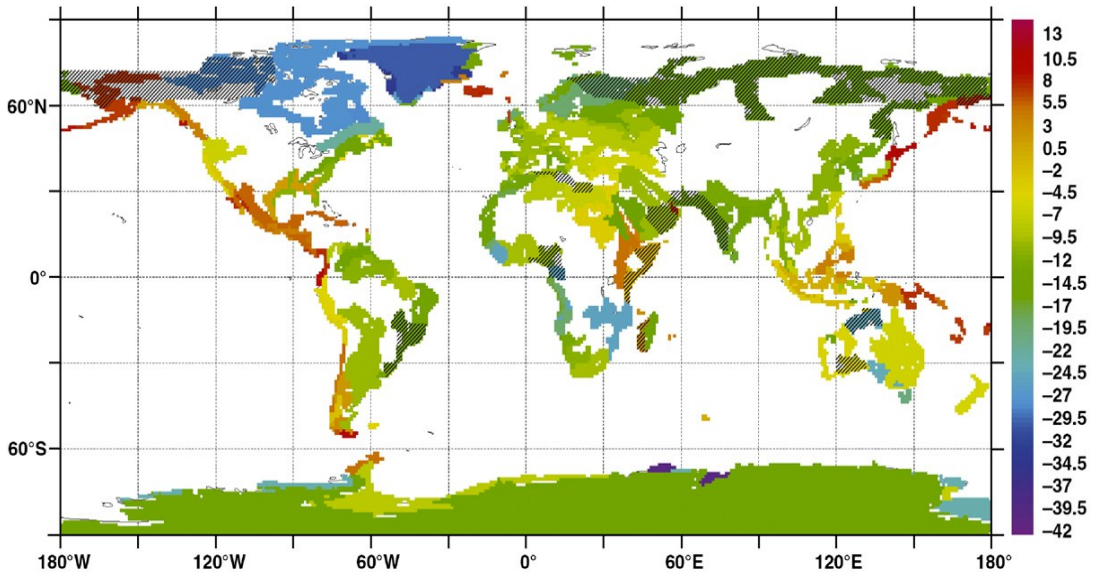

Fig. 1.8. Extrapolated map providing a picture of the εNd signatures of all the margins surrounding the ocean. Figure from Jeandel et al., (2007).

Seawater-derived Nd isotope signatures recorded in marine sediments extracted from the authigenic Fe-Mn oxyhydroxide fraction (expressed as $\varepsilon Nd = [(^{143}Nd/^{144}Nd_{(sample)}/ (^{143}Nd/^{144}Nd_{(CHUR)} - 1]*10^4)$ allow distinguishing the different major water

masses circulating in the ocean (Frank, 2002; Huang *et al.*, 2020; Pöppelmeier *et al.*, 2020; Piotrowski *et al.*, 2005). NADW is characterized by distinctively less radiogenic signatures (εNd = −13 to −16) (Bohm *et al.*, 2015; Lippold *et al.*, 2019) compared to more radiogenic signatures of PDW (εNd = 0 to −4) (Amakawa *et al.*, 2009; Du *et al.*, 2016; Fröllje *et al.*, 2016). The end-member εNd signatures of PDW and NADW have been suggested that remained constant at least for the past 2 million years (Pena and Goldstein, 2014). Intense mixing of NADW and PDW signatures in the ACC may play a role on modern homogenous εNd distribution (εNd = –7.5 to –8.5, Fig. 1.9) in the Drake Passage (Stichel *et al.*, 2012).

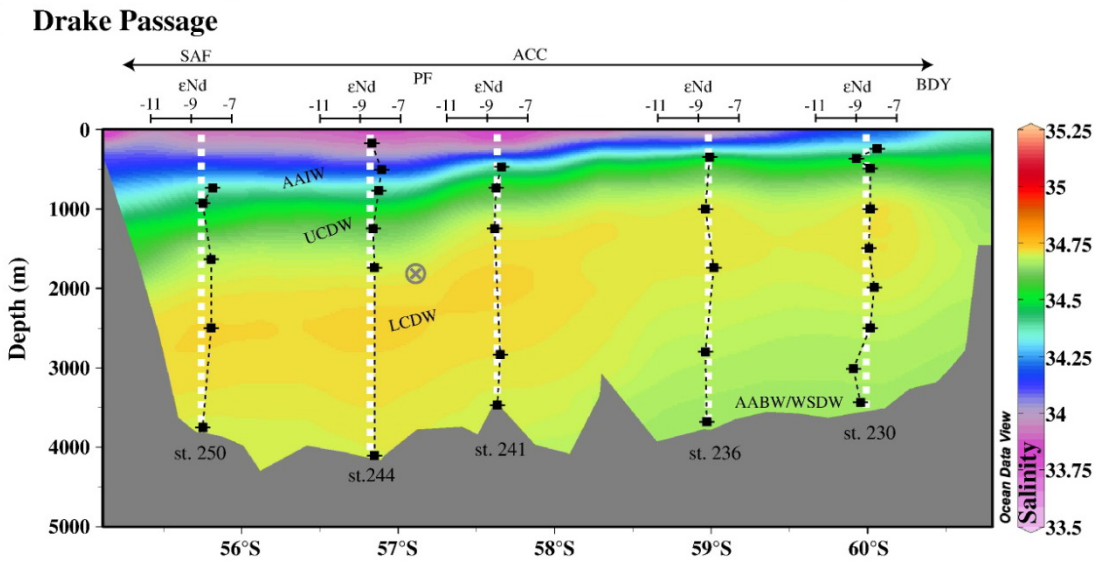

Fig. 1.9. The seawater Nd isotope distribution across the Drake Passage (Stichel *et al.*, 2012).

Similar to Nd, weathering of continental crust is the main input source of pre-anthropogenic natural Pb into the ocean (Abouchami and Goldstein, 1995). The decay of U and Th within the rocks produce the radiogenic isotopes of Pb (^{206}Pb, ^{207}Pb, ^{208}Pb), which are easier to mobilize from rocks and minerals during weathering than nonradiogenic ^{204}Pb (Frank, 2002). Present NADW is characterized by high ^{206}Pb/^{204}Pb ratios (~19.3), whereas deep Pacific water masses yield low ^{206}Pb/^{204}Pb ratios (~18.5 to ~18.8) (Abouchami and Goldstein, 1995; Frank, 2002). The other radiogenic Pb isotope pairs (^{208}Pb/^{204}Pb and ^{207}Pb/^{204}Pb) also reveal distinct features

for the different main deep-water masses (Abouchami and Goldstein, 1995; Frank, 2002). In contrast to Nd isotopes, hydrothermal input may influence the local dissolved Pb isotope signal, but it is considered to provide only a minor contribution (~2%) to the total oceanic budget (Chen and Wasserburg, 1986). The short residence time of Pb in seawater (~50 to 200 years) has been taken as an advantage for recording rapid water mass mixing (Huang *et al.*, 2020).

Previous studies showed more radiogenic εNd signatures in the Southern Ocean during the glacial periods (Piotrowski *et al.*, 2005; Piotrowski *et al.*, 2008; Skinner *et al.*, 2013) with a reduced NADW formation (Curry and Oppo, 2005) and thus more radiogenic signatures exported to the Southern Ocean. Measurements on cold water corals in the Drake Passage revealed a 2-εNd offset between LCDW (εNd = -8.2 ± 0.3) and UCDW (εNd = -6.3 ± 0.2) during the mid-Holocene, suggesting that PDW expanded into the Southern Ocean at this period (Struve *et al.*, 2019). Radiogenic εNd signatures of about -6.4 ± 0.3 occurred as well in the Drake Passage during Heinrich Event 1 (Robinson and van de Flierdt, 2009). These radiogenic signals imply that the Pacific-derived waters during cold stages might have primarily contributed to the deep Southern Ocean in contrast to a reduced export of NADW to the Southern Ocean. However, the scarcity of available data limits our understanding about how these water masses evolved in the Southern Ocean beyond the last glacial.

1.7 Objectives of this thesis

Palaeoceanographic research in the Drake Passage is still sparse due to lack of systematic sediment coring. Sampling in this region was executed with the American Navy Ship USNS Eltanin in the 1960s (Goodell, 1965). Severe weather conditions impeded sampling operation and strong bottom currents led to large areas with no sediment cover on oceanic crust. Most previous studies in this region are restricted to continental margins like the Chilean Margin (Caniupan *et al.*, 2011; Lamy *et al.*, 2015; Marinoni *et al.*, 2008) and the Antarctic Peninsula (Hillenbrand *et al.*, 2009; Park *et al.*, 2019). The terrigenous sediment supply into the Drake Passage is still poorly constrained. However, which is important for understanding the terrigenous sources

(ice caps) and transport processes.

The Drake Passage is the narrowest constriction on the ACC strength (Meredith *et al.*, 2011b), however, proxy evidence for the ACC flow intensity remains controversial (Lamy *et al.*, 2015; McCave *et al.*, 2014; Roberts *et al.*, 2017). Understanding the magnitude and sensitivity in the central ACC during the geological past is crucial for assessing its role within the global overturning circulation, in particular with regard to ongoing and future anthropogenic climate change. During RV Polarstern expedition PS97, we were happy to find a sediment drift in the rough terrain northeast of the Shackelton Fracture Zone where it cuts off the northern ridges of the West Scotia Ridge for successful sediment coring (Lamy, 2016) and for an interesting paleoenvironmental interpretation.

The specific objectives of the four studies that constitute this thesis are:

1) To determine the provenance of terrigenous sediment supply into the Drake Passage and its current-related grain size sorting with respect to modern ACC dynamics. I used a suite of surface sediments to decipher the following questions:

- *What is the terrigenous source for modern Drake Passage sediments?*
- *How do sediment proxy data compare with the modern ACC flow speed from ocean meter observation to provide a reliable flow speed calibration?*
- *What kind of factors might affect the correction between current meters and sortable silt?*

2) To understand the orbital- and millennial-scale changes in the ACC over the past 140,000 years. Grain size and geochemical properties (Zr/Rb ratio) are used to reveal the variability of the ACC in the central Drake Passage on multiple geological timescales, which will foster our understanding about the following questions:

- *How did the ACC change in response to paleoclimate change?*
- *What kind of mechanisms drove the ACC changes in the past?*
- *How did the ACC affect the AMOC in concert with the Agulhas leakage?*
- *Can warm phases of the last interglacial serve as analogues for future warmer*

conditions?

3) To reconstruct the late Quaternary terrigenous sediment supply to the Drake Passage in response to ice dynamics. The mineralogical, magnetic and geochemical properties were analyzed to answer the following questions:

- *Did the terrigenous sediment supply change in the Drake Passage region through glacial-interglacial cycles?*
- *How did changes in the terrigenous source affect the sediment characteristics?*
- *How did terrigenous sediment supply into the Drake Passage changes in response to ice sheet dynamics in southern Patagonia and on the Antarctic Peninsula?*

4) To reconstruct the stratification in the Southern Ocean linked to CO_2 changes over the past 140,000 years. The seawater-derived Nd and Pb isotope signatures are applied to answer the following questions:

- *What were the water mass sources in the Pacific sector of the Southern Ocean during the glaciation?*
- *How did the deep stratification change and regulate atmospheric CO_2 level during the last two glacial cycles?*

1.8 Author's contribution

Manuscript 1 (Chapter 3)

I carried out the most part of sortable silt and all XRD measurements at AWI in Bremerhaven. S. Ehrhardt performed a part of sortable silt measurement along the Chilean Margin. B. Diekmann, G. Kuhn and me contributed the XRD data analysis using MacDiff software. All the co-authors contributed to the interpretation of the data. I wrote the entire manuscript with substantial comments and suggestions by all co-authors.

Manuscript 2 (Chapter 4)

I performed high resolution grain size measurement with a total of 1520 sediment samples from the trigger and piston cores (PS97/085-3) using CILAS 1180 L laser diffraction particle-size analyzer. L. Dumm carried out 80 samples for the sortable silt measurement by Micromeritics SediGraph 5100. J. Titschack measured the ice rafted debris (IRD) content with the X-ray computed tomography. I preceded the IRD data aided by J. Titschack. H.W. Arz and G. Kuhn contributed the X-ray fluorescence (XRF) core scanning and magnetic susceptibility datasets. X.F. Zheng and J. Liu carried out the magnetic property measurement. L. Lembke-Jene and D. Nürnberg contributed the ^{14}C and ^{18}O data. H.W. Arz, N. Nowaczyk, F. Lamy and I generated the age model for core PS97/085-3. All the co-authors contributed to the interpretation of the results. I wrote the entire manuscript. All co-authors reviewed the draft version and contributed to the discussion.

Manuscript 3 (Chapter 5)

I prepared the samples and performed the clay mineral measurement with XRD. H.W. Arz and G. Kuhn contributed the XRF and magnetic susceptibility data. G. Kuhn calculated the mass specific magnetic susceptibility. G. Kuhn, B. Diekmann and me interpreted the clay mineral data. I wrote the manuscript and all authors discussed the results and improved the manuscript.

Manuscript 4 (Chapter 6)

I carried out the samples preparation and the authigenic Nd and Pb isotopes measurements at GEOMAR, Kiel. H. Huang and M. Gutjahr assisted with these measurements. G. Kuhn and R. Tiedemann arranged the measurement. All the co-authors contributed to the analysis of the results. I wrote the manuscript. All authors discussed the results and contributed to the final manuscript.

2 Material and Methods

2.1 The Expedition PS97 to the Drake Passage

This study is part of the "Paleoceanography of the Drake Passage (PaleoDrake)" program. The principle scientific goal of "PaleoDrake" is to enhance our understanding of the palaeoceanographic role of the Drake Passage during Quaternary global climate variations at orbital and sub-orbital timescales (Lamy, 2016).

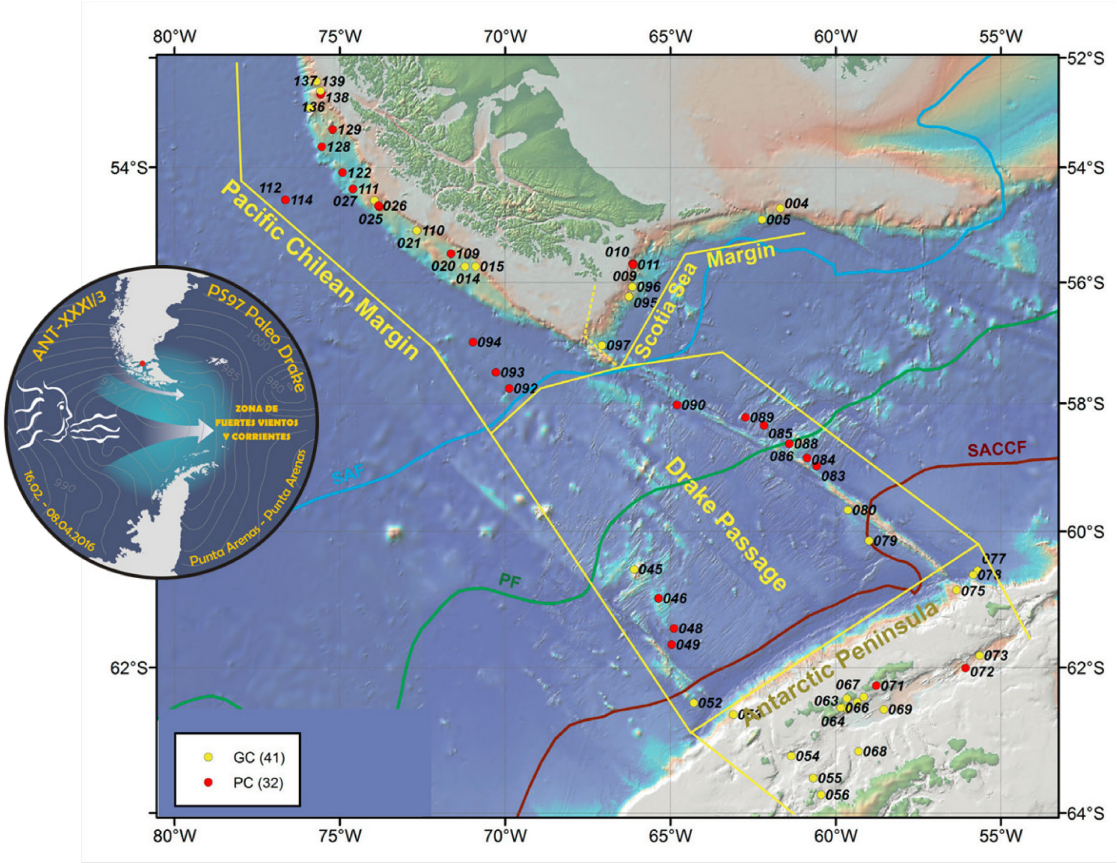

Fig. 2.1. Overview map with sampling stations (piston cores (PC) and gravity cores (GC)) in the Drake Passage region. Adapted from Lamy (2016).

The Polarstern expedition PS97 "PaleoDrake" took place from February to April in 2016. This expedition focused on marine geological investigations on two north-south transects across the western and central Drake Passage (Fig. 2.1) (Lamy, 2016). The recovered surface sediment samples and sediment cores from the open Drake Passage are the first deep-sea sediments taken in this area since the geological work performed with the American research vessel Eltanin in the 1960s (Goodell, 1965; Lamy, 2016). A second major geological working area was the

Argentinian/Chilean continental slope in the Scotia Sea and the Pacific southern Chilean continental margin between Cape Horn and the Magellan Strait. In the area of the Antarctic Peninsula, surface sediment samples and sediment cores were recovered in the Bransfield Strait.

All surface sample and sediment core PS97/085-3 used for this study were recovered during the PS 97 expedition. The sediment cores are located in the central Drake Passage, in the hope to provide important information about past changes in the ACC dynamics.

2.2 Sediment samples

A total of 51 seafloor surface samples were recovered in the Drake Passage region (Lamy, 2016). Samples were taken with a Multicorer and, in a few cases, with a Giant Box Corer from a depth range of ~650–4000 m water depth, in order to obtain undisturbed surface samples of the uppermost centimeter of the sediment. The detailed locations of the sampling stations are shown in Fig. 2.1. All surface sediments were investigated for bulk composition (carbonate, biogenic opal, organic carbon) and lithogenic mineralogy, silt mineralogy, silt grain-size distribution, and clay mineralogy.

Sediment core PS97/085-3 (58° 21.28′S, 62° 10.02′W; water depth 3090 m; 14.4 m core length) was obtained from the central Drake Passage, 22 nm north of the Polar Front. This core primarily consists of terrigenous materials and carbonate. Sediment layers of terrigenous material are characterized by brownish fine sand to sandy silt during warm periods. Cold periods are marked by grayish silt to blue-gray silty clay (Lamy, 2016).

2.3 Methods

2.3.1 Physical properties

The physical properties of the sediment cores were measured on board, using a GEOTEK Multi Sensor Core Logger (MSCL) (Lamy, 2016). The nondestructive method of logging yielded magnetic susceptibility (MS), pressure wave velocity (vP),

gamma ray attenuation (GRA) density and wet bulk density. Details can be found in the cruise report chapter 3.4 (Lamy, 2016). These physical property data have been used to correlate sediment record PS97/085-3 with Antarctic ice core records.

2.3.2 Sediment composition and their measurements

The determination of total carbon (TC) was carried out with a CNS analyzer (Elementar Vario EL III) at the Alfred Wegener Institute (AWI) in Bremerhaven on freeze-dried and homogenized sediment samples. Total organic carbon (TOC) contents were determined by a carbonsulfur determinator (CS-2000, ELTRA) after the removal of inorganic carbon (TIC, carbonates) by adding hydrochloric acid. The TC and TOC contents were used to calculate the $CaCO_3$ content using the formula:
[$CaCO_3$ (wt.%) = (TC-TOC)* 8.333].

We analyzed the biogenic opal content on 145 samples (measured every 10 cm) from core PS97/085-3 with the sequential leaching method after Müller and Schneider (1993). The weight percent of the biogenic opal was calculated from the simple leachable biogenic Si (BSi) by molybdate-blue spectrophotometry, assuming a nominal water content of 10% (SiO_2•$10H_2O$) (Müller and Schneider, 1993). Percentages of siliciclastic material were estimated as: [Siliciclastic (wt.%) = 100 wt.% − ($CaCO_3$ wt.% + 2 × TOC wt. % + biogenic opal wt.%)] (Fig. 2.2). All data were corrected for pore water salt content (Kuhn, 2013).

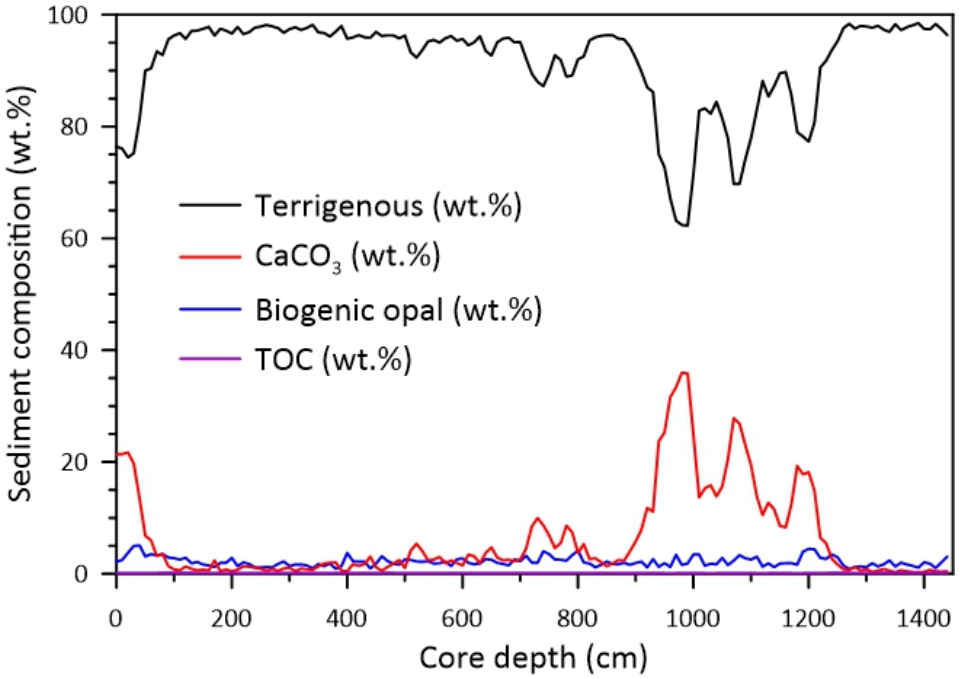

Fig. 2.2. Bulk sediment compositions from core PS97/085-3. Terrigenous fractions (black); carbonate contents ($CaCO_3$, red); biogenic opal content (blue); total organic carbon (TOC, purple).

2.3.3 Grain size measurement

1520 sediment samples were taken in consecutive 1 cm intervals from piston core PS97/085-3 and the corresponding trigger core for grain size measurements. The detrital fraction of the sediments was isolated from the bulk sediment after removal of the organic matter by hydrogen peroxide (15%) and the carbonates by hydrochloric acid (0.5 mol/L). Since the content of bio-siliceous is low (<5 wt%), it is not necessary to be removed. 1 mL (0.05 mol/L) sodium metaphosphate ($Na_4P_2O_7$*$10H_2O$) was used to ensure disaggregation of all particles. Grain-size analyses were carried out with a CILAS 1180 L laser diffraction particle-size analyzer (CILAS, Orleans, France) at the Alfred Wegener Institute, List/Sylt. The device provides a measuring range between 14.6 Φ and -1.32 Φ corresponding to 0.04 µm–2500 µm. The analysis error of replicate testing is less than 3%.

Grain-size analyses of the silt fraction (2–63 µm) of 80 parallel samples were performed by measurements with a Micromeritics SediGraph 5100 at AWI. The SediGraph analyses provide a high-resolution grain-size distribution in steps of 0.1 Φ and are based on the X-ray density scanning of a settling suspension assuming Stokes'

law settling. The instrument precision of the SediGraph 5100 for pure standard analysis ranges from ± 0.3% to ± 1.9% (Bianchi *et al.*, 1999). These methods are mainly used in Chapters 3 and 4.

2.3.4 Mineralogy X-ray diffraction

The mineralogical composition of the bulk sediment and silt faction were analyzed at the Alfred Wegener Institute (AWI) Bremerhaven by X-ray diffractometry (XRD) using a PANalytical Empyrean goniometer (40 kV, 40 mA, 4.5 to 85°, step-rate 0.013°, Cu-Kα radiation). Sample preparation and semi-quantitative evaluation of XRD followed techniques explained in detail elsewhere (Ehrmann *et al.*, 1992; Petschick *et al.*, 1996).

51 surface samples and 380 samples from piston and trigger cores for every 4 cm interval were measured. The analysis of the mineral spectra of each sample was performed by manual evaluation of the main mineral peaks using the MacDiff 4.0.7 software (Petschick *et al.*, 1996). The used mineral peaks were: quartz (3.34 and 4.26 Å), plagioclase (3.19 Å), K-feldspar (3.24 Å), hornblende (8.4 Å), mica (10 Å), and chlorite (7 Å). Quartz/feldspar (Qz/Fsp) ratios in bulk and silt samples refer to the quotient of the 3.34 Å peak intensities of quartz divided by the 3.19-3.24 Å double peak intensities of plagioclase and K-feldspar. This ratio can be applied to determine the sediment supply and weathering signals and in addition quartz in the silt fraction is a good tracer for current transported mud (Diekmann and Kuhn, 1999; Diekmann *et al.*, 2000).

The separated clay fraction was analyzed by XRD measurements on glycolated preferentially oriented mounts, following standard procedures described in detail elsewhere (Petschick *et al.*, 1996). Semi-quantitative estimates of peak areas of the basal reflection for the main clay mineral groups (smectite at 17 Å, illite at 10 Å, and chlorite at 7 Å; no kaolinite was found in the samples) were carried out on the glycolated samples using the MacDiff software. The relative abundance of the clay mineral groups in the clay fraction is summed to 100% using standard weighting factors (Biscaye, 1965). The 5 Å /10 Å peak intensity ratio is a measure of illite

chemistry. Values >0.40 indicate the presence of Al-rich illites (muscovite), values <0.15 indicate Fe/Mg-bearing illites (biotitic illite) (Esquevin, 1969). The clay mineralogical data is a powerful tool to trace the sources and transport paths of detrital matter. The integral-breadth (IB) of glycolated 17 Å -smectite and 10 Å -illite peaks were used to indicate clay mineral crystallinity (Petschick *et al.*, 1996). Additionally, the relative intensities of the chlorite 00l series were used to determine the total Fe content of chlorite (Moore and Reynolds, 1989). These methods are mainly used in Chapters 3 and 5.

2.3.5 Magnetic Susceptibility

High-resolution logging of magnetic susceptibility on core PS97-085-3 was performed with a Bartington MS2E sensor in combination with a MS2 control unit, integrated into a fully automated split-core logger. Magnetic susceptibility was obtained every 1 mm directly on the split surface of the cores. The response function of the MS2E sensor with respect to a thin magnetic layer is equivalent to a Gaussian curve with a half-width of slightly less than 4 mm (Nowaczyk, 2001). The amplitude resolution of the sensor is 10^{-5} (SI-unit, volume corrected) in combination with the MS2 unit. During data acquisition, after every 10^{th} measurement on sediment, the sensor is lifted to about 4 cm above the sediment in order to take a blank reading in the air. This is done in order to monitor the shift of the sensor's background due to temperature drift. Subsequently, the air readings were linearly interpolated and subtracted from the readings on sediment. These methods are mainly used in Chapters 4 and 5.

2.3.6 X-ray computed tomography

The sediment core PS97/085-3 was scanned by a Toshiba Aquilion 64^{TM} computer tomography (CT) at the hospital “Klinikum Bremen-Mitte” (Bremen, Germany). The X-ray source voltage was 120 kV and the current was 600 mA. The CT scan resolution is 0.35 mm in the x-y direction and 0.5 mm in the z direction (0.3 mm

reconstruction interval). The CT images were reconstructed by the Toshiba patented helical cone beam reconstruction technique (TCOT). The CT data were processed with the Amira ZIB edition software (version 2015.37; http://amira.zib.de) (Stalling *et al.*, 2005). All lithic clasts >1 mm and bioturbation traces were segmented in each reconstruction slice with the "Threshold" segmentation tool of the Segmentation Editor. The used density threshold values were >1500 (Hounsfield units) for lithic clasts, 601–1499 for matrix sediment, 1–600 for bioturbation traces, and <1 for the surrounding air and water. Each material was quantified with the "Material Statistics" module (Volume per slice). Subsequently, the lithic clasts were separated with the "Connected Components" module, parameterized with the "Shape Analysis" module and a grain-size and orientation analysis (relative to z as well as within the x-y plane) performed following the methodology from (Bartels *et al.*, 2017; Titschack *et al.*, 2015). Each analysis considered a core interval of ~1 cm and moved slice by slice. The result (unit: vol. % of all segmented clasts) was written to the central slice of the interval. These methods are used in chapters 4 and 5.

2.3.7 X-ray fluorescence core scanning

The X-ray fluorescence core scanner (XRF-CS) provides non-destructive, high resolution, and semi-quantitative chemical composition data for bulk sediment records. The sediment cores were measured by every 1 mm with an ITRAX XRF-CS at Leibniz-Institute for Baltic Sea Research, Warnemünde. The XRF-CS data were collected in two runs using generator settings of a Cr-tube at 60 kV and 30 kV with 30 mA. The exposure times are 1200 ms with 200 µm steps at 60 kV and 30 s with 500 µm steps at 30 kV. The specific element peak area intensity of the fluorescence spectrum is proportional to the concentration of the corresponding element. There methods are mainly used in Chapters 4 and 5.

2.3.8 Authigenic Nd and Pb isotopic compositions

The authigenic Nd isotope signal was extracted from the Fe–Mn oxyhydroxide fraction of bulk sediment from site PS97/085 (a total of 108 samples), following the

leaching procedure from previous studies (Blaser *et al.*, 2016; Gutjahr *et al.*, 2007; Huang *et al.*, 2020). Rare Earth Elements (REE) were separated from the bulk sample by cation exchange chromatography using 50W-X8 resins. The Ln-spec resin was applied to further extract the Nd fraction from the other light REE (Blaser *et al.*, 2019; Gutjahr *et al.*, 2007).

Nd isotope measurements were carried out on a Thermo Scientific Neptune Plus Multicollector Inductively Coupled Plasma Mass Spectrometry (MC-ICP-MS) at GEOMAR, Kiel. Instrumental mass fractionation was corrected by normalizing the measured ratio of $^{143}Nd/^{144}Nd$ to $^{146}Nd/^{144}Nd = 0.7219$ following the Vance and Thirlwall procedure (Vance and Thirlwall, 2002). Corrected $^{143}Nd/^{144}Nd$ were normalized to repeated measured standards of JNdi-1 with a value of 0.512115 (Tanaka *et al.*, 2000). Nd isotope signatures are expressed as $\varepsilon Nd = [(^{143}Nd/^{144}Nd_{(sample)}/(^{143}Nd/^{144}Nd_{(CHUR)}-1]*10^4$, where CHUR is chondritic undifferentiated reservoir. Total procedural blanks for Nd are below 30 pg and hence negligible (n = 15). A secondary standard solution NIST 3135a reproduced within 0.20 εNd throughout the course of this study (n = 32).

The same leaching method of Nd isotope was applied to extract the Pb isotope signals from the authigenic Fe-Mn oxyhydroxide fraction of bulk sediment. Pb isotope measurements (a total of 108 samples) were carried out with a Thermo Scientific Neptune Plus MC-ICP-MS at GEOMAR, Kiel. We used the Tl-doping technique spiked by a NIST997 Tl standard solution (Pb:Tl = ~4:1) for mass bias correction during Pb isotope measurements (Thirlwall, 2002; Vance and Thirlwall, 2002). Given that Tl and Pb have different fractionation factors during ionization, $^{205}Tl/^{203}Tl$ ratios were determined on a session-by-session basis so that NBS981 Pb isotope compositions matched published values (Süfke *et al.*, 2019). Total procedural blanks were below 50 pg (n = 18), thus were negligible. The reproducibility of the secondary standard USGS NOD-A-1 reproduced Pb isotope compositions with a precision of 0.007 for $^{206}Pb/^{204}Pb$ and 0.030 for $^{208}Pb/^{204}Pb$ (n = 58). These methods are applied in Chapter 6.

2.3.9 Chronology

For the establishment of a preliminary age model, we used the MSCL-records (Chapter 2.3.1) as described in (Lamy, 2016). Generally, increased terrigenous input (high MS and GRA-density) in the ocean basins prevailed during glacial periods and that high carbonate deposition (low MS and GRA-density) occurred during interglacials. Accordingly, the MS and GRA-density variations were correlated to different Marine Isotope Stages [MIS; (Lisiecki and Raymo, 2005)] and provided an initial, ship-board age model (Fig. 2.3) (Lamy, 2016). For the development of the precise age model used in this thesis, I refer to chapter 4.6.

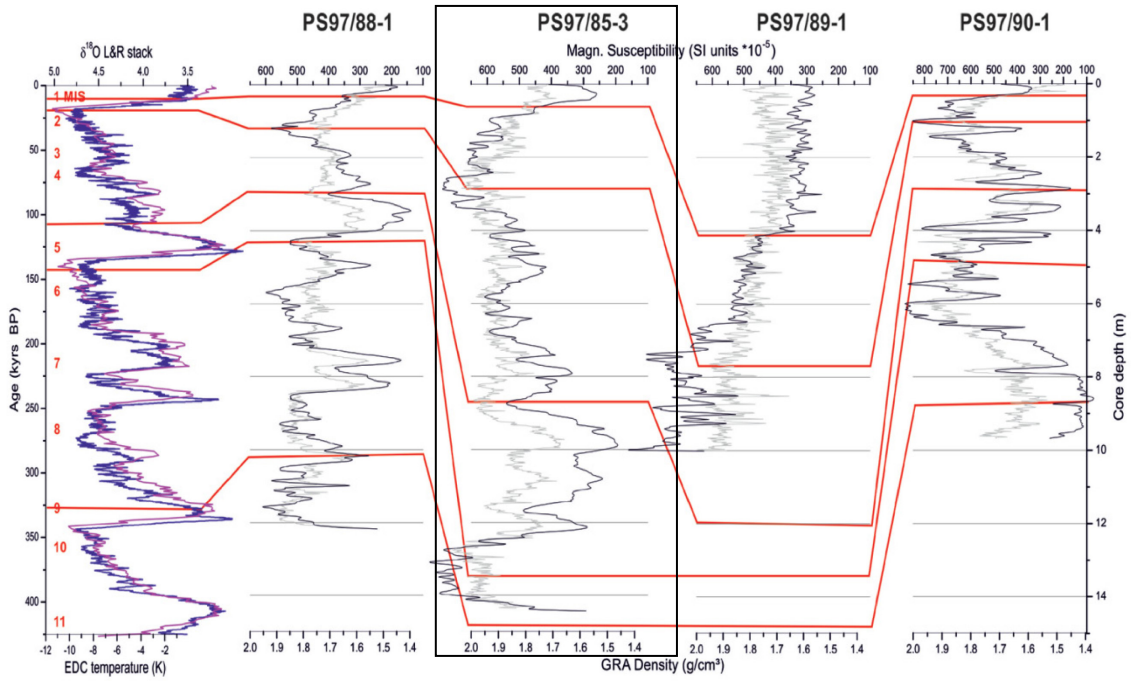

Fig. 2.3. Tentative correlation of magnetic susceptibility and GRA density records of cores PS97/088-1, 085-3 (black frame, this study), 089-1, and 090-1 to dated reference records (blue = EPICA Dome C temperature record; pink = LR04 oxygen isotope reference stack of Lisiecki and Raymo, 2005). Adapted from Lamy (2016).

3 Surface sediment characteristics related to provenance and ocean circulation in the Drake Passage sector of the Southern Ocean

Shuzhuang Wu[1], Gerhard Kuhn[1], Bernhard Diekmann[2], Lester Lembke-Jene[1], Ralf Tiedemann[1], Xufeng Zheng[3], Sophie Ehrhardt[4], Helge W. Arz[5], Frank Lamy[1]

[1]Alfred-Wegener-Institut Helmholtz-Zentrum für Meeres- und Polarforschung, 27568 Bremerhaven, Germany;
[2]Alfred-Wegener-Institut Helmholtz-Zentrum für Meeres- und Polarforschung, 14473 Potsdam, Germany;
[3]Key Laboratory of Marginal Sea Geology, South China Sea Institute of Oceanology, Chinese Academy of Sciences, 510301 Guangzhou, China;
[4]Helmholtz Centre for Environmental Research - UFZ, 04318 Leipzig, Germany;
[5]Department of Marine Geology, Leibniz Institute for Baltic Sea Research, 18119 Rostock Warnemünde, Germany

Published in Deep Sea Research Part I: Oceanographic Research Paper (October 2019).

Abstract

Understanding present-day sediment provenance and transport processes is crucial for studies about the dynamics of ocean circulation, as well as for paleoclimate reconstructions in the Drake Passage, a key area for Earth's global oceanic circulation and climate during past and future. Based on a comprehensive set of surface sediment samples, we used spatial variations in grain-size distribution, bulk sediment mineralogy, silt and clay mineralogy across the entire Drake Passage region to elucidate the terrigenous sources and transport mechanisms. The statistical evaluation of these data identifies southern Patagonia (carbonate, illite, chlorite, feldspar and quartz) and the Antarctic Peninsula (chlorite, smectite, and amphibole) as the main sources for terrigenous sediments in the Drake Passage region. Different current systems are transporting the sediment material. Here, we provide a new, robust flow speed calibration for silt grain-sizes to enable the reconstruction of Antarctic Circumpolar Current (ACC) dynamics in the Drake Passage sector of the Southern Ocean. We correlated the sortable silt mean grain-size records of surface sediments with adjacent long-term current meter data. A clear bottom current speed pattern shows the variability of the ACC in the Drake Passage responding to the dynamics of

oceanic fronts, in agreement with modern observation.

Keywords: Drake Passage; provenance; mineralogy; sortable-silt; current speed

3.1 Introduction

The Drake Passage is the major choke point for the Antarctic Circumpolar Current (ACC), which is the largest current system in the world ocean. The ACC connects the three major ocean basins, thus enabling the inter-basin water mass exchange in the Southern Ocean (Marshall and Speer, 2012). The strong density surfaces tilt upward toward the south and expose the dense, deeper layers of the ocean to interactions with the atmosphere and cryosphere. This process transforms upwelled deep waters into either denser bottom water or lighter intermediate waters, which leads to a vigorous overturning circulation in the Southern Ocean (Meredith *et al.*, 2011b; Rintoul, 2018). As a consequence of its strong lateral and vertical extension, the ACC exerts a profound influence on Earth's global climate variability (Marshall and Speer, 2012; Rintoul, 2018).

Located between the tip of South America and the Antarctic Peninsula (AP), the Drake Passage is the narrowest constriction of the ACC with a width of ~800 km. Although the precise opening time of the Drake Passage in geological history remains controversial, there is clear evidence for a deep water connection in the Southern Ocean around the late Eocene (34 to 30 Ma) (Livermore *et al.*, 2005; Maldonado *et al.*, 2014) at a time of substantial expansion of the Antarctic Ice Sheet (34 to 33 Ma) (Zachos *et al.*, 2001). Owing to its unique geographical setting, the Drake Passage is a very important area to constrain the strength of the ACC and its relation to a variety of sedimentary processes and transport mechanisms in the Southern Ocean. The average baroclinic transport of the ACC through Drake Passage is 150 ± 20 Sv, dominantly carried along the Subantarctic Front and Polar Front (Cunningham *et al.*, 2003; Donohue *et al.*, 2016; Renault *et al.*, 2011). Direct full-depth velocity sections in the Drake Passage have been recorded by long-term near-seabed current meters, which

provide accurate total transport estimation and vertical velocity structure (Koenig *et al.*, 2014; Renault *et al.*, 2011). As a result, the Drake Passage is a relatively well-monitored region in modern oceanographic current velocity observations compared to other parts of the Southern Ocean (Chidichimo *et al.*, 2014; Donohue *et al.*, 2016; Koenig *et al.*, 2014; Meredith *et al.*, 2011b; Naveira Garabato *et al.*, 2009; Piola *et al.*, 2003; Renault *et al.*, 2011). However, paleo-reconstructions of bottom currents in the Drake Passage region based on marine sediments remain scarce since the pivotal USNS Eltanin expeditions in the 1960s (Goodell, 1965) because of severe sea and weather conditions, and the wide-spread absence of recent sediments due to strong bottom currents. Three current speed reconstructions of the ACC based on grain-size in the northernmost of Drake Passage (Lamy *et al.*, 2015) and downstream of Drake Passage (McCave *et al.*, 2014; Roberts *et al.*, 2017) indicate strongly reduced Drake Passage transport during the last glacial in the subantarctic ACC, but little change further south, demonstrating the currently incomplete and fragmented understanding of this complex current system. Resolving the ACC variability and pathways of sediment transport related to sediment sources in this gateway is, therefore, critical for advancing our understanding of the Southern Ocean's role in global ocean circulation.

The terrigenous non-cohesive sortable silt ($\overline{SS}$, mean of the 10–63 μm sediment grain size fraction) has been used as a powerful tool to infer flow speeds of near-bottom currents in the deep-sea (McCave and Andrews, 2019; McCave and Hall, 2006; McCave et al., 1995). This proxy is controlled by selective deposition, while it is also influenced by the source effect (McCave and Hall, 2006; McCave et al., 1995), especially near the continent. Additionally, the absolute calibrations of the $\overline{SS}$ grain-size flow speed vary between different areas, e.g., the Iceland-Scotland overflow region, Rockall Trough and the Weddell/Scotia Sea. Furthermore, there are only five calibration data points available in the downstream of the Drake Passage (McCave et al., 2017). Therefore, more representative samples that cover a wide range of bottom current speeds with adequate sampling density are needed for a precise evaluation of bottom current speeds in the Drake Passage region.

Terrigenous particles that were deposited in the marine environment are mixed materials of various sources and experienced different transport processes, such as fluvial runoff, aeolian influx, ocean current transport, delivery by sea ice or iceberg rafting. In the Drake Passage region, the provenance of marine terrigenous sediments has been explored by analyzing the mineralogy of bulk sediment and clay minerals (Diekmann *et al.*, 2003; Diekmann *et al.*, 2000; Ehrmann *et al.*, 1992; Hillenbrand *et al.*, 2003; Marinoni *et al.*, 2000; Marinoni *et al.*, 2008; Petschick *et al.*, 1996), Sr and Nd isotopic compositions of sediment (Lee *et al.*, 2012; Walter *et al.*, 2000), and heavy minerals in the sand fraction (Barbeau *et al.*, 2009). To distinguish between different sediment provenances and transport processes, we analyzed the mineralogy of the bulk sediment, the silt and clay fractions.

The aims of our study are to investigate the regional distribution patterns (1) of the surface sediments mineralogy in relation to the sediment provenance and (2) of the modern bottom current speed regime reflected by the terrigenous silt fraction.

3.2 Study area

The investigated area extends from the southern Chilean margin (SCM), across the Drake Passage to the AP (52°S to 64°S) (Fig. 3.1). This area is characterized by a strong latitudinal gradient in sea surface temperature and salinity, high concentrations of dissolved oxygen (Provost *et al.*, 2011), and high inputs of dissolved iron from the shelf off the AP (Meredith *et al.*, 2018) combined with strong changes in surface and deep water current strength (Donohue *et al.*, 2016; Koenig *et al.*, 2014; Renault *et al.*, 2011).

3.2.1 Geological setting

The complex geotectonic setting of the southernmost part of South America roughly corresponds to physiographic units aligned parallel to the active Pacific margin of the continent (Barker *et al.*, 1991; Pérez *et al.*, 2019). Calcalkaline tonalites and granodiorites of the Late Jurassic–Cretaceous Patagonian batholith, which intruded

into metamorphosed basement rocks, occupy the south Chilean Archipelago along the arcuate Pacific side. A belt of deformed ophiolithes and mafic volcaniclastics of a former back-arc basin, resting on Upper Jurassic rhyolithes, forms the western flank and the spine of the modern South Andean cordillera (Dalziel *et al.*, 1974). Quartz-poor sediments of basic to intermediate composition from undifferentiated source rocks dominate along the Chilean continental margin. Chlorite and illite with low smectite concentrations (≤10%), derived from low-grade metamorphic and magmatic rocks, constitute the clay mineral spectrum (Diekmann *et al.*, 2000).

The AP represents a calc-alkaline magmatic arc that formed during the subduction of Pacific lithosphere beneath Gondwana (Barker *et al.*, 1991). It comprises sedimentary rocks of Late Palaeozoic to Cenozoic age that were intruded by intermediate to acidic plutonic rocks and were overlain by intermediate–mafic composition volcanic rocks (Burton-Johnson and Riley, 2015; Diekmann *et al.*, 2000). Mafic to felsic plutonic rocks with dominantly calc-alkaline continental-margin affinities are prevalent on the AP (Burton-Johnson and Riley, 2015; Leat *et al.*, 1995), as are partly sedimentary rocks, which exhibit slight metamorphism (Burton-Johnson and Riley, 2015; Smellie *et al.*, 1996). Fine-grained sediments occur along the continental rise of the AP were delivered by turbidity currents and lateral transport of fines within nepheloid layer of bottom water flow (Amblas *et al.*, 2006; Gardner *et al.*, 2018; Rebesco *et al.*, 2002).

On the northern AP and the South Shetland Islands (SSI), several volcanoes developed in this tectonically active region, related to the modern back-arc spreading basin of Bransfield Strait (Antoniades *et al.*, 2018; Hillenbrand *et al.*, 2008). Detritus from this young and less evolved continental crust is characterized by low quartz/feldspar ratios contrasts markedly with the sediment derived from the old upper continental crust (East Antarctica) (Diekmann *et al.*, 2000; Hemming *et al.*, 2007; Lee *et al.*, 2012; Walter *et al.*, 2000).

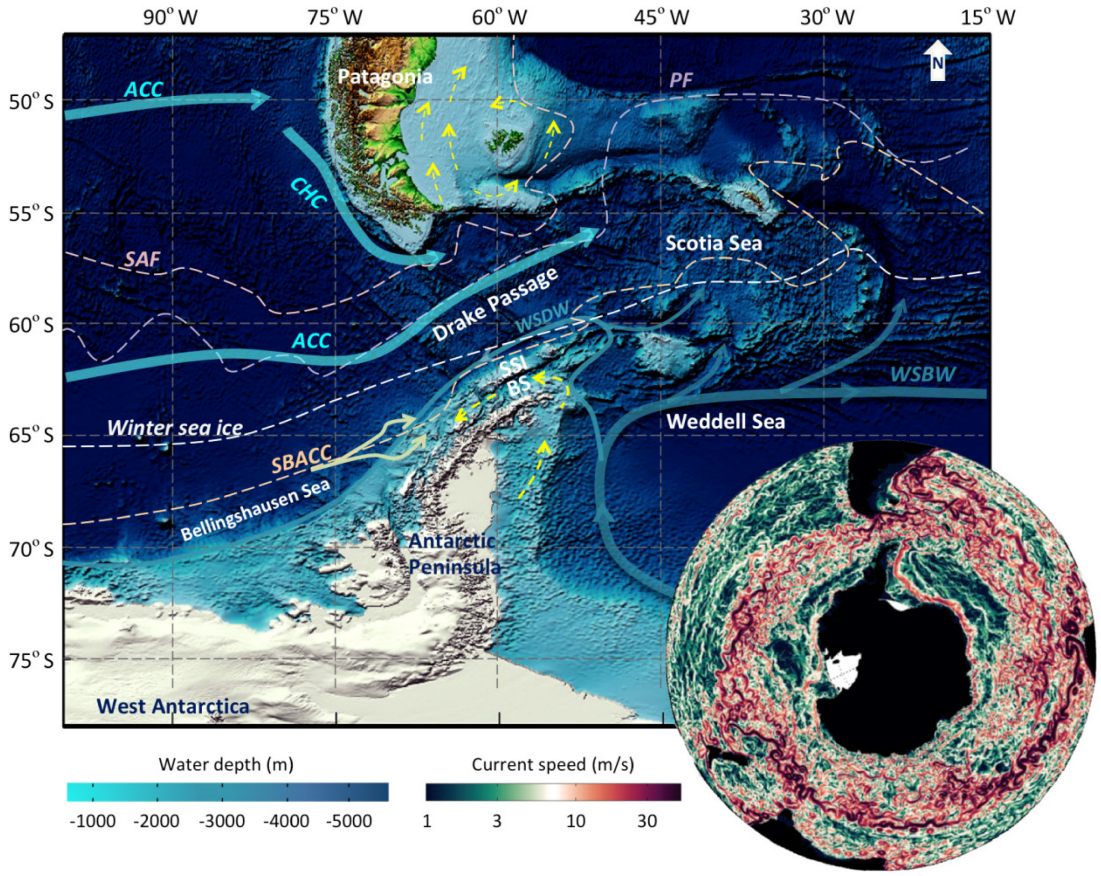

Fig. 3.1. Overview of ocean circulation in the Drake Passage region and adjacent basins. Light blue arrows show Antarctic Circumpolar Current (ACC) and Cape Horn Current (CHC) (Chaigneau and Pizarro, 2005), while dark green-blue arrows are Weddell Sea bottom water (WSBW, thick) and Weddell Sea deep water (WSDW, thin) flows (Eagles *et al.*, 2006; Hernández-Molina *et al.*, 2017). Yellow dash arrows are shelf surface water circulation. White dashed lines average winter sea ice. Locations of Subantarctic Front (SAF, light pink), Polar Front (PF, light purple) and the southern boundary of the Antarctic Circumpolar Current (SBACC, light brown) are from (Orsi *et al.*, 1995). SSI = South Shetland Islands, BS = Bransfield Strait. The right bottom insert map shows the current speed in the Southern Ocean, with warmer red colors representing higher current speeds (Rintoul, 2018).

3.2.2 Oceanographic setting

The ACC flows eastward through the Drake Passage, mainly driven by strong southern westerly winds (SWW) together with buoyancy forcing and topography that generate velocities of 15-60 cm/s at the surface and 2-30 cm/s near the seafloor (Donohue *et al.*, 2016; Koenig *et al.*, 2014; Meredith *et al.*, 2011b). The SCM is dominated by the southward-flowing Cape Horn Current (CHC) that reaches surface velocities of ~15-35 cm/s (Chaigneau and Pizarro, 2005) and joins the northern branch of the ACC flowing through the Drake Passage (Fig. 3.1). The Subantarctic

Front (SAF), the Polar Front (PF), and the Southern ACC Front (SACCF) were identified as the three major ACC oceanographic fronts (Orsi *et al.*, 1995); these fronts were observed to be split into different sub-fronts. At the entrance to Drake Passage, two branches of the SAF were detected: the northern SAF (SAF-N) and the main SAF (SAF-M). Three branches of the PF were found: the northern PF (PF-N), main PF (PF-M) and southern PF (PF-S). The SACCF was observed to be separated in two branches: the northern SACCF (SACCF-N) and the southern SACCF (SACCF-S) (Barré *et al.*, 2011; Sokolov and Rintoul, 2009). The water mass in the Drake Passage is composed of Antarctic Intermediate Water (AAIW), Circumpolar Deep Water (CDW) and Antarctic Bottom Water (AABW). The most voluminous among these is the CDW, divided into the Upper Circumpolar Deep Water (UCDW) and Lower Circumpolar Deep Water (LCDW) (Orsi *et al.*, 1995; Sloyan and Rintoul, 2001). The UCDW contributes, after upwelling and significant modification into Antarctic Surface Water along northward transport, to the formation of the AAIW emerging to the north of the SAF (Bostock *et al.*, 2013; Naveira Garabato *et al.*, 2009; Sloyan and Rintoul, 2001), while the LCDW transforms into denser AABW primarily in the Weddell Sea (Meredith *et al.*, 2011a; Orsi *et al.*, 1999; Schmittner *et al.*, 2003).

The strong three-dimensional circulation of the ACC represents the southern limb of the Meridional Overturning Circulation and affects global oceanography and climate (Meijers, 2014; Rintoul, 2018; Sloyan and Rintoul, 2001). Strong SWW affects the northward transport of surface waters in the Ekman layer, with convergence (downwelling) north of the wind-stress maximum and divergence (upwelling) south of it (Rintoul, 2018). In contrast to the generally eastward flowing ACC in the Drake Passage, in the AP region relatively warm, fresh water flows northeastward from the Bellingshausen Sea to Bransfield Strait (BS) (Fig. 3.1), whereas a relatively cold and dense water from the Weddell Sea (the Weddell Sea Deep Water, WSDW) flows south-westward along the Pacific margin of the AP (Orsi *et al.*, 1999) (Fig. 3.1).

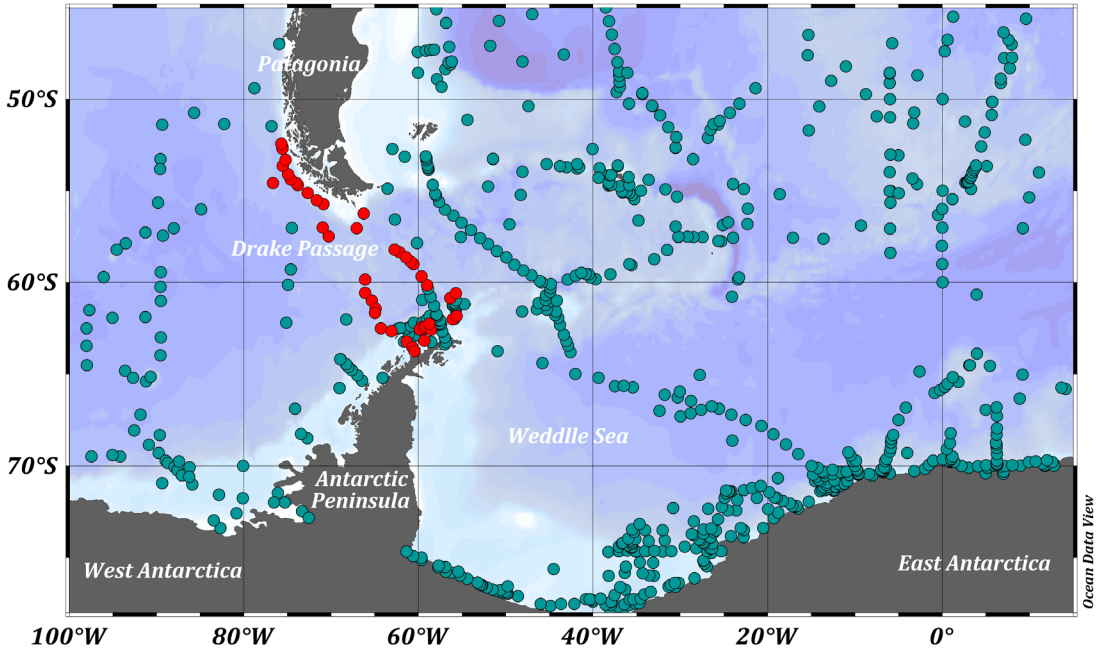

Fig. 3.2. Location of sampling sites for seafloor surface sediments. Red dots are from Polarstern cruise PS97 (this study) and greenish-blue dots are sampling locations from literature (Biscaye, 1965; Diekmann and Kuhn, 1999; Ehrmann *et al.*, 1992; Hillenbrand *et al.*, 2003; Petschick *et al.*, 1996).

3.3 Material and Methods

A total of 51 seafloor surface samples were recovered in the Drake Passage region during RV Polarstern Cruise PS97 in 2016 (Lamy, 2016). Samples were taken by a Multicorer and, in a few cases, with a Giant Box Corer within a depth range of ~650 - 4000 m water depth in order to obtain undisturbed surface samples of the uppermost centimeter of the sediment. The detailed locations of the sampling stations (Table 1) are shown in Fig. 3.2 (red dots). All surface sediments were investigated for bulk composition (carbonate, biogenic opal, organic carbon) and lithogenic mineralogy, silt mineralogy, silt grain-size distribution, and clay mineralogy. All data are available within the Pangaea data base (https: //doi.pangaea.de/10.1594/PANGAEA.907140). For a few samples there was only restricted availability of material to perform all analyses.

Table 1 Sample locations in the Drake Passage region (Lamy, 2016).

Station	Latitude	Longitude	Water Depth (m)	Station	Latitude	Longitude	Water Depth (m)
PS97/015-2	55° 43.91' S	70° 53.54' W	1872	PS97/072-2	62° 0.50' S	56° 03.93' W	1993
PS97/020-1	55° 30.80' S	71° 38.25' W	2070	PS97/073-2	61° 49.72' S	55° 38.72' W	2624
PS97/021-1	55° 06.92' S	72° 40.15' W	1839	PS97/074-1	60° 52.02' S	56° 20.43' W	1831
PS97/022-1	54° 42.00' S	73° 48.45' W	1616	PS97/077-1	60° 35.44' S	55° 42.07' W	3543
PS97/024-2	54° 35.32' S	73° 57.32' W	1273	PS97/079-1	60° 08.58' S	58° 59.36' W	3539
PS97/027-1	54° 23.08' S	74° 36.39' W	2342	PS97/080-2	59° 40.43' S	59° 37.73' W	3106
PS97/042-1	59° 50.59' S	66° 05.59' W	4172	PS97/083-1	58° 59.64' S	60° 34.25' W	3762
PS97/044-1	60° 36.79' S	66° 01.30' W	1203	PS97/084-2	58° 52.14' S	60° 52.03' W	3557
PS97/045-1	60° 34.25' S	66° 05.65' W	2293	PS97/085-2	58° 21.28' S	62° 10.00' W	3091
PS97/046-6	60° 59.84' S	65° 21.43' W	2789	PS97/086-2	58° 38.66' S	61° 23.87' W	2969
PS97/048-1	61° 26.39' S	64° 53.20' W	3448	PS97/089-2	58° 13.54' S	62° 43.43' W	3437
PS97/049-2	61° 40.27' S	64° 57.69' W	3758	PS97/093-3	57° 29.91' S	70° 16.47' W	3781
PS97/052-3	62° 29.94' S	64° 17.59' W	2890	PS97/094-1	57° 0.16' S	70° 58.28' W	3993
PS97/053-1	62° 39.83' S	63° 05.67' W	2016	PS97/095-1	56° 14.68' S	66° 14.93' W	1652
PS97/054-2	63° 14.02' S	61° 20.57' W	1279	PS97/096-1	56° 04.54' S	66° 08.95' W	1613
PS97/055-2	63° 32.08' S	60° 40.38' W	723	PS97/097-1	57° 03.20' S	67° 03.94' W	2319
PS97/056-1	63° 45.42' S	60° 26.48' W	635	PS97/114-1	54° 34.74' S	76° 38.79' W	3863
PS97/059-1	62° 26.25' S	59° 39.49' W	354	PS97/122-2	54° 06.03' S	74° 55.15' W	2560
PS97/060-1	62° 35.00' S	59° 38.66' W	462	PS97/128-1	53° 38.02' S	75° 32.57' W	2294
PS97/061-1	62° 33.53' S	59° 47.96' W	467	PS97/129-2	53° 19.32' S	75° 12.78' W	1879
PS97/062-1	62° 34.17' S	59° 50.82' W	478	PS97/131-1	52° 39.56' S	75° 33.91' W	1028
PS97/065-2	62° 29.18' S	59° 20.97' W	481	PS97/132-2	52° 36.98' S	75° 35.21' W	843
PS97/067-2	62° 25.00' S	59° 08.64' W	550	PS97/134-1	52° 40.98' S	75° 34.88' W	1075
PS97/068-2	63° 10.06' S	59° 18.10' W	793	PS97/135-1	52° 42.03' S	75° 35.44' W	1094
PS97/069-1	62° 35.35' S	58° 32.59' W	1635	PS97/139-2	52° 26.57' S	75° 42.46' W	640
PS97/071-2	62° 15.50' S	58° 46.31' W	442				

3.3.1 Bulk and silt mineralogy

The mineralogical composition of the bulk sediment and silt faction were analyzed at the Alfred Wegener Institute (AWI) Bremerhaven by X-ray diffractometry (XRD) using a PANalytical Empyrean goniometer (40 kV, 40 mA, 4.5 to 85°, step-rate 0.013°, Cu-Kα radiation). Sample preparation and semi-quantitative evaluation of XRD followed techniques explained in detail elsewhere (Ehrmann *et al.*, 1992; Petschick *et al.*, 1996). On freeze-dried and ground bulk samples the carbonate content (Cc) and total organic carbon (TOC) were from Cárdenas et al., (2018). Biogenic opal ($BSi{\bullet}10H_2O$) was reanalyzed by the sequential leaching method (Müller and Schneider, 1993).

For grain size separation organic materials, biogenic carbonate and biogenic silica were removed with 3% H_2O_2, 10% HCl, and 2M NaOH. The clay and silt fractions were obtained from subsamples after removing sand (63–2000 μm) and gravel (>2 mm) by wet sieving. Clay (<2 μm) was then separated from silt (2–63 μm) by application of Stokes' law of settling using Atterberg tubes (Petschick *et al.*, 1996). To separate these two fractions almost completely, a 9- to 12-times repetition of the settling procedure was necessary. The mass ratios of the lithogenic components within the sand, silt and clay fractions (Table. S3.1) were calculated from weights before and after leaching and from carbonate and biogenic opal determinations as described above.

The analysis of the mineral spectra of each sample was performed by manual evaluation of the main mineral peaks using the MacDiff 4.0.7 software (Petschick *et al.*, 1996). The used mineral peaks were: quartz (3.34 and 4.26 Å), plagioclase (3.19 Å), K-feldspar (3.24 Å), amphibole (8.4 Å), mica (10 Å), and chlorite (7 Å). Quartz/feldspar (Qz/Fsp) ratios in bulk and silt samples are calculated by 3.34 Å / (3.18 Å + 3.24 Å) XRD intensities. This ratio can be applied to determine the sediment supply and weathering signals and quartz in the silt fraction is a good tracer for current transported mud (Diekmann and Kuhn, 1999; Diekmann *et al.*, 2000). Although these ratios are based on uncorrected intensities of the respective mineral phases and thus do not reflect the exact proportions within the bulk sediment, we suggest that the ratios are sufficient to characterize the sediment supply and weathering signal.

3.3.2 Clay mineralogy

The separated clay fraction was analyzed by XRD measurements on glycolated preferentially oriented mounts following standard procedures described in detail earlier (Petschick *et al.*, 1996). Semi-quantitative estimates of peak areas of the basal reflection for the main clay mineral groups (smectite at 17 Å, illite at 10 Å, and chlorite at 7 Å) were carried out on the glycolated samples using the MacDiff software. The relative abundance of the clay mineral groups in the clay fraction is

summed to 100% using standard weighting factors (Biscaye, 1965). The 5 Å /10 Å peak intensity ratio is approximately a measure of illite chemistry. Values >0.40 indicate the presence of Al-rich illites (muscovite), values <0.15 indicate Fe/Mg-bearing illites (biotitic illite) (Esquevin, 1969). The clay mineralogical data is a powerful tool to trace the sources and transport paths of detrital matter. The integral-breadth (IB) of glycolated 17 Å -smectite and 10 Å -illite peaks were used to indicate clay mineral crystallinity (Petschick *et al.*, 1996). The relative intensities of the chlorite 00*l* series (001, 002, 003, 004 and 005 reflections) were used to determine the total number of Fe atoms in six octahedral sites of chlorite (Moore and Reynolds, 1989). As a first step, we calculated the intensity ratios I(003)/I(005) and subsequently we estimated the symmetry of Fe substitution (D) according to Brindley and Brown's table, which presented the relationship between I(003)/I(005) and D (Brindley and Brown, 1980). Secondly, I(003) needs to be corrected to give I′(003) by following Brindley and Brown's equation (1) (Brindley and Brown, 1980). Finally, estimation of the total number of Fe atoms (Y) in six octahedral sites is based on the relationship table between Y and [I(002)+ I(004)]/ I′(003) (Moore and Reynolds, 1989).

$$I'(003) = I(003)\frac{I(003) * (114^2)}{(114 - 12.1D)^2} \quad (1)$$

3.3.3 Grain-size

Grain-size analyses of the silt fraction (2–63 μm) were performed by measurements with a Micromeritics SediGraph 5100 at AWI. The SediGraph analyses provide a high-resolution grain-size distribution in steps of 0.1 ϕ and are based on the X-ray scanning of a settling suspension assuming Stokes' law settling. The instrument precision of the SediGraph 5100 for pure standard analysis ranges from ± 0.3% to ± 1.9% (Bianchi *et al.*, 1999).

The coarse and medium fractions of silt, which comprise the grain size spectrum between 10 and 63μm, is referred to as Sortable Silt (SS) because of its non-cohesive behavior. The SS fraction is sensitive for sediment sorting processes and then the

mean grain size of the Sortable Silt ($\overline{SS}$) was defined as paleocurrent indicator (McCave *et al.*, 1995). A statistically significant, positive correlation between $\overline{SS}$ and SS percentage [%(10−63μm) from <63μm] provides evidence that $\overline{SS}$ values reliably indicate sorting and thus reflect bottom current speed (McCave and Andrews, 2019; McCave and Hall, 2006) (Fig. 3.6c). Hence, coarser (finer) mean grain sizes indicate faster (slower) near-bottom current flow speeds.

3.3.4 Current meters

The long-term current meters were moored across the Drake Passage at water depths from 1800 to 4400 m, at a height of approximately 50 m above the sea-floor. The duration of the deployments was up to four years (2007-2011) (Donohue *et al.*, 2016). We compared the low-pass filtered mean current speeds (U) in similar water depth from the cDrake section (Donohue *et al.*, 2016) to adjacent Jason Track 104 data (Koenig *et al.*, 2014) This comparison shows overall similar values, suggests that the current meter data are representative in our study area (Table. S3.3). We assume that although the current meters are not exactly at our surface sample locations, the similar current speeds with depth in our study area supports a robust relationship between current speed and $\overline{SS}$. Therefore, the nearest current meters (hourly mean speed) to both location and water depth were chosen to calibrate our $\overline{SS}$ sediment data. A similar approach has been used in a previous study in the Vema Channel (Ledbetter, 1986).

3.4 Results

Surface sediments along the SCM are mainly composed of coarse sands, pebbles, and rocks, while silty to fine sands and sandy silty clays are present along the Chilean/Argentinian continental margin in the Scotia Sea. Ice rafted debris (IRD) and large dropstones (>1 cm in diameter) are rarely found in surface samples. Sediments contain higher amounts of silt and clay further away from the continental margin toward the center of Drake Passage. Clay-bearing sandy silt and silty clay are

dominant in the southern of Drake Passage and the AP region (Lamy, 2016). On average sediments contain 61% terrigenous material (including 21% sand, 34% silt and 6% clay, respectively) (Table. S3.1). With regard to the biogenic components, a general N-S transition from carbonate-rich sediments (>45% carbonate: mostly foraminifera shells) along the SCM to biogenic opal-rich sediments (avg. 14.6%, diatoms, radiolarians and sponge spiculae) north of the AP was detected in the Drake Passage region (Cárdenas *et al.*, 2018), together with lithogenic components that are part of this study. For the biogenic opal we obtained a good correlation with a determination coefficient of $r^2 = 0.8$ to the data by Cárdenas et al., (2018), but on average 28% relative lower opal values due to not leaching clay minerals like smectite (Schlüter and Rickert, 1998). The differences between the Cárdenas et al. (mean 8.0%) and our opal data (mean 5.6%) are also well correlated with the smectite content ($r^2 = 0.42$; estimated by XRD, Section 3.2) and bulk siliciclastic percentages calculated after Cárdenas et al., (2018) ($r^2 = 0.37$). All data were corrected for pore water salt content (Kuhn, 2013).

3.4.1 Bulk mineralogy

Spatial variations in bulk mineralogy are evident for the Qz/Fsp, chlorite/mica and amphibole/quartz ratios (Fig. 3.3). High Qz/Fsp ratios (2.7-5.3) are clearly present near the western entrance of the Strait of Magellan (Fig. 3.3a), and then decrease dramatically along the SCM to the northern PF, except one sample (PS97/097) with a high value. In contrast to Qz/Fsp ratios, comparatively low chlorite/mica ratios (<2.0) were observed along the SCM to the northern PF (Fig. 3.3b). The chlorite/mica ratios rapidly increased from the PF to AP (from 1.1 to 5.4), but the Qz/Fsp slightly increased along the Shackleton Fracture Zone to the SSI and stayed low ratios along the Hero Fracture Zone. In general, these two ratios have no correlation (Fig. 3.3d). Very low amphibole/quartz ratios (<0.2) were observed in the entire study area (Fig. 3.3c).

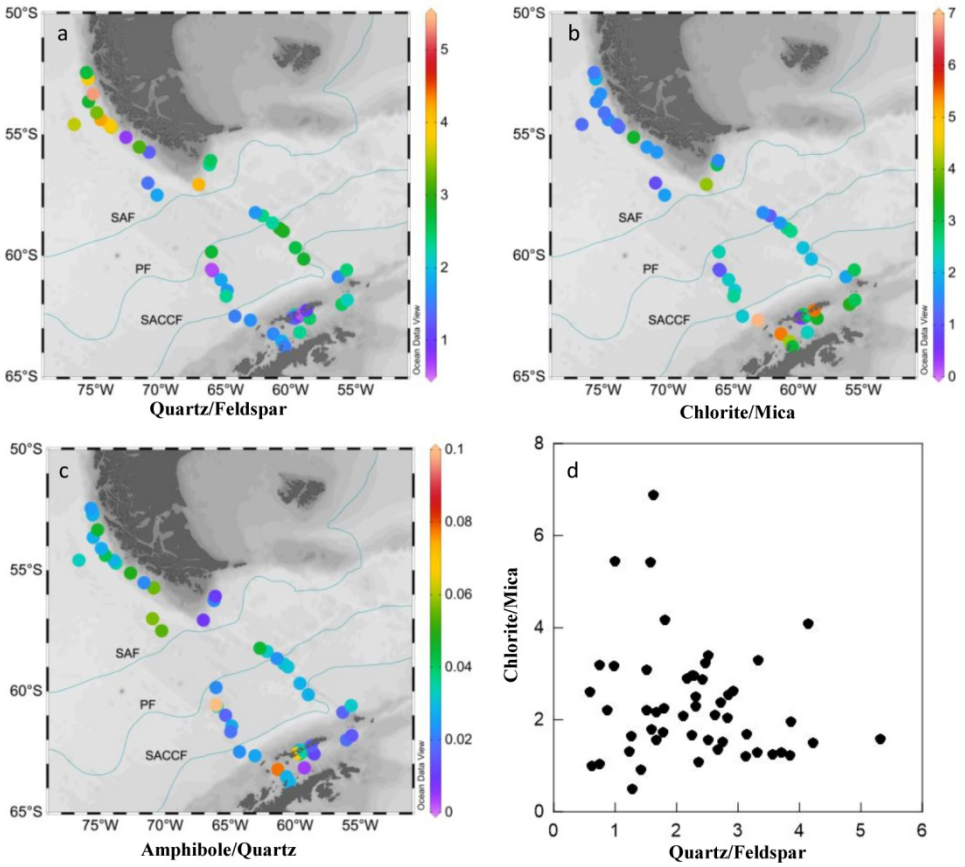

Fig. 3.3. Spatial distribution of bulk mineralogy in seafloor surface sediments of the study area based on XRD intensity ratios (a) Quartz/Feldspar; (b) Chlorite/Mica; (c) Amphibole/Quartz ratios. (d) scatter plot of Chlorite/Mica against Quartz/Feldspar.

3.4.2 Silt mineralogy

High Qz/Fsp ratios (3.0-4.5) in the silt fraction were also detected near the entrance of the Strait of Magellan from bulk mineralogy, with homogeneously distributed ratios (avg = 2.8) along the SCM only slightly increasing around the PF (Fig. 3.4a). The pattern of chlorite/mica ratios was similar to the Qz/Fsp ratios along the SCM and through the Drake Passage, except around the Strait of Magellan and the shelf of the AP (Fig. 3.4b). These two ratios had their minimum values in the Hero Fracture Zone, but higher ratios of chlorite/mica (>3.2) and lower ratios of Qz/Fsp (<2.0) were present on the shelf of the AP. In general, there was no clear correlation between the Qz/Fsp and chlorite/mica ratios, and the amphibole/quartz ratios (<0.1) are very low in the study area. Offshore the tip of South America (PS97/095, 096, 097) the silt fractions samples yielded insufficient material for these analyses.

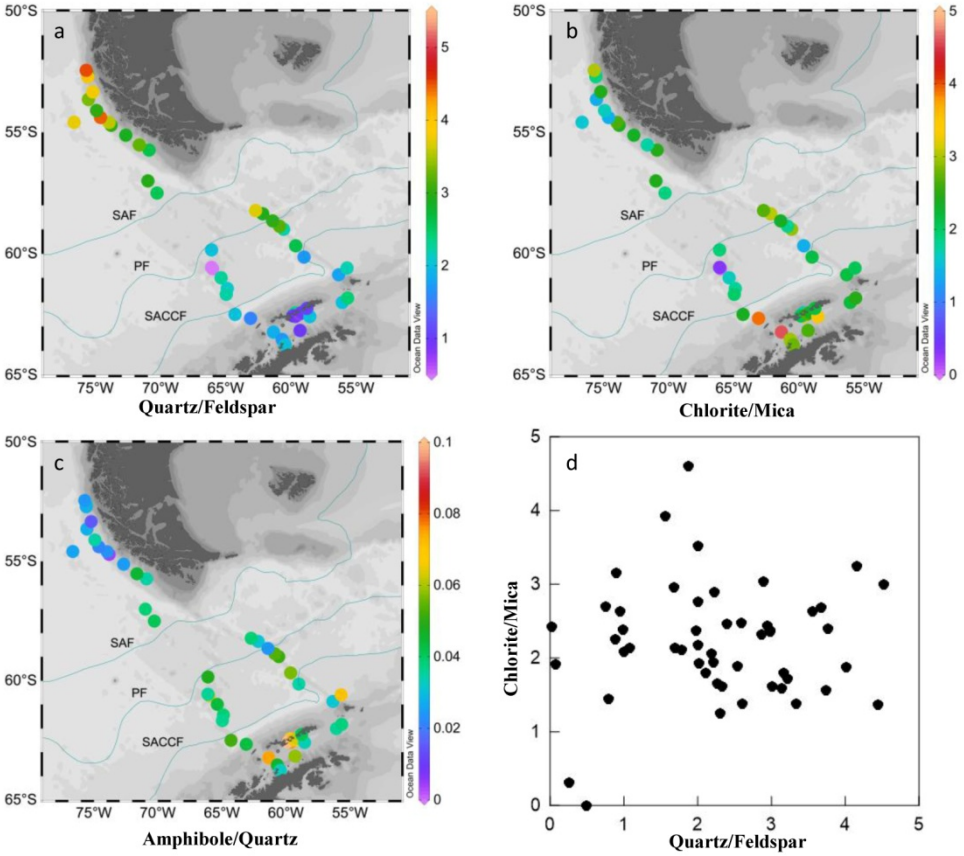

Fig. 3.4. Spatial distribution of silt mineralogy in seafloor surface sediments of the study area (a) Quartz/Feldspar; (b) Chlorite/Mica; (c) Amphibole/Quartz ratios. (d) Scatter plot of Chlorite/Mica versus Quartz/Feldspar.

3.4.3 Clay mineralogy

Distribution patterns of the relative abundance of the three main clay mineral groups chlorite, illite and smectite, as well as crystallinity and chemical parameters of selected clay minerals, reveal significant regional patterns, but also local variations within the study area. We could not trace any kaolinite in this region within the detection range of our XRD set-up. Chlorite is the most abundant clay mineral, with contents ranging from 36% to 73% (Fig. 3.5a). Higher chlorite amounts (54%-73%) occurred from the center of Drake Passage to the shelf of the AP, comparable to the northern Drake Passage and along the SCM (36%-55%). The same pattern is reflected in the Fe content in chlorite, with low Fe content (<0.75) occurring along the SCM and comparatively higher, Fe-rich chlorite (>0.75) dominating from the center of Drake Passage to the shelf of the AP (Fig. 3.5b). Illite represents another major

component of the clay mineral spectrum, with values varying between 25% and 62% (Fig. 3.5c) and maxima located along the SCM with a moderate crystallinity (IB = 0.4-0.6 Δ°2θ). Its content decreased to less than 25% offshore the AP, where the crystallinity (IB = 0.3-0.4 Δ°2θ) was comparatively high. There was no distinct pattern in the 5 Å /10 Å ratio of illite, except in two samples that yielded relative high ratios (>0.8, Fig. 3.5d). Smectite content is very low along the SCM (<5%) with a mostly high crystallinity (IB < 1.5 Δ°2θ). Its content increased from south of the PF (<10%) to comparatively high values (20-33%) with moderate crystallinity (IB = 1.4-1.9 Δ°2θ) on the shelf of the AP (Fig. 3.5e).

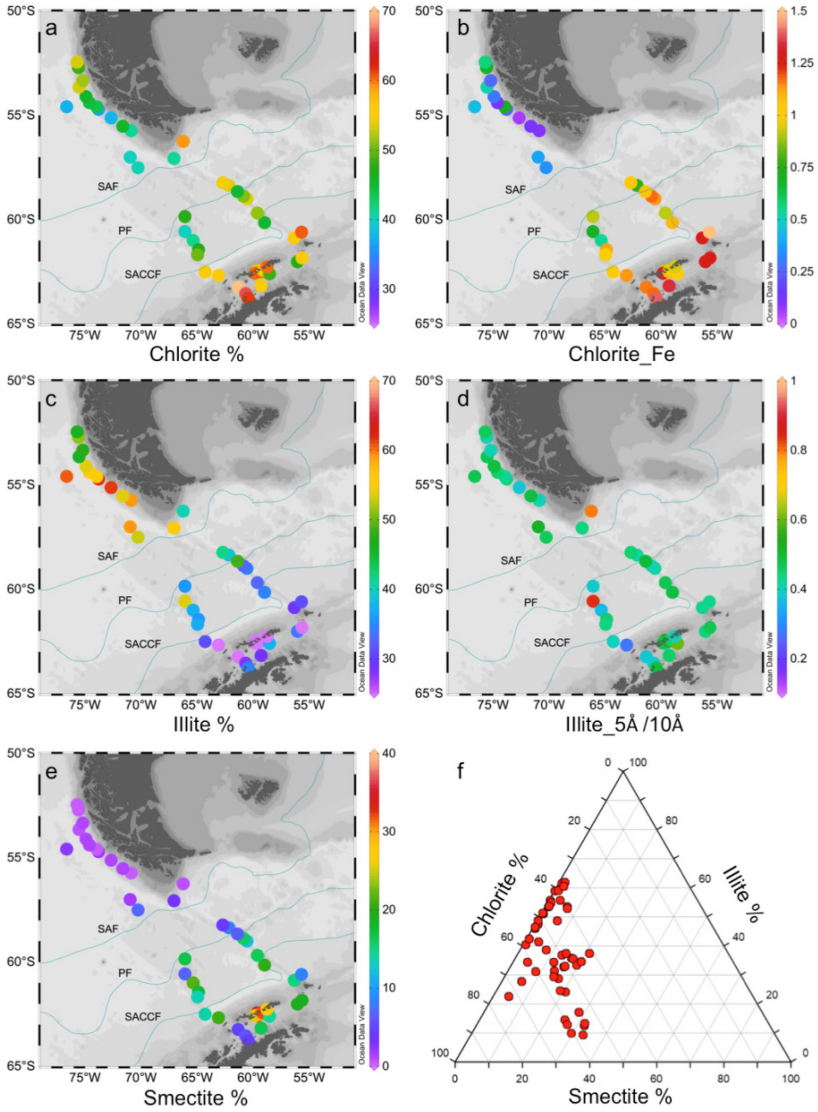

Fig. 3.5. Clay-mineral distributions in the study area: (a) chlorite (%); (b) Fe-rich chlorite; (c) illite %; (d) illite_5 Å /10 Å; (e) smectite (%); (f) ternary diagram of major clay minerals.

3.4.4 Sortable silt

The highest $\overline{SS}$ values of up to 40 μm were measured along the upper SCM at the Pacific entrance of the Strait of Magellan at relatively shallow water depths (~640-1080 m). These high values are characterized by a large standard deviation (σ = 2.7-3.0). Values substantially decrease offshore with increasing water depth (Fig. 3.6b). High $\overline{SS}$ values extend southward into the northern sector of the Drake Passage. There, values between 24 to 34 μm occur at water depths between ~1650 and 4000 m, with a standard deviation from 1.0 to 2.6. Relatively low $\overline{SS}$ values (18-25 μm) occur from south of the PF to the shelf of the AP, with small standard deviations (σ<1.2). $\overline{SS}$ values are positively correlated with the weight percentage of SS component (<63 μm) in all samples in this region (Fig. 3.6c).

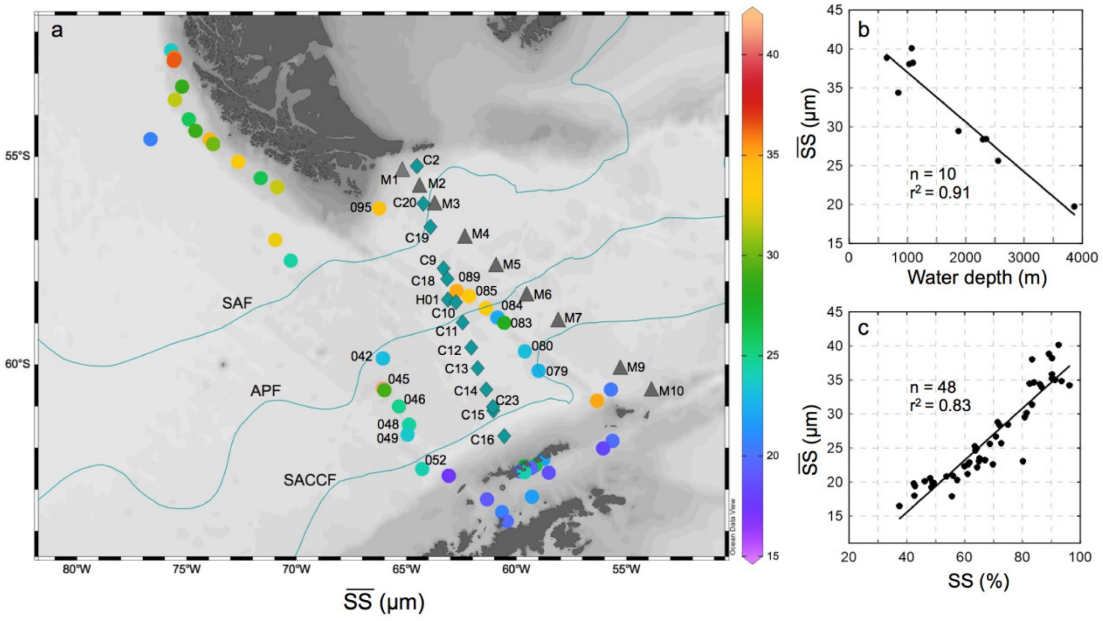

Fig. 3.6. (a) Spatial distribution of sortable silt mean grain-size, filled circles are sampling locations in this study and grey triangle points from Koenig et al., (2014) and the blue diamond points are current meter moorings from Donohue et al., (2016); (b) $\overline{SS}$ versus water depth along the southern Chilean margin; (c) $\overline{SS}$ versus SS percentage [%(10−63μm) from <63μm].

3.5 Discussion

3.5.1 Provenances and current transport of terrigenous sediment in the Drake Passage region

In general, surface sediments obtained from the SCM close to the PF contain higher

amounts of carbonate (mainly fragmented foraminifera, $CaCO_3$ = ~45%-70%, opal <5%), while sediments from south of the SACCF are characterized by relatively lower biogenic component contents (opal = ~10-20%, $CaCO_3$ < 3%). Accordingly, the terrigenous input ranges from 30% to 50% along the SCM and increases to up to 90% on the AP shelf (Table. S3.1) (Cárdenas *et al.*, 2018; Lamy, 2016).

The mineralogical assemblages in surface sediments on the SCM are mainly derived through riverine input from surrounding coastal mountain ranges, but may also be introduced through distal aeolian transport or by ocean currents from adjacent ocean basins. The bulk and silt mineralogy are primarily composed of calcite, chlorite, mica, quartz, feldspars and amphibole. The composition of the detrital minerals is typical of high-latitude regions and indicates that the sources of the sediments are principally represented by basic to intermediate magmatic or metamorphic rocks. Moreover, this mineral assemblage emphasizes that the pedogenesis on the continent is generally weak leading to rather low maturity of the sediments, because of limited chemical weathering and the increase of physical weathering processes especially by glaciers that lead to direct rock erosion in Patagonia (Diekmann *et al.*, 2000; Marinoni *et al.*, 2000; Marinoni *et al.*, 2008). The Qz/Fsp ratios on the bulk and silt show different broad spatial patterns that indicate they were derived from various transport processes (Fig. 3.3, 3.4). In general, quartz is virtually unaffected by chemical weathering, while feldspar is much easier to be dissolved (Nesbitt *et al.*, 1997). Due to strong tidal currents in the Pacific entrance of the Strait of Magellan, more feldspar has been altered or has been shredded and washed out, thus high values of Qz/Fsp ratios in bulk samples are distributed very patchily in this area (Fig. 3.3a). In contrast, high ratios of Qz/Fsp in the silt faction are more homogenously distributed along the SCM (Fig. 3.4a), which indicates feldspar in the coarse fraction has been altered into other minerals and then transported by the CHC/ACC flowing along the continental slope and through the Drake Passage. These results are supported by the coarse $\overline{SS}$ values (Fig. 3.6a), which are consistent with high current velocities along the SCM.

Since the study area is located in a high latitude setting with prevailing physical weathering and negligible chemical weathering, detrital clay mineral assemblages in

the marine sediments reflect the average rock composition in the source areas (Chamley, 1989; Petschick *et al.*, 1996). In the clay fraction, we observe an opposite trend of the illite and chlorite contents along the SCM, which indicates a gradual shift in the sediment provenance. Metamorphic and sedimentary lithologies that outcrop in the central part of Tierra del Fuego may supply a greater amount of chlorite, while the acidic rocks of the Andean Batholith on the western margin may contribute more illite (Marinoni *et al.*, 2008). The dry and cold climate limits chemical weathering and the source rocks are highly crystalline. Smectite content is very low along the SCM consistent with previous studies (Marinoni *et al.*, 2008). Therefore, it is unlikely that clay minerals were derived from the Atlantic sectors of Patagonia (Diekmann *et al.*, 2000; Marinoni *et al.*, 2000; Petschick *et al.*, 1996) or from the northern Chile margin (Lamy *et al.*, 1998; Siani *et al.*, 2010), as sediments in these areas show higher smectite contents.

The Drake Passage region is possibly influenced by very strong westerly winds that can transport dust from Patagonia and Australia around Antarctica (Lamy *et al.*, 2014; Pugh *et al.*, 2009; Weber *et al.*, 2012). The clay composition of Patagonian dust is characterized by smectite to Fe/Mg-bearing illite assemblages with some kaolinite and subordinate chlorite (Camilión, 1993; Diekmann *et al.*, 2000; Ito and Wagai, 2017). Because of the absence of kaolinite and the low abundance of smectite and an Al-rich illite dominance in the Drake Passage region, we suggest that an aeolian transport from Patagonian dust can be ruled out as a major contributor to our study area. On the other hand, dust from Australia likely does not reach the Drake Passage region, because accumulation rates in the central south Pacific are already very low (Lamy *et al.*, 2014; Wengler *et al.*, 2019), so a significant dust contribution to the Drake Passage region can be excluded as well. Compared to the northern Drake Passage region, the AP shelf is characterized by low carbonate (<3%) and high biogenic opal contents (avg.15%) (Cárdenas *et al.*, 2018), associated with high chlorite and smectite, and low illite contents (Fig. 3.7). These high chlorite and smectite values on the shelf of the AP are due to physical weathering of basic volcanic and metamorphic source rocks (Diekmann *et al.*, 2000), which were originally

supplied from the SSI area. The Fe-rich chlorite maximum in the same area (Fig. 3.5b) indicates a primarily basic igneous origin where Fe-rich chlorite is often formed from hydrothermally ferromagnesian minerals of basic source rocks (Camilión, 1993; Diekmann *et al.*, 2000; Ito and Wagai, 2017; Lamy *et al.*, 2014). Al-rich illite with a high crystallinity may have originated from Ellsworth Land, where intrusive and gneissic rocks outcrop (Hillenbrand *et al.*, 2003). In contrast, East Antarctica, which is dominated by Fe/Mg-bearing illite with a poor crystallinity, can be excluded as a major contributor (Fig. 3.7d, e) (Diekmann *et al.*, 2000; Petschick *et al.*, 1996). Notably, poorly crystalline and low 5Å/10Å ratios of illite indicate sediments that could be transported by the southwestward flowing deep water current from the Weddell Sea to the AP shelf (Fig. 3.7e).

In summary, the provenance of terrigenous sediment in the Drake Passage region is restricted to regional source regions: Patagonia at the southernmost part of South America and the AP, including parts of West Antarctica. East Antarctica is not an important source of continental detritus because the ACC represents a barrier for the oceanic transport of sediment. We assume aeolian supply of material from Patagonia and Australia to be rather unlikely according to our clay minerals composition results in the context of previous studies (Lamy *et al.*, 2014; Li *et al.*, 2008). The distinct boundary zone at the entrance to the Drake Passage with increasing chlorite and low smectite contents (Fig. 3.7a, c) in the Drake Passage as well underlines a minor sediment contribution from the Pacific sector of the Southern Ocean.

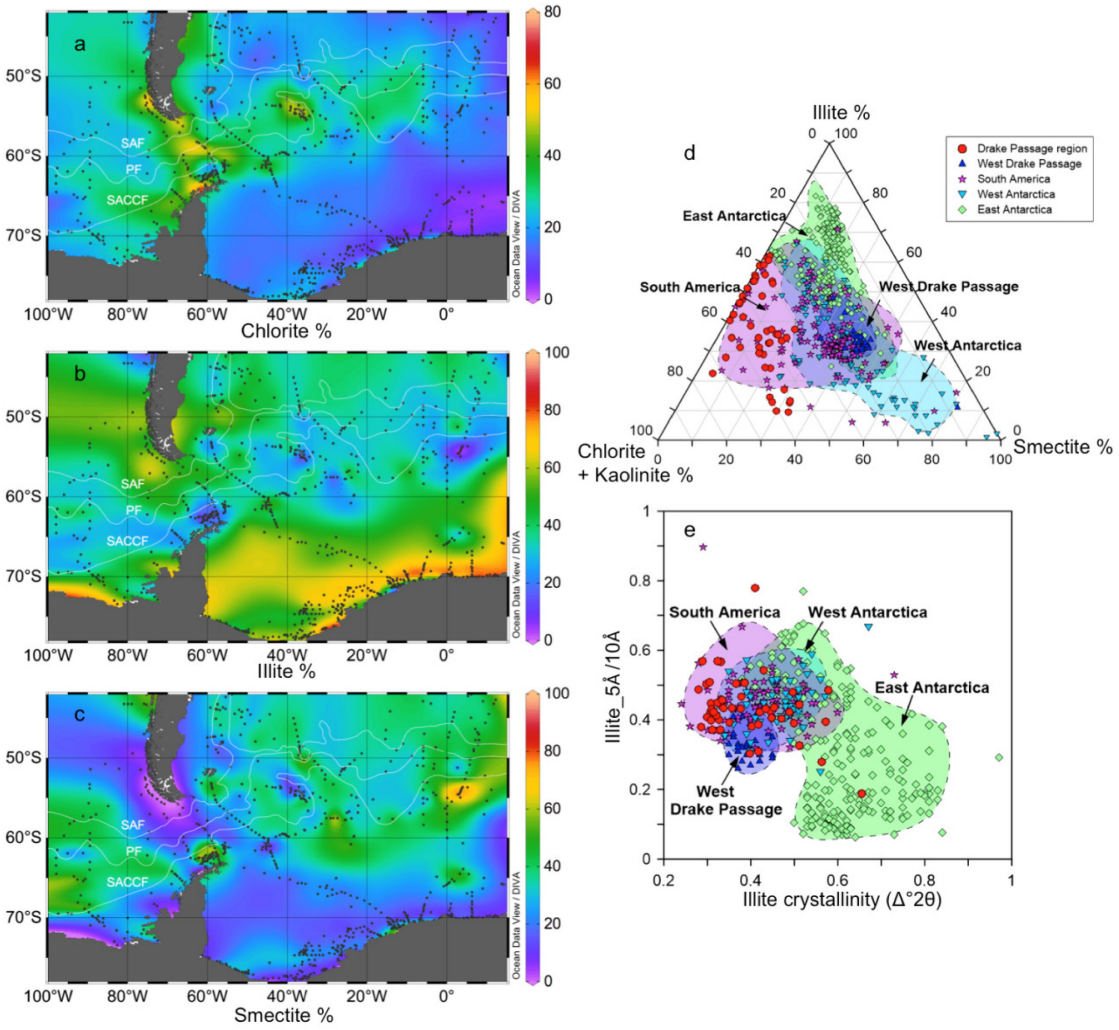

Fig. 3.7. Compilation of new and literature-derived data on clay mineral distributions in the study area: (a) chlorite (%), (b) illite (%), (c) smectite (%), (d) ternary diagram of major clay minerals and (e) Illite 5 Å /10 Å versus crystallinity index (IB, Δ°2θ). The locations of samples are shown in Fig. 3.2.

3.5.2 Reconstructed spatial variability of modern current speeds in the Drake Passage region

Ocean bottom currents often carry sediments and deposit them as so-called sediment drifts, which as a result provide valuable archives of changes in current intensity (Hall *et al.*, 2001). Since the ACC with its dense eddy structure extends from the sea surface to the sea floor, variations in bottom flow can provide a direct link to total changes in the ACC current strength and transport volume. The $\overline{SS}$ has been suggested to be the most suitable proxy signal for current speed reconstruction (McCave *et al.*, 1995), when potential problems involving source effects, downslope supply on continental margins, winnowing effects and ice delivery are considered adequately (McCave and

Andrews, 2019; McCave and Hall, 2006; McCave *et al.*, 2017).

Along the SCM, sediment core MD07-3128 previously yielded high Holocene $\overline{SS}$ values (avg. 38.3 μm) that have been interpreted in terms of strong current influence by the CHC along the continental margin (Lamy *et al.*, 2015). High Holocene current speeds were also recorded on the southern flank of the Falkland Plateau, downstream of the Drake Passage study region (Roberts *et al.*, 2017). Our new comprehensive, spatially resolved surface sediment $\overline{SS}$ records confirm the results of previous studies and extend them to a wider range of water depths across the margin. Generally, high $\overline{SS}$ values occur at the upper continental slope of Southern Chile and decrease downslope into the basin (Fig. 3.6a). This decrease is consistent with the relatively shallower maximum depth extent of the CHC (Boisvert, 1969), which is much more pronounced compared to the ACC in the Drake Passage. The maximum $\overline{SS}$ value with relatively large standard deviation at the entrance of the Strait of Magellan (Fig. 3.6a, b) correlates with maximum Qz/Fsp ratios (Fig. 3.4a). This might be explained by a strong grain-size influence on the mineralogy in this area and more sediment redistribution by (tidal) currents in the shallow water area. One sample (PS97/114), recovered from ~3900m water depth further offshore (west of the trench) yielded very low $\overline{SS}$ value (<20 μm), which can be explained by weak deep currents offshore and away from the CHC flowing along the continental margin.

In the central Drake Passage, sediments are characterized by higher silt contents predominantly transported by bottom currents, with little source influence from continental margins. Therefore, we will focus on the $\overline{SS}$ records in the Drake Passage (54ºS-62ºS) for the quantitative reconstruction of the bottom current speeds through comparison with instrumental current meter data across Drake Passage (Donohue *et al.*, 2016; Koenig *et al.*, 2014).

We produced a new calculation based on our wide range of $\overline{SS}$ values and mean flow speed (U) from the long-term current meters within the Drake Passage (Table 2). The data are fitted with a Reduced Major Axis (RMA) analysis (Miller and Kahn, 1962). The new calibration defined by twelve points for the Drake Passage region along the ACC ($\overline{SS} = 1.31U + 14.22, r = 0.92$) (Fig. 3.8E and Table 2). The

calibration line in the Drake Passage is characterized by a steeper slope compared to the Weddell/Scotia Sea line ($\overline{SS} = 0.59U + 12.23, r = 0.96$) (McCave *et al.*, 2017) (Fig. 3.8E), because our values significantly increase the range of the $\overline{SS}$ data covered. This supports the argument that the deposition of coarser silt upstream in the Drake Passage area may reduce the availability of coarse silt in the Weddell/Scotia Sea (McCave *et al.*, 2014; McCave *et al.*, 2017). In such a situation, the $\overline{SS}$ values become finer downstream than for the same flow speed at the upstream position (McCave and Hall, 2006). For the same flow speed (U = 11 cm/s), the $\overline{SS}$ value is 28 μm in the Drake Passage in contrast to 19μm in the Weddell/Scotia Sea (McCave *et al.*, 2017). Therefore, the deficiency of coarse silt probably resulted in an underestimation of the reconstructed change of the ACC strength (<10%) in the central Scotia Sea from the last glacial to the Holocene (McCave *et al.*, 2014). Further north, sediment cores from the northern Drake Passage and SCM records significantly higher changes over the last glacial termination (~40%) (Lamy *et al.*, 2015; Roberts *et al.*, 2017). The weak positive correlation ($r^2 = 0.66$) between the $\overline{SS}$ and eddy kinetic energy (K_E) for the twelve calibration points suggest the K_E does not play a strong role for the $\overline{SS}$ values on the bottom of the Drake Passage (Table 2). Therefore, we assume our new calibration provides a reliable evaluation of the flow speed in this region.

Our reconstructed current speed across the Drake Passage shows clear maxima at the main SAF and between the PF and SACCF (Fig. 3.8C), in parallel with the modern observed trend in speeds (Fig. 3.8B, D) (Donohue *et al.*, 2016; Koenig *et al.*, 2014; Renault *et al.*, 2011). The highest current speed (15.0 ± 2.1 cm s^{-1}) occurs around the main SAF, which is consistent with modern observations (Donohue *et al.*, 2016; Koenig *et al.*, 2014; Meredith *et al.*, 2011b; Renault *et al.*, 2011). Our reconstructed bottom flow speeds around the PF are as high as at the SAF (Fig. 3.8C, D), but the measured surface speeds are slower than at the main SAF in the current meter records (Fig. 3.8B). Three plausible explanations are: (1) the coarse grains are probably influenced by short term maxima in current speed and not only by the mean speed (Fig. S3.1), (2) the winnowing effect might play an role (McCave *et al.*, 2017),

or (3) the current meters may not capture the strong signals during their short term measurements (Koenig *et al.*, 2014), whereas our sediment data represent a longer time interval. Notwithstanding, both the grain-size data and the instrumental current meter data do show strong current signals around the PF and the northern SACCF and only the absolute magnitudes of the current speed peaks slightly diverge (Fig. 3.8). Relatively high and variable bottom flow speeds in the southern SACCF, however, are present responding to low and stable surface flow speeds. The divergence may be influenced by active cyclonic and anticyclonic eddies (Donohue *et al.*, 2016; Renault *et al.*, 2011), an assumption which is supported by the weak positive correlation between $\overline{SS}$ and K_E (Table 2). The variability of current speed reconstructed by the $\overline{SS}$ shows small amplitudes in the southern SACCF, which might indicate that only weak energy remains at the bottom that is not enough to disturb the sediment significantly. Unfortunately, this suggestion cannot be validated for the northern PF, because of the sparse sampling density and lacking sedimentary deposits in this area. More seafloor sediment samples combined with long-term current meter moorings are needed to diagnose finer-scale regional differences.

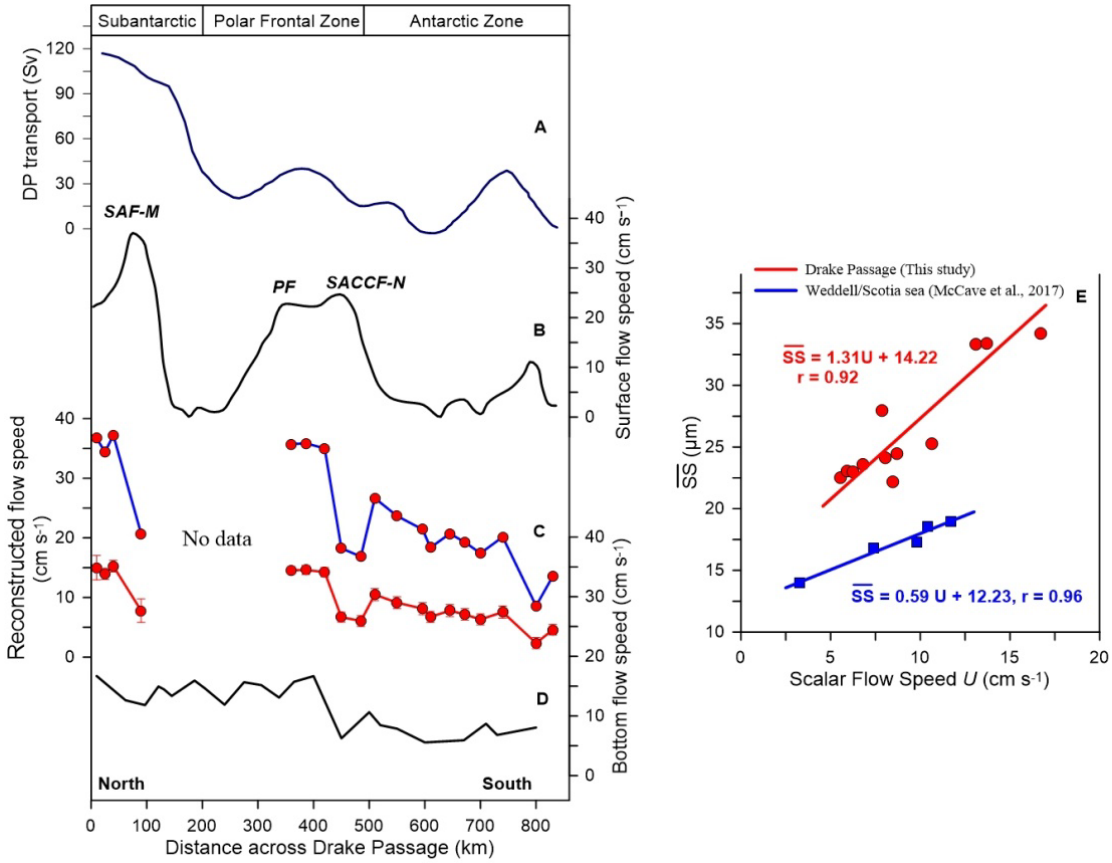

Fig. 3.8. Modern Drake Passage throughflow compared with modern current speed observations. (A) Modern Drake Passage cumulative volume transport above 3000 m water depth. Volume transport values are cumulated along Drake Passage Jason Track 104 (Koenig *et al.*, 2014) (Fig. 3.6) from south to north. (B) Across-track surface geostrophic velocities (Koenig *et al.*, 2014). (C) Flow speed across the Drake Passage reconstructed by our new calibrations (red line) compared with previous calculation in the Weddell/Scotia Sea (blue line) responding to (E). The location of each sample was projected on the oceanographic Jason Track 104. (D) The bottom current speeds are the long-term observational pattern showing by hourly mean speeds from Tracey et al., (2015). (E) Data from sediment samples and nearby current meters plotted as $\overline{SS}$ = f(U). Red circles are correlated with mean flow speed near-bottom current meter data from the cDrake project measurements (Donohue *et al.*, 2016; Tracey, 2015). Blue squares data are from McCave et al., (2017). Lines are Reduced Major Axes regression.

Table 2 Sediment samples $\overline{SS}$ compared to the near-bottom current meter data *U* (Donohue *et al.*, 2016; Tracey, 2015)

Station Number	Latitude	Longitude	Water depth (m)	$\overline{SS}$ (μm)	σ (μm)	Moorings	Latitude	Longitude	Water depth (m)	Length (days)	Mean *U* (cm/s)	KM# (cm^2/s^2)	KE# (cm^2/s^2)	KE/KM
PS97/095-1	56° 14.68' S	66° 14.93' W	1652	34.20	2.6	C02	55° 14.3' S	64° 31.1' W	1800	1060	16.71	139.60	68.71	0.49
PS97/089-2	58° 13.54' S	62° 43.43' W	3437	33.31	1.15	C09	57° 57.0' S	63° 08.6' W	4084	1449	13.09	85.63	38.60	0.45
PS97/045-1	60° 34.25' S	66° 05.65' W	2293	25.28	1.32	C10	58° 30.1' S	62° 45.3' W	2541	1458	10.64	56.60	25.94	0.46
PS97/084-2	58° 52.14' S	60° 52.03' W	3557	22.18	1.16	C11	58° 59.5' S	62° 26.5' W	3912	1451	8.46	35.76	19.59	0.55
PS97/083-1	58° 59.64' S	60° 34.25' W	3762	27.97	1.3	C12	59° 35.8' S	62° 03.4' W	4084	360	7.87	31.00	8.84	0.29
PS97/079-1	60° 8.58' S	58° 59.36' W	3539	22.52	1.1	C13	60° 05.5' S	61° 45.9' W	4061	1451	5.57	15.52	5.76	0.37
PS97/080-2	59° 40.43' S	59° 37.73' W	3105	23.07	0.7	C14	60° 36.0' S	61° 22.4' W	3735	1451	5.92	17.52	7.63	0.44
PS97/049-2	61° 40.27' S	64° 57.69' W	3758	23.61	1.26	C15	61° 06.7' S	61° 02.8' W	3908	1451	6.81	23.21	10.75	0.46
PS97/052-3	62° 29.94' S	64° 17.59' W	2890	24.12	1.33	C16	61° 43.4' S	61° 32.9' W	2549	1327	8.07	32.53	13.94	0.43
PS97/085-2	58° 21.28' S	62° 10.00' W	3091	33.39	1.13	C18	57° 41.8' S	63° 18.3' W	3673	377	13.71	93.95	34.40	0.37
PS97/048-1	61° 26.39' S	64° 53.20' W	3448	24.46	1.31	C23	61° 01.3' S	61° 03.7' W	3923	393	8.70	37.83	20.82	0.55
PS97/042-1	59° 50.59' S	66° 5.59' W	4172	23.00	1.07	H01	58° 26.5' S	63° 06.5' W	3849	376	6.25	19.56	13.98	0.72

Note the scalar flow speeds were chosen from the hourly mean current speeds in the near-bottom current meters data (Donohue et al., 2016; Tacey et al., 2015).

Mean (KM) or eddy kinetic energy (per unit mass) (KE) were calculated as (McCave et al., 2017).

The height above the bottom of current meters is 50 m.

3.6 Conclusions

We presented a synthesis of mineralogical (bulk, silt and clay fractions) and grain-size investigations (terrigenous silt grain-size distributions) based on a new set of surface sediment samples across the Drake Passage sector of the Southern Ocean that latitudinally extends from the southern Chilean margin to the Antarctic Peninsula to fill an important gap of marine sediment sample coverage.

Terrigenous sediments in the Drake Passage region mainly originate from proximal terrestrial sources as indicated by the mineralogical proxy distribution. The most important sources are Patagonia in the southernmost region of South America and the Antarctic Peninsula, including West Antarctica, while East Antarctica can be ruled out as a major source of continental detritus. An aeolian supply of dust from Patagonia and Australia was excluded based on major wind trajectories, low dust fluxes in the southeastern Pacific and a clear local mineral provenance pattern.

Finally, we produced a new calibration equation based on sortable silt grain size measurements and long-term current meters, to improve quantitative current strength reconstructions along the ACC in the Drake Passage sector of the Southern Ocean. A clear current speed pattern could be reconstructed from the sortable silt mean grain-size in the Drake Passage region, which is correlating with the instrumental observations of transport velocity across the Drake Passage (Donohue *et al.*, 2016; Koenig *et al.*, 2014; Meredith *et al.*, 2011b). Our new results thus enable future (semi-)quantitative studies that explore major past dynamic ACC responses to climate variations on geological time scales, which are critically needed to understand potentially large feedbacks within this largest ocean current system under future climate change scenarios.

Author Contributions

S.Z.W., G.K. and F.L. conceived and designed the experiments; S.E. carried out sortable silt data along the Chilean Margin; S.Z.W. carried out other sortable silt and all XRD measurement. S.Z.W. and G. K. led the data analysis with assistance of all

co-authors; B.D. and G.K. contributed MacDiff software; F.L., G.K., B.D., L.L.J., R.T., X.F.Z. and H.W.A. assisted with data interpretation; S.Z.W. drafted the manuscript with substantial comments and suggestions by all co-authors.

Acknowledgements

We thank the master crew and science party of RV Polarstern Expedition PS97 for their professional help in retrieving the samples. We are grateful to Prof. KA. Donohue for providing the Drake Passage current meter data. This paper is a contribution to PACES II Topic3 funded by the Alfred Wegener Institute Helmholtz Centre for Polar and Marine Research. Shuzhuang Wu is supported by the China Scholarship Council (CSC No. 201604910671) and AWI. We sincerely thank Susanne Wiebe and Rita Fröhlking-Teichert at AWI for technical assistance in sample preparation and analytical measurements.

Supporting Information:

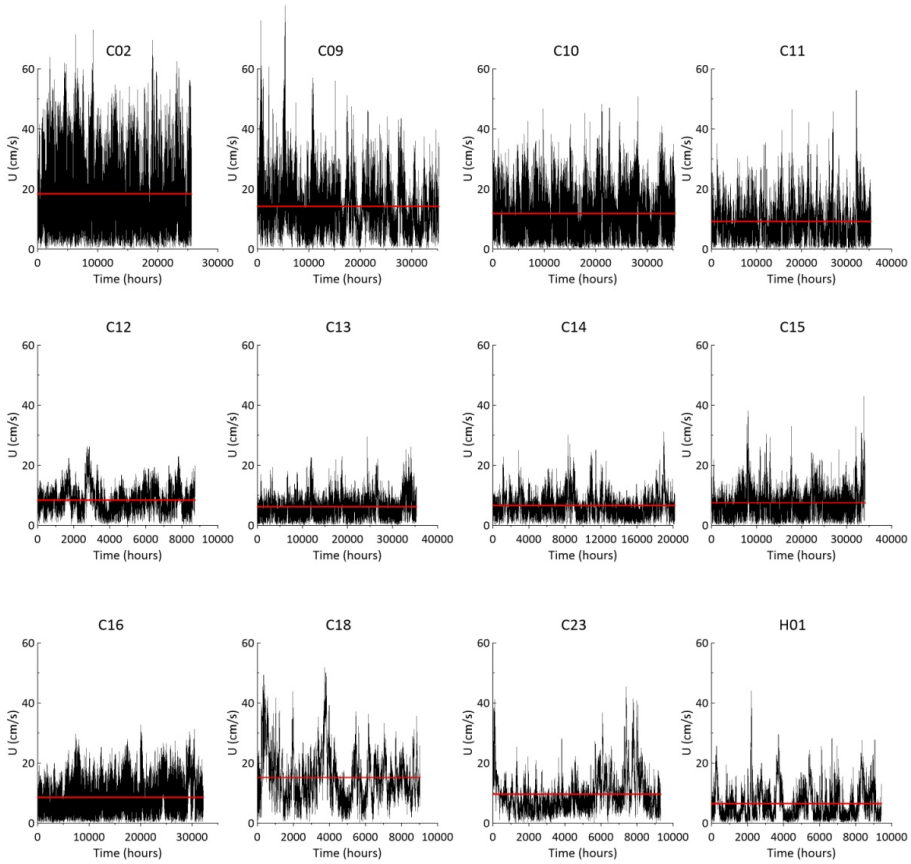

Fig. S3.1. Current meter hourly speeds in the Drake Passage (Tracey, 2015). Red lines are the mean flow speed at each site. These show high variability in hourly speed.

4 Orbital- and millennial-scale variability of the Antarctic Circumpolar Current over the past 140,000 years

Shuzhuang Wu[1], Lester Lembke-Jene[1], Frank Lamy[1], Helge W. Arz[2], Norbert Nowaczyk[3], Jiabo Liu[3,4], Xu Zhang[1,5], H. Christian Hass[6], Bernhard Diekmann[7], Levin Dumm[8], Jürgen Titschack[8,9], Xufeng Zheng[10], Dirk Nürnberg[11], Ralf Tiedemann[1], Gerhard Kuhn[1]

[1]Alfred-Wegener-Institut Helmholtz-Zentrum für Meeres- und Polarforschung, 27568 Bremerhaven, Germany

[2]Leibniz Institute for Baltic Sea Research Warnemünde, 18119 Rostock, Germany

[3]Helmoltz Centre Potsdam GFZ German Research Centre for Geosciences, 14473 Potsdam, Germany

[4]Southern University of Science and Technology, Department of Ocean Science and Engineering, 518055 Shenzhen, China

[5]College of Earth and Environmental Sciences, Lanzhou University, 730000 Lanzhou, China

[6]Alfred-Wegener-Institut Helmholtz-Zentrum für Meeres- und Polarforschung, 25980 Sylt, Germany

[7]Alfred-Wegener-Institut Helmholtz-Zentrum für Meeres- und Polarforschung, 14473 Potsdam, Germany

[8]MARUM–Center for Marine Environmental Sciences, University of Bremen, 28359 Bremen, Germany

[9]Senckenberg am Meer, Marine Research Department, 26382 Wilhelmshaven, Germany

[10]Key Laboratory of Marginal Sea Geology, South China Sea Institute of Oceanology, Chinese Academy of Sciences, 510301 Guangzhou, China

[11]GEOMAR, Helmholtz Centre for Ocean Research Kiel, 24148 Kiel, Germany

In preparation for Nature Communication

Abstract

The Antarctic Circumpolar Current (ACC), through promoting deep water upwelling and new water masses formation, plays a crucial role in global ocean circulation and climate change. However, on geological time scales the physical variability of the ACC is poorly constrained beyond the last glacial cycle. Here, we reconstruct changes in ACC strength over the past 140,000 years, based on grain size and geochemical characteristics from a highly-resolved marine sedimentary record in the central Drake Passage. We found significant glacial-interglacial changes of ACC flow speed in the vicinity of the Polar Front (PF), distinctively minimal change in the south of PF. Superimposed on these long-term changes, we found strong millennial-scale fluctuations in ACC intensity are in line with Antarctic temperature variations. Our grain size record revealed increased the millennial amplitude of the ACC towards the

Last Glacial Maximum (LGM). We hypothesize that the central ACC increases its sensitivity to Southern Hemisphere millennial-scale climate oscillations, likely related to westerlies' wind stress, oceanic fronts and Antarctic sea ice extent during the LGM. This strong variation of the ACC regulates Pacific-Atlantic water mass exchange via the "cold water route" and could significantly affect the Atlantic Meridional Overturning Circulation (AMOC).

4.1 Introduction

The Antarctic Circumpolar Current (ACC), the largest oceanic current system in the world, connects the Pacific, Atlantic and Indian Ocean basins. It exerts strong influence on the global MOC and climate variability (Marshall and Speer, 2012; Rintoul, 2018). The ACC transports cold and fresh water from the Pacific to the Atlantic through the Drake Passage, known as "cold water route" (Rintoul, 1991). This cold water route complements the warm westward Agulhas Current or "leakage" off the South African Cape of Good Hope known as "warm water route". Together, they constitute a major portion of the southern-sourced water return flow into the Atlantic, balancing the AMOC (Beal *et al.*, 2011; Gordon, 1986; Knorr and Lohmann, 2003; Rintoul, 1991) with influence up to the North Atlantic (McCarthy *et al.*, 2020).

The Drake Passage, located between South America and the Antarctic Peninsula, serves as a constriction for the ACC (Meredith *et al.*, 2011b) (Fig. 4.1). The ACC can be separated by three major oceanographic fronts: the Subantarctic Front (SAF), the Polar Front (PF), and the Southern ACC Front (SACCF) (Orsi *et al.*, 1995). Subdivisions of the ACC dynamics have been reconstructed in the northern Subantarctic Front (SAF) (Lamy *et al.*, 2015; Roberts *et al.*, 2017) and south of the Polar Front (PF) (McCave *et al.*, 2014) in the Drake Passage region.

Understanding the magnitude and sensitivity in the central ACC during the geological past is crucial for assessing its role in the global MOC, in particular with regard to ongoing and future anthropogenic climate change. However, available proxy evidence remains controversial for changes in ACC transport on glacial-interglacial

timescales (Lamy *et al.*, 2015; Lynch‐Stieglitz *et al.*, 2016; Mazaud *et al.*, 2010; McCave *et al.*, 2014; Roberts *et al.*, 2017) and knowledge for the central ACC evolution is still missing. In this study, we reconstruct changes in this central ACC on millennial to glacial-interglacial time scales, based on high-resolution grain size and bulk geochemistry time series data from a sediment core retrieved directly from the central Drake Passage (Site PS97/085, 58° 21.28′S, 62° 10.02′W; water depth 3090 m).

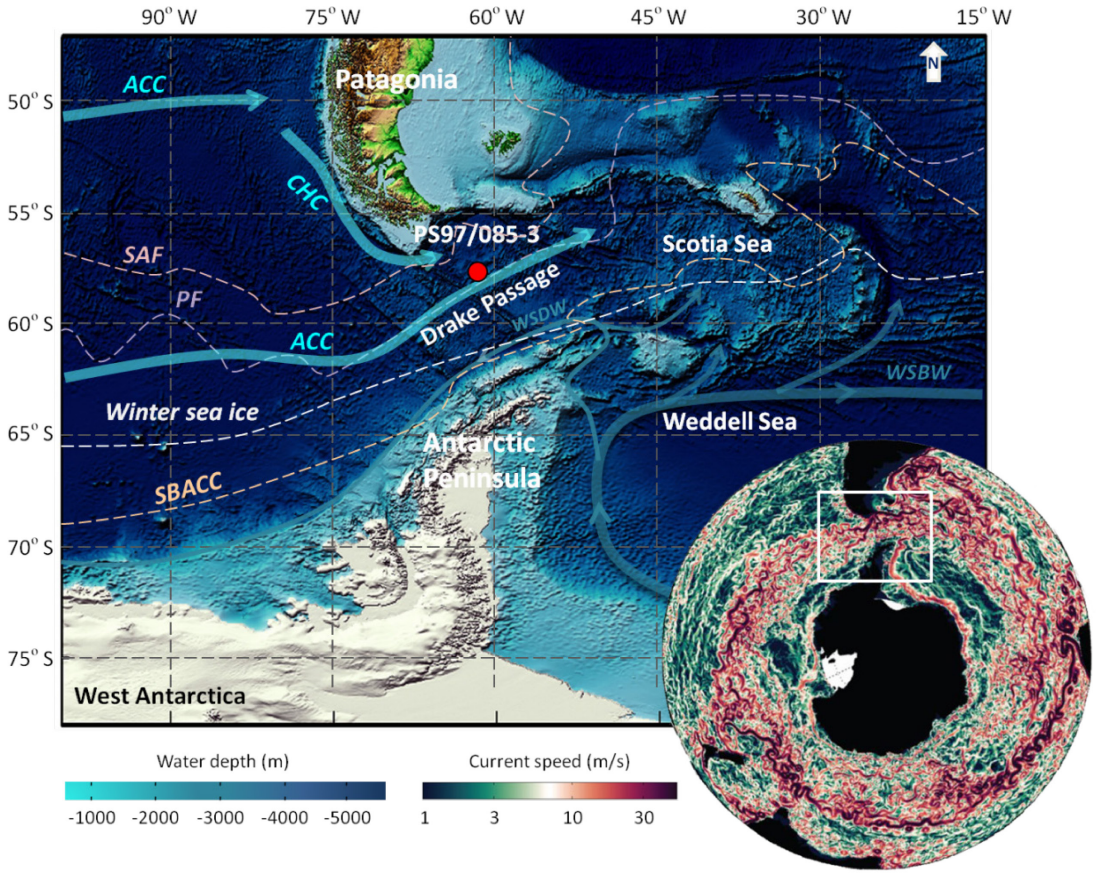

Fig. 4.1. Location map. Core PS97/085-3 is located in the central Drake Passage (red dot). Light blue arrows show the Antarctic Circumpolar Current (ACC) and the Cape Horn Current (CHC) (Chaigneau and Pizarro, 2005), while dark green-blue arrows are Weddell Sea Bottom Water (WSBW, thick) (Huang *et al.*, 2020) and Weddell Sea Deep Water (WSDW, thin) flows (Eagles *et al.*, 2006; Hernández-Molina *et al.*, 2017). White dashed line is average winter sea ice. Dashed lines are the Subantarctic Front (SAF, pink), Polar Front (PF, purple) and the southern boundary of the Antarctic Circumpolar Current (SBACC, light brown) (Orsi *et al.*, 1995). The right bottom insert map shows our study area in the white frame and the current speed in the Southern Ocean, with warmer red colors representing higher current speeds (Rintoul, 2018). This figure was adapted from Wu et al., (2019).

4.2 The ACC flow speed proxies

We use changes in grain size and geochemical properties of the terrigenous sediment fraction to reconstruct changes in ACC intensity (Fig. 4.2). The sortable silt mean grain size ($\overline{SS}$, 10−63 μm) is typically applied for evaluating relative changes in the near-bottom flow speed in deep sea sediments (McCave and Hall, 2006; McCave *et al.*, 1995). We correlated near-bottom flow speed mooring measurements with $\overline{SS}$ of seafloor sediments on a north-south Drake Passage transect (Wu *et al.*, 2019). However, modern observations reveal that the ACC deep-flow speeds are frequently faster than 15 cm/s (Donohue *et al.*, 2016); such high speeds can potentially remove parts of the silt and even the sand fractions (McCave and Hall, 2006). The grain size distribution mode would thus shift to the coarser fractions dominated by fine sand (Supplementary Fig. S4.4), and hence impair the $\overline{SS}$ as a current speed proxy. Accordingly, the $\overline{SS}$ may not capture the entire magnitude of the flow speed variations in our record (Fig. 4.2D). End member modeling analysis of the grain-size distributions indicate that the dominant mode of sediment transport can be shifted as well in response to current strength (Supplementary Fig. S4.5). High ACC speed can extend the sorting range beyond the sand-silt boundary (Supplementary Fig. S4.4B), which was also observed at the Chilean Margin and the northernmost Drake Passage (Lamy *et al.*, 2015). Therefore, we use the mean grain size of the sortable silt plus the fine sand fractions ($\overline{SSFS}$, 10-125 μm) as the flow speed proxy to reconstruct the deep ACC dynamics throughout the past 140 ka (Fig. 4.2E). Since our site is located far away from the continent, the terrigenous sand fractions are most likely transported by ice and then reworked by bottom currents. Generally, unsorted ice-rafted debris (IRD) from glacial sources may affect the $\overline{SS}$-based flow speed proxy (McCave and Andrews, 2019). However, the content of IRD in our site samples is generally less than 2 vol. % except for one spike (18 vol. %) at the end of Marine Isotope Stage (MIS) 4 (Fig. 4.2G) and its fluctuations are independent of $\overline{SSFS}$ changes (Supplementary Fig. S4.6). Furthermore, variations in $\overline{SSFS}$ and SSFS% component are positively correlated (Supplementary Fig. S4.6), suggesting bottom currents are

the principal driver for changes in the grain size fraction (10-125 μm) at our site (McCave and Andrews, 2019; McCave and Hall, 2006).

Zirconium (Zr) is typically accumulating in the heavy mineral fraction associated with coarser grain sizes, while Rubidium (Rb) is preferentially retained in the clay mineral faction (Fralick and Kronberg, 1997). Previous studies found a positive correlation between grain size and the Zr/Rb ratio (Chen *et al.*, 2006; Dypvik and Harris, 2001). Therefore, the Zr/Rb (XRF-CS peak area count) ratio (Fig. 4.2C) can reflect changes in sediment fractions by current transport (Lamy *et al.*, 2015; Toyos *et al.*, 2020), or aeolian input (Chen *et al.*, 2006). Major aeolian input can be ruled out in our study area supported by mineralogical and geochemical properties (Walter *et al.*, 2000; Wu *et al.*, 2019). High-resolution records of grain size and Zr/Rb ratio from the same core can thus provide a robust signature of ACC variability.

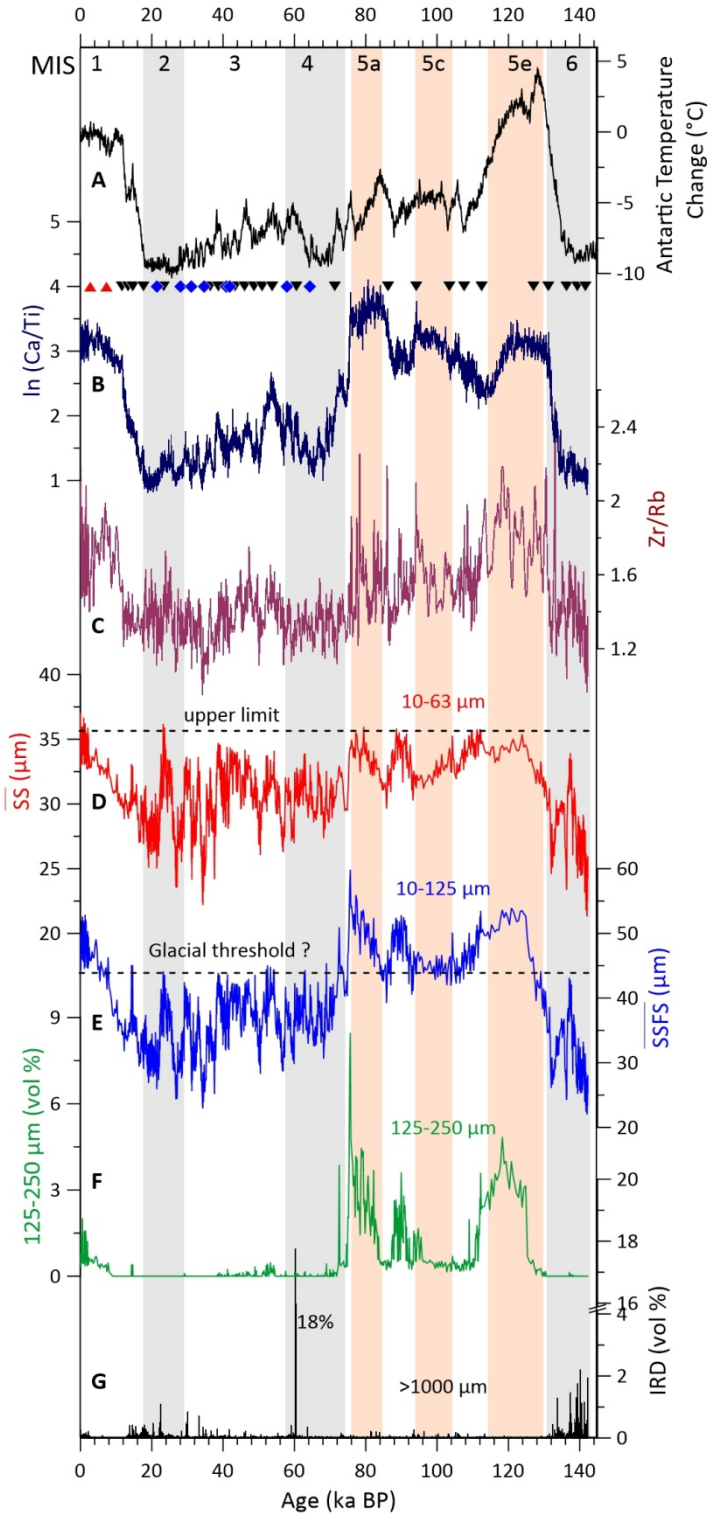

Fig. 4.2. Reconstructed changes in ACC intensity and compared with Southern Hemisphere temperature signature. A, Antarctic temperature changes from the European Project for Ice Coring in Antarctica (EPICA) Dome C ice core (Jouzel *et al.*, 2007). B, High-resolution XRF scanner-derived records of ln(Ca/Ti) (peak area count ratios) were applied to fine-tune to the Antarctic temperature anomalies together with radiocarbon dates, relative paleointensity and paleomagnetic excursions age control points from core PS97/085-3 (see Supplementary Method, Fig. S4.2; S4.3). C, XRF-derived Zr/Rb variations indicate changes in sediment grain size

fractions. D, mean sortable silt grain size ($\overline{SS}$, 10-63 μm) reaches up its limit under high flow speeds. E, mean grain size of sortable silt and fine sand ($\overline{SSFS}$, 10-125 μm) as the ACC proxy in this study. F, Coarse sand fraction (125-250 μm), mainly in interglacials, inferring high current speeds highlights the extension of the sorting effect to coarser grain sizes. G, Ice-rafted debris (IRD vol. %), defined by larger than 1 mm grain size from X-ray computer topography scan (see Supplementary Methods). Vertical gray bars mark inferred glacial periods and pink bars inferred the sub-interglacial during Marine Isotope Stage (MIS) 5.

4.3 Changes in ACC strength in the central Drake Passage

Our sediment record documents the glacial-interglacial variability of the ACC in the central Drake Passage over the past 140 ka (Fig. 4.2). The timing of the major ACC changes follows Antarctic temperature anomalies on glacial-interglacial timescale (Veres *et al.*, 2013), implying the ACC strength in the Drake Passage is sensitive to Southern Hemisphere climate oscillations (Fig. 4.2A, C, E). During the penultimate interglacial (MIS 5e, ~129-116 ka), the average $\overline{SSFS}$ value is ~49 μm, which is slightly higher than the Holocene average (~47 μm, ~0-10 ka). This suggests that the ACC flow speeds during MIS 5 was higher than at present, supported by consistent changes in Zr/Rb ratios (Fig. 4.2C). In contrast to the MIS 5e and the Holocene, the ACC strength significantly decreased during the Penultimate Glacial Maximum [PGM, ~140 ka; ($\overline{SSFS} = \sim 28$ μm)] and the LGM (~26-19 ka, $\overline{SSFS} = \sim 34$ μm). The grain size proxy records reveal a ~43% decrease in the ACC strength during the PGM compared to MIS 5e, larger than the LGM to Holocene change of ~28%.

Our observed glacial reductions of the ACC speed in the central Drake Passage are broadly consistent with previous studies (Lamy *et al.*, 2015; Roberts *et al.*, 2017). Various glacial-interglacial amplitudes of the ACC changes prevailed in the Drake Passage region (Lamy *et al.*, 2015; McCave *et al.*, 2014; Roberts *et al.*, 2017). Larger glacial-interglacial changes in flow speeds were observed in the northern SAF with a range of ~20-50% at the intermediate water depth (600-1030 m) (Lamy *et al.*, 2015; Roberts *et al.*, 2017). Smaller fluctuations in ACC changes (~10-16%) occurred in deep water with ~3781 m nearby the SAF (Toyos *et al.*, 2020). In the central Drake Passage nearby the PF, the ACC throughflow exhibits a ~28-43% glacial reduction at ~3090 m water depth, which are much greater than the variations along the Scotia Sea

transect in the southern PF (≤ 10%, 2000-4300 m water depth) (McCave *et al.*, 2014). Differences between these results are likely due to the geographical settings within latitudinal subdivisions of the ACC and the related fronts, as well as to their water depth. Therefore, we suggest an enhanced sensitivity of the ACC around the PF and the SAF (Lamy *et al.*, 2015; Roberts *et al.*, 2017) to the glacial-interglacial climate changes compared to minimal changes occurred in south of the PF along the Scotia Sea transect (McCave *et al.*, 2014). These are consistent with modern ACC transport and the highest current velocities prevailing in the vicinity of the SAF and PF in the Drake Passage region (Donohue *et al.*, 2016; Koenig *et al.*, 2014). Since lack of sample in south of the PF in the Drake Passage, future works are required to explore this area and provide a comprehensive view of the ACC dynamics and its connection to Southern Ocean annual sea ice coverage and Antarctic Bottom Water (AABW) production (Huang *et al.*, 2020).

Several processes might cause these changes in the ACC strength at site PS97/085, including changes in the southern westerly winds (SWW) (Toggweiler *et al.*, 2006), the ACC oceanic fronts (Gersonde *et al.*, 2005) and buoyancy forcing (McCave *et al.*, 2014). Although the intensity and position of the glacial SWW are still uncertain, a northward displacement of the SWW is widely assumed during the LGM (Kohfeld *et al.*, 2013; Sime *et al.*, 2013), with reduced impact on the ACC in the Drake Passage sector (Lamy *et al.*, 2015; McCave *et al.*, 2014). The glacial oceanic fronts were likewise suggested to have shifted equatorward (Gersonde *et al.*, 2005), thus the South American continent would have obstructed the ACC flowing through the Drake Passage (Roberts *et al.*, 2017). Moreover, our ACC flow speed reconstruction is correspondent with the sea salt sodium record from the Antarctic Dronning Maud Land ice core (Fischer *et al.*, 2007) (Fig. 4.4D, E). These indicate changes in sea ice production and coverage might have been linked to the observed ACC changes, in line with earlier suggestions (Lamy *et al.*, 2015; McCave *et al.*, 2014). During the LGM, summer sea ice likely expanded northward by more than 500 km (Ferrari *et al.*, 2014; Gersonde *et al.*, 2005; Stein *et al.*, 2020). Such large sea ice coverage could have significantly decreased the effectiveness of wind stress acting on

the ocean surface (Lamy *et al.*, 2015; Martin *et al.*, 2014; McCave *et al.*, 2014) and thus reduced the ACC strength. Conversely, at interglacial stages, sea ice retreat and southward displacement of the SWW and oceanic fronts would have increased wind stress efficiency on the ocean surface and accelerated the ACC (Ferrari *et al.*, 2014; Lamy *et al.*, 2015; McCave *et al.*, 2014).

Relatively low atmospheric temperature with increasing sea ice concentration prevailed during MIS 5b and 5a compared to the MIS 5e (Fischer *et al.*, 2007; Veres *et al.*, 2013), however, these two stages both registered a strong ACC (Fig. 4.2C, E). Previous study found that the sea ice surface can provide greater drag than the ice-free surface and suggested an optimal ice concentration of 80-90% that amplifies wind stress momentum transfer threefold on the ocean surface (Martin *et al.*, 2014). Consequently, expansion of sea ice during MIS 5b and 5a would have increased the SWW efficiency on the ACC, and thereby resulted in high ACC flow speeds at these sub-interglacial stages (Fig. 4.2E). We found the $\overline{\text{SSFS}}$ exhibits a rapid step-like change at ~43 ± 2 μm between the glacial and interglacial stages (Fig. 4.2E, dashed line), indicating a threshold-like nonlinear behavior for the ACC changes between glacial and interglacial conditions.

4.4 Millennial-scale variations of ACC during the last glacial

Superimposed on the glacial-interglacial changes, our records exhibit markedly high-amplitude, millennial-scale variations in the ACC flow speeds covering the last glacial cycle (Fig. 4.2E, 4.3D). Within age model uncertainties, a close correspondence between the ACC millennial maxima and Antarctic ice core (EDML) oxygen isotope maxima (Fig. 4.3D, G), suggesting the ACC strength is sensitive to millennial-scale climate oscillations. A stronger ACC coincides with a weakened AMOC during cold phases in the Northern Hemisphere (Fig. 4.3A, D). This may have been caused by the combined influence of the bipolar seesaw mechanism (Stocker and Johnsen, 2003), the Antarctic sea ice retreat and the southward shift of SWW (Ferrari *et al.*, 2014; Lamy *et al.*, 2015; Pedro *et al.*, 2018).

We found increased amplitudes of ACC millennial variations (~38- 23 ka) as the climate was approaching the LGM (Fig. 4.3D), in contrast to a steady decline of the Antarctic temperatures (Fig. 4.3G). Enhanced sensitivity of the ACC toward the LGM was also recorded in the variation of the fine sand fraction percentages in the northern SAF (Lamy *et al.*, 2015) (Supplementary Fig. S4.8). This suggests the ACC may have reached its highest sensitivity in response to the Southern Hemisphere millennial-scale climate oscillations. Consequently, the ACC reaccelerated to higher flow speeds (Fig. 4.3D) during the cold stadials in the Northern Hemisphere, like the Heinrich events H2 and H3 (Bond *et al.*, 1992). This probably related to sea ice retreat (Ferrari *et al.*, 2014) and the southward shift of the westerlies (Lamy *et al.*, 2015; Toggweiler *et al.*, 2006) and large shift of the oceanic fronts (Gersonde *et al.*, 2005).

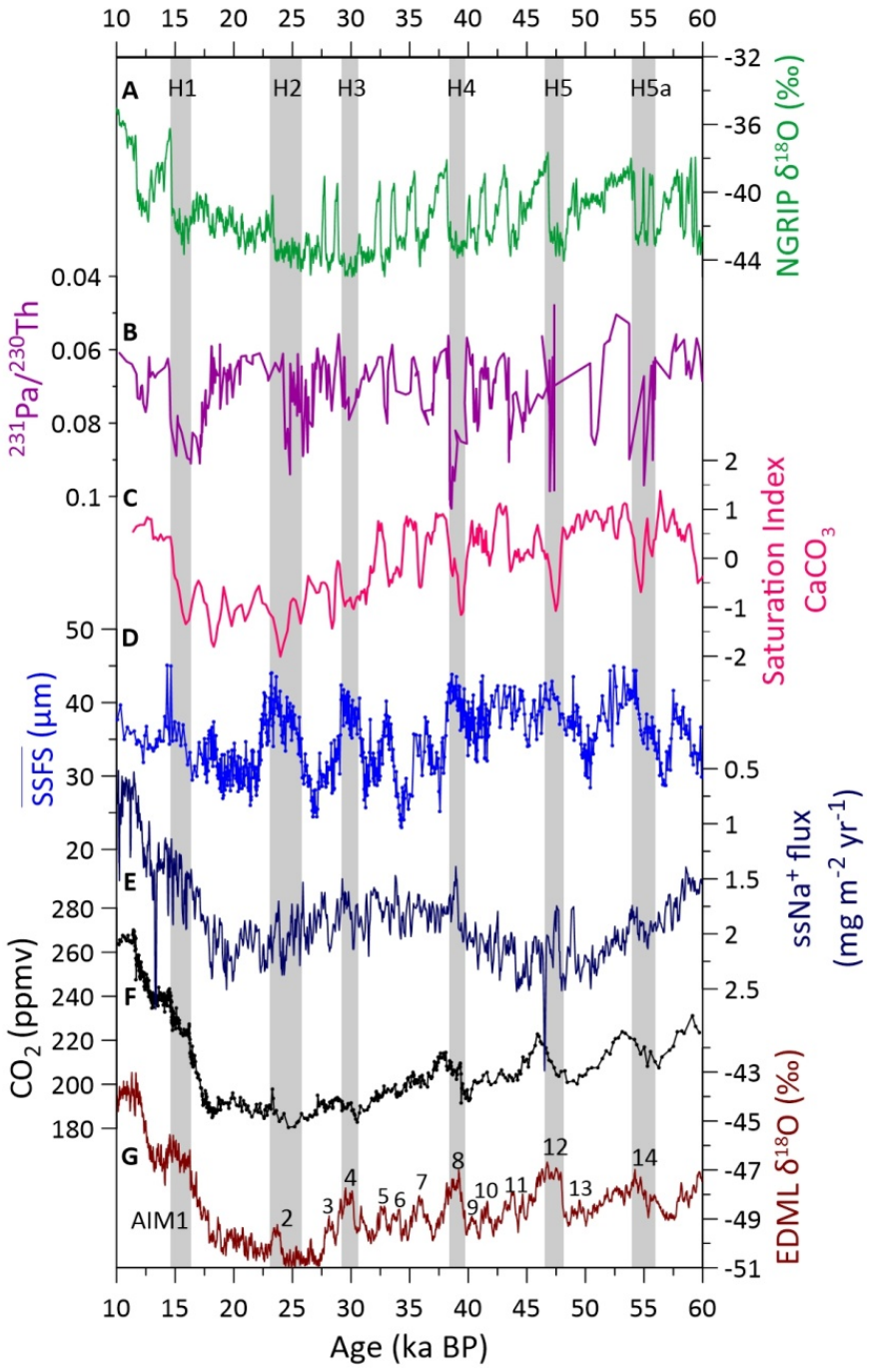

Fig. 4.3. Millennium-scale changes in ACC strength compared to paleoclimatic records over the last 60 ka. A, NGRIP oxygen isotope record ($\delta^{18}O$ vs. VSMOW) (Andersen *et al.*, 2004). B, Bermuda Rise $^{231}Pa/^{230}Th$ data (Bohm *et al.*, 2015; Henry *et al.*, 2016), a proxy for the Atlantic Meridional Overturning Circulation (AMOC) strength. C, Saturation index as a proxy for reconstructed carbonate saturation changes in the South Atlantic (Gottschalk *et al.*, 2015). D, $\overline{SSFS}$ as flow speed proxies for the ACC strength (this study). E, sea salt sodium ($ssNa^+$) flux, a proxy for sea ice (Fischer *et al.*, 2007). F, Synchronized ice-core atmospheric pCO_2 (EPICA Community Members, 2006). G, Oxygen isotope record from the EPICA Dronning Maud Land (EDML) ice core (EPICA Community Members, 2006). Vertical gray bars mark inferred millennial-scale ACC peaks that correspond with millennial scale temperature maxima in Antarctica (AIM) and Heinrich events (H) in Greenland.

4.5 Physical changes in the ACC linked to the AMOC stability

The ACC transports cold and fresh water from the Pacific via the "cold water route" to the South Atlantic (Rintoul, 1991), while warm, salty water from the Indian Ocean via the "warm water route" flows into the South Atlantic (Gordon, 1986). These two sources with upwelling North Atlantic Deep Water (NADW) in the Southern Ocean mainly comprise the northward-flowing return in the upper branch of the AMOC (Marshall and Speer, 2012). The wind-driven isopycnal upwelling in the Southern Ocean has been suggested to maintain the AMOC strength and stability (Anderson *et al.*, 2009; Christo and Andreas, 2015), which was supported by data on opal flux, an upwelling proxy during the last glacial cycle (Anderson *et al.*, 2009). We focus on comparing physical changes in the two oceanographic systems and their potential influence on the AMOC strength and stability in the past.

We compared the ACC strength based on grain size records from the central Drake Passage (Fig. 4.4D) with the Agulhas leakage intensity, reconstructed by planktic foraminiferal fauna census counts (Peeters *et al.*, 2004) in the South Africa margin over the past 140 ka (Fig. 4.4C). Both water route intensities increased during the deglaciations from proxy evidence (Peeters *et al.*, 2004) (Fig. 4.4C, D), suggest that they likely played a positive role on the AMOC recovered to active interglacial mode (Fig. 4.4B). The Agulhas leakage reached its transport maximum during the termination and subsequently significant decreased water volume transport to the South Atlantic (only ~8 Sv during MIS 5) (Caley *et al.*, 2014). In contrast, the ACC remained strong with smaller sub-interglacial fluctuations throughout the MIS 5 (Fig. 4.4D). Modern observation shows the total ACC transport is ~155 Sv, 62% of which is flowing through the Drake Passage into the South Atlantic (Drouin and Lozier, 2019). We reconstructed higher ACC flow speeds during MIS 5 than today (Fig. 4.4D), thus the ACC transport should be larger than its modern one. The ACC can induce the formation of surface and intermediate water to fuel the upper overturning cell in the Southern Ocean (Marshall and Speer, 2012). Compared to the lower Agulhas leakage transport volume contribution, the ACC may play a crucial role in

keeping the AMOC strong throughout the MIS 5, which was indicated by low $^{231}Pa/^{230}Th$ ratios (Bohm *et al.*, 2015; Henry *et al.*, 2016). This argument is supported by model simulations, which suggested that transport of more fresh water via the ACC into the South Atlantic would increase meridional density gradients in the Atlantic and therefore increase the AMOC (Kuhlbrodt *et al.*, 2007; Sijp and England, 2004). A slow-down of the ACC at the MIS 5/4 transition followed by high frequency variations of the ACC through MIS 4-2 might potentially be linked to AMOC instability during the glaciation (Bohm *et al.*, 2015; Henry *et al.*, 2016) (Fig. 4.4B, D). In contrast, a weak Agulhas leakage transport into the South Atlantic prevailed during the glacial periods (Peeters *et al.*, 2004) (Fig. 4.4C).

Overall, we suggest the ACC via physical changes likely played a crucial role in the AMOC strength and stability over the past 140 ka. Although the ACC provided a dynamical link with the AMOC, several other important processes, like fresh water flux, salinity and sea ice extent (Christo and Andreas, 2015; Ferrari *et al.*, 2014; Kuhlbrodt *et al.*, 2007), may act together to explain the full changes of AMOC.

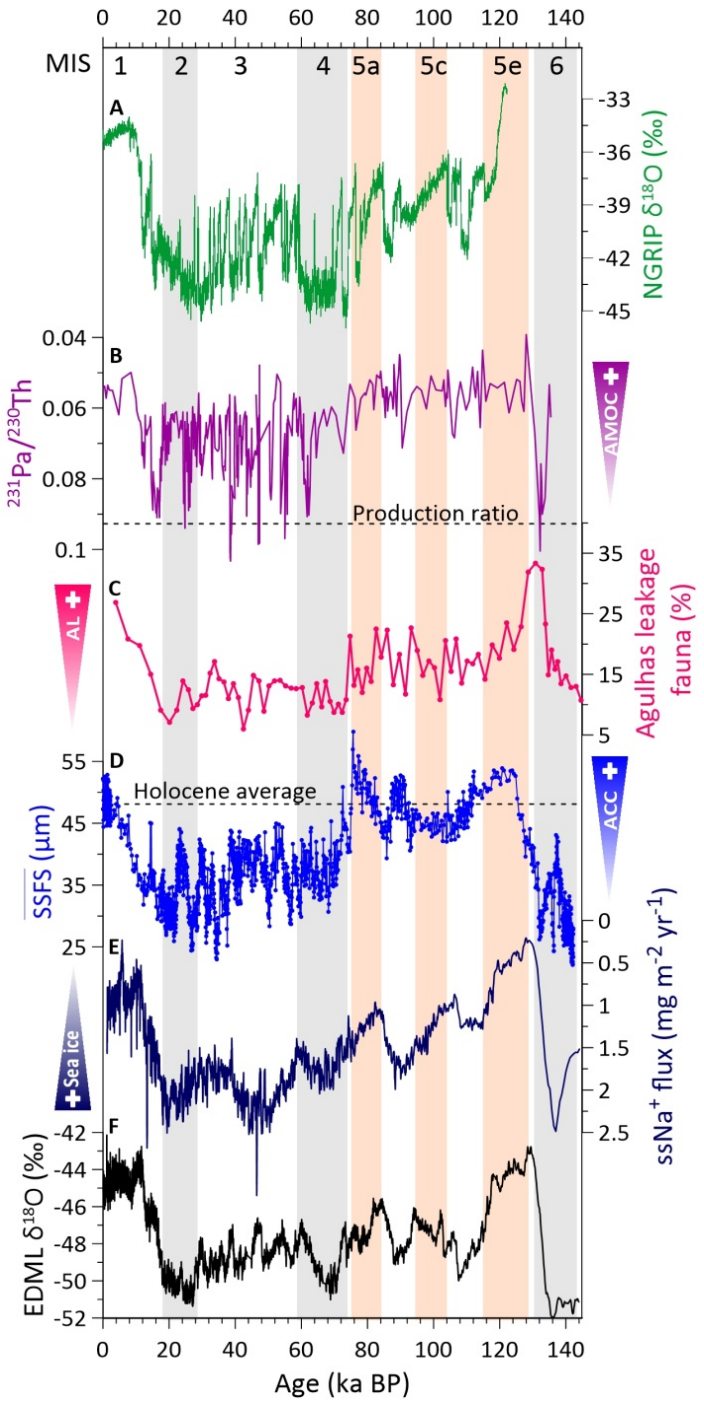

Fig. 4.4. Reconstructed changes in ACC strength compared with palaeoclimatic records over the past 140 ka. A, Oxygen isotope record from North Greenland Ice Core Project (NGRIP) (Andersen *et al.*, 2004). B, Bermuda Rise $^{231}Pa/^{230}Th$ data (Bohm *et al.*, 2015; Henry *et al.*, 2016), indicating the AMOC strength. Dashed line is production ratio ($^{231}Pa/^{230}Th$ = 0.093), suggesting no transport. C, planktic foraminiferal fauna reflect the intensity of the Agulhas leakage (Peeters *et al.*, 2004). D, $\overline{SSFS}$ as flow-speed proxy for the ACC strength (blue, this study). E, sea salt sodium flux from EDML ice core, a proxy for sea ice, smoothed with a three-points running mean(Fischer *et al.*, 2007). F, $\delta^{18}O$ time series from the EDML ice core (EPICA Community Members, 2006). Vertical gray bars mark glacial periods and pink bars mark the warm stages during MIS 5.

Physical and chemical Pacific-Atlantic exchange together with the NADW export might regulate changes in carbonate saturation (Gottschalk *et al.*, 2015) in the South Atlantic (Fig. 4.3B-D). These processes with wind-driven upwelling (Anderson *et al.*, 2009) and sea ice condition (Ferrari *et al.*, 2014; Stein *et al.*, 2020) modulate the sequestered CO_2 exchange with atmosphere over millennial timescales (Fig. 4.3F).

Our results show significant ACC flow speed variations in the central Drake Passage on both orbital and millennial timescales. These changes in ACC and Drake Passage throughflow were likely driven by a combination of changes in wind stress efficiency (Martin *et al.*, 2014), oceanic fronts (Gersonde *et al.*, 2005), and sea ice coverage (Ferrari *et al.*, 2014; Lamy *et al.*, 2015; McCave *et al.*, 2014). Our records imply enhanced sensitivity of millennial-scale ACC variations toward the LGM. These strong variations of the ACC regulating the Pacific-Atlantic exchange via the cold water route may have played a significant role in shaping the AMOC strength and stability. Since a vigorous ACC prevailed during MIS 5, a consequently active mode of the global MOC will be likely persistent in the long-term future, although the AMOC has been showing signs of weakening since past decades (Srokosz and Bryden, 2015).

Acknowledgements

We thank the captain, crew and scientific party of RV Polarstern Expedition PS97 for their professional help in retrieving the sediment samples. We also thank C. Lange, X. Gong and A. C. Ravelo for discussions. We sincerely thank S. Wiebe and R. Fröhlking-Teichert at Alfred Wegener Institute (AWI) for technical assistance in sample preparation and grain size measurements and XRF scans. This study was supported by the China Scholarship Council (CSC No. 201604910671) and AWI.

Supporting Information

4.6 Material and methods

Sediment composition. During Polarstern Expedition PS97 two sediment cores were taken with a piston corer and a trigger corer in the central Drake Passage at site PS97-085 (PS97/085-3, 58° 21.27′S, 62°10.03′W, water depth 3090.8 m; 14.43 m core length and trigger corer, 0.89 m core length) (Lamy, 2016). The piston and trigger corers were spliced together, based on correcting magnetic susceptibility and X-ray fluorescence core scanner data. The upper 56 cm of the trigger corer complement the missing section of the piston corer yielding a composite depth for Site PS97-085 (Table. S4.1). Our site PS97-085 is located in the West Scotia Ridge spreading center and sits on a crest of the northern flank of the West Scotia Ridge next to the Shackleton Fracture Zone (Fig. S4.1) (Lamy, 2016).

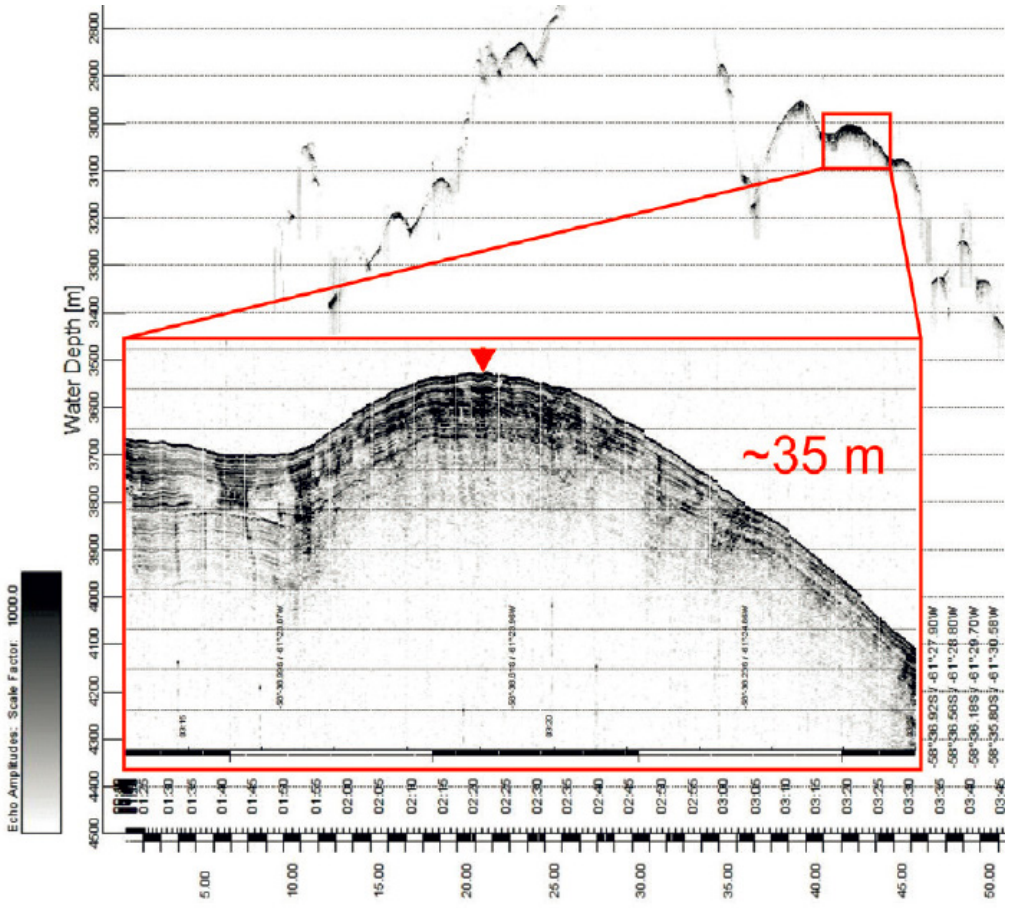

Fig. S4.1. Parasound profile across the West Scotia Ridge east of the Shackleton Fracture Zone with the coring site PS97/085 from Lamy (2016).

The core PS97/085-3 primarily consists of terrigenous materials (mean 90.5% [weight %], min. 62.3%, max. 98.5%) and biogenic carbonate (mean 7.3%, min. 0.3%, max. 36.0%), mainly foraminifera shells in the coarse sand fraction. The terrigenous sediments are characterized by brownish fine sand to sandy silt during warm periods, whereas cold periods correspond to grayish silt to blue-gray silty clay (Lamy, 2016). Measurement of the total carbon (TC) and organic carbon (TOC) contents with element analyzes were used to calculate the $CaCO_3$ content by [$CaCO_3$ = (TC-TOC)* 8.333]. $CaCO_3$ contents range from ~20 to 35% during the interglacials and are less than 10% for the glacial periods. TOC contents vary from 0.05 to 0.18 wt % and biogenic opal content is very low (mean 2.2%, min. 0.8%, max. 5.1%) throughout the core.

Magnetic Susceptibility

High-resolution logging of magnetic volume susceptibility on core PS97/085-3 was performed with a Bartington MS2E sensor at Leibniz-Institute for Baltic Sea Research Warnemünde. Detail measurement information was described in Chapter 2.3.5.

Paleomagnetic measurements

For paleo- and rock magnetic investigation core PS97/085-3 was sampled with clear plastic boxes with an internal size of 20×20×15 mm (6 cm^3) pressed side by side into the split core. The anisotropy of magnetic susceptibility (AMS) was determined on these boxes using an AGICO Multi-Function Kappabridge MFK-1S, applying a field of 200 mAm^{-1} at a frequency of 976 Hz. The orientations of the principle axes of the AMS ellipsoid, giving information about the status of the magnetic fabric, were provided by the AGICO software 'Safyr6'. The natural remanent magnetization (NRM) was measured and stepwise demagnetized with a superconducting 2G Enterprises 755 SRM long-core magnetometer, with in-line tri-axial alternating field demagnetizer, and an automated sample handler for 8 discrete samples. Demagnetization was accomplished in 10 steps at AF peak levels of 5, 10, 15, 20, 30, 40, 50, 65, 80, and 100 mT. Obtained NRM demagnetization results were analysed

with principle component analysis (PCA) according to (Kirschvink, 1980), in order to determine the direction of the characteristic remanent magnetization (ChRM). An anhysteretic remanent magnetization (ARM) was imparted using a separate 2G Enterprises 600 AF demagnetizer equipped with an additional coil for a static field. ARMs were stepwise demagnetized with a reduced number of steps: 10, 20, 30, 40, 50, 65, and 80 mT. The slope of NRM intensity versus ARM intensity of common demagnetization steps was determined in order to provide a proxy for the relative paleointensity (RPI).

X-ray fluorescence core scanning

The X-ray fluorescence core scanner (XRF-CS) provides non-destructive, high resolution, and semi-quantitative chemical composition records. The sediment cores were measured with an ITRAX XRF-CS at Leibniz-Institute for Baltic Sea Research Warnemünde. Detail measurement information was described in Chapter 2.3.7.

Age Models. We established the age model based on radiocarbon dates, paleomagnetic excursion, corrected relative paleointensity (RPI) with the RPI stack and tuning points from high resolution XRF-CS ln (Ca/Ti) (Table S4.1). Planktonic foraminifera Neogloboquadrina pachyderma were selected for radiocarbon measurements, performed in the Mini Carbon Dating System (MICADAS) lab at the Alfred Wegener Institute (AWI), Bremerhaven. The RPI from core PS97/085-3 was correlated with the paleomagnetic intensity stack from 18 sediment core records in the Black Sea (Liu *et al.*, 2020). The high-resolution XRF scanner-derived records of ln(Ca/Ti) (peak area count ratios) were applied to fine-tune to the Antarctic temperature anomalies with ice core chronology (AICC2012) using the AnalySeries Software (Jouzel *et al.*, 2007; Paillard *et al.*, 1996). Bayesian age-depth modeling program Bacon 2.3 (Blaauw and Christen, 2011) was applied to develop an age model based on radiocarbon dates, paleomagnetic and tuning points (Fig. S4.2). The error estimate (Table S4.1) for tuning points and paleomagnetic corrected points was using

mean squared estimate following the method produced by Grant et al., (2012).

The high-resolution XRF scanner-derived records of ln(Ca/Ti) and ln(Ca/Fe) from PS97/085-3 show identical pattern (Fig. S4.3). The variations of Ti and Fe in relation to Ca suggest the input variability of Ca-carbonates (mainly foraminifers) to the terrigenous sediment fraction in this area under various climatic conditions. The carbonate content is primarily related to biogenic productivity and by carbonate compensation depths (lysocline), which is determined by the carbonate saturation state in the deep water (Bohm *et al.*, 2015; Sigman *et al.*, 2010). We assigned 24 tuning points (Table S4.1) from ln(Ca/Ti) correlated to the Antarctic temperature anomaly throughout the entire core. High sedimentation rates prevailed during the full glacial periods (20~40 cm/kyr) (Fig. S4.3).

Grain size measurement. Grain-size analyses were carried out with a CILAS 1180 L laser diffraction particle-size analyzer (CILAS, Orleans, France) at the Alfred Wegener Institute, Sylt. For the comparison of data gathered with different equipment, 80 samples were selected to be measured as well with a Micromeritics SediGraph 5100 at AWI, Bremerhaven (Fig. S4.7). Detail measurement information was described in Chapter 2.3.3.

End member modeling decomposition. The end-member modeling algorithm (EMMA) has been successfully applied to distinguish individual subpopulations in mixed siliciclastic grain size distribution (Arz *et al.*, 2003; Paterson and Heslop, 2015; Weltje, 1997). Here, we used the AnalySize program with general Weibull distribution parameters for the EMMA (Paterson and Heslop, 2015). The EMMA modeling results show three end members and 0.97 in the coefficient of determination (R^2), indicating these three end members can explain 97% of the variance (Fig. S4.5). The modeled end-members reflect that fine sand and coarse silt fractions (EM1) are likely transported by strong currents, medium silt fractions (EM2) are transported by weaker

currents, and fine silt and clay fractions (EM3) are delivered by suspension (Fig. S4.5).

Computer tomography

The sediment core PS97/085-3 was scanned by a Toshiba Aquilion 64^{TM} computer tomography (CT) at the hospital "Klinikum Bremen-Mitte" (Bremen, Germany). Detail measurement information was described in Chapter 2.3.6.

Clasts (> ~1 mm) from CT results were classified as ice-rafted debris (IRD). The IRD content is based on the volume percentages. CT data show that relatively higher IRD contents prevailed during the glacial periods, but most of the contents are lower than 2 vol. % except for a spike 18 vol. % at ~60 ka. The IRD contents significantly decreased during the deglaciation and interglacial periods (down to 0 vol. %) (Fig. S4.6).

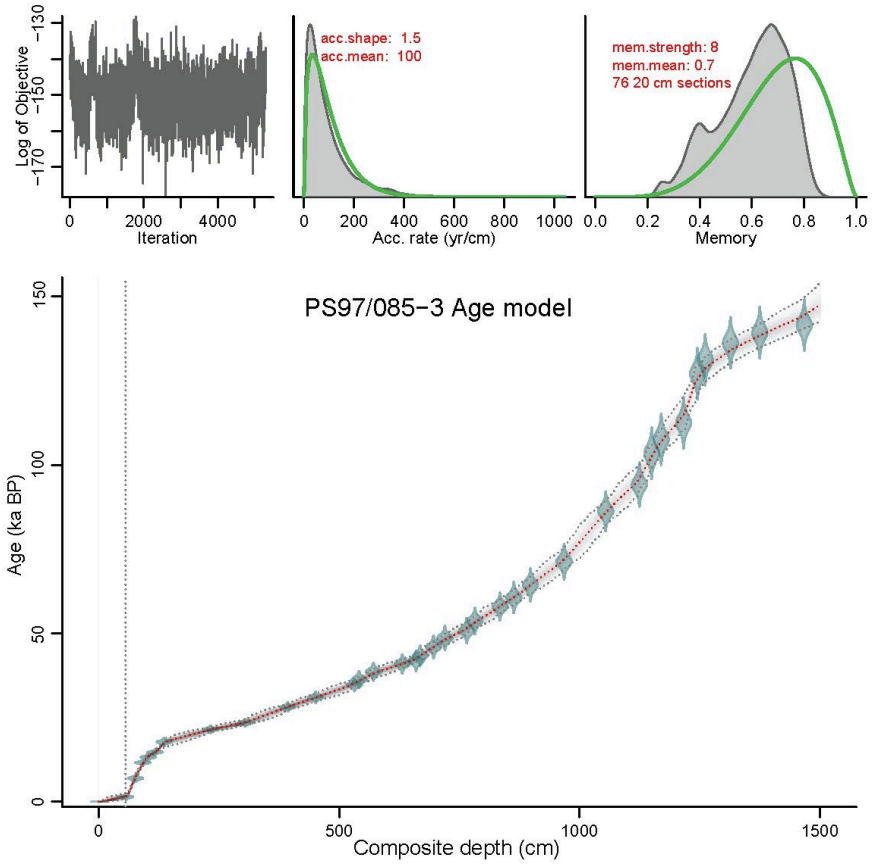

Fig. S4.2. Bayesian age-depth model of core PS97/085-3 calculated with BACON (Blaauw and Christen, 2011). The vertical dash line is the merging depth between trigger and piston cores.

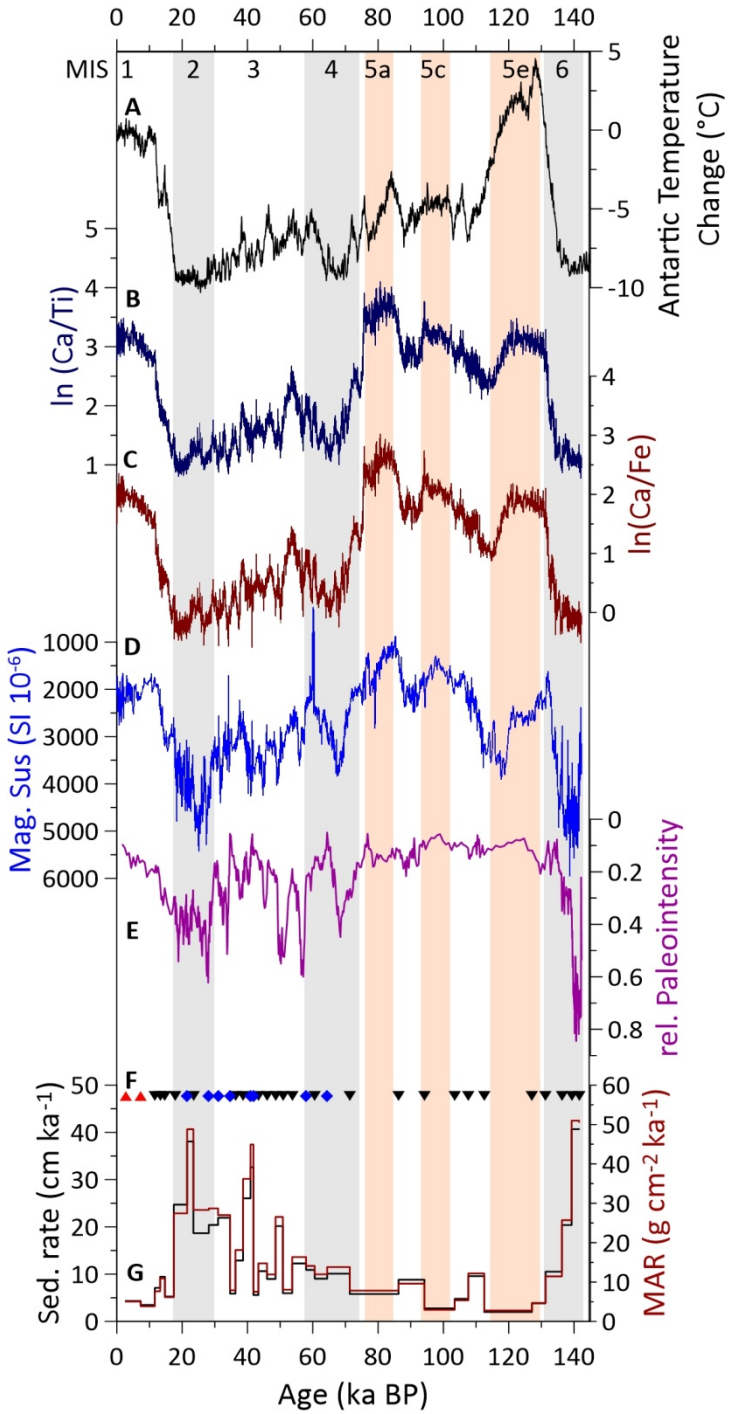

Fig. S4.3. Age model for sediment core PS97/085-3. Age control points showing in F are based on radiocarbon dates (red triangles) and the paleomagnetic excursions (Benson *et al.*, 2003; Nowaczyk *et al.*, 2012) (blue diamonds). Additional control points (black down triangles) are from (B) XRF-derived ln(Ca/Ti) profile of PS97/085-3 tuning with (A) the Antarctic temperature anomaly time series (Jouzel *et al.*, 2007). XRF-derived ln(Ca/Ti) is consistent prevailed climate induces changes of the ln(Ca/Fe) in B, C. D, Volume magnetic susceptibility (Mag.Sus, inverted axis) record in our core. E, Relative paleointensity variations (RPI, inverted axis). G, Linear sedimentation rates (sed. rate, black) and mass accumulation rates (MAR, red). Vertical gray bars mark inferred glacial periods and pink bars inferred the sub-interglacials during Marine Isotope Stages (MIS) 5.

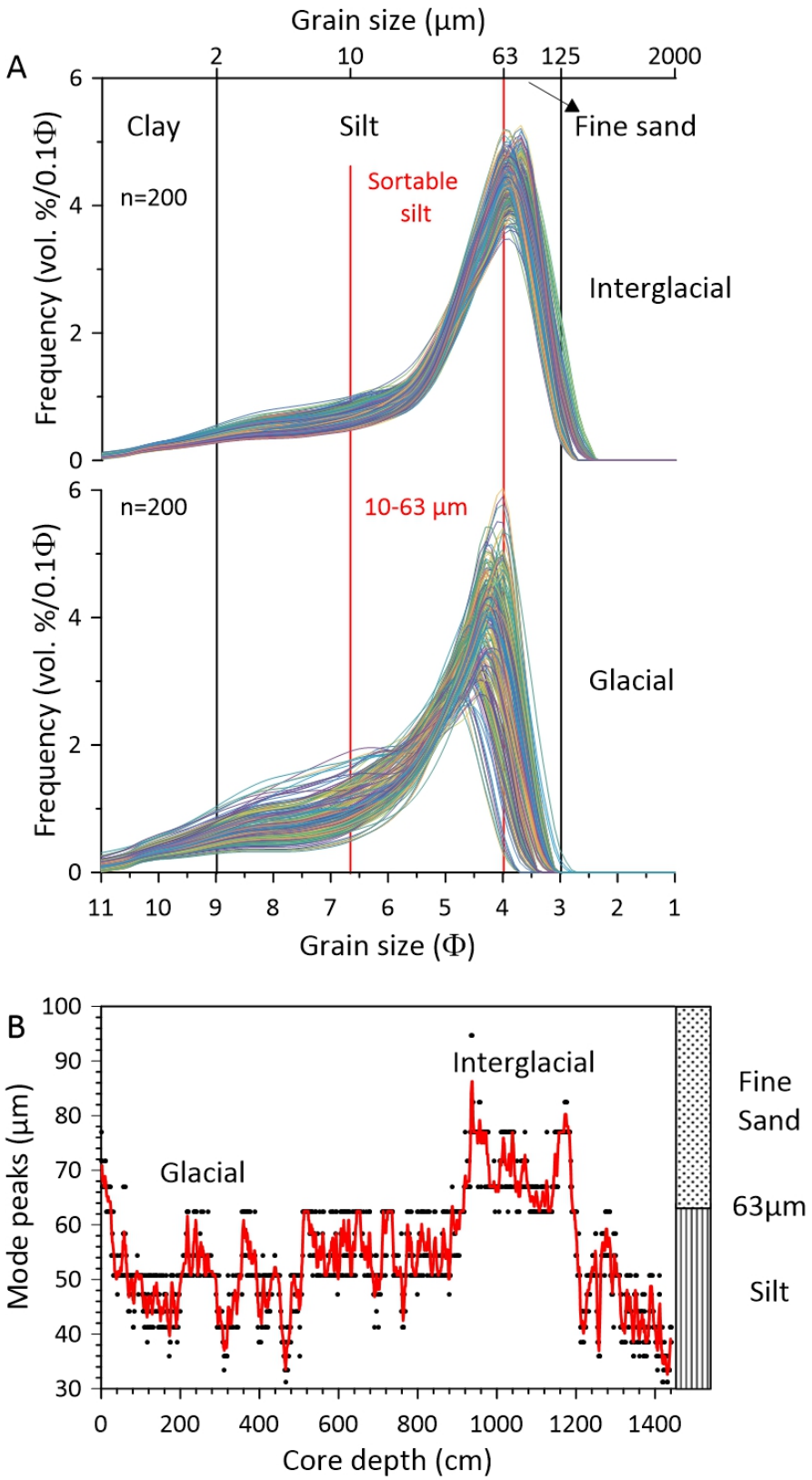

Fig. S4.4. The grain size distribution of terrigenous sediments from core PS97/085-3. A, The mode of grain size distribution moved to coarser fractions under high flow speed during the interglacial compared to glacial period. B, Mode peaks shifted beyond the sand-silt boundary (63 µm) during interglacial but stayed below the boundary during the glacial periods.

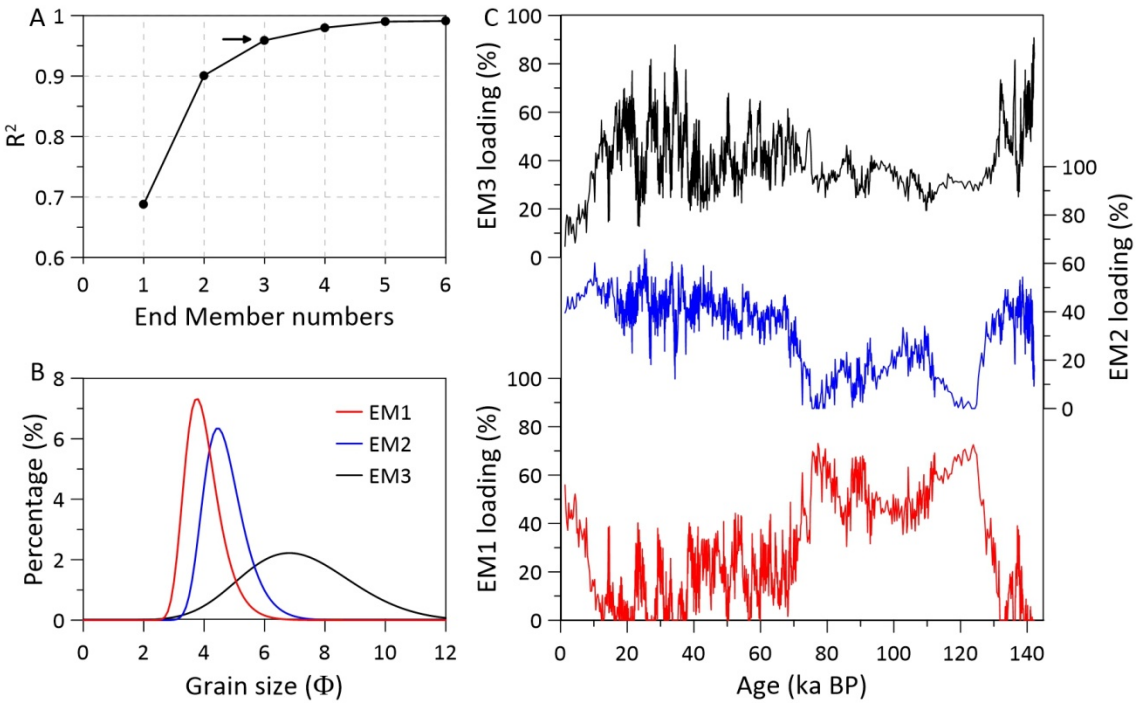

Fig. S4.5. End-member modeling results of the grain-size distribution of terrigenous sediment fraction from core PS97/085-3. A, The explained cumulative variance and mean coefficient of determination (R^2) for each size class of different end-member solutions (1-6 end-members). Three end members explain 97% of total variance. (B) The distributions of each end-member. (C) End-member loadings through downcore.

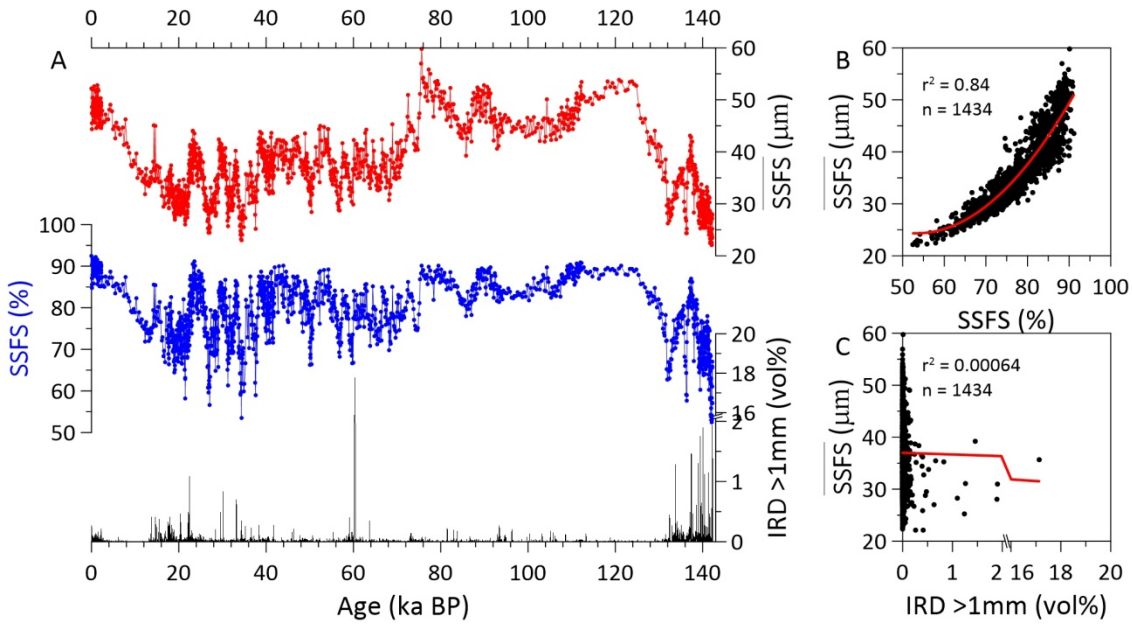

Fig. S4.6. Grain size data and ice-rafted debris (IRD) contents from core PS97/085-3. A, mean silt and fine-sand ($\overline{SSFS}$) (red), SSFS percentage (blue) and >1mm fraction IRD; B, polynomial regression between $\overline{SSFS}$ and SSFS; C, $\overline{SSFS}$ and IRD are independent of each other.

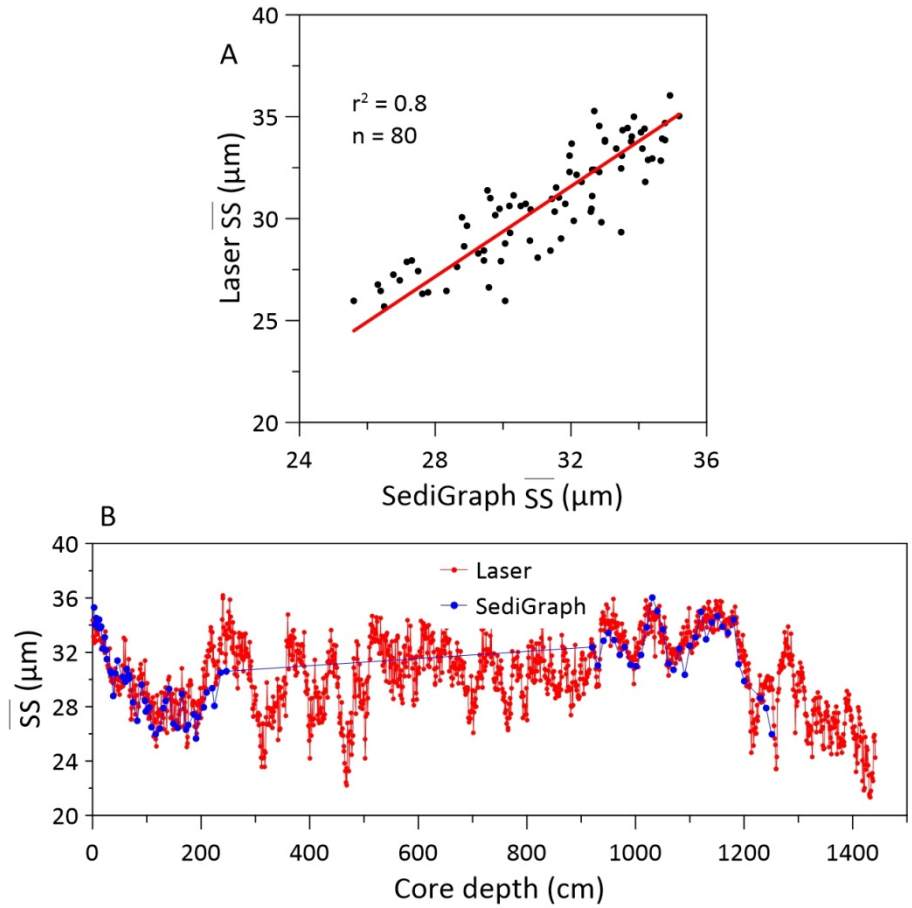

Fig. S4.7. Comparison of $\overline{SS}$ values analyzed with the SediGraph (blue) and CILAS laser measurements (red) in core PS97/085-3. A, The similar results obtained by these different devices support the robustness of our grain size measurement. B, Absolute $\overline{SS}$ values from Laser measurement tend to be slightly coarser than the results from SediGraph, because the sand fraction was separated before the SediGraph measurements and with that as well some of the coarse silt was removed, but amplitudes are generally consistent.

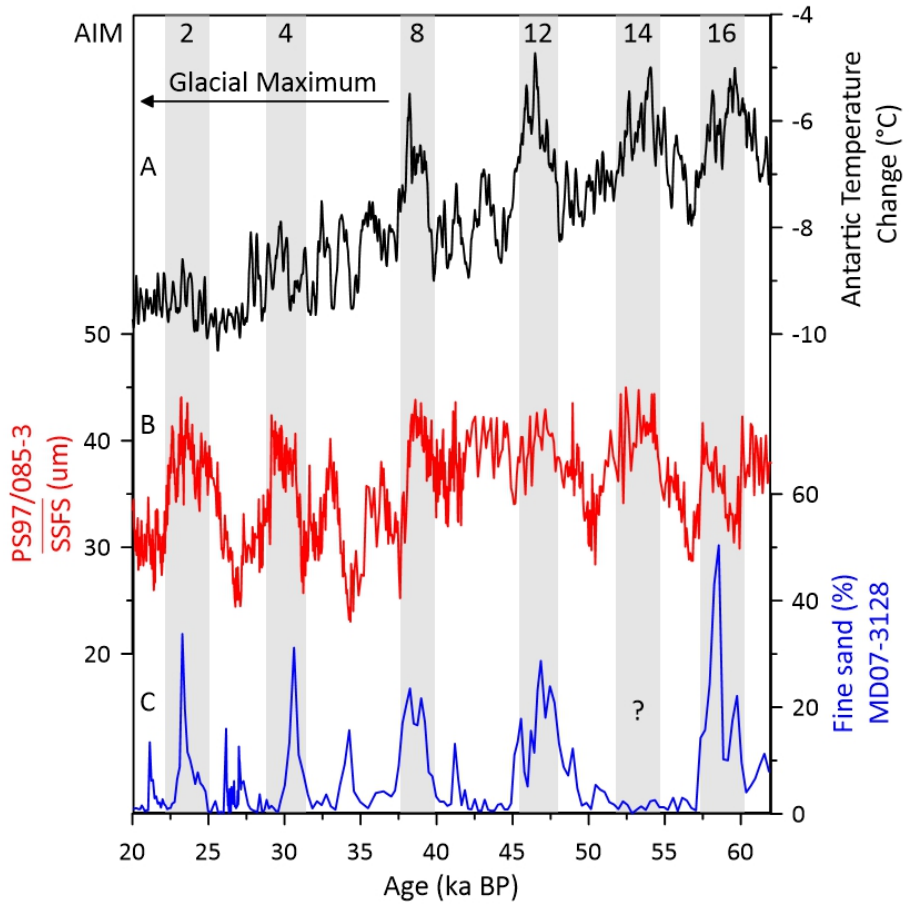

Fig. S4.8. Enhanced sensitivity of the millennial ACC variations to the Southern Hemisphere climate oscillation. A. The Antarctic temperature declined to the minimum value during the glacial maximum (Jouzel *et al.*, 2007). B and C, The proxies for the ACC flow speeds, $\overline{\text{SSFS}}$ from the central Drake Passage (this study) and find sand percentage from sediment core MD07-3128 at the Chilean Margin (Lamy *et al.*, 2015), are corresponding to the Southern Hemisphere climate oscillation and increased sensitivity of the ACC under the glacial maximum climate background. AIM, Antarctic Isotope Maximum.

Table S4.1. Age control points for the construction of age model for core PS97/085-3

Composite depth (cm)	Piston core depth (cm)	^{14}C age (ky)	±Error (ky)	Reservoir age (ky)	Calibrated age (ka)	±Error (ky)	Dating materials
56.5	0.5	2.7	0.11	0.8	1.47	0.26	Foraminifera
76.5	20.5	7.32	0.13	0.8	6.99	0.31	Foraminifera

Composite depth (cm)	Piston core depth (cm)	Age (ka BP)	±Error* (ka)	Dating method
0.0		0	0	Trigger core surface
56.5	0.5	1.47	0.26	14C/Marine13
76.5	20.5	6.99	0.31	14C/Marine13
91.5	35.5	11.64	0.24	ln(Ca/Ti) tuning
103.0	47.0	13.26	0.28	ln(Ca/Ti) tuning
117.0	61.0	14.74	0.24	ln(Ca/Ti) tuning
136.0	80.0	17.78	0.33	ln(Ca/Ti) tuning
232.5	176.5	21.55	0.31	Paleomagnetic
305.0	249.0	23.45	0.37	ln(Ca/Ti) tuning
393.0	337.0	28.16	0.46	Paleomagnetic
451.0	395.0	31.01	0.51	Paleomagnetic
532.0	476.0	34.70	0.68	Mono Lake
541.5	485.5	36.32	0.73	ln(Ca/Ti) tuning
571.5	515.5	38.64	0.78	ln(Ca/Ti) tuning
631.5	575.5	40.95	0.81	Laschamp
660.0	604.0	41.82	0.81	Laschamp
668.5	612.5	43.34	0.93	ln(Ca/Ti) tuning
696.5	640.5	45.98	0.98	ln(Ca/Ti) tuning
720.0	664.0	48.59	1.02	ln(Ca/Ti) tuning
765.5	709.5	50.85	1.07	ln(Ca/Ti) tuning
782.5	726.5	53.70	1.12	ln(Ca/Ti) tuning
834.5	778.5	57.94	1.25	Paleomagnetic
863.5	807.5	60.60	1.32	ln(Ca/Ti) tuning
898.0	842.0	64.42	1.44	Norwegian-Greenland Sea
968.0	912.0	71.35	1.59	ln(Ca/Ti) tuning
1054.5	998.5	86.26	1.78	ln(Ca/Ti) tuning
1124.5	1068.5	94.20	2.07	ln(Ca/Ti) tuning
1150.0	1094.0	103.46	2.07	ln(Ca/Ti) tuning
1170.0	1114.0	107.65	2.07	ln(Ca/Ti) tuning
1216.5	1160.5	112.49	2.07	ln(Ca/Ti) tuning
1245.5	1189.5	127.11	2.07	ln(Ca/Ti) tuning
1261.5	1205.5	131.28	2.07	ln(Ca/Ti) tuning
1314.0	1258.0	136.27	2.08	ln(Ca/Ti) tuning
1375.0	1319.0	139.26	2.07	ln(Ca/Ti) tuning
1467.5	1411.5	141.54	2.07	ln(Ca/Ti) tuning

* The error estimate for tuning points and paleomagnetic points was using mean squared estimate following the method produced by (Grant *et al.*, 2012).

5 Late Quaternary terrigenous sediment supply into the Drake Passage in response to ice dynamics

Shuzhuang Wu[1], Gerhard Kuhn[1], Helge W. Arz[2], Lester Lembke-Jene[1], Ralf Tiedemann[1], Frank Lamy[1], Bernhard Diekmann[3]

[1]Alfred-Wegener-Institut Helmholtz-Zentrum für Meeres- und Polarforschung, 27568 Bremerhaven, Germany;
[2]Department of Marine Geology, Leibniz Institute for Baltic Sea Research Warnemünde, 18119 Rostock, Germany;
[3]Alfred-Wegener-Institut Helmholtz-Zentrum für Meeres- und Polarforschung, 14473 Potsdam, Germany.

In preparation for Quaternary Science Reviews

Abstract

Terrigenous sediment transport in response to climate changes in the Southern Ocean remains a long-standing debate. We studied mineralogical and geochemical compositions of a deep-sea sediment core from the central Drake Passage to identify terrigenous sources and to reconstruct ice dynamics in southern Patagonia and on the Antarctic Peninsula over the past 140 ka. The clay mineral assemblages reveal that the fine-grained sediments mainly derive from nearby terrestrial sources. The Antarctic Circumpolar Current serves as the major driver for sediment disposal in this region. The glacial periods were dominated by illite and chlorite with high mass-specific magnetic susceptibility and Ti/K ratios. These detrital sediments are mainly derived from basic volcanic and metamorphic rocks prevailing in the western part of Patagonia and on the Antarctic Peninsula. Large extensions of the glaciers in these two areas would outwash and drain more glaciogenic sediments from the hinterland into the open ocean. In addition, sea level lowstands during the glacial times may have amplified the efficiency of sediment supply into the deep ocean since larger continental shelves were exposed and the shore line has been located at the shelf edge. At interglacials, significant glacier shrinkage and high sea level condition may have

reduced the input of glacial debris. The terrigenous sediment supply is characterized by relatively high smectite and quartz/feldspar ratios associated with low mass-specific magnetic susceptibility and Ti/K ratios. These sediments originate from the acidic Andean cordillera batholiths in the southeast Pacific, which were likely reworked by strong erosion and transported by ocean currents. Hence, high resolution mass-specific magnetic susceptibility values and Ti/K ratios are considered to reflect the waxing and waning of glaciers in southern Patagonia and on the Antarctic Peninsula.

5.1 Introduction

The Drake Passage, a small oceanic gateway between the southern Patagonia and the Antarctic Peninsula, is a key area for understanding the interactions of the ocean–atmospheric system during global climate change (Rintoul, 2018). The southern westerly wind belt (SWW) primarily drives the Antarctic Circumpolar Current (ACC) and its flow through the Drake Passage (Toggweiler and Samuels, 1995). Atmospheric and oceanic processes regulate the spatial distribution of sediment material in the high latitude of Southern Hemisphere (Kuhn and Diekmann, 2002; Petschick *et al.*, 1996; Toggweiler *et al.*, 2006). The SWW was proposed to transport dust from South America to the South Atlantic and the Antarctic continent (Lambert *et al.*, 2008; Lamy *et al.*, 2014; Martínez-García *et al.*, 2014; Sugden *et al.*, 2009). However, Southern Ocean proxy records indicative of changes in the dust source and transport remain a question of conflicting interpretation (Diekmann *et al.*, 2000; Lamy *et al.*, 2014; Petit *et al.*, 1990; Pugh *et al.*, 2009; Weber *et al.*, 2012; Yamazaki and Ikehara, 2012).

The strong ACC system plays an important role for the spatial distribution of terrigenous sediments in the Southern Ocean (Marshall and Speer, 2012; Petschick *et al.*, 1996). Today, the eastward ACC transports materials from the South Pacific to the South Atlantic, as indicated by a clear longitudinal distribution of chlorite (Fig. 5.1) (Diekmann *et al.*, 2000; Petschick *et al.*, 1996; Wu *et al.*, 2019). However, the

terrigenous source of sediments transported through the central Drake Passage is still poorly constrained for the past, owing to a combination of factors — strong bottom currents leading to large areas with no sediment deposition, and uniquely complex ocean-atmosphere interactions.

Clay mineral, geochemical and magnetic properties from marine sediment have been applied to reconstruct past variations in terrigenous supply (Diekmann *et al.*, 2000; Govin *et al.*, 2012; Itambi *et al.*, 2009; Petschick *et al.*, 1996; Stuut *et al.*, 2007). Felsic plutonic rocks are generally characterized by high amounts of quartz, illite, Al, and K. Feldspar, chlorite, Fe, and Ti are mainly derived from metamorphic rocks and basaltic to andesitic volcanic lithologies (Biscaye, 1965; Petschick *et al.*, 1996; Stuut *et al.*, 2007). High magnetic susceptibility values are typical for glacial periods, since terrigenous sources supply ferromagnetic-rich materials (Diekmann *et al.*, 2000; Weber *et al.*, 2012). These may originate from the Argentine Pampas via aeolian transport and the expansion of Patagonian and Antarctic ice sheets transporting materials into the open ocean (Diekmann *et al.*, 2000; Petschick *et al.*, 1996; Weber *et al.*, 2012).

Here we aim to identify the specific sources and temporal variations in terrigenous sediment supply to the Drake Passage based on mineralogical, geochemical and magnetic properties. Specific characteristics in sediment composition are thought to provide hints for sediment transport processes and ice dynamics in southern Patagonia and on the Antarctic Peninsula over the last glacial-interglacial cycles.

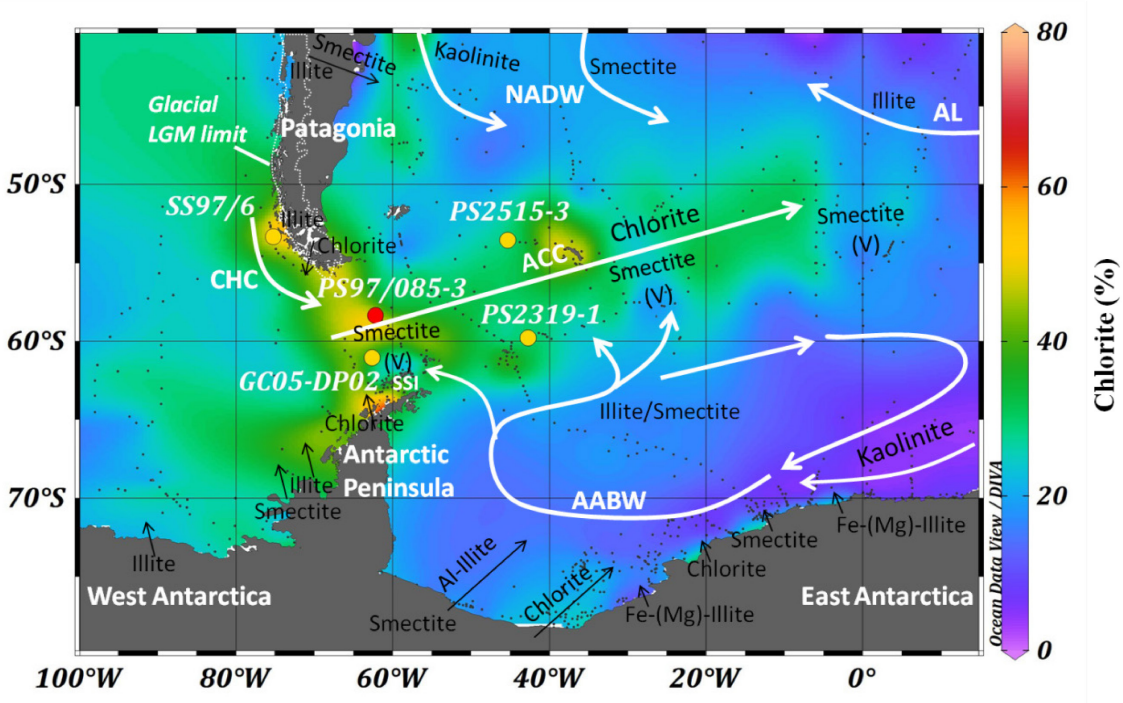

Fig. 5.1. Clay mineral distribution in the modern Southern Ocean as shown by chlorite with potential terrigenous sources and sedimentary transport pathways. Red dot marks the location of site PS97/085. Yellow dots show locations of sediment cores from previous studies (Diekmann *et al.*, 2000; Marinoni *et al.*, 2008; Park *et al.*, 2019). Small back points mark surface samples in this region (Biscaye, 1965; Diekmann and Kuhn, 1999; Diekmann *et al.*, 2000; Petschick *et al.*, 1996; Wu *et al.*, 2019). The white dotted line indicates the expansion of the Patagonian ice sheet during the Last Glacial Maximum (LGM) (Davies *et al.*, 2020). Black arrows imply potential clay mineral supply and V symbols represent volcanic sources (Petschick *et al.*, 1996). SSI, South Shetland Islands. White arrows indicate potential transport trajectories by current. AABW, Antarctic Bottom Water; ACC, Antarctic Circumpolar Current; AL, Agulhas Leakage; CHC, Cape Horn Current; NADW, North Atlantic Deep Water.

5.2 Geological setting

The studied sediment core PS97/085-3 was collected in the central Drake Passage. Southern Patagonia is characterized by Andean cordillera batholiths, Quaternary sedimentary rocks and volcanic units associated with the Triassic metamorphosed basement (Clapperton, 1993; Marinoni *et al.*, 2008; Ramos and Ghiglione, 2008). A sharp contrast of the geological units exists between the Pacific and Atlantic sides of Southern Patagonia. The southeastern Pacific margin mainly comprises the Cretaceous to lower Eocene granitoids of the Andean cordillera batholiths, intruded eastward into metamorphosed basement rocks (Clapperton, 1993; Marinoni *et al.*,

2008; Ramos and Ghiglione, 2008). These acidic rocks of the Andean Batholith could provide more illite and low mass-specific magnetic susceptibility materials to the open ocean (Diekmann *et al.*, 2000; Marinoni *et al.*, 2008). By contrast, on the Atlantic side consists of Lower Cretaceous through Tertiary sedimentary rocks, continental volcanic rocks and large Quaternary periglacial deposits on the plains (Clapperton, 1993; Marinoni *et al.*, 2008). Detritus from these lithologies are carrying small amounts of chlorite and high mass-specific magnetic susceptibility signals (Diekmann *et al.*, 2000; Marinoni *et al.*, 2008).

The geological units of the Antarctic Peninsula are characterized by Jurassic to recent volcanic rocks, the non-metamorphic intrusive and metamorphic basements, and Paleozoic to Cenozoic sedimentary rocks (Barker *et al.*, 1991; Burton-Johnson and Riley, 2015; Diekmann *et al.*, 2000). Mafic to felsic plutonic rocks intruded the Late Paleozoic to Cenozoic sedimentary rocks, which were overlain by basic-intermediate composition volcanic rocks (Barker *et al.*, 1991; Burton-Johnson and Riley, 2015; Diekmann *et al.*, 2000). Relatively high smectite and chlorite contents and high mass-specific magnetic susceptibility are the sediment material features derived from the Antarctic Peninsula (Diekmann *et al.*, 2000; Park *et al.*, 2019; Petschick *et al.*, 1996; Wu *et al.*, 2019).

5.3 Material and method

Sediment core PS97/085-3 (58° 21.28′ S, 62° 10.02′ W; water depth 3090 m; 14.4 m core length) was retrieved from the central Drake Passage (Fig. 5.1). The site PS97/085 is located in the north of the spreading center of the West Scotia Ridge and on the northern flank of the ridge next to the Shackleton Fracture Zone (Lamy, 2016).

5.3.1 Stratigraphy

We used the age models of PS97/085-3 as defined in Manuscript “Chapter 4” (see Supporting Information, Chapter 4.6 Material and methods). The age model was based on radiocarbon dates, paleomagnetic excursion, corrected relative

paleointensity (RPI) with the RPI stack and tuning points from high resolution XRF-CS ln (Ca/Ti) records (Table S4.1). High sedimentation rates and mass accumulation rates prevailed during the full glacial periods (20~40 cm ka^{-1}; 20~50 g cm^{-2} ka^{-1}).

5.3.2 Clay mineralogy

Clay mineral analysis (< 2 μm sediment fraction) was performed at 4 cm intervals. Measurement details were described in Chapter 2.3.4 and performed after Petschick et al. 1996 and Wu et al. 2019. We compiled available data from surface samples and sediment cores in the adjacent region to trace the terrigenous sources, which would advance our understanding of sediment transport and ice dynamics.

5.3.3 Magnetic susceptibility

High-resolution logging of magnetic volume susceptibility (κMS_{bulk}) on core PS97/085-3 was performed with a Bartington MS2E sensor in combination with a MS2 control unit, integrated into a fully automated split-core logger. Measurement settings were described in Chapter 2.3.5. To see the variations in composition of the pure terrigenous material, without any dilution by pore water and carbonate contents, we calculated the mass-specific magnetic susceptibility of the terrigenous fraction (χMS_{terr}), following (Dearing, 1994; Diekmann *et al.*, 2000).

5.3.4 Geochemistry

The major elemental compositions were measured with an ITRAX X-ray fluorescence (XRF) core scanner (more detail information see Chapter 2.3.7). For this study, we used Ti- and K- counts as a proxy for terrigenous sediment supply. To minimize sample inhomogeneity, variable water content and grain-size distribution effects, we based our interpretation on intensity ratios. The intensity ratios are close to the element concentration ratios, with a relative standard deviation of less than 2% (Weltje and Tjallingii, 2008). In marine sediments, Ti mainly derives from basic

volcanic rocks or metamorphic and sedimentary rocks, whereas K dominates in potassium feldspar from felsic plutonic rocks or in the clay mineral illite (Govin *et al.*, 2012; Yarincik *et al.*, 2000; Zabel *et al.*, 2001). The Ti/K ratios in the bulk sediment like the χMS_{terr} therefore allow deducing the distinctive terrigenous material sources input (Siani *et al.*, 2010; Stuut *et al.*, 2007).

5.3.5 Ice-rafted debris

The ice-rafted debris (IRD, >1mm) volume contents were identified and determined by a Toshiba Aquilion 64^{TM} computer tomography scanner (for detailed information see Chapter 2.3.6).

5.4 Results

5.4.1 Clay mineralogy

The clay mineral (<2 μm sediment fraction) of core PS97/085-3 is mainly composed of chlorite (30~67%) and illite (30~60%), while the amount of smectite is relatively small to intermediate (0~30%) (Fig. 5.2A-C). Kaolinite was not found in any sample at our site. In general, chlorite and illite contents exhibit inversely correlation with smectite distributions throughout downcore. The glacial periods are characterized by low smectite contents (0~10%) associated with low amplitude variability. Chlorite (42~67%) and illite (34~60%) contents are higher and fluctuations show a reverse pattern in comparison to smectite. In contrast, during deglaciations, the relative abundance of smectite increases abruptly from ~4 to 24% and remains at high values (17~30%) during the interglacials. At the same time, the chlorite and illite contents decrease to their minimum. Notably, the variations of chlorite and illite indicate different behaviors throughout the core. Relative constant low chlorite abundances prevailed during MIS 5 and then increased from MIS 5/4 transition to MIS 2. However, illite contents increased abruptly from MIS 5d (30%) to its maximum (60%) during MIS 4 and subsequently decreased to MIS 2. The 5 Å/10 Å peak intensity ratios can provide illite crystallinity conditions. High ratios (>0.4) correspond to

Al-rich illites while low ratios (< 0.25) indicate Fe-Mg rich illite (Esquevin, 1969; Petschick *et al.*, 1996). The 5 Å/10 Å ratios are generally larger than 0.4 in our core (Fig. 5.2D).

Since clay minerals reveal distinct temporal evolutions, we applied the ratios of smectite/chlorite, chlorite/illite and quartz/feldspar within the clay fraction to describe the mineralogical variations shown in Fig. 5.3. High smectite/chlorite ratios dominated at the glacial-interglacial transitions and during warmer stages, parallel with changes in quartz/feldspar ratio. The fluctuations in chlorite/illite show higher values during the glacial excursions against with smectite/chlorite and quartz/feldspar ratios. The chlorite/illite ratio experienced an increasing trend from MIS 4 to the LGM (Fig. 5.3C).

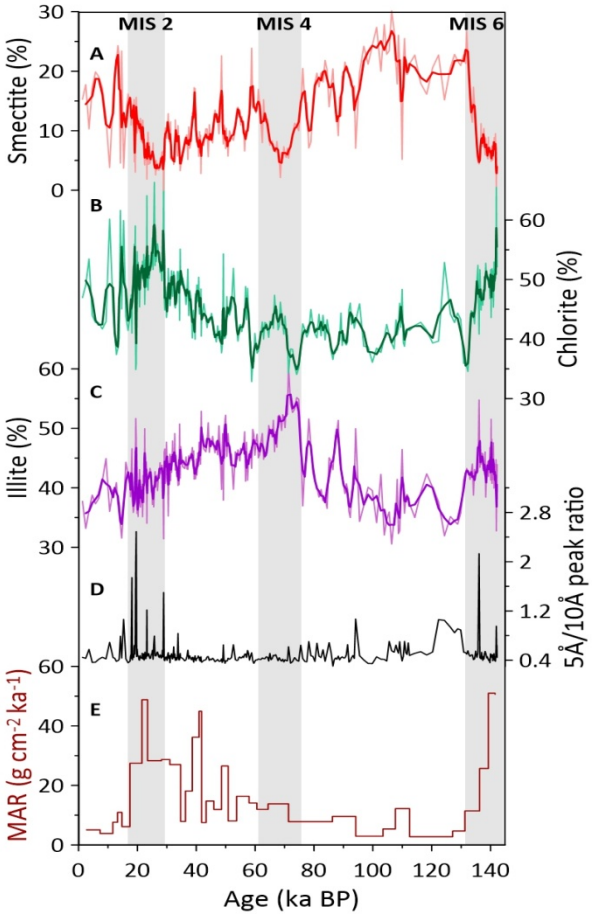

Fig. 5.2. Clay mineral contents (< 2 µm fraction) and illite crystallinity of core PS97/085-3. A, smectite content with three points smoothing (red line); B, chlorite content with three points smoothing (green line); C, illite content with three points smoothing (purple line); D, 5 Å /10 Å peak intensity ratio was applied to indicate illite crystallinity. E, mass accumulation rate (MAR).

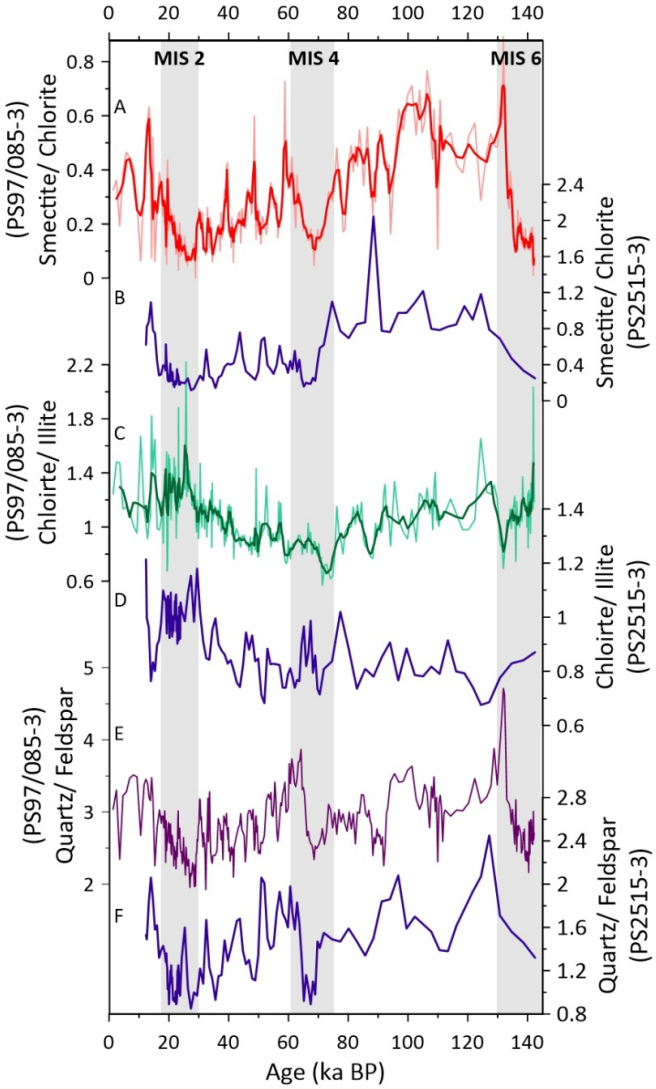

Fig. 5.3. Comparison the clay mineral records past variability records in the Drake Passage (PS97/085-3) and the Scotia Sea [PS2515-3, (Diekmann *et al.*, 2000)] during the glacial-interglacial cycles. A, B smectite/chlorite ratios in PS97/085-3 (red) and PS2515-3 (blue); C, D chlorite/illite ratios in PS97/085-3 (green) and PS2515-3 (blue). E, F Quartz/ feldspar ratios in PS97/085-3 (violet) and PS2515-3 (blue).

5.4.2 Mass-specific magnetic susceptibility and geochemistry

Changes in χMS_{terr} are generally consistent with the variations of chlorite/illite, with maxima values of χMS_{terr} during the glacial periods and minimum values during the interglacials. Relatively high χMS_{terr} values display during MIS 5.4 and MIS 5.2 as well (Fig. 5.4A). The glacial-interglacial fluctuations in the χMS_{terr} coincide with ice volume changes from the European Project for Ice Coring in Antarctica (EPICA) Dronning Maud Land ice core (EPICA Community Members, 2006), suggesting its changes closely correspond to the Southern Hemisphere climate oscillations (Fig.

5.6A). Characteristic short-term fluctuations with small magnitudes in χMS_{terr} prevailed during MIS 3, which might as well relate to millennial climate oscillations (EPICA Community Members, 2006).

Changes in ln(Ti/K) in parallel with the χMS_{terr} variations exhibit higher values during the glacial periods and stadials MIS 5.4 and MIS 5.2 (Fig. 5.4A, B). In contrast, the interglacial phases are characterized by low ln(Ti/K) values with large amplitude (like MIS 5, Fig. 5.4B). The fluctuations of ln(Ti/K) ratio are comparable with the chlorite/illite ratios, particularly the interval between MIS 4 and MIS 2 (Fig. 5.3C; 5.4B).

5.4.3 Ice rafted debris variations

Clasts (> ~1 mm) from CT results were classified as IRD. The IRD content is based on the volume percentages. CT data show that higher IRD contents prevailed during glacials, but most of the contents are lower than 2 vol. % except for a spike 18 vol. % at ~60 ka. The IRD contents significantly decreased during the deglaciation and interglacial periods (down to 0 vol. %, Fig. 5.4C).

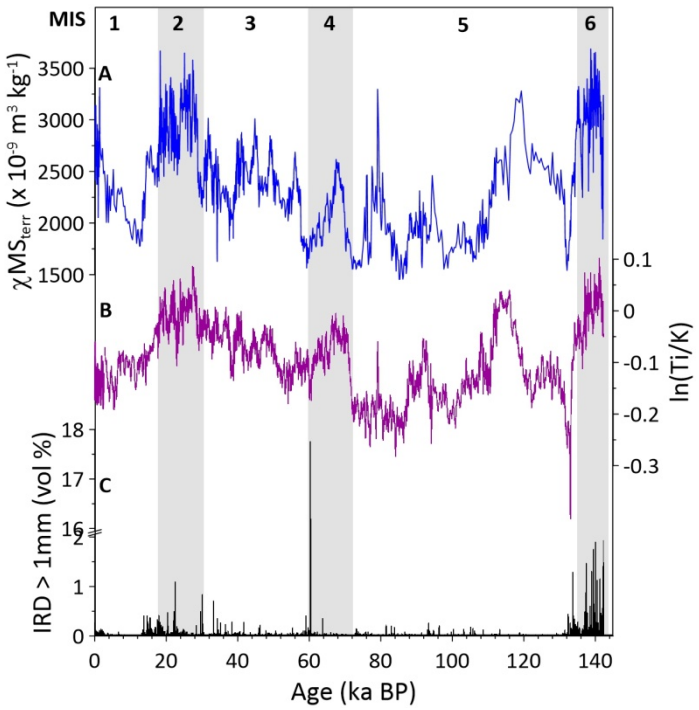

Fig. 5.4. A, The variation of mass-specific magnetic susceptibility (χMS_{terr}, blue); B, Ti/K ratios (purple); C, Ice rafted debris (IRD, black) in core PS97/085-3.

5.5 Discussion

5.5.1 Sediment provenance

In sediment core PS97/085-3, the clay mineral assemblage, magnetic and geochemical properties exhibit pronounced glacial-interglacial fluctuations over the past 140 ka. The variability of clay mineral assemblages in the sediment core are reflecting past changes in the clay mineral distribution of ocean floor surface sediments (Wu *et al.*, 2019). During MIS 6 and MIS 2, terrigenous provenance signatures in the central Drake Passage are characterized by high chlorite/illite ratios, χMS_{terr} and Ti/K ratios associated with low smectite/chlorite and quartz/feldspar ratios (Fig. 5.2-5.4). These component features match with those from the basic to intermediate and undifferentiated parent rocks in the western Patagonia and the Antarctic Peninsula (Fig. 5.5B) (Burton-Johnson and Riley, 2015; Diekmann *et al.*, 2000; Hillenbrand *et al.*, 2009; Marinoni *et al.*, 2008). The clay mineral spectrum from these sources is characterized by illite- and chlorite-dominated sediments associated with low smectite contents and quartz/feldspar ratios (Diekmann *et al.*, 2000; Hillenbrand *et al.*, 2009; Marinoni *et al.*, 2008; Wu *et al.*, 2019). The variations of clay mineral assemblage in the central Drake Passage are broadly consistent with the clay mineral spectrum in the northern Scotia Sea (Fig. 5.3) (Diekmann *et al.*, 2000). Moreover, detritus from metamorphic and basic lithologies generally contain large amounts of magnetite minerals, which result in high χMS_{terr} (Diekmann *et al.*, 2000). Therefore, we suggest that the terrigenous materials in the Drake Passage during the glacial maximum mainly derived from western Patagonia and from the Antarctic Peninsula. In contrast to the MIS 6 and MIS 2, the sediment materials include highest contents of illite (~ 60%) during the MIS 4 (Fig. 5.2C). Such high values might primarily originate from the acidic rocks of the Andean Batholith on the southeast Pacific margin (Marinoni *et al.*, 2008; Wu *et al.*, 2019).

During the MIS 5 and MIS 1, terrigenous materials at our site consist of high smectite contents and quartz/feldspar ratios with low χMS_{terr} (Fig. 5.2-5.4). These features indicate the reworked sediments were transported from the southeast Pacific

into the central Drake Passage (Fig. 5.5A), which were observed as well in the northern Scotia Sea (Diekmann *et al.*, 2000). High quartz/feldspars ratios have been found along the Chilean Margin in the surface samples and sediment cores during the warm stages (Marinoni *et al.*, 2000; Marinoni *et al.*, 2008; Wu *et al.*, 2019). Therefore, we suggest the detritus sediments in the central Drake Passage mainly derived from the southeast Pacific during MIS 5 and MIS 1 (Fig. 5.5A). Since several volcanoes developed in the Antarctic Peninsula (mainly on the South Shetland Islands), that may potentially be a source for smectite (Diekmann *et al.*, 2000; Park *et al.*, 2019; Petschick *et al.*, 1996; Wu *et al.*, 2019). Wu et al., (2019) mapped a maximum of smectite around the volcanic South Shetland Islands. However, volcanic rocks generally provide high χMS_{terr} and low quartz/feldspar ratios (Diekmann *et al.*, 2000; Hillenbrand *et al.*, 2009; Park *et al.*, 2019; Petschick *et al.*, 1996; Wu *et al.*, 2019), Therefore, this area can be subordinate source for the central Drake Passage during the interglacial periods. The strong eastward flow of the ACC will prevent input of higher smectite contents from the Atlantic-side of Patagonia (Diekmann *et al.*, 2000; Marinoni *et al.*, 2000).

Clay mineral assemblage, quartz/feldspar ratios and χMS_{terr} present medium values during MIS 3, oscillating between glacial and interglacial conditions (Fig. 5.2-5.4). This suggests the Drake Passage had received materials from mixed sources during the MIS 3 (Fig. 5.5A).

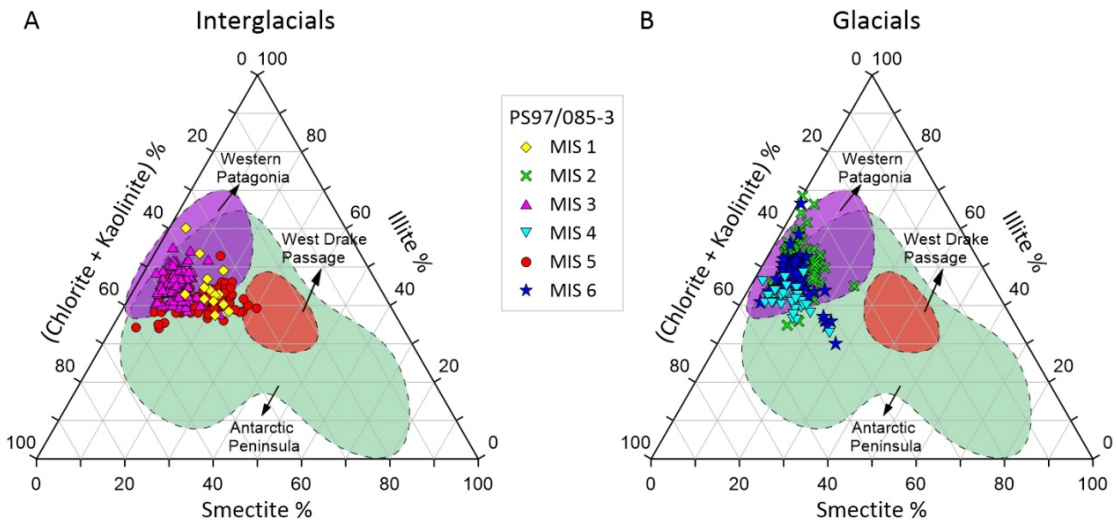

Fig. 5.5. Ternary diagram of smectite-illite-(chlorite + kaolinite) during the interglacial (A) and glacial periods (B). Kaolinite was not detected in our samples. The yellow diamonds represent MIS 1; the green cross represent MIS 2; the violet triangles represent MIS 3; the blue down triangles represent MIS 4; the red dots represent MIS 5; the blue stars represent MIS 6; Purple shapes represent western Patagonia recent sediment source; Green shapes represent the Antarctic Peninsula source; Red shapes represent central South Pacific source (Diekmann *et al.*, 2000; Marinoni *et al.*, 2000; Petschick *et al.*, 1996; Wu *et al.*, 2019).

5.5.2 Impact of transport mechanism on source signals

Aeolian supply, ocean currents, turbidity currents and ice-rafting may serve as transport processes to deliver terrigenous sediment to our study area (Diekmann *et al.*, 2000; Lamy *et al.*, 2015; Weber *et al.*, 2014; Weber *et al.*, 2012). The 5 Å/10 Å ratios are generally over 0.4 in our core (Fig. 5.2D), suggesting the Al-rich illite with a good crystallinity was dominant in our study area over the past 140 ka. The well-crystallinity Al-rich illite and lack of detectable kaolinite in the central Drake Passage could exclude the possibility of aeolian transport from Patagonian dust, which is rather characterized by Fe-Mg rich illite and kaolinite (Camilión, 1993; Diekmann *et al.*, 2000; Ito and Wagai, 2017; Petschick *et al.*, 1996). The mineralogical and geochemical features in the Drake Passage and the Scotia Sea are not supporting for aeolian transport either (Diekmann *et al.*, 2000; Walter *et al.*, 2000; Wu *et al.*, 2019). Turbidity currents are crucial for sediment dispersal on the continent slope and abyssal plains (Barker and Burrell, 1977; Campbell and Clark, 1977). Since our site is located on the crest of the ridge next to the Shackleton Fracture Zone

(Lamy, 2016), the turbidity currents may have a minor effect on our core. IRD contents are general low (<2 vol.%) throughout the core, except for one spike during late MIS 4 (Fig. 5.4C). The ice-rafted transport can hence be excluded as a significant source of sediment transport in the central Drake Passage. During the glacial periods, expansion of sea ice might be another potential transport agent (Ferrari *et al.*, 2014; Nielsen *et al.*, 2007). However, increased sea ice coverage may have hindered ice bergs to float through the Drake Passage, therefore it could be difficult to evaluate sediment contribution by sea ice and ice berg rafting.

Today, the ACC has an average baroclinic transport with ~150 ± 20 Sv through the Drake Passage (Donohue *et al.*, 2016; Koenig *et al.*, 2014; Meredith *et al.*, 2011b), therefore, the ocean current transport should be the major transport source in the Drake Passage region. Although the reconstructed ACC dynamics during the last climate cycle are still on debate (Lamy *et al.*, 2015; McCave *et al.*, 2014; Roberts *et al.*, 2017), such large transport by the ACC can play a significant role on sediment dispersal in our study area. We found stronger currents indicated by grain size variation during the interglacial and weaker ones during the glacial periods (see Chapter 4).

5.5.3 Linking the terrigenous sediment input to Patagonian and Antarctic Peninsula ice dynamics

Our records exhibit significant terrigenous input into the central Drake Passage in response to the expansion of the Patagonian and the Antarctic Peninsula ice sheets during the glacial periods and stadials (Fig. 5.6). Since changes in terrigenous input were sensitively recorded by chlorite/illite ratios, χMS_{terr} as well as the Ti/K ratios in core PS97/085-3, we use these proxies to track past changes of glaciogenic sediment supply into the deep ocean.

We found a distinctive pattern for the glacial stages MIS 6 and MIS 2, which however deviates from MIS 4. MIS 6 and MIS 2 are characterized by the highest values of χMS_{terr} and Ti/K ratios as well chlorite/illite ratios. Accordingly these sediments are mainly originated from western Patagonia and the Antarctic Peninsula,

which reached their maximum extents during MIS 6 and MIS 2 (Davies *et al.*, 2020; EPICA Community Members, 2006; Kaplan *et al.*, 2005; Moreno *et al.*, 2015; Sugden *et al.*, 2009; Weber *et al.*, 2014). In addition, low regional sea level stands during the glaciations led to subaerial exposure of large continental shelf regions, which would increase the erosion erosion efficiency and the sediment flux into the deep ocean (Rohling *et al.*, 2014). Thus, we consider sea level change is also a major player in explaining the variations in the terrigenous sediment supply.

In contrast, medium high values of χMS_{terr} and Ti/K ratios and the lowest chlorite/illite ratios prevailed during MIS 4. Such sediment material is mainly derived from basic to acidic rocks pointing to the Pacific margin of Patagonia and its partial hinterland. Past instability of the Patagonian Ice Sheet may have led occasionally to enhanced meltwater plumes, which may have fed the transport of terrigenous sediments into the Drake Passage (Diekmann *et al.*, 2000; Marinoni *et al.*, 2008). In contrast, less meltwater supply and glacier transport from a relative stable the Antarctic Peninsula Ice Sheet may have occurred during during MIS 4 (Diekmann *et al.*, 2000; EPICA Community Members, 2006). Rapid glacier advance has been reconstructed in southern Patagonia during MIS 4 (Mendelová *et al.*, 2020; Sugden *et al.*, 2009; Weber *et al.*, 2012). These ice sheet expansions may have contributed to a spike of IRD content in our records (Fig. 5.6F). However, the ice sheets probably grew to medium size at this onset of glaciation (Mendelová *et al.*, 2020; Sugden *et al.*, 2009) and may not have reached the sea level. The detritus were thus possibly trapped in the Chilean Archipelago and the Antarctic Peninsula fjords due to a relatively high global sea level at this interval (Rohling *et al.*, 2014).

We observed increased trends in χMS_{terr}, Ti/K and chlorite/illite ratios from MIS 4 to MIS 2, indicative of a gradual shift in the terrigenous sources at times of the ice sheet expansion. Basic-intermediate and metamorphic lithologies that outcrop in the western Patagonia potentially provide the sediment materials rich in Ti, magnetite and chlorite, while the acidic rocks of the Andean Batholith on the Pacific margin preferentially produce illite- and K-rich sediment (Barker and Burrell, 1977; Diekmann *et al.*, 2000; Marinoni *et al.*, 2008). The glacial expansion of the

Patagonian and the Antarctic Peninsula Ice Sheets toward the open ocean and the accompanying simultaneous drops in sea level would activate the large continental shelf areas as an additional source of sediment erosion (Kilian and Lamy, 2012; Rohling *et al.*, 2014; Sugden *et al.*, 2009). Therefore, we ascribe the glacial maxima in terrigenous sediment supply to the Drake Passage primarily to the advancement of glaciers in the Patagonian and the Antarctic Peninsula and to the exposure of large continental shelf regions during sea level lowstands. This is supported by high chlorite/illite ratios as well prevailed in the Chilean Margin (Marinoni *et al.*, 2008) and the northern Scotia Sea (Diekmann *et al.*, 2000) at glacial expansions.

The deglacial and interglacial periods are marked by significant retreat of glaciers and increased relative sea levels (Davies *et al.*, 2020; Kilian and Lamy, 2012; Rohling *et al.*, 2014; Sugden *et al.*, 2009). Significant meltwater plumes are especially expected at the glacial terminations in responding to periods of rapid melting. However, the χMS_{terr} values are marked by deglacial decreases indicative of a reduced terrigenous sediment input across the glacial terminations. The short-lived spikes in smectite/chlorite ratios and quartz/feldspar ratios at the end of glacial Termination I and Termination II might be an expression of meltwater-related changes. Most of the terrigenous sediments was probably supplied to the southeast Pacific margin (Marinoni *et al.*, 2008). Consequently, the interglacial terrigenous sediments recorded low χMS_{terr}, Ti/K ratio and chlorite/illite ratio during the interglacial periods.

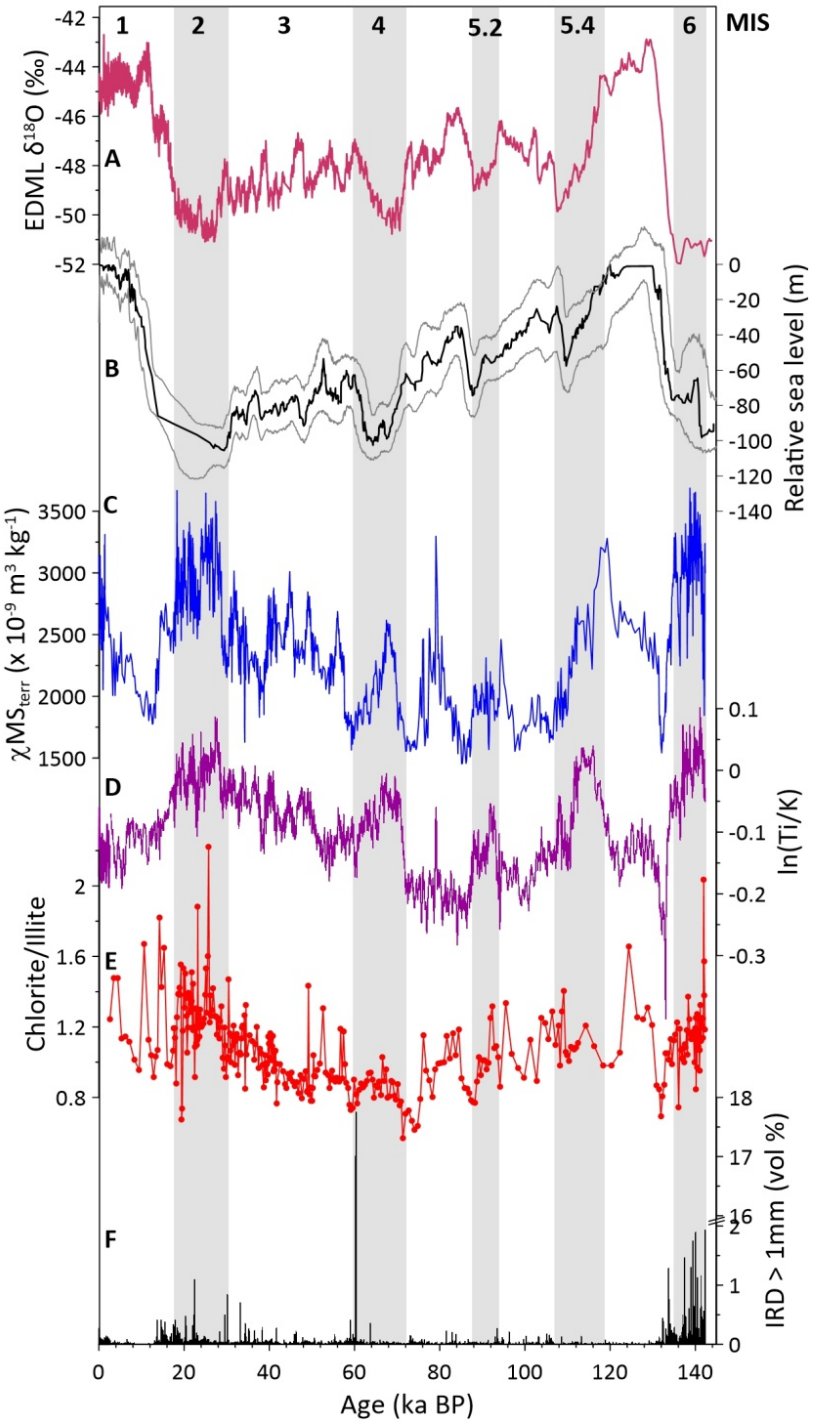

Fig. 5.6. The variability of ice sheet dynamics over the past 140 ka. A. Oxygen isotope records from the EPICA Dronning Maud Land (EDML) ice core can be a proxy as ice volume (EPICA Community Members, 2006); B, Relative sea level with five points smooth, grey lines are upper and lower bound of 95% probability interval (Rohling *et al.*, 2014); C, Mass-specific magnetic susceptibility record followed the Southern Hemisphere climate changes, which is applied to indirectly reflect the ice dynamics. D, ln(Ti/K) variation in parallel with the mass-specific magnetic susceptibility; E, chlorite/illite ratio indicate a pronounced shift provenance at MIS 4. F, IRD records exhibit the ice dynamics. Grey bars indicate the advancement of ice sheets during the glacial periods and stadials.

5.6 Conclusion

The clay mineral assemblage with magnetic and geochemical properties reveal significant changes in the amount and provenance of terrigenous sediment supply into the central Drake Passage over the past 140 ka. The detrital materials are mainly derived from western Patagonia and the Antarctic Peninsula. The ACC might have served as the major driver for the sediment transport in the Drake Passage region. Because of clear regional signals no credible evidence for far distant dust transport was recorded at our site. Expansion of ice sheets in southern Patagonia and on the Antarctic Peninsula together with relative sea-level lowstands led to enhance the efficiency of terrigenous input during glacial maxima.

Our records reveal the continuing evolution of glaciers in southern Patagonia and on the Antarctic Peninsula over the past 140 ka. High-resolution records provide evidences for the ice sheet advancement from the onset of glaciation towards the glacial maximum, which is not well resolved by land fragmentary records.

Acknowledgements

We acknowledge Susanne Wiebe and Valea Schumacher at Alfred Wegener Institute Helmholtz Centre for Polar and Marine Research (AWI) for technical assistance in sample preparation and analytical measurements. This work has been supported by the China Scholarship Council (CSC No. 201604910671) and the AWI.

6 Deep stratification in the Southern Ocean linked to CO_2 changes over the past 140,000 years

Shuzhuang Wu[1], Gerhard Kuhn[1], Frank Lamy[1], Lester Lembke-Jene[1], Huang Huang[2], Marcus Gutjahr[2], Helge W. Arz[3], Ralf Tiedemann[1]

[1]Alfred-Wegener-Institut Helmholtz-Zentrum für Meeres- und Polarforschung, 27568 Bremerhaven, Germany;
[2] GEOMAR, Helmholtz Centre for Ocean Research Kiel, 24148 Kiel, Germany
[3] Leibniz Institute for Baltic Sea Research Warnemünde, 18119 Rostock, Germany

In preparation for Paleoclimatology and Paleoceanography

Abstract

Deep ocean stratification has been proposed as one mechanism to intensify and isolate the oceanic carbon reservoir in the deep Southern Ocean during glacial times. However, water masses sourcing in the Pacific sector of the Southern Ocean is not well constrained. Here, we used authigenic neodymium and lead isotopic signatures from sediment samples to evaluate the relative contributions of Atlantic- and Pacific-derived waters to Circumpolar Deep Water over the past 140 ka. Our records reveal increased glacial expansion of Pacific-derived water into the deep Southern Ocean at the expense of North Atlantic-derived water. Comparison of the seawater-derived Nd signatures in different water depths shows a pronounced gradient between mid-depth and deep waters during glacials (Marine Isotope Stage 4-2). This gradient indicates a stratified deep ocean during the glacial periods. Enhanced stratification together with a strengthened biological pump would lead to an increased CO_2 storage in the deep Southern Ocean during the glacial periods.

6.1 Introduction

The Southern Ocean played a crucial role in regulating the storage of CO_2 on glacial-interglacial timescales (Anderson *et al.*, 2009; Gottschalk *et al.*, 2020; Jaccard *et al.*, 2016; Ronge *et al.*, 2016). Deep density stratification has been proposed as an

efficient mechanism to enhanced the carbon storage in the Southern Ocean during glacials, whereas the glacial enhancement of the biological pump fostered the drawdown of atmospheric CO_2 and the related transfer of carbon into the deep ocean (Hain *et al.*, 2010; Sigman *et al.*, 2010). Previous studies have identified a strong "chemical divide" between intermediate and deep waters in the Southern Ocean during glacial times. This sharp chemocline is based on benthic $\delta^{13}C$ reconstructions and divides well-ventilated water above ca. 2500 m from poorly ventilated water below. This gradient is best developed in the Atlantic sector of the Southern Ocean and points to a strong influence through glacial changes in North Atlantic Deep Water (NADW) production (Charles *et al.*, 2010; Curry and Oppo, 2005; Herguera *et al.*, 1992; Hodell *et al.*, 2003; Ninnemann and Charles, 2002; Roberts *et al.*, 2016). This "chemical divide" is likely related to the altered geometry of deep ocean circulation (Charles *et al.*, 2010; Hodell *et al.*, 2003; Ninnemann and Charles, 2002), however, the structure and source of glacial deep Southern Ocean water masses remain equivocal.

Today, the southward export of NADW is balanced by northward flow of Antarctic Intermediate Water (AAIW) and Antarctic Bottom Water (AABW) (Talley, 2013). NADW, Pacific Deep Water (PDW) and Indian Deep Water (IDW) are mixing into the Antarctic Circumpolar Current as Circumpolar Deep Water (CDW). The denser NADW transforms into Lower Circumpolar Deep Water (LCDW), whereas PDW and IDW are converted into Upper Circumpolar Deep Water (UCDW) (Talley, 2013). During the Last Glacial Maximum (LGM), the NADW occupied shallower depths than today and is known as the Glacial North Atlantic Intermediate Water (GNAIW) (Bohm *et al.*, 2015; Curry and Oppo, 2005; Lynch-Stieglitz *et al.*, 2007). As a consequence, the proportion of NADW was significantly reduced in the deep Southern Ocean (Hu and Piotrowski, 2018; Negre *et al.*, 2010; Piotrowski *et al.*, 2005). The shoaled GNAIW may contribute to UCDW and Antarctic Intermediate Water (AAIW) during glacial periods (Sikes *et al.*, 2017; Talley, 2013).

Seawater-derived Nd isotope signatures recorded in marine sediments ($^{143}Nd/^{144}Nd$, expressed as εNd) allow to trace the source regions of major water

masses (Basak *et al.*, 2018; Frank, 2002; Hu and Piotrowski, 2018; Huang *et al.*, 2020; Pöppelmeier *et al.*, 2020). NADW is characterized by less radiogenic signatures (εNd = ~-13 to -16) (Bohm *et al.*, 2015; Lippold *et al.*, 2016; Lippold *et al.*, 2019) and AABW is marked by relative less radiogenic signatures (εNd = -7 to -9) (Basak *et al.*, 2018; Basak *et al.*, 2015; Huang *et al.*, 2020). In contrast, PDW is marked by more radiogenic signatures (εNd = ~0 to -4) (Amakawa *et al.*, 2009; Du *et al.*, 2016; Fröllje *et al.*, 2016; Lacan *et al.*, 2012). Mixing these sources of water masses determine the εNd signature of modern CDW (εNd = –8 to –9) (Basak *et al.*, 2018; Basak *et al.*, 2015; Stichel *et al.*, 2012). Today, relatively homogenous Nd isotope signatures prevail in the Drake Passage due to intense mixing (Stichel *et al.*, 2012). Seawater Pb isotopic signatures also serve as a reliable tracer for water masses similar to Nd isotope (Abouchami and Goldstein, 1995; Frank, 2002; Huang *et al.*, 2020; Molina-Kescher *et al.*, 2016). Today, Atlantic-derived waters are characterized by high $^{206}Pb/^{204}Pb$, whereas Pacific-derived waters show relatively low $^{206}Pb/^{204}Pb$ (Frank, 2002).

In this study, we aim at tracing the water mass sources in the Southern Ocean based on the authigenic Fe–Mn oxyhydroxide-bound Nd and Pb isotopic compositions. By comparing the Nd signatures from different water depths in the Drake Passage, we provide evidence for a distinctive separation between mid-depth and deep waters in the Pacific sector of the Southern Ocean during the last glacial period.

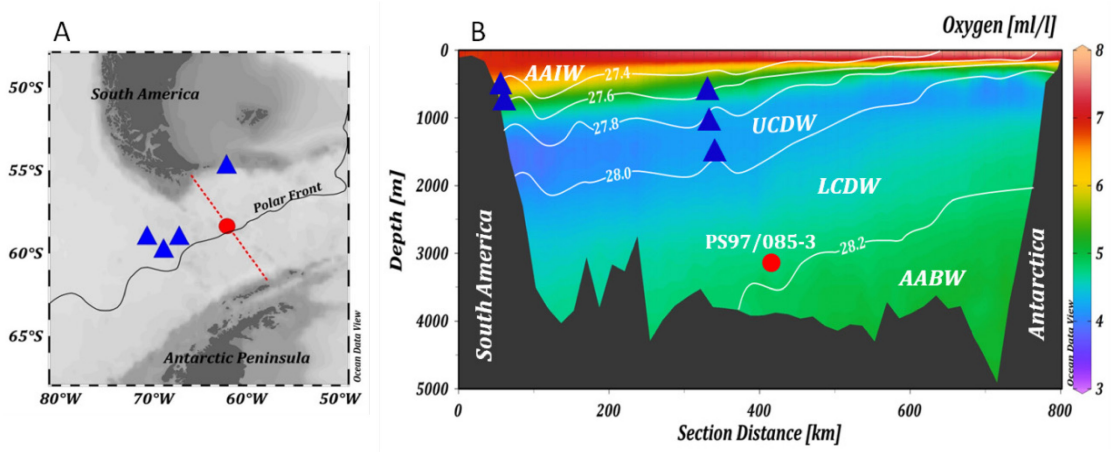

Fig. 6.1. A, Sample locations of sediment core PS97/085-3 (red circle) and cold-water corals (Struve, 2016) (blue triangles). Red dot line defines a section shown in B. B, Oxygen concentration section across the Drake Passage (Garcia *et al.*, 2013). Thin white lines indicate surfaces of neutral density anomaly γn (in kg/m^3) (Olsen *et al.*, 2016). AAIW: Antarctic Intermediate Water; UCDW: Upper Circumpolar Deep Water; LCDW: Lower Circumpolar Deep Water; AABW: Antarctic Bottom Water.

6.2 Material and methods

Sediment core PS97/085-3 (58° 21.28′ S, 62° 10.02′ W; water depth 3090 m; 14.4 m core length) was retrieved from the central Drake Passage, ~22 nm north of the modern Polar Front (Fig. 6.1). Since our site is bathed by the LCDW, the core is deemed to have sensitively recorded past changes in water masses in the Pacific sector of the Southern Ocean.

6.2.1 Authigenic neodymium and lead isotopes analyses

The seawater Nd and Pb isotope signals were extracted from the Fe–Mn oxyhydroxide fraction of bulk sediment from core PS97/085-3, following the leaching procedures from previous studies (Blaser *et al.*, 2016; Gutjahr *et al.*, 2007; Huang *et al.*, 2020). Detail measurement information was described in Chapter 2.3.8.

6.2.2 Chronology

We used the age models of PS97/085-3 as defined in Manuscript “Chapter 4” (see Supporting Information, Chapter 4.6 Material and methods). The age model was based on radiocarbon dates, paleomagnetic excursion, corrected relative

paleointensity (RPI) with the RPI stack and tuning points from high resolution XRF-CS ln (Ca/Ti) records. High sedimentation rates and mass accumulation rates prevailed during the full glacial periods (20~40 cm ka^{-1}; 20~50 g cm^{-2} ka^{-1}).

6.3 Results

6.3.1 Authigenic Nd isotopes

Neodymium isotopic compositions extracted from the authigenic Fe–Mn oxyhydroxide fractions ranged between εNd = -2.5 ± 0.2 and εNd = -7.3 ± 0.2 over the past 140 ka (Fig. 6.2A). The core top εNd signatures (εNd = -7.3 ± 0.2) are consistent with Holocene data from cold-water corals in the Drake Passage (εNd = -7.5 ± 0.2) (Struve *et al.*, 2019) and close to modern seawater values (εNd = -8.3 ± 0.4) (Stichel *et al.*, 2012). The interglacial periods are characterized by less radiogenic εNd signatures, with an average of -7.3 during the Holocene and exhibit slightly more radiogenic εNd values of -6.2 during Marine Isotope Stage (MIS) 5. The average εNd values during MIS 5.4 and MIS 5.2 were ~-5.5 and ~-5.7, respectively. In contrast, more radiogenic εNd signatures prevailed during the glacial stages with a range of εNd = -2.5~-5.5 (Fig. 6.2A). During the LGM and the Penultimate Glacial Maximum (PGM), the εNd signatures reached the highest value with -2.5 ± 0.2.

6.3.2 Authigenic Pb isotopes

$^{206}Pb/^{204}Pb$ signatures (~18.79) extracted from the core tops corroborate available Fe-Mn nodules data (~18.76) in the Drake Passage region (Abouchami and Goldstein, 1995) (Fig. 6.3A), which suggests that the signatures at our site are not affected by anthropogenic Pb contamination (Bollhöfer and Rosman, 2000). $^{206}Pb/^{204}Pb$ and $^{208}Pb/^{204}Pb$ leachate results at site PS97/085 exhibited consistently less radiogenic Pb isotopic compositions during the glacial periods (Fig. 6.2B,C). Following the terminations to the full interglacial, $^{206}Pb/^{204}Pb$ and $^{208}Pb/^{204}Pb$ significantly shifted to more radiogenic values (Fig. 6.2B, C).

In the $^{206}Pb/^{204}Pb$-$^{208}Pb/^{206}Pb$ comparison plot (Fig. 6.3B), Pb isotopic signatures

in the Drake Passage generally cluster during the glaciations, pointing toward Pacific-like Pb isotopic composition, especially at the southeast Pacific (40ºS) (Abouchami and Goldstein, 1995). In contrast, the interglacial Pb isotopic signals leaned to more Atlantic-like indicated by high $^{206}Pb/^{204}Pb$ and low $^{208}Pb/^{206}Pb$ (Abouchami and Goldstein, 1995; Frank, 2002).

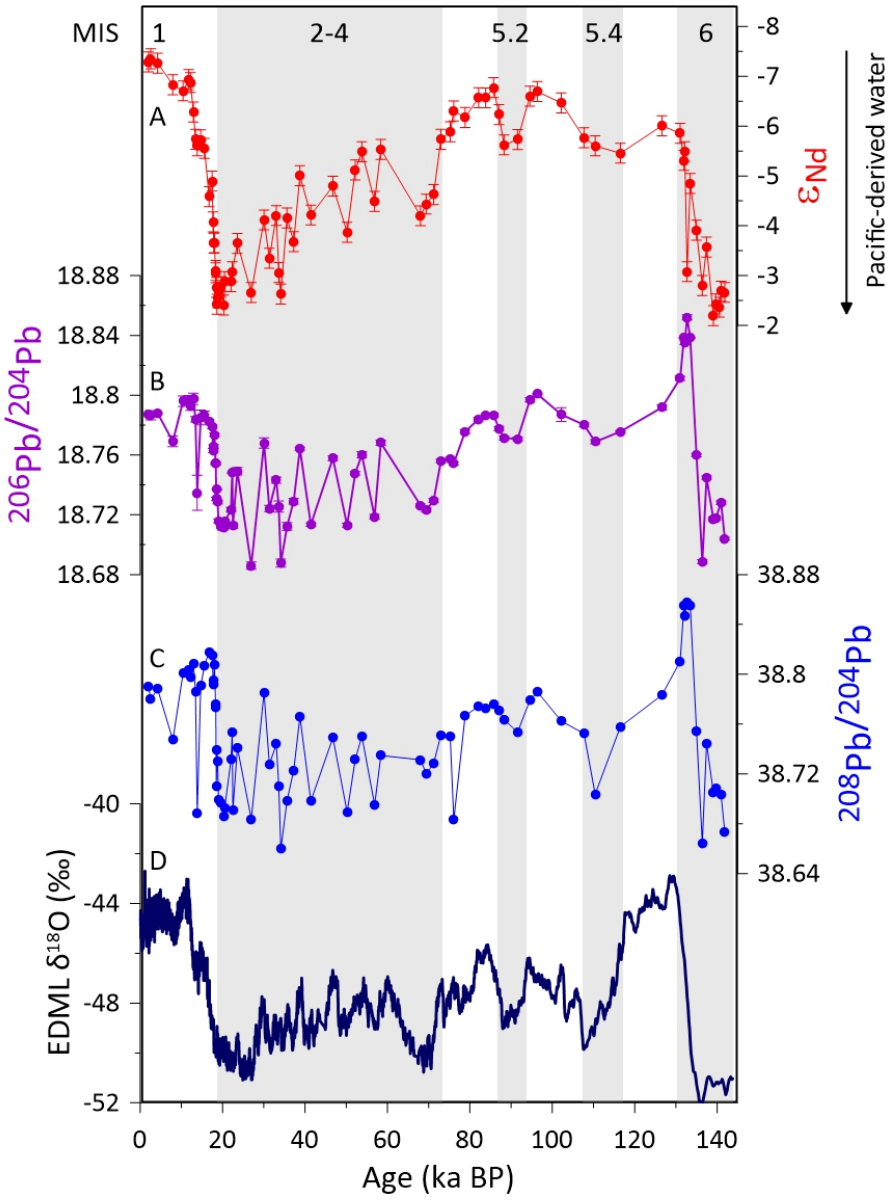

Fig. 6.2. Nd and Pb isotopic variations from core PS97/085-3 in the deep Southern Ocean over the past 140 ka. A, Neodymium isotope compositions from authigenic Fe-Mn oxyhydroxides. B, Authigenic Fe–Mn oxyhydroxide-based $^{206}Pb/^{204}Pb$ and C, $^{208}Pb/^{204}Pb$ records. D, Ice core ^{18}O records from the EPICA Dronning Maud Land (EDML) (EPICA Community Members, 2006). Vertical gray bars mark the glacial periods and stadials during Marine Isotope Stage (MIS) 5.4 and MIS 5.2.

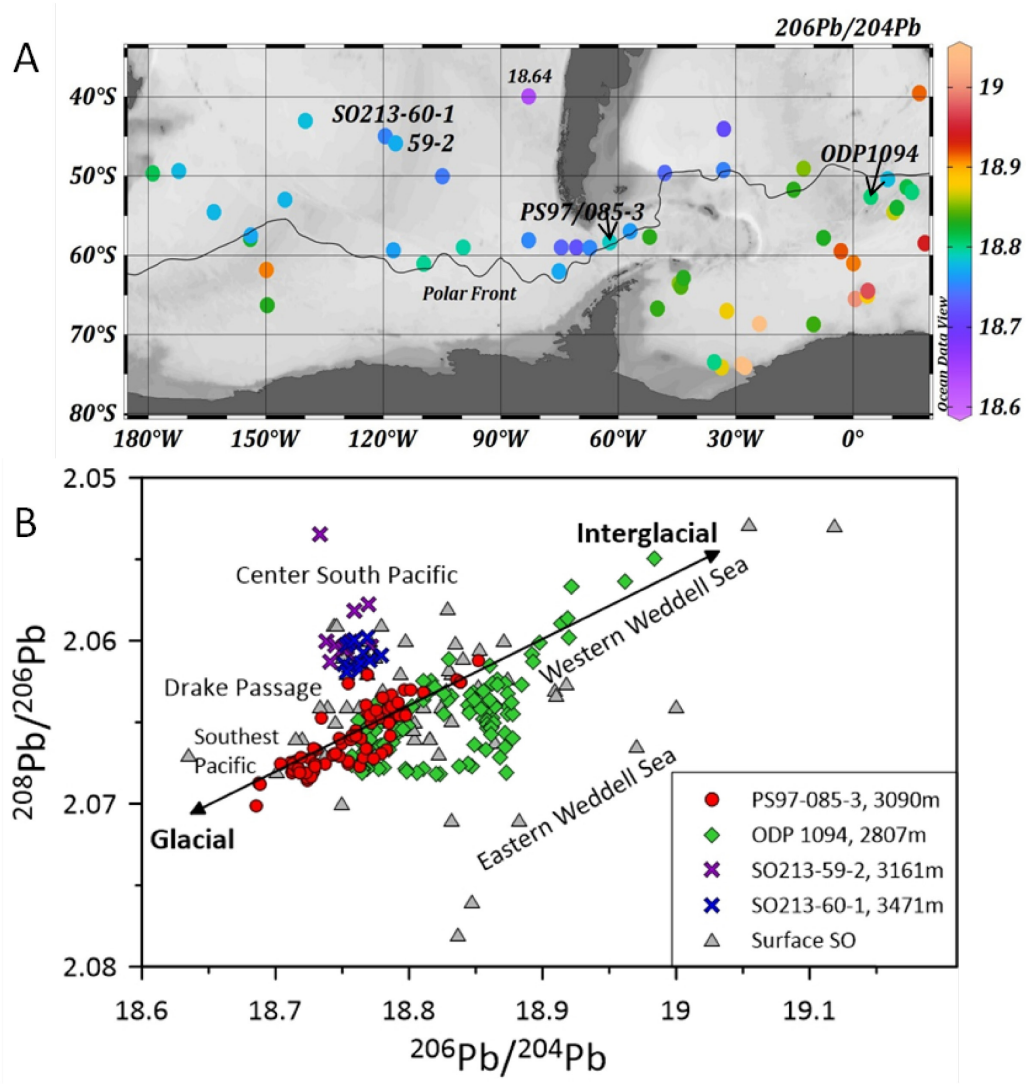

Fig. 6.3. A, $^{206}Pb/^{204}Pb$ distribution of Fe–Mn nodules and core-top sediment samples in the Southern Ocean(Abouchami and Goldstein, 1995; Huang *et al.*, 2020). B, $^{206}Pb/^{204}Pb$–$^{208}Pb/^{206}Pb$ trends point to Pacific-derived water during the glacial periods. Seawater Pb isotopic evolution at Site PS97-085-3 (red circles) compared with available Pb isotope data in the Southern Ocean. South Atlantic (ODP 1094, green diamonds) (Huang *et al.*, 2020) and South Pacific (SO213-59-2, purple cross; SO213-60-1 blue cross) (Molina-Kescher *et al.*, 2016) sediment cores, together with surface Fe–Mn nodules and core-top sediment samples (grey triangles) (Abouchami and Goldstein, 1995; Huang *et al.*, 2020).

6.4 Discussion

6.4.1 The authigenic Nd and Pb isotope as tracers of past deep water masses

Authigenic Nd and Pb isotopes both have been used as tracers to identify the source region of the water masses (Basak *et al.*, 2018; Frank, 2002; Gutjahr *et al.*, 2007; Huang *et al.*, 2020; Molina-Kescher *et al.*, 2016; Pöppelmeier *et al.*, 2020). Nd and Pb isotopic data reveal marked glacial-interglacial variability at our site (Fig. 6.2), which

are consistent with other records in the Southern Ocean (Hu and Piotrowski, 2018; Huang *et al.*, 2020; Molina-Kescher *et al.*, 2016; Piotrowski *et al.*, 2009; Skinner *et al.*, 2013).

For changes in authigenic Nd and Pb isotope compositions, several processes may play a role on Nd and Pb isotopic signatures including dust input, fluvial supply, ice-rafted debris (IRD) as well as mixing of water masses (Blaser *et al.*, 2019; Bollhöfer and Rosman, 2000; Lacan and Jeandel, 2005). The lithogenic input from dust can alter the seawater Nd and Pb isotopic compositions (Bollhöfer and Rosman, 2000; Bridgestock *et al.*, 2016). Aeolian transport can be excluded in the Drake Passage region (see Chapter 5), therefore dust input has a negligible effect on Nd isotopic signatures in this area (Struve *et al.*, 2019; Walter *et al.*, 2000). Furthermore, the seawater Pb isotopic signatures are not in line with dust Pb isotopic signatures from the ice core (Vallelonga *et al.*, 2010) (Fig. S6.1). Thus, we rule out dust-derived signatures as contributors to our Nd and Pb isotopic compositions.

IRD fluxes into the water column might form authigenic phases and thus affect Nd and Pb isotope compositions in high latitude oceans (Blaser *et al.*, 2019; Crocket *et al.*, 2012; Kurzweil *et al.*, 2010). Indeed, we observe increased IRD contents during the glacial periods, however, the contents of IRD at our site are generally less than 2 vol. %, except for one spike (18 vol. %) during MIS 4 (see Chapter 5, Fig. S6.2). Furthermore, the IRD fluctuations are apparently inconsistent with Nd and Pb records (Fig. S6.2). Therefore, we suggest that the IRD input only has a small impact on our Nd and Pb isotopic signatures as well.

Our record show more radiogenic Nd isotopic signatures (εNd = -2.5~ -4.0) during the LGM and PGM (Fig. 6.2A). Such radiogenic seawater signatures are only found in the PDW (Amakawa *et al.*, 2009; Du *et al.*, 2016; Du *et al.*, 2018; Hu and Piotrowski, 2018). It is plausible that more PDW may have contributed to CDW during the LGM and the PGM. However, no comparable radiogenic compositions have been resolved in the Southern Ocean before (Fig. 6.4). Previous studies proposed that the pore water could alter the Nd signature toward non-hydrogenic phases, which have been found in the North Pacific (Du *et al.*, 2016) and the North Atlantic (Blaser

et al., 2019). The latest study in the South Atlantic based on core PS1768-8 revealed more radiogenic values (εNd = ~-4.0) during the glacial periods as well, which were likely influenced by the porewater alteration (Huang *et al.*, 2020). Accordingly, our glacial Nd isotopic compositions (εNd > -4.0) might reflect the porewater signatures released from sediments under very sluggish circulation (Blaser *et al.*, 2019). This inference is supported by substantial reduction of the ACC flow speeds during glacial times (Lamy *et al.*, 2015; Roberts *et al.*, 2017).

Although water mass signatures reconstructed by authigenic Nd compositions might be diagenetically overprinted at our site, shifting to more radiogenic signatures during the glacial periods are broadly consistent with previous studies (Fig. 6.4, 6.5) (Basak *et al.*, 2018; Hu and Piotrowski, 2018; Huang *et al.*, 2020; Molina-Kescher *et al.*, 2016; Piotrowski *et al.*, 2009; Piotrowski *et al.*, 2005; Skinner *et al.*, 2013). During glacials, more radiogenic Nd compositions with a range of ~-4 to -6 were found in the South Pacific (Basak *et al.*, 2018; Hu and Piotrowski, 2018; Molina-Kescher *et al.*, 2016) as well as the South Atlantic (Fig. 6.4) (Huang *et al.*, 2020; Skinner *et al.*, 2013).

In contrast to Nd isotope, shorter residence time and higher particle reactivity of Pb is unlikely to have been altered by pore water (Henderson and Maier-Reimer, 2002). Our core top Pb isotopic signatures are consistent with the adjacent ferromanganese crust values in this region (Abouchami and Goldstein, 1995) and glacial Pb isotopic values are in line with the signatures of the South Pacific (Molina-Kescher *et al.*, 2016). This suggests authigenic Pb in our records provides reliable seawater signatures (Fig. 6.3A). Both water mass mixing and particles sinking can affect the seawater-derived Pb isotope signature (Huang *et al.*, 2020; Wu *et al.*, 2010), thus the seawater-derived Pb isotopic signals may reflect changes in both the upper and lower overturning cells in the Southern Ocean (Huang *et al.*, 2020).

6.4.2 Expansion of glacial Pacific-derived water in the deep Southern Ocean

Compared to the present day, both Nd and Pb isotopic characteristics of glacial LCDW exhibit geochemical affinity to water found in the deep Pacific Ocean (Fig.

6.2, 6.3B). This indicates more deep Pacific-derived water prevailed at our site during the glacial periods. Since no significant changes in end-member εNd signatures of NPDW and NADW over the past two million years (Foster *et al.*, 2007; Pena and Goldstein, 2014), end-member changes can be excluded for the Nd isotope glacial shift in LCDW. A wealth of paleoceanographic evidence revealed significant reductions of NADW formation and sluggish export to the Southern Ocean during the glacial intervals (Bohm *et al.*, 2015; Curry and Oppo, 2005; Henry *et al.*, 2016; Piotrowski *et al.*, 2005). NADW was proposed to shoal to Glacial North Atlantic Intermediate Water (GNAIW) in the upper circulation cell (Bohm *et al.*, 2015; Curry and Oppo, 2005) and it may not able to penetrate into the deep Southern Ocean and thus restrict the contribution of North Atlantic-derived water to LCDW (Sikes *et al.*, 2017). AABW is characterized by unradiogenic Nd and high $^{206}Pb/^{204}Pb$ ratios (Huang *et al.*, 2020), which are incompatible with radiogenic Nd and low $^{206}Pb/^{204}Pb$ ratios in the Drake Passage over the glacial excursions. We suggest AABW from the Weddell Sea was thus highly unlikely to flow westward into the Drake Passage during the glacial period like today.

Previous studies found the deepening and extension of PDW in the Southwest Pacific during the last glacial period (Ronge *et al.*, 2016; Sikes *et al.*, 2016) and more radiogenic Nd signatures prevailed in the South Pacific during the LGM (Basak *et al.*, 2018; Basak *et al.*, 2015; Hu and Piotrowski, 2018; Molina-Kescher *et al.*, 2016). Our authigenic Nd signatures became more radiogenic during the glacial indicative of increased the PDW transport through the Drake Passage. More radiogenic Nd isotope signatures have been found in the South Atlantic and Indian Ocean sectors of the Southern Ocean as well (Huang *et al.*, 2020; Piotrowski *et al.*, 2009; Piotrowski *et al.*, 2005; Skinner *et al.*, 2013). Therefore, we propose that the proportions of Pacific-derived water in the deep Southern Ocean were increasing during glacial periods at the expense of NADW.

Low $^{206}Pb/^{204}Pb$ signatures (average = ~18.70) registered in the glacial LCDW are coherent with the unradiogenic values of ~18.72 in the South Pacific (Molina-Kescher *et al.*, 2016). The $^{206}Pb/^{204}Pb$ ratios showed slightly higher (~18.76) in the South

Atlantic during the glacial intervals (Huang *et al.*, 2020), since Pacific-derived signatures may be diluted in the South Atlantic. This longitudinal gradient is mirrored in the modern Southern Ocean (Abouchami and Goldstein, 1995; Molina-Kescher *et al.*, 2016). Therefore, low $^{206}Pb/^{204}Pb$ signatures during the glacial periods provide convincing support for the expansion of deep Pacific-derived water into the deep Southern Ocean.

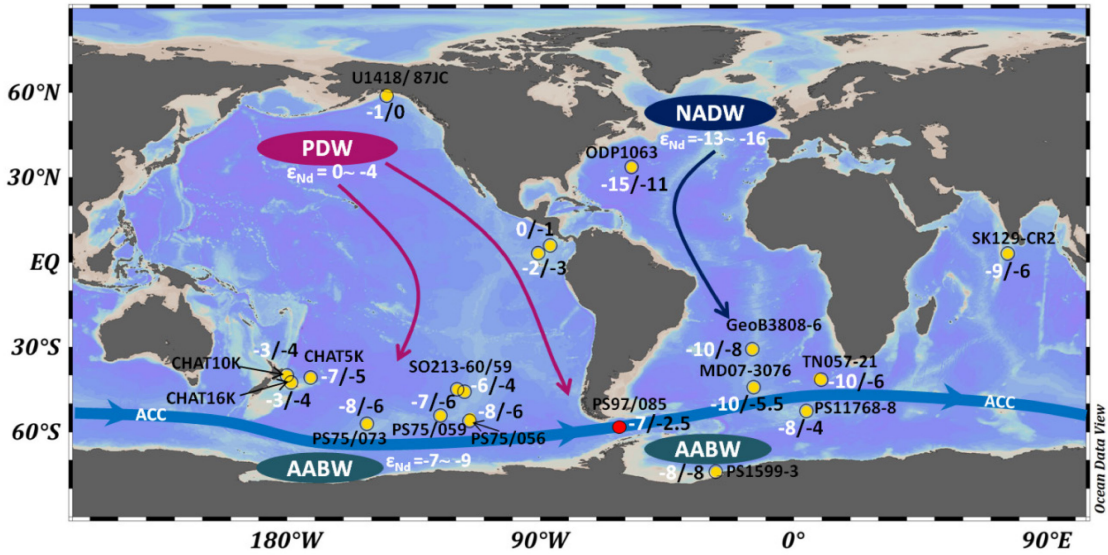

Fig. 6.4. Southern Ocean seawater Nd isotope signatures related to the end members: North Atlantic Deep Water (NADW, ε_{Nd} = -13~ -16) (Bohm *et al.*, 2015; Lippold *et al.*, 2019), Antarctic Bottom Water (AABW, ε_{Nd} = -7~ -9) (Basak *et al.*, 2018; Basak *et al.*, 2015; Huang *et al.*, 2020) and Pacific Deep Water (PDW, ε_{Nd} = 0~ -4) (Amakawa *et al.*, 2009; Du *et al.*, 2018). Modern (white) and LGM (black) ε_{Nd} values at each core site (Basak *et al.*, 2018; Du *et al.*, 2018; Hu and Piotrowski, 2018; Huang *et al.*, 2020; Jonkers *et al.*, 2015; Molina-Kescher *et al.*, 2016; Piotrowski *et al.*, 2009; Piotrowski *et al.*, 2005; Skinner *et al.*, 2013). ACC, Antarctic Circumpolar Current.

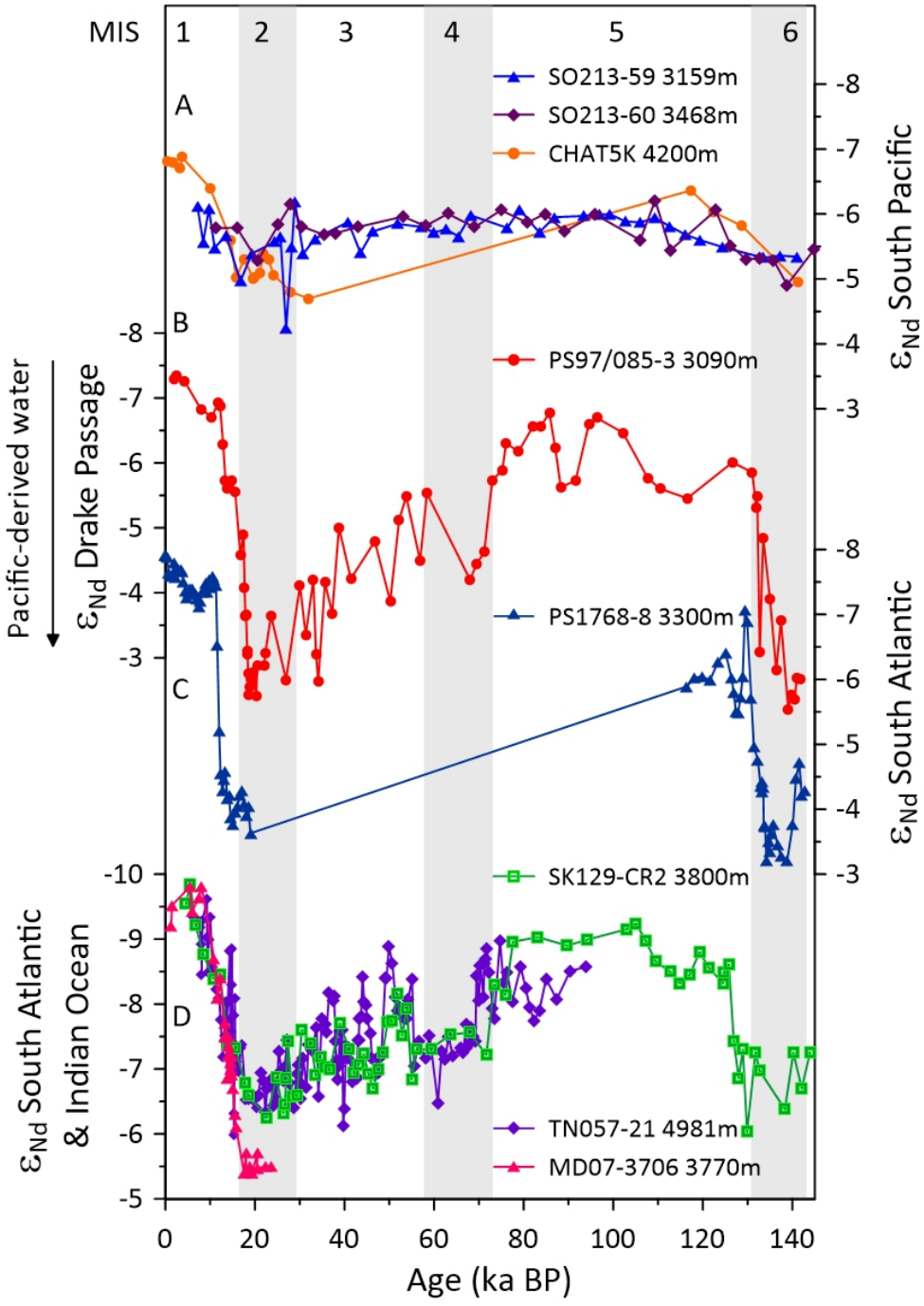

Fig. 6.5. Seawater Nd signatures variations in the Southern Ocean over the last 140 ka. A, Neodymium isotope signatures of South Pacific cores SO213-59-2 (East Pacific Rise 46 °S blue triangles), SO213-60-1 (East Pacific Rise 45 °S purple diamonds) (Molina-Kescher *et al.*, 2016) and CHAT5K (New Zealand Margin 41 °S orange dots) (Hu and Piotrowski, 2018). B, ε_{Nd} of core PS97/085-3 from the central Drake Passage (this study, 58 °S red circles). C, ε_{Nd} of South Atlantic cores PS1768-8 (52 °S blue triangles) (Huang *et al.*, 2020). D, ε_{Nd} of South Atlantic cores MD07-3076 (44 °S pink triangles) (Skinner *et al.*, 2013) and RC11-83/TNO57-21 (Cape Basin, 40/41 °S, purple diamonds) (Piotrowski *et al.*, 2005) and equatorial Indian Ocean core SK129-CR2 (3 °N, green squares) (Piotrowski *et al.*, 2009). Core locations are showing in Fig 6.4. Note same εNd scales in A, B and C, but D curve with a different scale. Grey bars indicate glacial stages.

6.4.3 Enhanced glacial stratification in the deep Southern Ocean

We found an enhanced Nd gradient between mid-depth (UCDW) and deep waters (LCDW) as climate approached the LGM (Fig. 6.6C), in contrast to a relative geochemical homogeneity in the modern Drake Passage (Stichel *et al.*, 2012). The UCDW and LCDW both exhibited more radiogenic Nd signatures during the glacial period, but the signatures within the LCDW show larger amplitudes. Although absent of high-resolution data for the UCDW from cold water corals (Struve, 2016), the discernible gradient occurred during MIS 4-2 (Fig. 6.6C). This gradient suggests the vertical mixing in the deep Southern Ocean was reduced during glacials, coinciding with reduced nutrient supply from deep ocean (Jaccard *et al.*, 2013; Studer *et al.*, 2015).

The pronounced gradient may have been caused by more Pacific-derived water dominating in the deep Southern Ocean at the expense of NADW. Shoaled GNAIW may have primarily fed the UCDW (Sikes *et al.*, 2017) and thus contributed to relatively unradiogenic Nd isotopic signatures on the UCDW layer. Whereas PDW is characterized by rather radiogenic Nd isotope signatures, it may have principally contributed to the LCDW during the glaciations (Sikes *et al.*, 2017) instead of the UCDW like today (Talley, 2013). The vertical gradient is also reflected by benthic foraminiferal $\delta^{13}C$ and $\delta^{18}O$ records in the Atlantic and Pacific sectors of the Southern Ocean during the last glaciation (Charles *et al.*, 2010; Hodell *et al.*, 2003; Ninnemann and Charles, 2002; Ronge *et al.*, 2016; Sikes *et al.*, 2017). Therefore, the vertical gradient indicates a stronger stratification in the deep Southern Ocean during the glacial times. Lower export productions in the Antarctic Zone support the deep stratification scenario throughout the glacial excursion (Jaccard *et al.*, 2013; Studer *et al.*, 2015).

Substantial reduction of the glacial ACC flow speeds would reduce mixing dynamics and thus further amplify the deep stratification (Fig. 6.6D). Most proxy records and modeling studies suggest that the southern westerly winds (SWW) shifted equatorward associated with expansion of Antarctic sea ice during the glacial stages (Ferrari *et al.*, 2014; Gersonde *et al.*, 2005; Kohfeld *et al.*, 2013; Toggweiler *et al.*,

2006), through these changes were probably zonally inhomogeneous across the Southern Ocean (Lamy *et al.*, 2019). The SWW shifting northward during the glacial periods would have minimized the wind stress effectiveness acting on the ocean surface, thereby slowing down the ACC flow speeds during the LGM (Lamy *et al.*, 2015; Roberts *et al.*, 2017) (see discussions in Chapter 4). The weaken ACC have reduced mixing processes and hence efficiently stratified the deep Southern Ocean during glacial times (Fig. 6.6D).

Enhanced deep stratification was paralleled by increased dust flux in the Southern Ocean during the glacial periods (Fig. 6.6B, C) (Martínez-García *et al.*, 2014). This suggests deep stratification and iron fertilization both raised the efficiency of carbon storage in the ocean inertia, thereby lowering the atmospheric CO_2 to the glacial maxima level (Hain *et al.*, 2010; Sigman *et al.*, 2010).

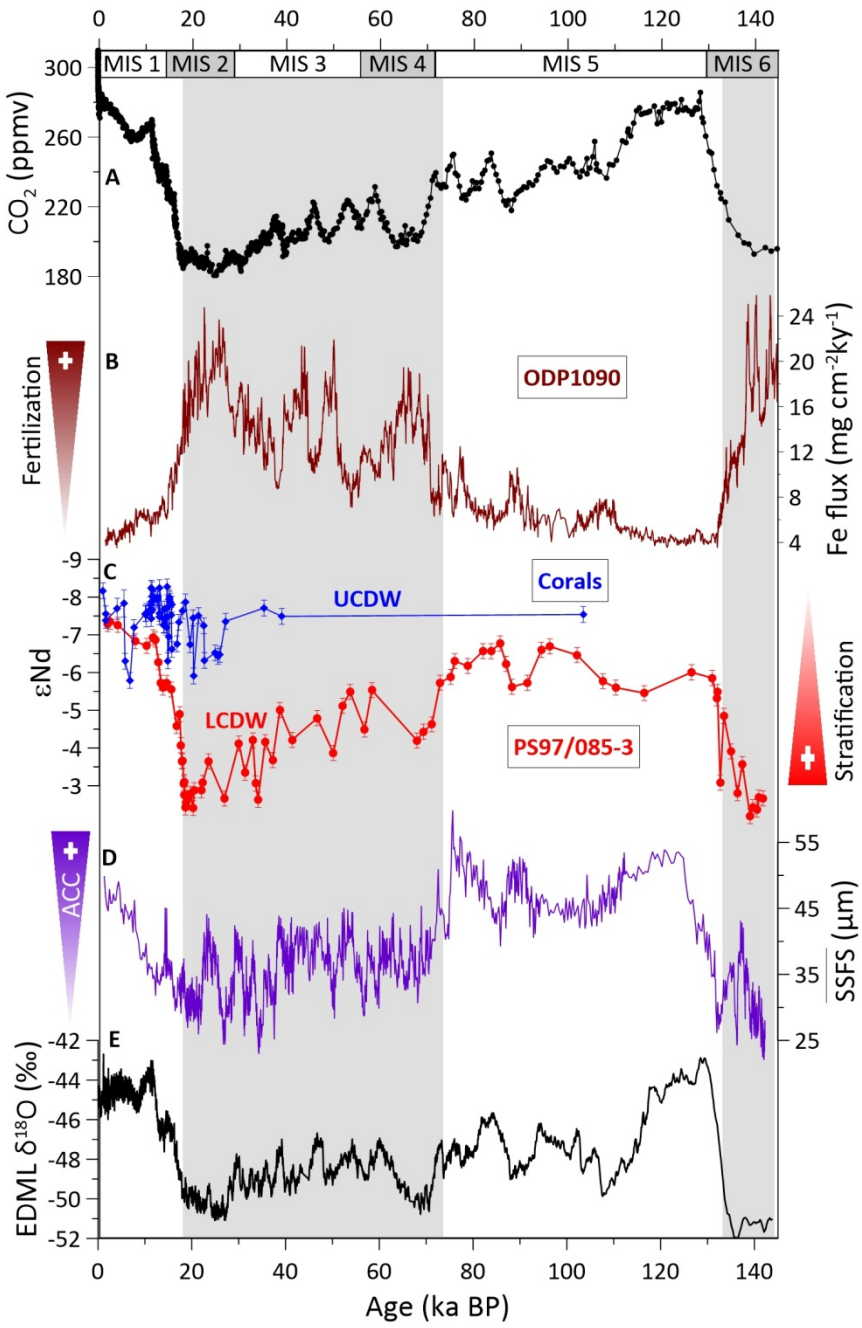

Fig. 6.6. Records of deep stratification in the Southern Ocean, export production and atmospheric CO_2 over the last 140 ka. A, Atmospheric CO_2 concentrations measured in Antarctic ice cores. B, ^{230}Th-normalized iron flux from ODP Site 1090 in the Subantarctic Zone (dark red) (Martínez-García *et al.*, 2014). C, Nd isotopic compositions from PS97/085-3 (red line, bathed by LCDW) and cold water corals (blue line, bathed by UCDW) (Struve, 2016). Higher ε_{Nd} values indicate more Pacific-derived water in the study area. The gradient between the LCDW and UCDW suggests a stronger stratification in the deep Southern Ocean. D, $\overline{SSFS}$ as a flow-speed proxy for the Antarctic Circumpolar Current (ACC) strength (purple). F, $\delta^{18}O$ ice series from EDML (EPICA Community Members, 2006). Vertical grey bars mark a probably strong stratification during the glacial periods. UCDW, Upper Circumpolar Deep Water; LCDW, Lower Circumpolar Deep Water.

6.5 Conclusions

Our Nd and Pb isotopic records from the central Drake Passage reveal remarkable glacial-interglacial variability, which is consistent with other sectors of the Southern Ocean. The glacial periods are characterized by more radiogenic Nd signatures and low $^{206}Pb/^{204}Pb$ ratios, indicative of increased proportion of Pacific-derived deep waters in the deep Southern Ocean at the expense of the NADW. We found a clear gradient between mid-depth and deep waters during glacials. This gradient suggests reduced vertical mixing and thereby enhanced stratification in the deep Southern Ocean throughout the last glaciation. A weaker ACC strength provides support to the notion of a more stratified deep Southern Ocean (Fig. 6.6).

Enhanced stratification in the Southern Ocean together with the strengthen biological pump might have significantly reduced atmospheric CO_2 level during glacials. In contrast, breakup of the deep stratification by strong upwelling and reduced biological pump efficiency can contribute to the CO_2 rise following the deglacial and interglacial periods.

Acknowledgement

We thank the master crew and science party of RV Polarstern Expedition PS97 for their professional help in retrieving the samples. We sincerely thank A. Kolevica at GEOMAR Kiel for technical support. This study was supported by the China Scholarship Council (CSC No. 201604910671) and the AWI.

Supplementary Materials

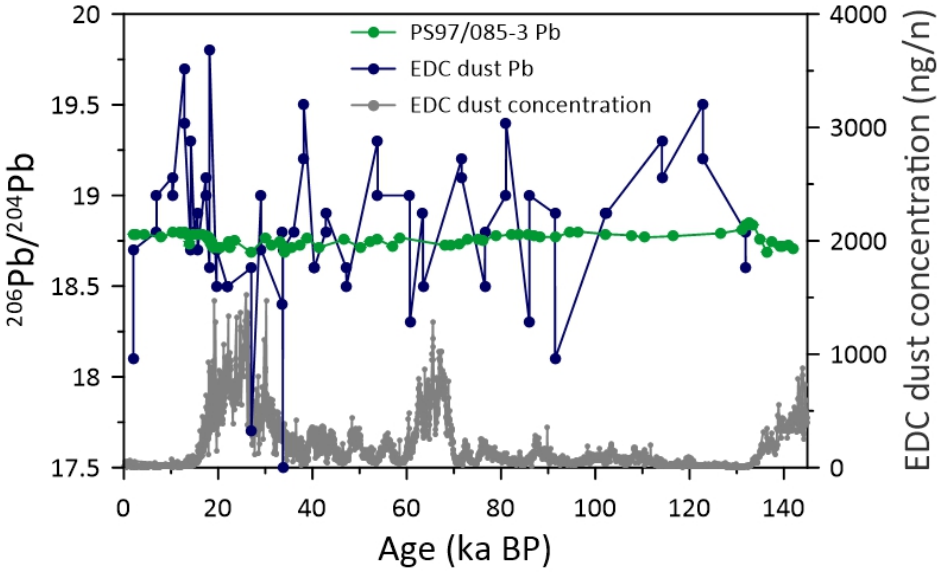

Fig. S6.1. Pb isotope composition from core PS97/085-3 compared to dust signal from ice core EPICA Dome C (EDC). Our core $^{206}Pb/^{204}Pb$ signatures show lower fluctuations (green) compared to the EDC dust Pb isotopic signals (blue) (Vallelonga *et al.*, 2010). Our $^{206}Pb/^{204}Pb$ record has no correlation with EDC dust concentrations (Lambert *et al.*, 2008) over the past 140 ka.

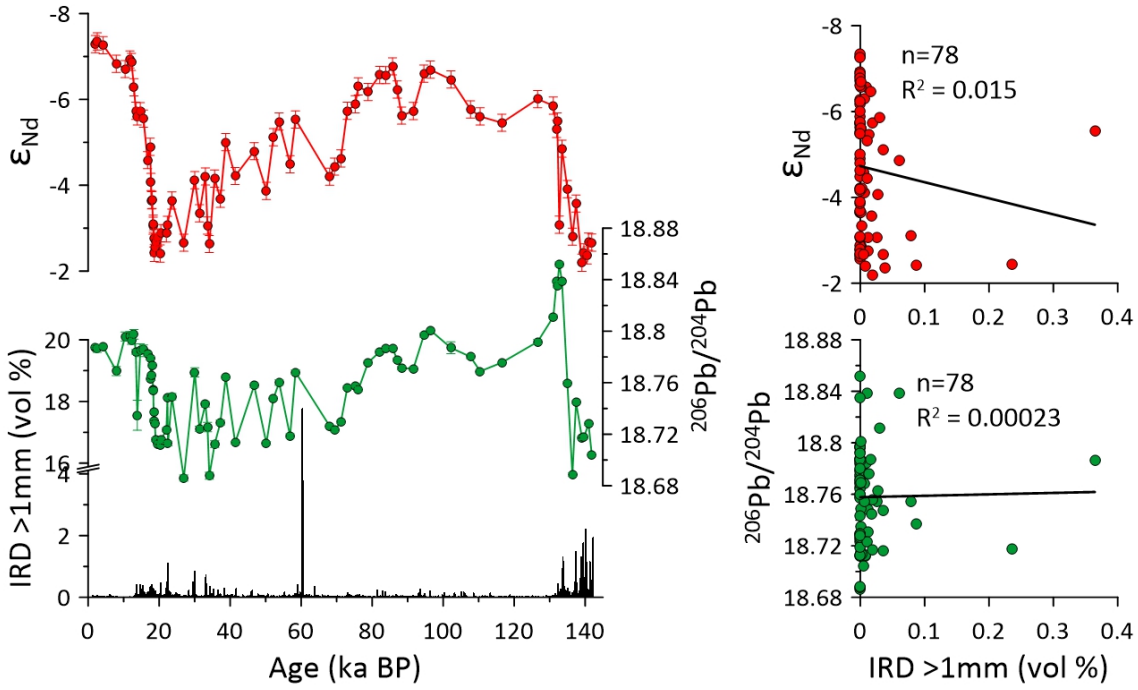

Fig. S6.2. Authigenic ε_{Nd} and $^{206}Pb/^{204}Pb$ from core PS97/085-3 compared with ice-rafted debris (IRD) volume content. ε_{Nd} and $^{206}Pb/^{204}Pb$ error bars are the 2σ external error from the measurements. Nd and Pb isotopic variations have no correlation with changes in IRD contents over the past 140 ka.

7 Conclusions and Outlook

7.1 Conclusions

The major objectives of this thesis were to reconstruct the evolution of the ACC dynamics and terrigenous sediment provenance variations on orbital and millennial timescales in the Drake Passage region, based on a combination of proxies. This thesis also deciphered sediment transport mechanisms in response to ocean circulation and ice dynamics over the last 140 ka. Past water mass mixing in the Pacific sector of the Southern Ocean was addressed in the last study, conducive to deduce large-scale oceanic reorganization during last two glacial cycles.

Southern Patagonia and the Antarctic Peninsula were identified as the main sources for terrigenous sediments in the Drake Passage region (in Chapter 3), based on a comprehensive set of surface sediment samples. Current transport is a major driver for distributing terrigenous sediment. The eastward ACC transport is responsible for a clear longitudinal distribution of chlorite in the Atlantic sector of Southern Ocean. Through correlated the $\overline{SS}$ records of surface sediments with adjacent long-term current meter data, we produced a new flow speed calibration for the $\overline{SS}$. This provided a first step towards semi-quantified the past ACC flow speed changes in responses to climate variations on geological time scales.

The reconstructions of ACC dynamics over the past 140 ka was described in chapter 4. Since high speeds can potentially remove parts of the silt and even the sand fractions (McCave and Hall, 2006), the $\overline{SS}$ proxy may not capture the entire magnitude of the flow speeds variations in our record. Therefore, the mean grain size of sortable silt plus fine sand ($\overline{SSFS}$) was applied as the flow speed proxy to reconstruct the ACC past changes. Proxy evidences exhibit significant glacial-interglacial changes in the ACC flow speed in the vicinity of the Polar Front. Comparable fluctuations have been found in the northern SAF (Lamy *et al.*, 2015; Roberts *et al.*, 2017). Such large changes in the north of PF and SAF are distinctive with minimal flow speed changes in the south of PF reconstructed in the Scotia Sea transect (McCave *et al.*, 2014). These suggest the magnitude of ACC flow speed

changes is likely corresponding to the oceanic frontal system. Superimposed on these long term changes, strong millennial-scale fluctuations in ACC intensity corresponded to the Southern Hemisphere climate oscillations. This strong variation of ACC probably regulates Pacific-Atlantic water mass exchange via the "cold water route" and could significantly affect the AMOC.

The mineralogical, magnetic and geochemical characteristics of terrigenous sediments from core PS97/085-3 reveal that the fine-grained sediments mainly derived from western part of Patagonia and the Antarctic Peninsula over the last 140 ka (Chapter 5). No credible evidence has been found at our site for dust transport as generally assumed (Weber *et al.*, 2012). Instead, a strong ACC has served as the major driver for sediment transport in the Drake Passage region. Expansion of ice sheets in southern Patagonia and on the Antarctic Peninsula, together with the relative sea-level lowstands would have enhanced the efficiency of terrigenous input during glacial maxima. Our high-resolution records provide evidence for the waxing and waning of glaciers in southern Patagonia and on the Antarctic Peninsula from the penultimate glacial period to the late Holocene.

The Nd and Pb isotopic records from the central Drake Passage deciphered past water mass mixing in the Southern Ocean during the last 140 ka (Chapter 6). The glacial periods are characterized by more radiogenic Nd signatures and low $^{206}Pb/^{204}Pb$ ratios, indicative of increased proportion of Pacific-derived deep waters in the deep Southern Ocean at the expense of the NADW. We found a pronounced gradient during glacials, which suggests a stratified deep ocean during the glacial periods. Enhanced stratification together with a stronger biological pump would efficiently increase the carbon storage in the deep Southern Ocean during glacial maxima.

7.2 Outlook

Within this thesis, I found high speeds can extend the grain size sorting range beyond the sand-silt boundary, which was noted in the northern Drake Passage before (Lamy *et al.*, 2015). Hence, I produced a new flow speed proxy ($\overline{SSFS}, 10-125\ \mu m$) to

reconstruct the ACC strength. For further quantification of the ACC flow speed, more sediment samples combined with long-term current meter measurement are needed to better constrain the correlation between the $\overline{SSFS}$ and flow speed.

The reconstructed ACC was stronger during most of MIS 5 compared to the Holocene. Previous studies found strengthened westerly winds were moving poleward during past decades (Beal *et al.*, 2011; Large and Yeager, 2004). These could indicate a stronger global meridional overturning circulation in the long-term future under anthropogenic climate warming.

Significant changes in the ACC at glacial-interglacial timescale prevailed in the north of PF (this study, chapter 4) as well as the northern SAF (Lamy *et al.*, 2015; Roberts *et al.*, 2017), compared to small variations in the Scotia Sea transect–most of samples are located in the south of PF (McCave *et al.*, 2014). The oceanic frontal system is plausibly responsible for different amplitudes of ACC changes. The next step is to reconstruct the ACC past changes across a latitudinal transect in the Drake Passage (Fig. 7.1) and to provide a relatively comprehensive history of the ACC and Drake Passage throughflow. Resolving past changes in the ACC through the Drake Passage is crucial for advancing our understanding of the Southern Ocean's impact on ocean circulation and climate change. This will shed new light on ongoing and future anthropogenic climate change.

With respect to water masses sourcing in the Pacific sector of Southern Ocean, it became evident that the proportion of Pacific-derived water increased during the glacial periods at expense of the North Atlantic-derived water. However, more radiogenic Nd signatures (εNd = -2.5~-4.0) during the LGM and PGM have not been resolved in the other sectors of the Southern Ocean. Future work is required to better constrain the water masses exchange between the Pacific with the Southern Ocean. For this purpose, additional high-resolution data from the southeast Pacific could help to explore such exchange in more detail. This could improve our understanding of the interaction between the Pacific Ocean and the Southern Ocean, and hence the structure of the global overturning circulation.

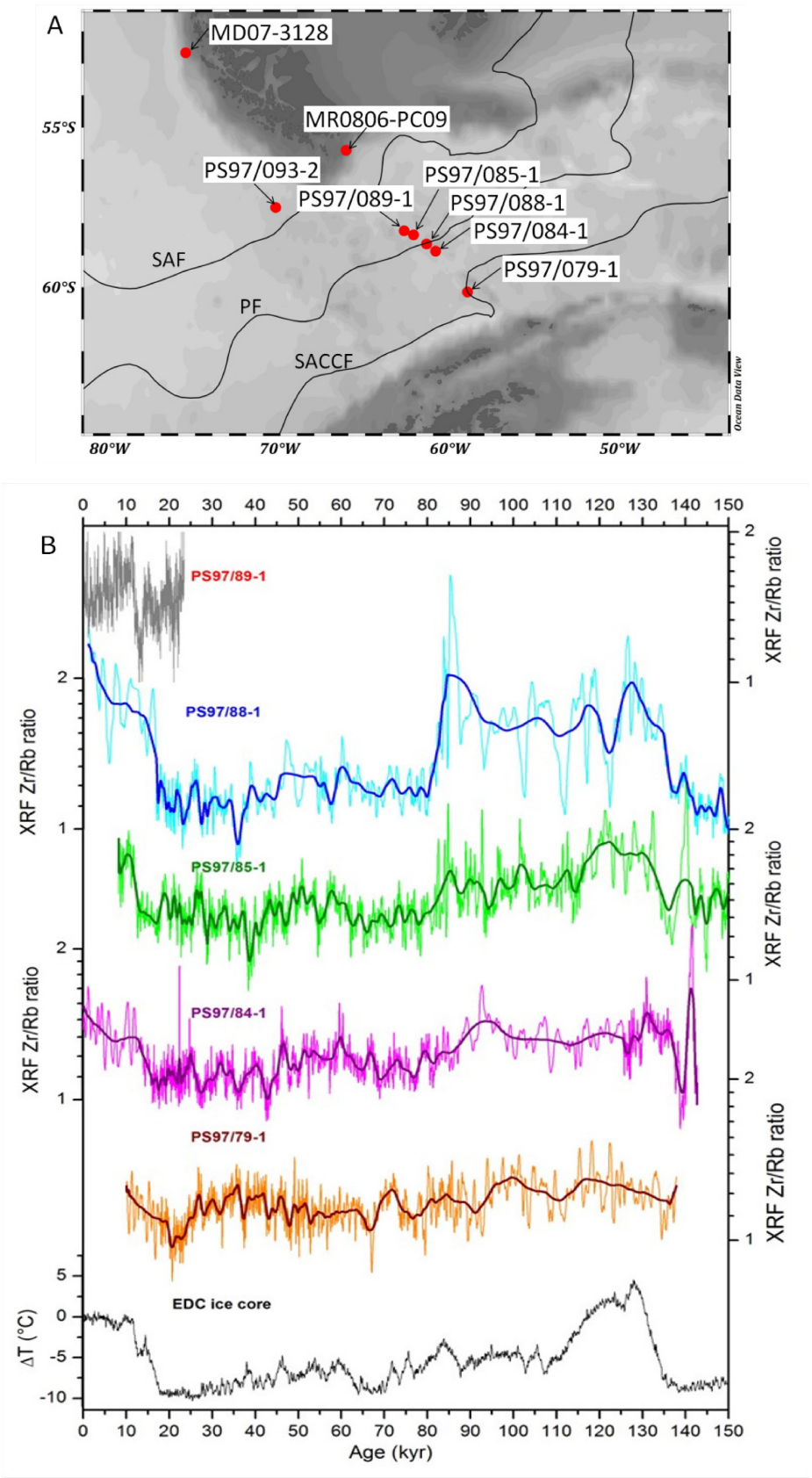

Fig. 7.1. Reconstruction of the ACC past changes across a latitudinal transect in the Drake Passage. A, Locations of sediment cores (Lamy, 2016; Lamy *et al.*, 2015). B, Preliminary results for the ACC past changes based on Zr/Rb ratios with preliminary age model (Lamy, 2016).

8 References

Abouchami, W., Goldstein, S., Gazer, S., Eisenhauer, A., Mangini, A., 1997. Secular changes of lead and neodymium in central Pacific seawater recorded by a Fe-Mn crust. Geochimica Et Cosmochimica Acta 61 (18), 3957-3974, doi:10.1016/S0016-7037(97)00218-4.

Abouchami, W., Goldstein, S.L., 1995. A lead isotopic study of circum-antarctic manganese nodules. Geochimica Et Cosmochimica Acta 59 (9), 1809-1820, doi:10.1016/0016-7037(95)00084-D.

Allison, L.C., Johnson, H.L., Marshall, D.P., Munday, D.R., 2010. Where do winds drive the Antarctic Circumpolar Current? Geophysical Research Letters 37 (12), doi:10.1029/2010gl043355.

Amakawa, H., Sasaki, K., Ebihara, M., 2009. Nd isotopic composition in the central North Pacific. Geochimica Et Cosmochimica Acta 73 (16), 4705-4719, doi:10.1016/j.gca.2009.05.058.

Amblas, D., Urgeles, R., Canals, M., Calafat, A.M., Rebesco, M., Camerlenghi, A., Estrada, F., De Batist, M., Hughes-Clarke, J.E., 2006. Relationship between continental rise development and palaeo-ice sheet dynamics, Northern Antarctic Peninsula Pacific margin. Quaternary Science Reviews 25 (9), 933-944, doi:10.1016/j.quascirev.2005.07.012.

Andersen, K.K., Azuma, N., Barnola, J.-M., Bigler, M., Biscaye, P., Caillon, N., Chappellaz, J., Clausen, H.B., Dahl-Jensen, D., Fischer, H., 2004. High-resolution record of Northern Hemisphere climate extending into the last interglacial period. Nature 431 (7005), 147-151, doi:10.1038/nature02805.

Anderson, R.F., Ali, S., Bradtmiller, L.I., Nielsen, S.H., Fleisher, M.Q., Anderson, B.E., Burckle, L.H., 2009. Wind-driven upwelling in the Southern Ocean and the deglacial rise in atmospheric CO2. Science 323 (5920), 1443-1448, doi: 10.1126/science.1167441.

Antoniades, D., Giralt, S., Geyer, A., Álvarez-Valero, A.M., Pla-Rabes, S., Granados, I., Liu, E.J., Toro, M., Smellie, J.L., Oliva, M., 2018. The timing and widespread effects of the largest Holocene volcanic eruption in Antarctica. Scientific Reports 8 (1), 17279, doi:10.1038/s41598-018-35460-x.

Arz, H.W., Lamy, F., Pätzold, J., Müller, P.J., Prins, M., 2003. Mediterranean moisture source for an early-Holocene humid period in the northern Red Sea. Science 300 (5616), 118-121, doi: 10.1126/science.1080325.

Bahr, A., Jiménez-Espejo, F.J., Kolasinac, N., Grunert, P., Hernández-Molina, F.J., Röhl, U., Voelker, A.H.L., Escutia, C., Stow, D.A.V., Hodell, D., Alvarez-Zarikian, C.A., 2014. Deciphering bottom current velocity and paleoclimate signals from contourite deposits in the Gulf of Cádiz during the last 140 kyr: An inorganic geochemical approach. Geochemistry, Geophysics, Geosystems 15 (8), 3145-3160, doi:10.1002/2014gc005356.

Barbeau, D.L., Olivero, E.B., Swanson-Hysell, N.L., Zahid, K.M., Murray, K.E., Gehrels, G.E., 2009. Detrital-zircon geochronology of the eastern Magallanes foreland basin: Implications for Eocene kinematics of the northern Scotia Arc and Drake Passage. Earth and Planetary Science Letters 284 (3), 489-503, doi:10.1016/j.epsl.2009.05.014.

Barker, P., 1982. The Cenozoic subduction history of the Pacific margin of the Antarctic Peninsula: ridge crest–trench interactions. Journal of the Geological Society 139 (6), 787-801, doi:10.1144/gsjgs.139.6.0787.

Barker, P., Burrell, J., 1977. The opening of Drake passage. Marine Geology 25 (1-3), 15-34, doi:10.1016/0025-3227(77)90045-7.

Barker, P.F., Dalziel, I., Storey, B., 1991. Tectonic development of the Scotia Arc region. In: Tingey, R.J. (Ed.) The geology of Antarctica. Clarendon Press, Oxford, pp. 215-248.

Barker, P.F., Filippelli, G.M., Florindo, F., Martin, E.E., Scher, H.D., 2007. Onset and role of the Antarctic Circumpolar Current. Deep Sea Research Part II: Topical Studies in Oceanography 54 (21-22), 2388-2398, doi:10.1016/j.dsr2.2007.07.028.

Barré, N., Provost, C., Renault, A., Sennéchael, N., 2011. Fronts, meanders and eddies in Drake Passage during the ANT-XXIII/3 cruise in January–February 2006: A satellite perspective. Deep Sea Research Part II: Topical Studies in Oceanography 58 (25), 2533-2554, doi:10.1016/j.dsr2.2011.01.003.

Bartels, M., Titschack, J., Fahl, K., Stein, R., Seidenkrantz, M.S., Hillaire-Marcel, C., Hebbeln, D., 2017. Atlantic Water advection vs. glacier dynamics in northern Spitsbergen since early deglaciation. Clim. Past 13 (12), 1717-1749, doi:10.5194/cp-13-1717-2017.

Basak, C., Fröllje, H., Lamy, F., Gersonde, R., Benz, V., Anderson, R.F., Molina-Kescher, M., Pahnke, K., 2018. Breakup of last glacial deep stratification in the South Pacific. Science 359 (6378), 900-904, doi:10.1126/science.aao2473.

Basak, C., Pahnke, K., Frank, M., Lamy, F., Gersonde, R., 2015. Neodymium isotopic characterization of Ross Sea Bottom Water and its advection through the southern South Pacific. Earth and Planetary Science Letters 419, 211-221, doi:10.1016/j.epsl.2015.03.011.

Beal, L.M., De Ruijter, W.P.M., Biastoch, A., Zahn, R., Grp, S.W.I.W., 2011. On the role of the Agulhas system in ocean circulation and climate. Nature 472 (7344), 429-436, doi:10.1038/nature09983.

Benson, L., Liddicoat, J., Smoot, J., Sarna-Wojcicki, A., Negrini, R., Lund, S., 2003. Age of the Mono Lake excursion and associated tephra. Quaternary Science Reviews 22 (2), 135-140, doi:10.1016/S0277-3791(02)00249-4.

Bianchi, G., Hall, I.R., McCave, I., Joseph, L., 1999. Measurement of the sortable silt current speed proxy using the Sedigraph 5100 and Coulter Multisizer IIe: Precision and accuracy. Sedimentology 46 (6), 1001-1014, doi:10.1046/j.1365-3091.1999.00256.x.

Biscaye, P.E., 1965. Mineralogy and sedimentation of recent deep-sea clay in the Atlantic Ocean and adjacent seas and oceans. Geological Society of America Bulletin 76 (7), 803-832, doi:10.1130/0016-7606(1965)76[803:MASORD]2.0.CO;2.

Blaauw, M., Christen, J.A., 2011. Flexible paleoclimate age-depth models using an autoregressive gamma process. Bayesian analysis 6 (3), 457-474, doi:10.1214/11-BA618.

Blaser, P., Lippold, J., Gutjahr, M., Frank, N., Link, J.M., Frank, M., 2016. Extracting foraminiferal seawater Nd isotope signatures from bulk deep sea sediment by chemical leaching. Chemical Geology 439, 189-204, doi:10.1016/j.chemgeo.2016.06.024.

Blaser, P., Pöppelmeier, F., Schulz, H., Gutjahr, M., Frank, M., Lippold, J., Heinrich, H., Link, J.M., Hoffmann, J., Szidat, S., Frank, N., 2019. The resilience and sensitivity of Northeast Atlantic deep water εNd to overprinting by detrital fluxes over the past 30,000 years. Geochimica Et Cosmochimica Acta 245, 79-97, doi:10.1016/j.gca.2018.10.018.

Bohm, E., Lippold, J., Gutjahr, M., Frank, M., Blaser, P., Antz, B., Fohlmeister, J., Frank, N., Andersen, M.B., Deininger, M., 2015. Strong and deep Atlantic meridional overturning circulation during the last glacial cycle. Nature 517 (7532), 73-76, doi:10.1038/nature14059.

Boisvert, W.E., 1969. Major currents off the west coasts of North and South America [R]. Naval oceanographic office NSTL station MS, pp. 16-19.

Bollhöfer, A., Rosman, K.J.R., 2000. Isotopic source signatures for atmospheric lead: the Southern Hemisphere. Geochimica Et Cosmochimica Acta 64 (19), 3251-3262, doi:10.1016/S0016-7037(00)00436-1.

Bond, G., Heinrich, H., Broecker, W., Labeyrie, L., McManus, J., Andrews, J., Huon, S., Jantschik, R., Clasen, S., Simet, C., Tedesco, K., Klas, M., Bonani, G., Ivy, S., 1992. Evidence for massive discharges of icebergs into the North Atlantic ocean during the last glacial period. Nature 360 (6401), 245-249, doi：10.1038/360245a0.

Bostock, H.C., Sutton, P.J., Williams, M.J.M., Opdyke, B.N., 2013. Reviewing the circulation and mixing of Antarctic Intermediate Water in the South Pacific using evidence from geochemical tracers and Argo float trajectories. Deep-Sea Research Part I-Oceanographic Research Papers 73, 84-98, doi：10.1016/j.dsr.2012.11.007.

Bridgestock, L., van de Flierdt, T., Rehkämper, M., Paul, M., Middag, R., Milne, A., Lohan, M.C., Baker, A.R., Chance, R., Khondoker, R., Strekopytov, S., Humphreys-Williams, E., Achterberg, E.P., Rijkenberg, M.J.A., Gerringa, L.J.A., de Baar, H.J.W., 2016. Return of naturally sourced Pb to Atlantic surface waters. Nature communications 7 (1), 12921, doi：10.1038/ncomms12921.

Brindley, G., Brown, G., 1980. Quantitative X-ray mineral analysis of clays. In: Crystal structures of clay minerals and their X-ray identification, pp. 411-438.

Burton-Johnson, A., Riley, T., 2015. Autochthonous v. accreted terrane development of continental margins: a revised in situ tectonic history of the Antarctic Peninsula. Journal of the Geological Society 172 (6), 822-835, doi：10.1144/jgs2014-110.

Cárdenas, P., Lange, C.B., Vernet, M., Esper, O., Srain, B., Vorrath, M.-E., Ehrhardt, S., Müller, J., Kuhn, G., Arz, H.W., 2018. Biogeochemical proxies and diatoms in surface sediments across the Drake Passage reflect oceanic domains and frontal systems in the region. Progress in Oceanography, doi：10.1016/j.pocean.2018.10.004.

Caley, T., Peeters, F.J., Biastoch, A., Rossignol, L., Sebille, E., Durgadoo, J., Malaizé, B., Giraudeau, J., Arthur, K., Zahn, R., 2014. Quantitative estimate of the paleo‐Agulhas leakage. Geophysical Research Letters 41 (4), 1238-1246, doi：10.1002/2014GL059278.

Camilión, M.C., 1993. Clay mineral composition of pampean loess (Argentina). Quaternary International 17, 27-31, doi：10.1016/1040-6182(93)90077-S.

Campbell, J.S., Clark, D.L., 1977. Pleistocene turbidites of the Canada abyssal plain of the Arctic Ocean. Journal of Sedimentary Research 47 (2), 657-670, doi：10.1306/212f7211-2b24-11d7-8648000102c1865d.

Caniupan, M., Lamy, F., Lange, C.B., Kaiser, J., Arz, H., Kilian, R., Urrea, O.B., Aracena, C., Hebbeln, D., Kissel, C., Laj, C., Mollenhauer, G., Tiedemann, R., 2011. Millennial-scale sea surface temperature and Patagonian Ice Sheet changes off southernmost Chile (53 degrees S) over the past similar to 60 kyr. Paleoceanography 26, doi：10.1029/2010pa002049.

Chaigneau, A., Pizarro, O., 2005. Surface circulation and fronts of the South Pacific Ocean, east of 120° W. Geophysical Research Letters 32 (8), doi：10.1029/2004gl022070.

Chamley, H., 1989. Clay Sorting and Settling in tbe Ocean. In: Clay sedimentology. Springer-Verkag Berlin Heidelberg, Germany, pp. 117-130.

Charles, C.D., Pahnke, K., Zahn, R., Mortyn, P.G., Ninnemann, U., Hodell, D.A., 2010. Millennial scale evolution of the Southern Ocean chemical divide. Quaternary Science Reviews 29 (3), 399-409, doi：10.1016/j.quascirev.2009.09.021.

Chen, J., Chen, Y., Liu, L.W., Ji, J.F., Balsam, W., Sun, Y.B., Lu, H.Y., 2006. Zr/Rb ratio in the Chinese loess sequences and its implication for changes in the East Asian winter monsoon strength. Geochimica Et Cosmochimica Acta 70 (6), 1471-1482, doi：10.1016/j.gca.2005.11.029.

Chen, J.H., Wasserburg, G.J., 1986. Formation ages and evolution of Shergotty and its parent planet

from U-Th-Pb systematics. Geochimica Et Cosmochimica Acta 50 (6), 955-968, doi:10.1016/0016-7037(86)90376-5.

Chidichimo, M.P., Donohue, K.A., Watts, D.R., Tracey, K.L., 2014. Baroclinic transport time series of the Antarctic Circumpolar Current measured in Drake Passage. Journal of Physical Oceanography 44 (7), 1829-1853, doi:10.1175/JPO-D-13-071.1.

Christo, B., Andreas, S., 2015. Southern Ocean control of glacial AMOC stability and Dansgaard‐Oeschger interstadial duration. Paleoceanography 30 (12), 1595-1612, doi:10.1002/2015PA002795.

Clapperton, C.M., 1993. Quaternary geology and geomorphology of South America. Elsevier Amsterdam etc.

Crocket, K.C., Vance, D., Foster, G.L., Richards, D.A., Tranter, M., 2012. Continental weathering fluxes during the last glacial/interglacial cycle: insights from the marine sedimentary Pb isotope record at Orphan Knoll, NW Atlantic. Quaternary Science Reviews 38, 89-99, doi:10.1016/j.quascirev.2012.02.004.

Cunningham, S., Alderson, S., King, B., Brandon, M., 2003. Transport and variability of the Antarctic circumpolar current in drake passage. Journal of Geophysical Research: Oceans 108 (C5), doi:10.1029/2001JC001147.

Curry, W.B., Oppo, D.W., 2005. Glacial water mass geometry and the distribution of δ13C of ΣCO2 in the western Atlantic Ocean. Paleoceanography 20 (1), doi:10.1029/2004pa001021.

Dalziel, I.W., de Wit, M.J., Palmer, K.F., 1974. Fossil marginal basin in the southern Andes. Nature 250, 291-294, doi:10.1038/250291a0.

Davies, B.J., Darvill, C.M., Lovell, H., Bendle, J.M., Dowdeswell, J.A., Fabel, D., García, J.-L., Geiger, A., Glasser, N.F., Gheorghiu, D.M., Harrison, S., Hein, A.S., Kaplan, M.R., Martin, J.R.V., Mendelova, M., Palmer, A., Pelto, M., Rodés, Á., Sagredo, E.A., Smedley, R.K., Smellie, J.L., Thorndycraft, V.R., 2020. The evolution of the Patagonian Ice Sheet from 35 ka to the present day (PATICE). Earth-Science Reviews 204, 103152, doi:10.1016/j.earscirev.2020.103152.

Dearing, J.A., 1994. Environmental magnetic susceptibility: using the Bartington MS2 system. doi:https://www.bartington.com/wp-content/uploads/pdfs/operation_manuals/MS2_Handbook_OM0409.pdf.

Diekmann, B., Fütterer, D., Grobe, H., Hillenbrand, C., Kuhn, G., Michels, K., Petschick, R., Pirrung, M., 2003. Terrigenous sediment supply in the polar to temperate South Atlantic: Land-ocean links of environmental changes during the late Quaternary. In: The South Atlantic in the Late Quaternary. Springer, Berlin, Heidelberg., pp. 375-399.

Diekmann, B., Kuhn, G., 1999. Provenance and dispersal of glacial–marine surface sediments in the Weddell Sea and adjoining areas, Antarctica: ice-rafting versus current transport. Marine Geology 158 (1), 209-231, doi:10.1016/S0025-3227(98)00165-0.

Diekmann, B., Kuhn, G., Rachold, V., Abelmann, A., Brathauer, U., Futterer, D.K., Gersonde, R., Grobe, H., 2000. Terrigenous sediment supply in the Scotia Sea (Southern Ocean): response to Late Quaternary ice dynamics in Patagonia and on the Antarctic Peninsula. Palaeogeography Palaeoclimatology Palaeoecology 162 (3-4), 357-387, doi:10.1016/S0031-0182(00)00138-3.

Donohue, K., Tracey, K., Watts, D., Chidichimo, M., Chereskin, T., 2016. Mean Antarctic Circumpolar Current transport measured in Drake Passage. Geophysical Research Letters 43 (22), doi:10.1002/2016GL070319.

Drouin, K.L., Lozier, M.S., 2019. The Surface Pathways of the South Atlantic: Revisiting the Cold and

Warm Water Routes Using Observational Data. Journal of Geophysical Research: Oceans 124 (10), 7082-7103, doi:10.1029/2019jc015267.

Du, J., Haley, B.A., Mix, A.C., 2016. Neodymium isotopes in authigenic phases, bottom waters and detrital sediments in the Gulf of Alaska and their implications for paleo-circulation reconstruction. Geochimica Et Cosmochimica Acta 193, 14-35, doi:10.1016/j.gca.2016.08.005.

Du, J., Haley, B.A., Mix, A.C., Walczak, M.H., Praetorius, S.K., 2018. Flushing of the deep Pacific Ocean and the deglacial rise of atmospheric CO2 concentrations. Nature Geoscience 11 (10), 749-755, doi:10.1038/s41561-018-0205-6.

Dypvik, H., Harris, N.B., 2001. Geochemical facies analysis of fine-grained siliciclastics using Th/U, Zr/Rb and (Zr+Rb)/Sr ratios. Chemical Geology 181 (1), 131-146, doi:10.1016/S0009-2541(01)00278-9.

Eagles, G., Livermore, R., Morris, P., 2006. Small basins in the Scotia Sea: The Eocene Drake Passage gateway. Earth and Planetary Science Letters 242 (3), 343-353, doi:10.1016/j.epsl.2005.11.060.

Ehrmann, W.U., Melles, M., Kuhn, G., Grobe, H., 1992. Significance of clay mineral assemblages in the Antarctic Ocean. Marine Geology 107 (4), 249-273, doi:10.1016/0025-3227(92)90075-S.

Elliot, D.H., 1997. The Planar Crest of Graham Land, Northern Antarctic Peninsula: Possible Origins and Timing of Uplift. Geology and Seismic Stratigraphy of the Antarctic Margin, 2, pp. 51-73.

EPICA Community Members, 2006. One-to-one coupling of glacial climate variability in Greenland and Antarctica. Nature 444 (7116), 195-198, doi: 10.1038/nature05301.

Esquevin, J., 1969. Influence de la composition chimique des illites sur leur cristallinité. Bull. Centre Rech. Pau-SNPA 3 (1), 147-153.

Ferrari, R., Jansen, M.F., Adkins, J.F., Burke, A., Stewart, A.L., Thompson, A.F., 2014. Antarctic sea ice control on ocean circulation in present and glacial climates. Proceedings of the National Academy of Sciences 111 (24), 8753-8758, doi: 10.1073/pnas.1323922111.

Fischer, H., Fundel, F., Ruth, U., Twarloh, B., Wegner, A., Udisti, R., Becagli, S., Castellano, E., Morganti, A., Severi, M., Wolff, E., Littot, G., Röthlisberger, R., Mulvaney, R., Hutterli, M.A., Kaufmann, P., Federer, U., Lambert, F., Bigler, M., Hansson, M., Jonsell, U., de Angelis, M., Boutron, C., Siggaard-Andersen, M.-L., Steffensen, J.P., Barbante, C., Gaspari, V., Gabrielli, P., Wagenbach, D., 2007. Reconstruction of millennial changes in dust emission, transport and regional sea ice coverage using the deep EPICA ice cores from the Atlantic and Indian Ocean sector of Antarctica. Earth and Planetary Science Letters 260 (1-2), 340-354, doi: 10.1016/j.epsl.2007.06.014.

Foster, G.L., Vance, D., Prytulak, J., 2007. No change in the neodymium isotope composition of deep water exported from the North Atlantic on glacial-interglacial time scales. Geology 35 (1), 37-40, doi:10.1130/g23204a.1.

Fröllje, H., Pahnke, K., Schnetger, B., Brumsack, H.-J., Dulai, H., Fitzsimmons, J.N., 2016. Hawaiian imprint on dissolved Nd and Ra isotopes and rare earth elements in the central North Pacific: Local survey and seasonal variability. Geochimica Et Cosmochimica Acta 189, 110-131, doi:10.1016/j.gca.2016.06.001.

Fralick, P.W., Kronberg, B.I., 1997. Geochemical discrimination of clastic sedimentary rock sources. Sedimentary Geology 113 (1), 111-124, doi:10.1016/S0037-0738(97)00049-3.

Frank, M., 2002. RADIOGENIC ISOTOPES: TRACERS OF PAST OCEAN CIRCULATION AND EROSIONAL INPUT. Reviews of Geophysics 40 (1), 1-1-1-38, doi:10.1029/2000rg000094.

Garcia, H.E., Boyer, T.P., Locarnini, R.A., Antonov, J.I., Mishonov, A.V., Baranova, O.K., Zweng,

M.M., Reagan, J.R., Johnson, D.R., Levitus, S., 2013. World ocean atlas 2013. Volume 3, Dissolved oxygen, apparent oxygen utilization, and oxygen saturation. doi:10.7289/V5XG9P2W.

Gardner, W.D., Richardson, M.J., Mishonov, A.V., 2018. Global assessment of benthic nepheloid layers and linkage with upper ocean dynamics. Earth and Planetary Science Letters 482, 126-134, doi:10.1016/j.epsl.2017.11.008.

Gersonde, R., Crosta, X., Abelmann, A., Armand, L., 2005. Sea-surface temperature and sea ice distribution of the Southern Ocean at the EPILOG Last Glacial Maximum—a circum-Antarctic view based on siliceous microfossil records. Quaternary Science Reviews 24 (7–9), 869-896, doi:10.1016/j.quascirev.2004.07.015.

Goodell, H., 1965. Marine geology, USNS Eltanin cruises 9-15. Sedimentol. Research Lab. contribution No. 11, Department of geology, Florida State University 7, 1-35, doi:http://www.arf.fsu.edu/publications/documents/ELT_09_15.pdf.

Gordon, A.L., 1986. Interocean exchange of thermocline water. Journal of Geophysical Research: Oceans 91 (C4), 5037-5046, doi:10.1029/JC091iC04p05037.

Gottschalk, J., Skinner, L.C., Jaccard, S.L., Menviel, L., Nehrbass-Ahles, C., Waelbroeck, C., 2020. Southern Ocean link between changes in atmospheric CO2 levels and northern-hemisphere climate anomalies during the last two glacial periods. Quaternary Science Reviews 230, 106067, doi:10.1016/j.quascirev.2019.106067.

Gottschalk, J., Skinner, L.C., Misra, S., Waelbroeck, C., Menviel, L., Timmermann, A., 2015. Abrupt changes in the southern extent of North Atlantic Deep Water during Dansgaard–Oeschger events. Nature Geoscience 8 (12), 950, doi:10.1038/ngeo2558.

Govin, A., Holzwarth, U., Heslop, D., Ford Keeling, L., Zabel, M., Mulitza, S., Collins, J.A., Chiessi, C.M., 2012. Distribution of major elements in Atlantic surface sediments (36°N–49°S): Imprint of terrigenous input and continental weathering. Geochemistry, Geophysics, Geosystems 13 (1), doi:10.1029/2011gc003785.

Grant, K.M., Rohling, E.J., Bar-Matthews, M., Ayalon, A., Medina-Elizalde, M., Ramsey, C.B., Satow, C., Roberts, A.P., 2012. Rapid coupling between ice volume and polar temperature over the past 150,000 years. Nature 491 (7426), 744-747, doi:10.1038/nature11593.

Griffin, J.J., Windom, H., Goldberg, E.D., 1968. The distribution of clay minerals in the World Ocean. Deep Sea Research and Oceanographic Abstracts 15 (4), 433-459, doi:10.1016/0011-7471(68)90051-X.

Grobe, H., 2007. Profile through the Drake Passage. Own work, doi:https://en.wikipedia.org/wiki/Drake_Passage#/media/File:Drake-Passage_profile_hg.png.

Gutjahr, M., Frank, M., Stirling, C.H., Klemm, V., van de Flierdt, T., Halliday, A.N., 2007. Reliable extraction of a deepwater trace metal isotope signal from Fe–Mn oxyhydroxide coatings of marine sediments. Chemical Geology 242 (3), 351-370, doi:10.1016/j.chemgeo.2007.03.021.

Hain, M.P., Sigman, D.M., Haug, G.H., 2010. Carbon dioxide effects of Antarctic stratification, North Atlantic Intermediate Water formation, and subantarctic nutrient drawdown during the last ice age: Diagnosis and synthesis in a geochemical box model. Global Biogeochemical Cycles 24 (4), doi:10.1029/2010gb003790.

Hall, I.R., McCave, I.N., Shackleton, N.J., Weedon, G.P., Harris, S.E., 2001. Intensified deep Pacfic inflow and ventilation in Pleistocene glacial times. Nature 412 (6849), 809-812, doi:10.1038/35090552.

Hatfield, R.G., Stoner, J.S., Carlson, A.E., Reyes, A.V., Housen, B.A., 2013. Source as a controlling

factor on the quality and interpretation of sediment magnetic records from the northern North Atlantic. Earth and Planetary Science Letters 368, 69-77, doi:10.1016/j.epsl.2013.03.001.

Haug, G.H., Hughen, K.A., Sigman, D.M., Peterson, L.C., Rohl, U., 2001. Southward migration of the intertropical convergence zone through the Holocene. Science 293 (5533), 1304-1308, doi:DOI 10.1126/science.1059725.

Hemming, S.L.G.a.S.R., 2003. Long-lived Isotopic Tracers in Oceanography, Paleoceanography, and Ice-sheet Dynamics. doi:10.1016/B0-08-043751-6/06179-X.

Hemming, S.R., van de Flierdt, T., Goldstein, S.L., Franzese, A.M., Roy, M., Gastineau, G., Landrot, G., 2007. Strontium isotope tracing of terrigenous sediment dispersal in the Antarctic Circumpolar Current: Implications for constraining frontal positions. Geochemistry, Geophysics, Geosystems 8 (6), doi:10.1029/2006gc001441.

Henderson, G.M., Maier-Reimer, E., 2002. Advection and removal of 210Pb and stable Pb isotopes in the oceans: a general circulation model study. Geochimica Et Cosmochimica Acta 66 (2), 257-272, doi:10.1016/S0016-7037(01)00779-7.

Henry, L.G., McManus, J.F., Curry, W.B., Roberts, N.L., Piotrowski, A.M., Keigwin, L.D., 2016. North Atlantic ocean circulation and abrupt climate change during the last glaciation. Science 353 (6298), 470-474, doi:10.1126/science.aaf5529.

Herguera, J.C., Jansen, E., Berger, W.H., 1992. Evidence for a bathyal front at 2000-M depth in the glacial Pacific, based on a depth transect on Ontong Java Plateau. Paleoceanography 7 (3), 273-288, doi:10.1029/92pa00869.

Hernández-Molina, F.J., Larter, R.D., Maldonado, A., 2017. Neogene to Quaternary stratigraphic evolution of the Antarctic Peninsula, Pacific Margin offshore of Adelaide Island: Transitions from a non-glacial, through glacially-influenced to a fully glacial state. Global and Planetary Change 156, 80-111, doi:10.1016/j.gloplacha.2017.07.002.

Hillaire-Marcel, C., De Vernal, A., 2007. Proxies in Late Cenozoic Paleoceanography. Elsevier.

Hillenbrand, C.-D., Ehrmann, W., Larter, R.D., Benetti, S., Dowdeswell, J., Cofaigh, C.Ó., Graham, A.G., Grobe, H., 2009. Clay mineral provenance of sediments in the southern Bellingshausen Sea reveals drainage changes of the West Antarctic Ice Sheet during the Late Quaternary. Marine Geology 265 (1), 1-18, doi:10.1016/j.margeo.2009.06.009.

Hillenbrand, C.-D., Grobe, H., Diekmann, B., Kuhn, G., Fütterer, D.K., 2003. Distribution of clay minerals and proxies for productivity in surface sediments of the Bellingshausen and Amundsen seas (West Antarctica)–Relation to modern environmental conditions. Marine Geology 193 (3), 253-271, doi:10.1016/S0025-3227(02)00659-X.

Hillenbrand, C.-D., Moreton, S., Caburlotto, A., Pudsey, C., Lucchi, R., Smellie, J., Benetti, S., Grobe, H., Hunt, J., Larter, R., 2008. Volcanic time-markers for Marine Isotopic Stages 6 and 5 in Southern Ocean sediments and Antarctic ice cores: implications for tephra correlations between palaeoclimatic records. Quaternary Science Reviews 27 (5), 518-540, doi:10.1016/j.quascirev.2007.11.009.

Hodell, D.A., Venz, K.A., Charles, C.D., Ninnemann, U.S., 2003. Pleistocene vertical carbon isotope and carbonate gradients in the South Atlantic sector of the Southern Ocean. Geochemistry, Geophysics, Geosystems 4 (1), 1-19, doi:10.1029/2002gc000367.

Hu, R., Piotrowski, A.M., 2018. Neodymium isotope evidence for glacial-interglacial variability of deepwater transit time in the Pacific Ocean. Nature communications 9 (1), 4709, doi:10.1038/s41467-018-07079-z.

Huang, H., Gutjahr, M., Eisenhauer, A., Kuhn, G., 2020. No detectable Weddell Sea Antarctic Bottom Water export during the Last and Penultimate Glacial Maximum. Nature communications 11 (1), 1-10, doi:10.1038/s41467-020-14302-3.

Itambi, A.C., von Dobeneck, T., Mulitza, S., Bickert, T., Heslop, D., 2009. Millennial-scale northwest African droughts related to Heinrich events and Dansgaard-Oeschger cycles: Evidence in marine sediments from offshore Senegal. Paleoceanography 24 (1), doi:10.1029/2007pa001570.

Ito, A., Wagai, R., 2017. Global distribution of clay-size minerals on land surface for biogeochemical and climatological studies. Scientific Data 4, 170103, doi:10.1038/sdata.2017.103.

Jaccard, S.L., Galbraith, E.D., Martínez-García, A., Anderson, R.F., 2016. Covariation of deep Southern Ocean oxygenation and atmospheric CO 2 through the last ice age. Nature 530 (7589), 207, doi: 10.1038/nature16514.

Jaccard, S.L., Hayes, C.T., Martinez-Garcia, A., Hodell, D.A., Anderson, R.F., Sigman, D.M., Haug, G.H., 2013. Two modes of change in Southern Ocean productivity over the past million years. Science 339 (6126), 1419-1423, doi:10.1126/science.1227545.

Jeandel, C., Arsouze, T., Lacan, F., Téchiné, P., Dutay, J.C., 2007. Isotopic Nd compositions and concentrations of the lithogenic inputs into the ocean: A compilation, with an emphasis on the margins. Chemical Geology 239 (1), 156-164, doi:10.1016/j.chemgeo.2006.11.013.

Jess F. Adkins, 2002. The Salinity, Temperature, and δ18O of the Glacial Deep Ocean. Science.

Jonkers, L., Zahn, R., Thomas, A., Henderson, G., Abouchami, W., François, R., Masque, P., Hall, I.R., Bickert, T., 2015. Deep circulation changes in the central South Atlantic during the past 145 kyrs reflected in a combined 231 Pa/ 230 Th, Neodymium isotope and benthic δ13C record. Earth and Planetary Science Letters 419, 14-21, doi:10.1016/j.epsl.2015.03.004.

Jouzel, J., Masson-Delmotte, V., Cattani, O., Dreyfus, G., Falourd, S., Hoffmann, G., Minster, B., Nouet, J., Barnola, J.M., Chappellaz, J., Fischer, H., Gallet, J.C., Johnsen, S., Leuenberger, M., Loulergue, L., Luethi, D., Oerter, H., Parrenin, F., Raisbeck, G., Raynaud, D., Schilt, A., Schwander, J., Selmo, E., Souchez, R., Spahni, R., Stauffer, B., Steffensen, J.P., Stenni, B., Stocker, T.F., Tison, J.L., Werner, M., Wolff, E.W., 2007. Orbital and millennial Antarctic climate variability over the past 800,000 years. Science 317 (5839), 793-796, doi:10.1126/science.1141038.

Kaplan, M.R., Douglass, D.C., Singer, B.S., Ackert, R.P., Caffee, M.W., 2005. Cosmogenic nuclide chronology of pre-last glacial maximum moraines at Lago Buenos Aires, 46°S, Argentina. Quaternary Research 63 (3), 301-315, doi:10.1016/j.yqres.2004.12.003.

Kilian, R., Lamy, F., 2012. A review of Glacial and Holocene paleoclimate records from southernmost Patagonia (49–55°S). Quaternary Science Reviews 53, 1-23, doi:10.1016/j.quascirev.2012.07.017.

Kirschvink, J.L., 1980. The least-squares line and plane and the analysis of palaeomagnetic data. Geophysical Journal International 62 (3), 699-718, doi:10.1111/j.1365-246X.1980.tb02601.x.

Kissel, C., Laj, C., Mulder, T., Wandres, C., Cremer, M., 2009. The magnetic fraction: A tracer of deep water circulation in the North Atlantic. Earth and Planetary Science Letters 288 (3-4), 444-454, doi:10.1016/j.epsl.2009.10.005.

Kissel, C., Van Toer, A., Laj, C., Cortijo, E., Michel, E., 2013. Variations in the strength of the North Atlantic bottom water during Holocene. Earth and Planetary Science Letters 369-370, 248-259, doi:10.1016/j.epsl.2013.03.042.

Knorr, G., Lohmann, G., 2003. Southern Ocean origin for the resumption of Atlantic thermohaline

circulation during deglaciation. Nature 424 (6948), 532, doi: 10.1038/nature01855.

Koenig, Z., Provost, C., Ferrari, R., Sennéchael, N., Rio, M.-H., 2014. Volume transport of the Antarctic Circumpolar Current: Production and validation of a 20 year long time series obtained from in situ and satellite observations. Journal of Geophysical Research: Oceans 119 (8), 5407-5433, doi: 10.1002/2014JC009966.

Kohfeld, K.E., Graham, R.M., de Boer, A.M., Sime, L.C., Wolff, E.W., Le Quere, C., Bopp, L., 2013. Southern Hemisphere westerly wind changes during the Last Glacial Maximum: paleo-data synthesis. Quaternary Science Reviews 68, 76-95, doi: 10.1016/j.quascirev.2013.01.017.

Kuhlbrodt, T., Griesel, A., Montoya, M., Levermann, A., Hofmann, M., Rahmstorf, S., 2007. On the driving processes of the Atlantic meridional overturning circulation. Reviews of Geophysics 45 (2), doi: 10.1029/2004rg000166.

Kuhn, G., 2013. Don't forget the salty soup: Calculations for bulk marine geochemistry and radionuclide geochronology. Mineralogical Magazine 77 (5), 1519, doi: 10.1180/minmag.2013.077.5.11.

Kuhn, G., Diekmann, B., 2002. Late Quaternary variability of ocean circulation in the southeastern South Atlantic inferred from the terrigenous sediment record of a drift deposit in the southern Cape Basin (ODP Site 1089). Palaeogeography Palaeoclimatology Palaeoecology 182 (3-4), 287-303, doi: 10.1016/S0031-0182(01)00500-4.

Kurzweil, F., Gutjahr, M., Vance, D., Keigwin, L., 2010. Authigenic Pb isotopes from the Laurentian Fan: Changes in chemical weathering and patterns of North American freshwater runoff during the last deglaciation. Earth and Planetary Science Letters 299 (3), 458-465, doi: 10.1016/j.epsl.2010.09.031.

Lacan, F., Jeandel, C., 2005. Neodymium isotopes as a new tool for quantifying exchange fluxes at the continent-ocean interface. Earth and Planetary Science Letters 232 (3-4), 245-257, doi: 10.1016/j.epsl.2005.01.004.

Lacan, F., Tachikawa, K., Jeandel, C., 2012. Neodymium isotopic composition of the oceans: A compilation of seawater data. Chemical Geology 300-301, 177-184, doi: 10.1016/j.chemgeo.2012.01.019.

Lambert, F., Delmonte, B., Petit, J.R., Bigler, M., Kaufmann, P.R., Hutterli, M.A., Stocker, T.F., Ruth, U., Steffensen, J.P., Maggi, V., 2008. Dust-climate couplings over the past 800,000 years from the EPICA Dome C ice core. Nature 452 (7187), 616-619, doi: 10.1038/nature06763.

Lamy, F., 2016. The Expedition PS97 of the Research Vessel POLARSTERN to the Drake Passage in 2016. Berichte zur Polar-und Meeresforschung Reports on polar and marine research 701, doi: 10.2312/BzPM_0701_2016.

Lamy, F., Arz, H.W., Kilian, R., Lange, C.B., Lembke-Jene, L., Wengler, M., Kaiser, J., Baeza-Urrea, O., Hall, I.R., Harada, N., Tiedemann, R., 2015. Glacial reduction and millennial-scale variations in Drake Passage throughflow. Proceedings of the National Academy of Sciences 112 (44), 13496-13501, doi: 10.1073/pnas.1509203112.

Lamy, F., Chiang, J.C.H., Martínez-Méndez, G., Thierens, M., Arz, H.W., Bosmans, J., Hebbeln, D., Lambert, F., Lembke-Jene, L., Stuut, J.-B., 2019. Precession modulation of the South Pacific westerly wind belt over the past million years. Proceedings of the National Academy of Sciences, 201905847, doi: 10.1073/pnas.1905847116.

Lamy, F., Gersonde, R., Winckler, G., Esper, O., Jaeschke, A., Kuhn, G., Ullermann, J., Martínez-Garcia, A., Lambert, F., Kilian, R., 2014. Increased dust deposition in the Pacific

Southern Ocean during glacial periods. Science 343 (6169), 403-407, doi:10.1126/science.1245424.

Lamy, F., Hebbeln, D., Wefer, G., 1998. Terrigenous sediment supply along the Chilean continental margin: modern regional patterns of texture and composition. Geologische Rundschau 87 (3), 477-494, doi:10.1007/s005310050223.

Large, W.G., Yeager, S.G., 2004. Diurnal to decadal global forcing for ocean and sea-ice models: The data sets and flux climatologies NCAR Tech. Note NCAR/TN-4601STR. doi:10.5065/D6KK98Q6.

Leat, P.T., Scarrow, J.H., Millar, I.L., 1995. On the Antarctic Peninsula batholith. Geological Magazine 132 (4), 399-412, doi:10.1017/S0016756800021464.

Ledbetter, M.T., 1986. A Late Pleistocene time-series of bottom-current speed in the Vema Channel. Palaeogeography, Palaeoclimatology, Palaeoecology 53 (1), 97-105, doi:10.1016/0031-0182(86)90040-4.

Lee, J.I., Yoon, H.I., Yoo, K.-C., Lim, H.S., Lee, Y.I., Kim, D., Bak, Y.-S., Itaki, T., 2012. Late Quaternary glacial–interglacial variations in sediment supply in the southern Drake Passage. Quaternary Research 78 (1), 119-129, doi:10.1016/j.yqres.2012.03.010.

Li, F., Ginoux, P., Ramaswamy, V., 2008. Distribution, transport, and deposition of mineral dust in the Southern Ocean and Antarctica: Contribution of major sources. Journal of Geophysical Research: Atmospheres 113 (D10), doi:10.1029/2007JD009190.

Lippold, J., Gutjahr, M., Blaser, P., Christner, E., de Carvalho Ferreira, M.L., Mulitza, S., Christl, M., Wombacher, F., Böhm, E., Antz, B., Cartapanis, O., Vogel, H., Jaccard, S.L., 2016. Deep water provenance and dynamics of the (de)glacial Atlantic meridional overturning circulation. Earth and Planetary Science Letters 445, 68-78, doi:https://doi.org/10.1016/j.epsl.2016.04.013.

Lippold, J., Pöppelmeier, F., Süfke, F., Gutjahr, M., Goepfert, T.J., Blaser, P., Friedrich, O., Link, J.M., Wacker, L., Rheinberger, S., Jaccard, S.L., 2019. Constraining the variability of the Atlantic Meridional Overturning Circulation during the Holocene. Geophysical Research Letters 0 (ja), doi:10.1029/2019gl084988.

Lisiecki, L.E., Raymo, M.E., 2005. A Pliocene-Pleistocene stack of 57 globally distributed benthic δ18O records. Paleoceanography 20 (1), n/a-n/a, doi:10.1029/2004pa001071.

Liu, J., Nowaczyk, N.R., Panovska, S., Korte, M., Arz, H.W., 2020. The Norwegian-Greenland Sea, the Laschamps and the Mono Lake excursions recorded in a Black Sea sedimentary sequence spanning from 68.9 to 14.5 ka. submitted to Journal of Geophysical Research: Solid Earth.

Livermore, R., Nankivell, A., Eagles, G., Morris, P., 2005. Paleogene opening of Drake Passage. Earth and Planetary Science Letters 236 (1-2), 459-470, doi:10.1016/j.epsl.2005.03.027.

Lynch-Stieglitz, J., Adkins, J.F., Curry, W.B., Dokken, T., Hall, I.R., Herguera, J.C., Hirschi, J.J., Ivanova, E.V., Kissel, C., Marchal, O., Marchitto, T.M., McCave, I.N., McManus, J.F., Mulitza, S., Ninnemann, U., Peeters, F., Yu, E.F., Zahn, R., 2007. Atlantic meridional overturning circulation during the Last Glacial Maximum. Science 316 (5821), 66-69, doi:10.1126/science.1137127.

Lynch‐Stieglitz, J., Ito, T., Michel, E., 2016. Antarctic density stratification and the strength of the circumpolar current during the Last Glacial Maximum. Paleoceanography 31 (5), 539-552, doi:10.1002/2015PA002915.

Müller, P.J., Schneider, R., 1993. An automated leaching method for the determination of opal in sediments and particulate matter. Deep Sea Research Part I: Oceanographic Research Papers 40 (3), 425-444, doi:10.1016/0967-0637(93)90140-X.

Maldonado, A., Bohoyo, F., Galindo-Zaldívar, J., Hernández-Molina, F.J., Lobo, F.J., Lodolo, E., Martos, Y.M., Pérez, L.F., Schreider, A.A., Somoza, L., 2014. A model of oceanic development by ridge jumping: Opening of the Scotia Sea. Global and Planetary Change 123, 152-173, doi:10.1016/j.gloplacha.2014.06.010.

Marinoni, L., Setti, M., Gauthier-Lafaye, F., 2000. Surface carbonate and land-derived clastic marine sediments from southern Chile: mineralogical and geochemical investigation. Journal of South American Earth Sciences 13 (8), 775-784, doi:10.1016/S0895-9811(00)00059-6.

Marinoni, L., Setti, M., Salvi, C., Lopez-Galindo, A., 2008. Clay minerals in late Quaternary sediments from the south Chilean margin as indicators of provenance and palaeoclimate. Clay Minerals 43 (2), 235-253, doi:10.1180/claymin.2008.043.2.07.

Marshall, J., Speer, K., 2012. Closure of the meridional overturning circulation through Southern Ocean upwelling. Nature Geoscience 5, 171-180, doi:10.1038/ngeo1391.

Martínez-García, A., Sigman, D.M., Ren, H., Anderson, R.F., Straub, M., Hodell, D.A., Jaccard, S.L., Eglinton, T.I., Haug, G.H., 2014. Iron fertilization of the Subantarctic Ocean during the last ice age. Science 343 (6177), 1347-1350, doi:10.1126/science.1246848.

Martin, T., Steele, M., Zhang, J., 2014. Seasonality and long-term trend of Arctic Ocean surface stress in a model. Journal of Geophysical Research: Oceans 119 (3), 1723-1738, doi:10.1002/2013jc009425.

Martinic, B.M., 2019. Entre el mito y la realidad. La situación de la misteriosa Isla Elizabeth de Francis Drake. Magallania (Punta Arenas) 47, 5-14, doi:10.4067/S0718-22442019000100005

Mazaud, A., Michel, E., Dewilde, F., Turon, J., 2010. Variations of the Antarctic Circumpolar Current intensity during the past 500 ka. Geochemistry, Geophysics, Geosystems 11 (8), doi:10.1029/2010GC003033.

McCarthy, G.D., Brown, P.J., Flagg, C.N., Goni, G., Houpert, L., Hughes, C.W., Hummels, R., Inall, M., Jochumsen, K., Larsen, K.M.H., Lherminier, P., Meinen, C.S., Moat, B.I., Rayner, D., Rhein, M., Roessler, A., Schmid, C., Smeed, D.A., 2020. Sustainable Observations of the AMOC: Methodology and Technology. Reviews of Geophysics 58 (1), e2019RG000654, doi:10.1029/2019rg000654.

McCave, I., Crowhurst, S., Kuhn, G., Hillenbrand, C., Meredith, M., 2014. Minimal change in Antarctic Circumpolar Current flow speed between the last glacial and Holocene. Nature Geoscience 7 (2), 113-116, doi:10.1038/ngeo2037.

McCave, I.N., Andrews, J.T., 2019. Distinguishing current effects in sediments delivered to the ocean by ice. I. Principles, methods and examples. Quaternary Science Reviews 212, 92-107, doi: 10.1016/j.quascirev.2019.03.031.

McCave, I.N., Hall, I.R., 2006. Size sorting in marine muds: Processes, pitfalls, and prospects for paleoflow-speed proxies. Geochemistry Geophysics Geosystems 7 (10), doi: 10.1029/2006gc001284.

McCave, I.N., Manighetti, B., Robinson, S.G., 1995. Sortable silt and fine sediment size/composition slicing: parameters for palaeocurrent speed and palaeoceanography. Paleoceanography 10 (3), 593-610, doi: 10.1029/94PA03039.

McCave, I.N., Thornalley, D.J.R., Hall, I.R., 2017. Relation of sortable silt grain-size to deep-sea current speeds: Calibration of the 'Mud Current Meter'. Deep Sea Research Part I: Oceanographic Research Papers 127, 1-12, doi:10.1016/j.dsr.2017.07.003.

Meijers, A.J.S., 2014. The Southern Ocean in the Coupled Model Intercomparison Project phase 5. Phil.

Trans. R. Soc. A 372 (2019), doi:10.1098/rsta.2013.0296.

Mendelová, M., Hein, A.S., Rodés, Á., Xu, S., 2020. Extensive mountain glaciation in central Patagonia during Marine Isotope Stage 5. Quaternary Science Reviews 227, 105996, doi:10.1016/j.quascirev.2019.105996.

Meredith, M.P., Falk, U., Bers, A.V., Mackensen, A., Schloss, I.R., Barlett, E.R., Jerosch, K., Busso, A.S., Abele, D., 2018. Anatomy of a glacial meltwater discharge event in an Antarctic cove. Phil. Trans. R. Soc. A 376 (2122), 20170163, doi:10.1098/rsta.2017.0163.

Meredith, M.P., Gordon, A.L., Naveira Garabato, A.C., Abrahamsen, E.P., Huber, B.A., Jullion, L., Venables, H.J., 2011a. Synchronous intensification and warming of Antarctic Bottom Water outflow from the Weddell Gyre. Geophysical Research Letters 38 (3), doi:10.1029/2010GL046265.

Meredith, M.P., Woodworth, P.L., Chereskin, T.K., Marshall, D.P., Allison, L.C., Bigg, G.R., Donohue, K., Heywood, K.J., Hughes, C.W., Hibbert, A., 2011b. Sustained monitoring of the Southern Ocean at Drake Passage: Past achievements and future priorities. Reviews of Geophysics 49 (4), doi:10.1029/2010RG000348.

Miller, R.L., Kahn, J.S., 1962. Statistical analysis in the geological sciences. Wiley, New York.

Molina-Kescher, M., Frank, M., Tapia, R., Ronge, T.A., Nürnberg, D., Tiedemann, R., 2016. Reduced admixture of North Atlantic Deep Water to the deep central South Pacific during the last two glacial periods. Paleoceanography 31 (6), 651-668, doi:10.1002/2015pa002863.

Molyneux, E.G., Hall, I.R., Zahn, R., Diz, P., 2007. Deep water variability on the southern Agulhas Plateau: Interhemispheric links over the past 170 ka. Paleoceanography 22 (4).

Moore, D.M., Reynolds, R.C., 1989. Identification of Clay Minerals and Associated Minerals. In: X-ray Diffraction and the Identification and Analysis of Clay Minerals. Oxford university press, New York, pp. 250-257.

Moreno, P.I., Denton, G.H., Moreno, H., Lowell, T.V., Putnam, A.E., Kaplan, M.R., 2015. Radiocarbon chronology of the last glacial maximum and its termination in northwestern Patagonia. Quaternary Science Reviews 122, 233-249, doi:10.1016/j.quascirev.2015.05.027.

Naveira Garabato, A.C., Jullion, L., Stevens, D.P., Heywood, K.J., King, B.A., 2009. Variability of Subantarctic Mode Water and Antarctic Intermediate Water in the Drake Passage during the late-twentieth and early-twenty-first centuries. Journal of Climate 22 (13), 3661-3688, doi:10.1175/2009JCLI2621.1.

Negre, C., Zahn, R., Thomas, A.L., Masque, P., Henderson, G.M., Martinez-Mendez, G., Hall, I.R., Mas, J.L., 2010. Reversed flow of Atlantic deep water during the Last Glacial Maximum. Nature 468 (7320), 84-88, doi:10.1038/nature09508.

Nesbitt, H.W., Fedo, C.M., Young, G.M., 1997. Quartz and feldspar stability, steady and non-steady-state weathering, and petrogenesis of siliciclastic sands and muds. The Journal of Geology 105 (2), 173-192, doi:10.1086/515908.

Nielsen, S.H.H., Hodell, D.A., Kamenov, G., Guilderson, T., Perfit, M.R., 2007. Origin and significance of ice-rafted detritus in the Atlantic sector of the Southern Ocean. Geochemistry, Geophysics, Geosystems 8 (12), doi:10.1029/2007gc001618.

Ninnemann, U.S., Charles, C.D., 2002. Changes in the mode of Southern Ocean circulation over the last glacial cycle revealed by foraminiferal stable isotopic variability. Earth and Planetary Science Letters 201 (2), 383-396, doi:10.1016/S0012-821X(02)00708-2.

Nowaczyk, N., 2001. Logging of magnetic susceptibility in Tracking environmental change using lake

sediments. Kluwer Academic Publishers, Dortrecht, Netherlands.

Nowaczyk, N.R., Arz, H.W., Frank, U., Kind, J., Plessen, B., 2012. Dynamics of the Laschamp geomagnetic excursion from Black Sea sediments. Earth and Planetary Science Letters 351-352, 54-69, doi:10.1016/j.epsl.2012.06.050.

Olsen, A., Key, R.M., van Heuven, S., Lauvset, S.K., Velo, A., Lin, X., Schirnick, C., Kozyr, A., Tanhua, T., Hoppema, M., Jutterström, S., Steinfeldt, R., Jeansson, E., Ishii, M., Pérez, F.F., Suzuki, T., 2016. The Global Ocean Data Analysis Project version 2 (GLODAPv2) – an internally consistent data product for the world ocean. Earth Syst. Sci. Data 8 (2), 297-323, doi:10.5194/essd-8-297-2016.

Orsi, A., Johnson, G., Bullister, J., 1999. Circulation, mixing, and production of Antarctic Bottom Water. Progress in Oceanography 43 (1), 55-109, doi:10.1016/S0079-6611(99)00004-X.

Orsi, A.H., Whitworth III, T., Nowlin Jr, W.D., 1995. On the meridional extent and fronts of the Antarctic Circumpolar Current. Deep Sea Research Part I: Oceanographic Research Papers 42 (5), 641-673, doi:10.1016/0967-0637(95)00021-W.

Pöppelmeier, F., Blaser, P., Gutjahr, M., Jaccard, S.L., Frank, M., Max, L., Lippold, J., 2020. Northern-sourced water dominated the Atlantic Ocean during the Last Glacial Maximum. Geology, doi:10.1130/g47628.1.

Pérez, L.F., Henández-Molina, F.J., Lodolo, E., Bohoyo, F., Galindo-Zaldívar, J., Maldonado, A., 2019. Oceanographic and climatic consequences of the tectonic evolution of the southern scotia sea basins, Antarctica. Earth-Science Reviews, 102922, doi:10.1016/j.earscirev.2019.102922.

Paillard, D., Labeyrie, L., Yiou, P., 1996. Macintosh Program performs time-series analysis. Eos, Transactions American Geophysical Union 77 (39), 379-379, doi:10.1029/96eo00259.

Park, Y.K., Lee, J.I., Jung, J., Hillenbrand, C.-D., Yoo, K.-C., Kim, J., 2019. Elemental Compositions of Smectites Reveal Detailed Sediment Provenance Changes during Glacial and Interglacial Periods: The Southern Drake Passage and Bellingshausen Sea, Antarctica. Minerals 9 (5), 322, doi:10.3390/min9050322.

Paterson, G.A., Heslop, D., 2015. New methods for unmixing sediment grain size data. Geochemistry, Geophysics, Geosystems 16 (12), 4494-4506, doi:10.1002/2015gc006070.

Pedro, J.B., Jochum, M., Buizert, C., He, F., Barker, S., Rasmussen, S.O., 2018. Beyond the bipolar seesaw: Toward a process understanding of interhemispheric coupling. Quaternary Science Reviews 192, 27-46, doi:10.1016/j.quascirev.2018.05.005.

Peeters, F.J., Acheson, R., Brummer, G.-J.A., De Ruijter, W.P., Schneider, R.R., Ganssen, G.M., Ufkes, E., Kroon, D., 2004. Vigorous exchange between the Indian and Atlantic oceans at the end of the past five glacial periods. Nature 430 (7000), 661, doi:10.1038/nature02785.

Pena, L.D., Goldstein, S.L., 2014. Thermohaline circulation crisis and impacts during the mid-Pleistocene transition. Science 345 (6194), 318-322, doi:10.1126/science.1249770.

Petit, J.R., Mourner, L., Jouzel, J., Korotkevich, Y.S., Kotlyakov, V.I., Lorius, C., 1990. Palaeoclimatological and chronological implications of the Vostok core dust record. Nature 343 (6253), 56-58, doi:10.1038/343056a0.

Petschick, R., Kuhn, G., Gingele, F., 1996. Clay mineral distribution in surface sediments of the South Atlantic: sources, transport, and relation to oceanography. Marine Geology 130 (3), 203-229, doi:10.1016/0025-3227(95)00148-4.

Piola, A.R., Campos, E.J., Donners, J., Gordon, A.L., Nof, D., 2003. 5.2 The South Atlantic contribution to the global thermohaline circulation [R]. In: CLIVAR SACOS workshop report.,

32.

Piotrowski, A.M., Banakar, V.K., Scrivner, A.E., Elderfield, H., Galy, A., Dennis, A., 2009. Indian Ocean circulation and productivity during the last glacial cycle. Earth and Planetary Science Letters 285 (1), 179-189, doi:10.1016/j.epsl.2009.06.007.

Piotrowski, A.M., Goldstein, S.L., Hemming, S.R., Fairbanks, R.G., 2005. Temporal relationships of carbon cycling and ocean circulation at glacial boundaries. Science 307 (5717), 1933-1938, doi:10.1126/science.1104883.

Piotrowski, A.M., Goldstein, S.L., Hemming, S.R., Fairbanks, R.G., Zylberberg, D.R., 2008. Oscillating glacial northern and southern deep water formation from combined neodymium and carbon isotopes. Earth and Planetary Science Letters 272 (1-2), 394-405, doi:10.1016/j.epsl.2008.05.011.

Provost, C., Renault, A., Barré, N., Sennéchael, N., Garçon, V., Sudre, J., Huhn, O., 2011. Two repeat crossings of Drake Passage in austral summer 2006: Short-term variations and evidence for considerable ventilation of intermediate and deep waters. Deep Sea Research Part II: Topical Studies in Oceanography 58 (25-26), 2555-2571, doi:10.1016/j.dsr2.2011.06.009.

Pugh, R., McCave, I., Hillenbrand, C.-D., Kuhn, G., 2009. Circum-Antarctic age modelling of Quaternary marine cores under the Antarctic Circumpolar Current: ice-core dust–magnetic correlation. Earth and Planetary Science Letters 284 (1-2), 113-123, doi:10.1016/j.epsl.2009.04.016.

Ramos, V.A., Ghiglione, M.C., 2008. Tectonic Evolution of the Patagonian Andes. In: Rabassa, J. (Ed.), Developments in Quaternary Sciences. Elsevier, pp. 57-71.

Rebesco, M., Pudsey, C., Canals, M., Camerlenghi, A., Barker, P., Estrada, F., Giorgetti, A., 2002. Sediment drifts and deep-sea channel systems, Antarctic Peninsula Pacific Margin. Geological Society, London, Memoirs 22 (1), 353-371, doi:10.1144/GSL.MEM.2002.022.01.25.

Renault, A., Provost, C., Sennéchael, N., Barré, N., Kartavtseff, A., 2011. Two full-depth velocity sections in the Drake Passage in 2006—Transport estimates. Deep Sea Research Part II: Topical Studies in Oceanography 58 (25), 2572-2591, doi:10.1016/j.dsr2.2011.01.004.

Rintoul, S.R., 1991. South Atlantic interbasin exchange. Journal of Geophysical Research: Oceans 96 (C2), 2675-2692, doi:10.1029/90jc02422.

Rintoul, S.R., 2018. The global influence of localized dynamics in the Southern Ocean. Nature 558 (7709), 209-218, doi: 10.1038/s41586-018-0182-3.

Roberts, J., Gottschalk, J., Skinner, L.C., Peck, V.L., Kender, S., Elderfield, H., Waelbroeck, C., Vázquez Riveiros, N., Hodell, D.A., 2016. Evolution of South Atlantic density and chemical stratification across the last deglaciation. Proc Natl Acad Sci U S A 114 (5), E904-E905, doi:10.1073/pnas.1621231114.

Roberts, J., McCave, I.N., McClymont, E.L., Kender, S., Hillenbrand, C.D., Matano, R., Hodell, D.A., Peck, V.L., 2017. Deglacial changes in flow and frontal structure through the Drake Passage. Earth and Planetary Science Letters 474, 397-408, doi: 10.1016/j.epsl.2017.07.004.

Robinson, L.F., van de Flierdt, T., 2009. Southern Ocean evidence for reduced export of North Atlantic Deep Water during Heinrich event 1. Geology 37 (3), 195-198, doi:10.1130/g25363a.1.

Rohling, E.J., Foster, G.L., Grant, K.M., Marino, G., Roberts, A.P., Tamisiea, M.E., Williams, F., 2014. Sea-level and deep-sea-temperature variability over the past 5.3 million years. Nature 508 (7497), 477-482, doi:10.1038/nature13230.

Ronge, T.A., Tiedemann, R., Lamy, F., Kohler, P., Alloway, B.V., De Pol-Holz, R., Pahnke, K., Southon,

J., Wacker, L., 2016. Radiocarbon constraints on the extent and evolution of the South Pacific glacial carbon pool. Nat Commun 7, 11487, doi:10.1038/ncomms11487.

Rowley, P., Kellogg, K., Vennum, W., Laudon, T., Thomson, J., 1991. Tectonic setting of the English Coast, eastern Ellsworth Land, Antarctica. International symposium on Antarctic earth sciences. 5, pp. 467-473.

Süfke, F., Gutjahr, M., Gilli, A., Anselmetti, F.S., Glur, L., Eisenhauer, A., 2019. Early stage weathering systematics of Pb and Nd isotopes derived from a high-Alpine Holocene lake sediment record. Chemical Geology 507, 42-53, doi:10.1016/j.chemgeo.2018.12.026.

Scher, H.D., Whittaker, J.M., Williams, S.E., Latimer, J.C., Kordesch, W.E., Delaney, M.L., 2015. Onset of Antarctic Circumpolar Current 30 million years ago as Tasmanian Gateway aligned with westerlies. Nature 523 (7562), 580-583, doi:10.1038/nature14598.

Schlüter, M., Rickert, D., 1998. Effect of pH on the measurement of biogenic silica. Marine Chemistry 63 (1-2), 81-92, doi:10.1016/S0304-4203(98)00052-8.

Schmittner, A., Saenko, O.A., Weaver, A.J., 2003. Coupling of the hemispheres in observations and simulations of glacial climate change. Quaternary Science Reviews 22 (5), 659-671, doi:10.1016/S0277-3791(02)00184-1.

Siani, G., Colin, C., Michel, E., Carel, M., Richter, T., Kissel, C., Dewilde, F., 2010. Late Glacial to Holocene terrigenous sediment record in the Northern Patagonian margin: Paleoclimate implications. Palaeogeography, Palaeoclimatology, Palaeoecology 297 (1), 26-36, doi:10.1016/j.palaeo.2010.07.011.

Sigman, D.M., Hain, M.P., Haug, G.H., 2010. The polar ocean and glacial cycles in atmospheric CO(2) concentration. Nature 466 (7302), 47-55, doi:10.1038/nature09149.

Sijp, W.P., England, M.H., 2004. Effect of the Drake Passage throughflow on global climate. Journal of Physical Oceanography 34 (5), 1254-1266, doi:10.1175/1520-0485(2004)034<1254:EOTDPT>2.0.CO;2.

Sikes, E.L., Allen, K.A., Lund, D.C., 2017. Enhanced δ13C and δ18O differences between the South Atlantic and South Pacific during the last glaciation: The deep gateway hypothesis. Paleoceanography 32 (10), 1000-1017, doi:10.1002/2017pa003118.

Sikes, E.L., Cook, M.S., Guilderson, T.P., 2016. Reduced deep ocean ventilation in the Southern Pacific Ocean during the last glaciation persisted into the deglaciation. Earth and Planetary Science Letters 438, 130-138, doi:10.1016/j.epsl.2015.12.039.

Sime, L.C., Kohfeld, K.E., Le Quere, C., Wolff, E.W., de Boer, A.M., Graham, R.M., Bopp, L., 2013. Southern Hemisphere westerly wind changes during the Last Glacial Maximum: model-data comparison. Quaternary Science Reviews 64, 104-120, doi:10.1016/j.quascirev.2012.12.008.

Skinner, L.C., Scrivner, A.E., Vance, D., Barker, S., Fallon, S., Waelbroeck, C., 2013. North Atlantic versus Southern Ocean contributions to a deglacial surge in deep ocean ventilation. Geology 41 (6), 667-670, doi:10.1130/g34133.1.

Sloyan, B.M., Rintoul, S.R., 2001. The Southern Ocean Limb of the Global Deep Overturning Circulation. Journal of Physical Oceanography 31 (1), 143-173, doi:10.1175/1520-0485(2001)031<0143:TSOLOT>2.0.CO;2.

Smellie, J., Pallàs, R., Sàbat, F., Zheng, X., 1996. Age and correlation of volcanism in central Livingston Island, South Shetland Islands: K-Ar and geochemical constraints. Journal of South American Earth Sciences 9 (3-4), 265-272, doi:10.1016/0895-9811(96)00012-0.

Sokolov, S., Rintoul, S.R., 2009. Circumpolar structure and distribution of the Antarctic Circumpolar

Current fronts: 1. Mean circumpolar paths. Journal of Geophysical Research-Oceans 114, doi:10.1029/2008jc005108.

Srokosz, M., Bryden, H., 2015. Observing the Atlantic Meridional Overturning Circulation yields a decade of inevitable surprises. Science 348 (6241), 1255575, doi: 10.1126/science.1255575.

Stalling, D., Westerhoff, M., Hege, H.-C., 2005. Amira: A highly interactive system for visual data analysis. The visualization handbook 38, 749-767.

Stein, K., Timmermann, A., Kwon, E.Y., Friedrich, T., 2020. Timing and magnitude of Southern Ocean sea ice/carbon cycle feedbacks. Proceedings of the National Academy of Sciences, 201908670, doi:10.1073/pnas.1908670117.

Stichel, T., Frank, M., Rickli, J., Haley, B.A., 2012. The hafnium and neodymium isotope composition of seawater in the Atlantic sector of the Southern Ocean. Earth and Planetary Science Letters 317-318, 282-294, doi:10.1016/j.epsl.2011.11.025.

Stocker, T.F., Johnsen, S.J., 2003. A minimum thermodynamic model for the bipolar seesaw. Paleoceanography 18 (4), doi: 10.1029/2003pa000920.

Struve, T., 2016. Deciphering glacial-interglacial Southern Ocean dynamics with deep-sea corals. Phd Thesis, doi:archimer.ifremer.fr/doc/00493/60456/.

Struve, T., Wilson, D.J., van de Flierdt, T., Pratt, N., Crocket, K.C., 2019. Middle Holocene expansion of Pacific Deep Water into the Southern Ocean. Proceedings of the National Academy of Sciences, 201908138, doi:10.1073/pnas.1908138117.

Studer, A.S., Sigman, D.M., Martínez‐García, A., Benz, V., Winckler, G., Kuhn, G., Esper, O., Lamy, F., Jaccard, S.L., Wacker, L., 2015. Antarctic Zone nutrient conditions during the last two glacial cycles. Paleoceanography 30 (7), 845-862, doi:10.1002/2014PA002745.

Stuut, J.-B.W., Kasten, S., Lamy, F., Hebbeln, D., 2007. Sources and modes of terrigenous sediment input to the Chilean continental slope. Quaternary International 161 (1), 67-76, doi:10.1016/j.quaint.2006.10.041.

Sugden, D.E., McCulloch, R.D., Bory, A.J.-M., Hein, A.S., 2009. Influence of Patagonian glaciers on Antarctic dust deposition during the last glacial period. Nature Geoscience 2 (4), 281-285, doi:10.1038/ngeo474.

Swart, N.C., Fyfe, J.C., 2012. Observed and simulated changes in the Southern Hemisphere surface westerly wind-stress. Geophysical Research Letters 39 (16), doi:10.1029/2012gl052810.

Talley, L., 2013. Closure of the Global Overturning Circulation Through the Indian, Pacific, and Southern Oceans: Schematics and Transports. Oceanography 26 (1), 80-97, doi:10.5670/oceanog.2013.07.

Tanaka, T., Togashi, S., Kamioka, H., Amakawa, H., Kagami, H., Hamamoto, T., Yuhara, M., Orihashi, Y., Yoneda, S., Shimizu, H., Kunimaru, T., Takahashi, K., Yanagi, T., Nakano, T., Fujimaki, H., Shinjo, R., Asahara, Y., Tanimizu, M., Dragusanu, C., 2000. JNdi-1: a neodymium isotopic reference in consistency with LaJolla neodymium. Chemical Geology 168 (3), 279-281, doi:10.1016/S0009-2541(00)00198-4.

Thirlwall, M.F., 2002. Multicollector ICP-MS analysis of Pb isotopes using a 207pb-204pb double spike demonstrates up to 400 ppm/amu systematic errors in Tl-normalization. Chemical Geology 184 (3), 255-279, doi:10.1016/S0009-2541(01)00365-5.

Thornalley, D.J., Oppo, D.W., Ortega, P., Robson, J.I., Brierley, C.M., Davis, R., Hall, I.R., Moffa-Sanchez, P., Rose, N.L., Spooner, P.T., 2018. Anomalously weak Labrador Sea convection and Atlantic overturning during the past 150 years. Nature 556 (7700), 227,

doi:10.1038/s41586-018-0007-4.

Tingey, R.J., 1991. The geology of Antarctica. Oxford University Press.

Titschack, J., Baum, D., De Pol-Holz, R., López Correa, M., Forster, N., Flögel, S., Hebbeln, D., Freiwald, A., Riegl, B., 2015. Aggradation and carbonate accumulation of Holocene Norwegian cold-water coral reefs. Sedimentology 62 (7), 1873-1898, doi:10.1111/sed.12206.

Toggweiler, J.R., Russell, J.L., Carson, S.R., 2006. Midlatitude westerlies, atmospheric CO2, and climate change during the ice ages. Paleoceanography 21 (2), doi:10.1029/2005pa001154.

Toggweiler, J.R., Samuels, B., 1995. Effect of Drake Passage on the Global Thermohaline Circulation. Deep-Sea Research Part I-Oceanographic Research Papers 42 (4), 477-500, doi:10.1016/0967-0637(95)00012-U.

Toyos, M.H., Lamy, F., Lange, C.B., Lembke-Jene, L., Saavedra-Pellitero, M., Esper, O., Arz, H.W., 2020. Antarctic Circumpolar Current dynamics at the Pacific entrance to the Drake Passage over the past 1.3 million years. Paleoceanography and Paleoclimatology n/a (n/a), e2019PA003773, doi:10.1029/2019pa003773.

Tracey, K.L., 2015. Data collected by current-and-pressure-recording inverted echo sounders (CPIES) and current meter moorings in Drake Passage as part of cDrake from November 2007 to December 2011 (NCEI Accession 0121256). doi:https://accession.nodc.noaa.gov/0121256.

Vallelonga, P., Gabrielli, P., Balliana, E., Wegner, A., Delmonte, B., Turetta, C., Burton, G., Vanhaecke, F., Rosman, K.J.R., Hong, S., Boutron, C.F., Cescon, P., Barbante, C., 2010. Lead isotopic compositions in the EPICA Dome C ice core and Southern Hemisphere Potential Source Areas. Quaternary Science Reviews 29 (1), 247-255, doi:10.1016/j.quascirev.2009.06.019.

Vance, D., Thirlwall, M., 2002. An assessment of mass discrimination in MC-ICPMS using Nd isotopes. Chemical Geology 185 (3), 227-240, doi:10.1016/S0009-2541(01)00402-8.

Veres, D., Bazin, L., Landais, A., Kele, H.T.M., Lemieux-Dudon, B., Parrenin, F., Martinerie, P., Blayo, E., Blunier, T., Capron, E., Chappellaz, J., Rasmussen, S.O., Severi, M., Svensson, A., Vinther, B., Wolff, E.W., 2013. The Antarctic ice core chronology (AICC2012): an optimized multi-parameter and multi-site dating approach for the last 120 thousand years. Climate of the Past 9 (4), 1733-1748, doi:10.5194/cp-9-1733-2013.

Walter, H., Hegner, E., Diekmann, B., Kuhn, G., 2000. Provenance and transport of terrigenous sediment in the South Atlantic Ocean and their relations to glacial and interglacial cycles: Nd and Sr isotopic evidence. Geochimica Et Cosmochimica Acta 64 (22), 3813-3827, doi:10.1016/S0016-7037(00)00476-2.

Weber, M., Clark, P., Kuhn, G., Timmermann, A., Sprenk, D., Gladstone, R., Zhang, X., Lohmann, G., Menviel, L., Chikamoto, M., 2014. Millennial-scale variability in Antarctic ice-sheet discharge during the last deglaciation. Nature 510 (7503), 134, doi:10.1038/nature13397.

Weber, M.E., Kuhn, G., Sprenk, D., Rolf, C., Ohlwein, C., Ricken, W., 2012. Dust transport from Patagonia to Antarctica – A new stratigraphic approach from the Scotia Sea and its implications for the last glacial cycle. Quaternary Science Reviews 36, 177-188, doi:10.1016/j.quascirev.2012.01.016.

Weltje, G.J., 1997. End-member modeling of compositional data: Numerical-statistical algorithms for solving the explicit mixing problem. Mathematical Geology 29 (4), 503-549, doi:10.1007/BF02775085.

Weltje, G.J., Tjallingii, R., 2008. Calibration of XRF core scanners for quantitative geochemical logging of sediment cores: Theory and application. Earth and Planetary Science Letters 274 (3),

423-438, doi:10.1016/j.epsl.2008.07.054.

Wengler, M., Lamy, F., Struve, T., Borunda, A., Böning, P., Geibert, W., Kuhn, G., Pahnke, K., Roberts, J., Tiedemann, R., 2019. A geochemical approach to reconstruct modern dust fluxes and sources to the South Pacific. Geochimica Et Cosmochimica Acta, doi:10.1016/j.gca.2019.08.024.

Winslow, M., 1982. The structural evolution of the Magallanes Basin and neotectonics in the Southernmost Andes. International Union of Geological Sciences 4, University of Winsconsin Press, Madison, USA.

Wu, J., Rember, R., Jin, M., Boyle, E.A., Flegal, A.R., 2010. Isotopic evidence for the source of lead in the North Pacific abyssal water. Geochimica Et Cosmochimica Acta 74 (16), 4629-4638, doi:10.1016/j.gca.2010.05.017.

Wu, S., Kuhn, G., Diekmann, B., Lembke-Jene, L., Tiedemann, R., Zheng, X., Ehrhardt, S., Arz, H.W., Lamy, F., 2019. Surface sediment characteristics related to provenance and ocean circulation in the Drake Passage sector of the Southern Ocean. Deep Sea Research Part I: Oceanographic Research Papers 154, 103135, doi:10.1016/j.dsr.2019.103135.

Wunsch, C., Ferrari, R., 2004. Vertical Mixing, Energy, and the General Circulation of the Oceans. Annual Review of Fluid Mechanics 36 (1), 281-314, doi:10.1146/annurev.fluid.36.050802.122121.

Xiao, W., Frederichs, T., Gersonde, R., Kuhn, G., Esper, O., Zhang, X., 2016. Constraining the dating of late Quaternary marine sediment records from the Scotia Sea (Southern Ocean). Quaternary Geochronology 31, 97-118.

Yamazaki, T., Ikehara, M., 2012. Origin of magnetic mineral concentration variation in the Southern Ocean. Paleoceanography 27 (2), doi:10.1029/2011pa002271.

Yarincik, K.M., Murray, R.W., Peterson, L.C., 2000. Climatically sensitive eolian and hemipelagic deposition in the Cariaco Basin, Venezuela, over the past 578,000 years: Results from Al/Ti and K/Al. Paleoceanography 15 (2), 210-228, doi:10.1029/1999pa900048.

Zabel, M., Schneider, R.R., Wagner, T., Adegbie, A.T., de Vries, U., Kolonic, S., 2001. Late Quaternary Climate Changes in Central Africa as Inferred from Terrigenous Input to the Niger Fan. Quaternary Research 56 (2), 207-217, doi:10.1006/qres.2001.2261.

Zachos, J., Pagani, M., Sloan, L., Thomas, E., Billups, K., 2001. Trends, rhythms, and aberrations in global climate 65 Ma to present. Science 292 (5517), 686-693, doi:10.1126/science.1059412.

9 Appendix

The appendices provide data that are presented and discussed in this thesis. Further data that were collected within the framework of this thesis will be archived within PANGAEA and made available whilst these results are published.

The data presented in Chapter 3 have been published and available on PANGAEA, https: //doi.pangaea.de/10.1594/PANGAEA.907140.

The data presented in Chapter 4 can be found in the folder (Chapter 4) in the CD.

The data presented in Chapter 5 can be found in the folder (Chapter 5) in the CD.

The data presented in Chapter 6 can be found in the folder (Chapter 6) in the CD.

Table S3.1 Components of surface samples in the Drake Passage from PS97 cruise.

Station Number	Latitude	Longitude	Water depth (m)	Biog. Opal (wt% sc)	Carbonate (%)	Terrigenous (%)	Sand (%)	Slit (%)	Clay (%)	$\overline{SS}$ (um)	SS (%)	σ
Southern Chilean Margin (SCM)												
PS97/015-2	55° 43.91' S	70° 53.54' W	1872	1.5	65.5	32.5	16.6	15.8	0.2	31.4	83.2	1.2
PS97/020-1	55° 30.80' S	71° 38.25' W	2070	2.5	68.7	28.2	9.3	18.8	0.1	25.7	72.7	1.3
PS97/021-1	55° 06.92' S	72° 40.15' W	1839	0.8	71.0	27.6	13.7	13.7	0.2	34.8	93.6	0.8
PS97/022-1	54° 42.00' S	73° 48.45' W	1616	4.0	69.8	24.7	9.2	13.0	2.4	35.8	90.2	1.0
PS97/024-2	54° 35.32' S	73° 57.32' W	1273	0.9	46.4	52.3	24.9	23.8	3.7	34.7	84.0	1.2
PS97/027-1	54° 23.08' S	74° 36.39' W	2342	0.9	62.1	36.5	13.2	21.6	1.7	28.4	75.0	1.3
PS97/114-1	54° 34.74' S	76° 38.79' W	3863	3.2	49.9	46.5	11.7	0.0	34.8	19.8	42.4	1.2
PS97/122-2	54° 6.03' S	74° 55.15' W	2560	2.2	62.6	34.8	5.2	25.0	4.6	25.6	68.6	1.3
PS97/128-1	53° 38.02' S	75° 32.57' W	2294	1.4	60.4	37.6	12.7	21.4	3.5	28.4	72.1	1.4
PS97/129-2	53° 19.32' S	75° 12.78' W	1879	1.7	63.7	33.9	9.1	22.3	2.5	29.5	80.9	1.2
PS97/131-1	52° 39.56' S	75° 33.91' W	1028	0.9	58.0	40.4	29.0	10.2	1.2	38.0	83.3	1.3
PS97/132-2	52° 36.98' S	75° 35.21' W	843	0.4	45.0	54.2	48.8	4.6	0.8	34.4	86.1	1.2
PS97/134-1	52° 40.98' S	75° 34.88' W	1075	0.8	56.2	42.3	19.6	21.9	0.7	40.1	92.4	1.0
PS97/135-1	52° 42.03' S	75° 35.44' W	1094	1.3	54.5	43.2	17.1	22.8	3.3	38.2	90.3	1.1
PS97/139-2	52° 26.57' S	75° 42.46' W	640	0.5	47.4	51.3	40.7	9.5	1.1	38.8	89.3	1.1
Drake Passage (DP)												
PS97/042-1	59° 50.59' S	66° 5.59' W	4172	9.1	33.1	57.2	16.9	32.0	8.3	23.0	80.1	1.1
PS97/044-1	60° 36.79' S	66° 1.30' W	1203	0.9	93.3	5.6	5.6	0.0	0	-	-	-
PS97/045-1	60° 34.25' S	66° 5.65' W	2293	2.1	92.7	4.9	4.9	0.0	0	25.3	63.4	1.3
PS97/046-6	60° 59.84' S	65° 21.43' W	2789	5.5	61.1	33.0	32.2	0.8	0	24.6	63.8	1.3
PS97/048-1	61° 26.39' S	64° 53.20' W	3448	5.9	28.6	65.1	20.9	38.0	6.2	22.6	61.2	1.3

Continued on new page

Table S3.1 Continued from previous page

Station Number	Latitude	Longitude	Water depth (m)	Biog. Opal (wt% sc)	Carbonate (%)	Terrigenous (%)	Sand (%)	Slit (%)	Clay (%)	$\overline{SS}$ (um)	SS (%)	σ
PS97/049-2	61° 40.27' S	64° 57.69' W	3758	9.3	7.5	82.7	17.7	59.0	6.0	22.9	61.6	1.3
PS97/052-3	62° 29.94' S	64° 17.59' W	2890	3.2	25.2	71.4	51.7	15.4	4.3	24.9	64.1	1.3
PS97/079-1	60° 08.58' S	58° 59.36' W	3539	11.7	7.5	80.1	2.1	61.0	17.0	19.9	48.9	1.2
PS97/080-2	59° 40.43' S	59° 37.73' W	3106	8.4	15.5	75.2	14.2	54.0	7.0	22.2	64.3	1.2
PS97/083-1	58° 59.64' S	60° 34.25' W	3762	5.6	20.6	73.5	25.5	42.0	6.0	28.0	73.2	1.0
PS97/084-2	58° 52.14' S	60° 52.03' W	3557	9.1	15.4	74.8	12.0	60.8	2.0	22.3	60.0	1.2
PS97/085-2	58° 21.28' S	62° 10.00' W	3091	1.6	21.1	77.0	37.1	36.6	3.3	33.4	89.8	2.1
PS97/086-2	58° 38.66' S	61° 23.87' W	2969	3.0	43.3	53.4	11.6	39.0	2.9	33.9	86.6	1.2
PS97/089-2	58° 13.54' S	62° 43.43' W	3437	0.9	17.4	81.4	42.9	36.6	2.0	33.3	91.2	1.0
PS97/093-3	57° 29.91' S	70° 16.47' W	3781	2.6	46.2	51.0	34.8	13.0	3.1	23.5	65.2	1.3
PS97/094-1	57° 0.16' S	70° 58.28' W	3993	1.0	30.3	68.6	32.5	35.0	1.1	30.1	81.4	1.2
PS97/095-1	56° 14.68' S	66° 14.93' W	1652	0.5	50.2	49.0	47.6	1.4	0	34.2	96.3	2.6
PS97/096-1	56° 4.54' S	66° 08.95' W	1613	0.4	67.2	32.2	30.6	1.6	0	-	-	-
PS97/097-1	57° 3.20' S	67° 03.94' W	2319	0.1	51.1	48.6	48.0	0.6	0	-	-	-
Antarctic Peninsula (AP)												
PS97/053-1	62° 39.83' S	63° 05.67' W	2016	11.1	1.2	87.0	3.0	69.0	15.0	23.2	67.1	1.2
PS97/054-2	63° 14.02' S	61° 20.57' W	1279	12.6	3.0	82.7	2.7	67.0	13.0	19.2	48.6	1.1
PS97/055-2	63° 32.08' S	60° 40.38' W	723	14.4	3.3	80.2	4.2	68.0	8.0	20.6	48.0	1.3
PS97/056-1	63° 45.42' S	60° 26.48' W	635	16.0	3.1	78.9	2.9	64.0	12.0	20.1	46.3	1.2
PS97/059-1	62° 26.25' S	59° 39.49' W	354	5.6	2.5	90.9	22.9	59.0	9.0	17.9	55.6	1.0
PS97/060-1	62° 35.00' S	59° 38.66' W	462	7.4	1.7	89.9	8.9	64.0	17.0	16.5	37.5	1.0
PS97/061-1	62° 33.53' S	59° 47.96' W	467	8.3	2.1	88.6	7.6	63.0	18.0	20.8	53.7	1.2

Continued on new page

Table S3.1 Continued from previous page

Station Number	Latitude	Longitude	Water depth (m)	Biog. Opal (wt% sc)	Carbonate (%)	Terrigenous (%)	Sand (%)	Slit (%)	Clay (%)	$\overline{SS}$ (um)	SS (%)	□
PS97/062-1	62° 34.17' S	59° 50.82' W	478	6.3	1.9	91.0	12.0	62.0	17.0	23.1	65.0	1.2
PS97/065-2	62° 29.18' S	59° 20.97' W	481	6.6	1.6	90.6	10.6	64.0	16.0	21.2	61.0	1.2
PS97/067-2	62° 25.00' S	59° 08.64' W	550	4.4	1.1	93.9	55.9	29.0	9.0	26.7	70.7	1.3
PS97/068-2	62° 15.50' S	58° 46.31' W	793	19.0	3.2	75.3	3.3	55.0	17.0	19.9	49.2	1.2
PS97/069-1	62° 0.50' S	56° 03.93' W	1635	14.4	2.9	80.4	4.4	53.0	23.0	19.4	42.8	1.2
PS97/071-2	61° 49.72' S	55° 38.72' W	442	6.5	2.4	89.8	5.8	68.0	16.0	22.6	69.8	1.1
PS97/072-2	61° 49.74' S	55° 38.80' W	1993	16.3	3.1	77.8	70.6	2.8	4.4	18.0	42.6	1.1
PS97/073-2	61° 49.70' S	55° 38.79' W	2624	16.7	2.1	79.3	1.3	53.0	25.0	20.9	56.1	1.2
PS97/074-1	60° 52.02' S	56° 20.43' W	1831	3.7	0.7	95.2	62.0	32.0	1.2	34.5	82.4	1.2
PS97/077-1	60° 35.44' S	55° 42.07' W	3543	11.6	1.8	85.4	3.4	68.0	14.0	20.3	57.4	1.2

Table S3.2. Mineralogy of bulk, silt and clay fractions in the surface samples.

Station Number	Bulk mineral			Silt mineral			Clay mineral					
	Qz/Fsp	Chl/Mica	Am/Qz	Qz/Fsp	Chl/Mica	Am/Qz	Sme (%)	Ill (%)	Chl (%)	Sme (IB,	Ill (IB, 10Å)	Ill (5Å/10Å)
Southern Chilean Margin (SCM)												
PS97/015-2	1.3	1.6	0.06	2.6	2.5	0.03	0	59	41	0.58	0.72	0.98
PS97/020-1	3.1	1.7	0.02	3.2	1.7	0.04	1	54	45	0.55	0.79	1.01
PS97/021-1	0.8	3.2	0.05	2.9	2.3	0.02	1	61	38	0.46	0.89	0.82
PS97/022-1	3.7	1.3	0.04	3.0	2.4	0.00	2	62	36	2.06	0.88	0.81
PS97/024-2	3.8	1.2	0.03	3.6	2.6	0.02	0	56	44	0.94	0.54	0.41
PS97/027-1	4.2	1.5	0.04	4.4	1.4	0.02	1	55	44	1.13	0.68	0.69
PS97/114-1	3.6	1.2	0.03	3.7	1.6	0.03	2	61	37	0.96	0.58	0.54

Continued on new page

Table S3.2 Continued from previous page

Station Number	Bulk mineral			Silt mineral			Clay mineral					
	Qz/Fsp	Chl/Mica	Am/Qz	Qz/Fsp	Chl/Mica	Am/Qz	Sme (%)	Ill (%)	Chl (%)	Sme (IB,17Å)	Ill (IB,10Å)	Ill (5Å/10Å)
PS97/122-2	3.3	1.3	0.03	3.0	1.6	0.03	1	54	45	0.90	0.65	0.67
PS97/128-1	2.8	1.5	0.03	3.3	1.4	0.03	1	46	53	1.19	0.66	0.74
PS97/129-2	5.3	1.6	0.05	3.8	2.4	0.01	1	47	52	3.00	0.69	0.84
PS97/131-1	3.3	3.3	0.02	4.2	3.2	0.02	1	42	57	0.96	0.62	0.88
PS97/132-2	2.1	2.1	0.02	3.1	1.6	0.04	0	49	51	0.94	0.67	0.63
PS97/134-1	3.1	1.2	0.03	2.3	1.2	0.04	1	51	48	1.18	0.77	0.59
PS97/135-1	3.9	2.0	0.03	4.0	1.9	0.03	0	51	48	0.66	0.79	0.68
PS97/139-2	2.7	1.4	0.02	4.5	3.0	0.02	1	46	53	1.28	0.64	0.61
Drake Passage (DP)												
PS97/042-1	2.7	2.4	0.02	2.0	1.9	0.05	17	36	48	1.25	0.48	0.58
PS97/044-1	0.7	1.0	0.03	0.5	0.0	0.06	-	-	-	-	-	-
PS97/045-1	0.6	1.0	0.16	0.3	0.3	0.04	7	54	40	0.70	0.63	4.09
PS97/046-6	1.8	2.2	0.02	2.3	1.7	0.04	21	37	41	1.39	0.56	0.97
PS97/048-1	1.7	2.2	0.03	2.1	1.8	0.04	17	36	47	1.46	0.47	0.55
PS97/049-2	2.3	2.5	0.02	2.2	1.9	0.04	13	37	50	1.50	0.48	0.48
PS97/052-3	1.5	2.2	0.02	2.0	2.4	0.05	14	31	55	1.41	0.51	0.72
PS97/079-1	2.8	2.0	0.03	1.7	2.1	0.03	20	35	45	1.67	0.48	0.49
PS97/080-2	2.6	2.1	0.03	2.6	1.4	0.06	16	33	51	1.79	0.50	0.63
PS97/083-1	2.8	2.5	0.03	2.2	2.9	0.05	12	34	53	1.49	0.49	0.48
PS97/084-2	2.9	2.6	0.03	3.2	1.8	0.05	16	33	51	1.51	0.48	0.55
PS97/085-2	2.4	1.1	0.03	2.9	3.0	0.03	8	38	54	1.66	0.51	0.50
PS97/086-2	2.3	1.7	0.02	3.0	2.4	0.02	6	49	45	1.65	0.75	0.45
PS97/089-2	1.7	1.6	0.04	3.7	2.7	0.04	4	41	54	1.88	0.52	0.55

Continued on new page

Table S3.2 Continued from previous page

Station Number	Bulk mineral			Silt mineral			Clay mineral					
	Qz/Fsp	Chl/Mica	Am/Qz	Qz/Fsp	Chl/Mica	Am/Qz	Sme (%)	Ill (%)	Chl (%)	Sme (IB,17Å)	Ill (IB,10Å)	Ill (5Å/10Å)
PS97/093-3	1.8	1.7	0.05	2.5	1.9	0.04	7	53	40	1.48	0.48	0.47
PS97/094-1	1.4	0.9	0.06	2.9	2.4	0.04	1	59	40	2.83	0.55	0.53
PS97/095-1	2.3	3.0	0.02	-	-	-	1	40	59	1.29	0.51	0.66
PS97/096-1	2.5	1.6	0.01	-	-	-	-	-	-	-	-	-
PS97/097-1	4.1	4.1	0.01	-	-	-	3	56	41	1.44	0.50	0.66
Antarctic Peninsula (AP)												
PS97/053-1	1.6	6.9	0.03	1.6	3.9	0.04	21	24	55	1.97	0.70	0.67
PS97/054-2	1.6	5.4	0.08	1.9	4.6	0.07	5	23	73	1.65	0.46	0.79
PS97/055-2	1.8	4.2	0.03	1.7	3.0	0.05	6	28	66	1.76	0.44	0.52
PS97/056-1	1.5	3.1	0.03	2.0	2.8	0.03	4	34	61	2.37	0.58	0.69
PS97/059-1	2.2	3.0	0.03	2.3	1.6	0.07	33	9	57	1.57	0.47	1.13
PS97/060-1	1.2	1.3	0.04	0.9	3.2	0.08	32	13	55	1.56	0.51	0.72
PS97/061-1	0.9	2.2	0.05	0.9	2.3	0.08	28	17	55	1.59	0.61	0.63
PS97/062-1	1.3	0.5	0.07	1.0	2.1	0.11	25	14	60	1.68	0.59	0.89
PS97/065-2	1.0	3.2	0.03	0.7	2.7	0.07	30	10	60	1.72	0.44	1.07
PS97/067-2	0.6	2.6	0.04	1.0	2.4	0.06	32	13	55	1.66	0.50	1.01
PS97/068-2	2.3	2.3	0.00	0.9	2.6	0.06	16	29	55	1.51	0.51	0.66
PS97/069-1	2.5	3.2	0.01	2.0	3.5	0.03	14	37	48	1.38	0.76	0.73
PS97/071-2	1.0	5.4	0.02	1.1	2.1	0.04	27	13	60	1.65	0.58	0.73
PS97/072-2	2.5	3.4	0.02	2.0	2.2	0.04	19	33	47	1.95	1.01	0.34
PS97/073-2	2.2	2.9	0.01	2.4	2.5	0.04	19	25	56	1.39	0.50	0.68
PS97/074-1	1.6	1.8	0.02	1.8	2.1	0.03	15	29	56	1.89	0.46	0.86
PS97/077-1	2.4	2.9	0.03	2.2	2.1	0.07	8	31	60	1.43	0.43	0.61

QZ: Quartz; Fsp: Feldspar; Am: Amphibole; Sme: Smectite; Ill: Illite; Chl: Chlorite; IB: Integral-breadth.

Table S3.3. Comparison of low-pass filtered moorings mean speed (U) in the Drake Passage.

[a]Sites	Latitude	Longitude	Water depth (m)	U_1 (cm/s)	[b]Sites	Latitude	Longitude	Water depth (m)	U_2 (cm/s)	$\Delta U = (U_2\text{-}U_1)$
M1	55° 21.0' S	65° 11.3' W	1000	11.6	C02	55° 14.2' S	64° 31.1' W	1800	12.73	1.1
M2	55° 43.2' S	64° 24.2' W	2000	11.6	C02	55° 14.3' S	64° 31.1' W	1800	12.73	1.1
M3	56° 08.4' S	63° 43.1' W	3000	10.8	C20	56° 08.2' S	64° 13.7' W	3899	9.92	-0.9
M4	56° 57.0' S	62° 20.0' W	2500	8.6	C19	56° 54.6' S	63° 54.7' W	3506	7.51	-1.1
M5	57° 37.8' S	60° 55.4' W	2500	2.1	C11	58° 59.5' S	62° 26.5' W	3912	3.57	1.5
M6	58° 19.8' S	59° 31.2' W	2410	5.1	C10	58° 30.1' S	62° 45.3' W	2541	7.62	2.5
M7	58° 57.6' S	58° 06.0' W	2515	3.7	C13	60° 05.5' S	61° 45.9' W	4031	5.42	1.7
M9	60° 06.0' S	55° 15.8' W	2510	0.7	C14	60° 36.0' S	61° 22.4' W	3735	1.47	0.8
M10	60° 37.2' S	53° 50.9' W	2560	3.8	C16	61° 43.4' S	61° 32.9' W	2549	6.07	2.3

a,current meter data are from Koenig et., al (2014); b, current meter data are from Donohue et al., (2016).